Multi-scale modeling of composites

Azizi, Reza

Publication date:
2011

Document Version
Publisher's PDF, also known as Version of record

Multi-scale modeling of composites

PhD Thesis

$$(EIv'')''=q-\rho A\ddot{v}$$

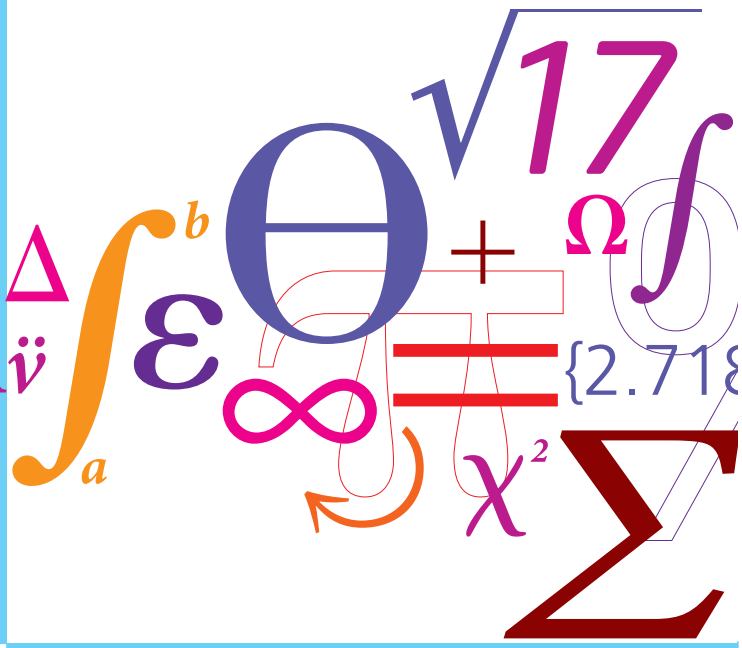

Reza Azizi
DCAMM Special Report No. S135
September 2011

DTU Mechanical Engineering
Department of Mechanical Engineering

Multi-scale modeling of composites

by

Reza Azizi

Title of the thesis:
Multi-scale modeling of composites

Ph.D. student:
Reza Azizi
E-mail: reaz@mek.dtu.dk

Supervisors:
Christian Frithiof Niordson
E-mail: cn@mek.dtu.dk

Brian Nyvang Legarth
E-mail: bnl@mek.dtu.dk

Viggo Tvergaard
E-mail: viggo@mek.dtu.dk

Address:
Department of Mechanical Engineering, Solid Mechanics
Technical University of Denmark
Nils Koppels Allé, Building 404, 2800 Kgs. Lyngby, Denmark

Preface

This thesis is submitted in partial fulfillment of the requirements for obtaining the degree of Ph.D. in mechanical engineering at the Technical University of Denmark (DTU). The Ph.D. project was carried out at the Department of Mechanical Engineering, Solid Mechanics, at DTU in the period September 15st 2008- September 14st 2011. Supervisors on the project were Associate Professors Christian Frithiof Niordson, Brian Nyvang Legarth and Professor Viggo Tvergaard from the department. This work is supported by the Danish Research Council for Technology and Production Sciences in a project entitled Plasticity Across the Scales. The computational resources have been provided by a hardware grant from the Danish Center of Scientific Computing (DCSC).

I am very grateful to my supervisors for their inspiring support and for always taking their time to discuss the work and the results during the project. The special appreciation goes to my main supervisor Christian Frithiof Niordson who has been a most friendly inspiration for me.

A part of this work was carried out with prof.dr.ir. M.G.D. Geers and dr.ir. R.H.J. Peerlings at Eindhoven University of Technology, Eindhoven, Netherlands, during my three months stay in the period April 2010-June 2010. I am very grateful that the stay was made possible and for the new academic input in a friendly and welcoming atmosphere.

I would like to express my gratitude to Professor John W. Hutchinson from Harvard university for his valuable comments on some important issues.

I am grateful to Carl F.O. Dahlberg from the Royal Institute of Technology (KTH) in Sweden and Kim Lau Nielsen from Denmark Technical University for their careful review of the thesis.

I finally wish to thank my colleagues at the section of Solid Mechanics and in particular the other Ph.D-students for creating a cheerful and inspiring working environment.

Kgs. Lyngby, September 14st 2011.

Reza Azizi

Abstrakt

En generel metode til at finde det homogeniserede respons af metal-matrix kompositter er udviklet. Det antages, at den mikroskopiske skala er tilstrækkelig lille sammenlignet med den makroskopiske skala, således at makro-responset ikke påvirker den mikro-mekaniske model. Mikroskalaen kan da analyseres ved hjælp af et Repræsentativt Volumen Element (RVE), hvor homogeniserede data gemmes og bruges som input til makroskalaen. Afhængigheden af fiberstørrelsen i materialet analyseres ved hjælp af en højere ordens plasticitetsteori, hvor oplagring af fri energi som følge af plastiske tøjningsgradienter på mikrometerskala er inkluderet. Hill-Mandels energiprincip benyttes til at finde makroskopiske operatorer baseret på mikromekaniske analyser, udført ved hjælp af finite element metoden under generaliseret plan tøjning. En makroskopisk fænomenologisk model for metal-matrix kompositter udvikles ved hjælp af konstitutive operatorer, som beskriver den elastiske opførsel og den frie energi i materialet, såvel som den plastiske opførsel gennem en flydeflade og dennes anisotrope udvikling. Det er vist, at en generalisering af Hill's anisotrope flydekriterium kan anvendes til at beskrive Bauschinger effekt, samt tryk- og størrelsesafhængighed. Udviklingen af den makroskopiske flydeflade som følge af deformationer er undersøgt, herunder både anisotrop hærdning (udvidelse af flydefladen), samt kinematisk hærdning (translation af flydefladen). Den kinematiske hærdningslov beskrives på baggrund af den oplagrede frie energi i materialet som følge af plastisk deformation. De fundne makroskopiske operatorer kan benyttes til at modellere metal-matrix kompositter på makroskopisk skala ved hjælp af hierarkisk multi-skala modellering. Til sidst er skade under træk- og tværbelastning studeret ved hjælp af en kohæsiv lov for interfacet mellem matrix- og fibermateriale.

Abstract

A general method to obtain the homogenized response of metal-matrix composites is developed. It is assumed that the microscopic scale is sufficiently small compared to the macroscopic scale such that the macro response does not affect the micromechanical model. Therefore, the microscopic scale is analyzed using a Representative Volume Element (RVE), while the homogenized data are saved and used as an input to the macro scale. The dependence of fiber size is analyzed using a higher order plasticity theory, where the free energy is stored due to plastic strain gradients at the micron scale. Hill-Mandel's energy principle is used to find macroscopic operators based on micro-mechanical analyses using the finite element method under generalized plane strain condition. A phenomenologically macroscopic model for metal matrix composites is developed based on constitutive operators describing the elastic behavior and the trapped free energy in the material, in addition to the plastic behavior in terms of the anisotropic development of the yield surface. It is shown that a generalization of Hill's anisotropic yield criterion can be used to model the Bauschinger effect, in addition to the pressure and size dependence. The development of the macroscopic yield surface upon deformation is investigated in terms of the anisotropic hardening (expansion of the yield surface) and kinematic hardening (translation of the yield surface). The kinematic hardening law is based on trapped free energy in the material due to plastic deformation. The macroscopic operators found, can be used to model metal matrix composites on the macroscopic scale using a hierarchical multi-scale approach. Finally, decohesion under tension and shear loading is studied using a cohesive law for the interface between matrix and fiber.

Publications

The following publications are part of the thesis

[P1] Reza Azizi, Effects of back stress in metal matrix composite due to the plastic strain gradients, Proceedings of the X International Conference on Computational Plasticity-COMPLAS X, Barcelona, Spain, September 2-4, 2009.

[P2] Reza Azizi, Christian F. Niordson and Brian N. Legarth, Metal matrix composite with size-effects, Proceedings of the 2th International Conference on Computational Mechanic-AfriCOMP11, Cape Town, South Africa, January 5-8, 2011.

[P3] Reza Azizi, Christian F. Niordson and Brian Nyvang Legarth, Size-effects on yield surfaces for micro reinforced composites, *International Journal of Plasticity*, 27, 1817-1832, 2011.

[P4] Reza Azizi, Christian F. Niordson and Brian N. Legarth, On homogenization of metal matrix composites using strain gradient theory, Submitted.

[P5] R. Azizi, C.F. Niordson, M.G.D. Geers, R.H.J. Peerlings and B.N. Legarth, On the Bauschinger effect and kinematic hardening in metal matrix composites modeled by strain gradient plasticity, To be submitted.

[P6] Reza Azizi, Brian N. Legarth and Christian F. Niordson, A new anisotropic pressure dependent yield function for metal matrix composite using strain gradient theory, Submitted.

[P7] Reza Azizi, Micromechanical modeling of damage in periodic composites using strain gradient plasticity, Submitted.

Contents

Chapter 1
Introduction

This thesis covers research on Metal Matrix Composites (MMCs) addressing some current issues. The study is an initial step of a new approach towards the evaluation of composite's behavior. The research is summarized here, while it is elaborated in the appended papers.

1.1 Definition

The possibility of combining various material systems like metals, ceramics and non-metals gives the opportunity for unlimited variation. The properties of these new materials are basically determined by the properties of their constituents. MMCs as the heterogeneous media are made by dispersing a reinforcing material (e.g. alumina, silicon carbide) into a metal matrix (e.g. aluminum, magnesium, titanium) and are classified according to the type of used reinforcement, e.g. long unidirectional fibers as continuous reinforcement, short fiber/whiskers and particles as noncontinuous reinforcement. The long unidirectional fiber reinforcements produce an anisotropic structure, while the noncontinuous reinforcement may be considered as isotropic. Different types of the reinforcement can have many different improved properties, e.g. temperature strength, stiffness, wear resistance, low density, damping capabilities, thermal expansion coefficients and corrosion resistance, but can also be accompanied by deficiencies like poor ductility and fracture properties (see McDanels, 1985). A conventional modeling approach for evaluating the mechanical behavior of MMCs has been considered by several authors including Tvergaard (1990a), Bao et al. (1991), Tvergaard (1995), Legarth (2003) and Legarth and Kuroda (2004).

1.2 Size effects

One of the important factors which plays a significant role on the strength of the composites is the size of the fiber. Lloyd (1994) showed that the response of composites, with the same volume fraction of SiC particles, depends on the size of the particles. Mughrabi (2001), Fleck et al. (2003) and Gao and Huang (2003) showed that in MMCs, dislocations can not pass from the matrix into the fiber and consequently pile up at the interface. This would lead to a suppression of plastic strain at the interfaces. Strain gradient plasticity has the capability to model this due to the inclusion of constitutive length parameters and the use of non-conventional

boundary conditions. Several non local plasticity theories have been developed. While some of these are of lower-order nature retaining the structure of conventional boundary value problems (see Acharya and Bassani, 2000; Bassani, 2001), most of the proposed theories are of higher order nature, employing higher order stress-measures as work-conjugates to strain gradients, demanding non-conventional higher order boundary conditions (e.g. Fleck and Hutchinson, 1997, 2001; Gao et al., 1999; Gurtin, 2002; Gudmundson, 2004; Gurtin and Anand, 2005; Lele and Anand, 2008; Fleck and Willis, 2009a,b).

1.3 Multi-scale modeling and homogenization

Multi-scale modeling is the analysis of a material, where the required information at each scale is enriched by the information emanated from the lower scales. Both Hierarchical and Concurrent models are two different types of multi-scale modeling methods. With hierarchical models, it is assumed that the scales are separated such that they don't affect each other. Therefore, the properties of the material are obtained prior to the modeling of any more complex problem (e.g. Tamma and Chung, 1999; Feyel, 1999, 2000). With Concurrent models, the global constitutive behavior is determined simultaneously throughout the analysis based on the behavior of the constituents and their interactions (e.g. Zohdi and Wriggers, 1999; Vemaganti and Oden, 2001).
The connection between the scales is considered by homogenization. Different homogenization techniques have been proposed to estimate the overall macroscopic properties; like the effective medium approximation by Eshelby (1957) and Budiansky (1965), the self consistent method by Hill (1965) and the variational bounding methods by Hashin (1983). Recently, due to the powerful computational resources, the most efficient method has been the computational unit cell method as was proposed by (e.g. Hashin and Shtrikman, 1963; Suquet, 1985; Keller et al., 1990; Ghosh et al., 1995; Terada et al., 2000; Wieckowski, 2000; Kouznetsova et al., 2001). Homogenization techniques have also been extended to cover the gradient theories. Niordson and Tvergaard (2001, 2002) used strain gradient plasticity to model the matrix material in order to predict the particle size dependent overall properties of metal matrix composites. Kouznetsova et al. (2004) developed a second order computational homogenization, where the higher order stress conjugate to the full strain gradient tensor is available at the macro scale while using a conventional model at the micro scale.

1.4 Homogenized yield function

For multi-scale modeling, it is needed to introduce a homogenized yield function for composites where the work hardening is traceable. Different hardening rules have been proposed to specify the evolution of the yield surface during plastic deformation including expansion (anisotropic hardening) and translation (kinematic hardening) (e.g. Jansson, 1992, 1995; Iyera et al., 2000; Lee et al., 2004; Chung and Ryou, 2009; Lissenden, 2010). However, experimental results show a distinct change of the shape of the yield surface (rotated or dented) depending on the loading conditions and load paths, (see Phillips and Juh-Ling, 1972; Gupta and H.A., 1983; Kowalsky et al., 1999). One of the more interesting findings from finite element micromechanic analyses is that for an elastic fiber and an inelastic metal matrix, the overall inelastic response is not necessarily pressure independent, even if the local response is pressure independent, see Dvorak et al. (1973). This is associated with the constraint provided by the fiber and the large difference between the local stress (and strain) field with respect to the overall stress (and strain). On the other hand, due to the elastic mismatch of the microstructure constituents, the elastic compressibility at the microscopic scale shows up as plastic compressibility at the macroscopic scale. There have been several numerical attempts to evaluate the anisotropic behavior of metal-matrix composite such as Bao et al. (1991) and Asaro and Needleman (1985). A variety of criteria for anisotropic homogeneous materials, independent of hydrostatic pressure were proposed by Hill (1948), Barlat et al. (1991). Drucker and Prager (1952), Liu et al. (1997), Deshpande et al. (2001) improved previous yield criteria to consider the hydrostatic pressure dependency.

1.5 Research overview

In this research, MMC with long unidirectional fibers is chosen to be studied. The study includes both elastic and plastic deformations. The goal is to specify the phenomenological behavior of MMC with mathematical descriptions, e.g. the yield surface, flow rule and hardening, where it can be used at the higher scale using heirachical method in multi-scale modeling. The study assumes a conventional plasticity theory with an anisotropic pressure dependent yield function at the macro scale and an energetic rate independent strain gradient plasticity theory with an isotropic pressure independent yield function at the micro scale. Fig. 1.1 shows a schematic description of the research including the input and output of the study.
Chapter 2 elaborates the material model at both scales.
Chapter 3 considers a multi-scale modeling method, where the connection between the scales is justified with homogenization using Hill-Mandel energy condition.
Chapter 4 includes the summary of the results presented in papers [P1] to [P7] as

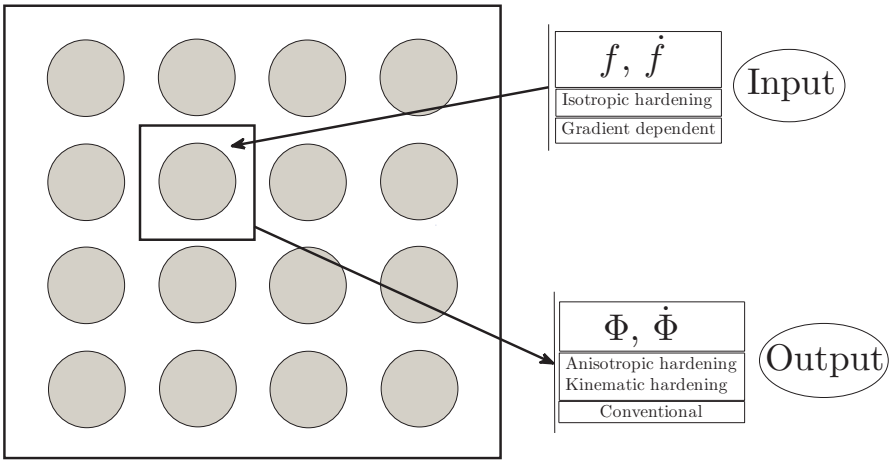

Figure 1.1 A schematic description of the research. Input: f and $\dot{f}$ as the micro yield function and the evolution of the micro yield function, respectively. Output: Φ and $\dot{\Phi}$ as the macro yield function and the evolution of the macro yield function, respectively.

well as additional findings.
Chapter 5 includes the conclusion.

Chapter 2
Model description

The material model is considered to be gradient dependent at the micro scale, where the free energy holds elastic strains and plastic strain gradients, while it is conventional at the macro scale, where the free energy holds elastic strains and plastic strains.

2.1 Material model at the micro scale

The matrix is considered to be a gradient enhanced isotropic elasto-plastic material governed by the rate independent energetic strain-gradient plasticity theory proposed by Gudmundson (2004), while the fibers are assumed to be purely elastic. The first law of thermodynamics in the incremental form is written as

$$\dot{w} = \dot{d} + \dot{\psi} \tag{2.1}$$

where $\dot{w}$ is the rate of total work, $\dot{d}$ is the dissipation rate and $\dot{\psi}$ is the rate of the free energy. In a more general thermodynamic framework, Eq. (2.1) would contain additional heat flux and entropy production terms but the purely mechanical calculations here provide no basis for including these contributions. The second law of thermodynamics, see Chaboche (1993b), must be satisfied as

$$\dot{d} = \dot{w} - \dot{\psi} \geq 0 \tag{2.2}$$

The variation of the internal virtual work, δw_I, is considered as

$$\delta w_I = \int_v [\sigma_{ij}\delta\epsilon_{ij} + (q_{ij} - s_{ij})\delta\epsilon^p_{ij} + m_{ijk}\delta\epsilon^p_{ij,k}]\mathrm{d}v \tag{2.3}$$

where v is the micro volume and ϵ_{ij} is the total strain as the summation of the elastic strain, ϵ^e_{ij}, and the plastic strain, ϵ^p_{ij}, as $\epsilon_{ij} = \epsilon^e_{ij} + \epsilon^p_{ij}$. The Cauchy stress, the deviatoric part of the Cauchy stress, the micro stress (work conjugate to the plastic strain) and the higher order stress (work conjugate to the plastic strain gradients) are denoted by σ_{ij}, s_{ij}, q_{ij} and m_{ijk}, respectively. By application of the Gauss

theorem,

$$\delta w_I = \int_s [\sigma_{ij} n_j \delta u_i + m_{ijk} n_k \delta \epsilon^p_{ij}] \mathtt{d}s - \int_v [\sigma_{ij,j} \delta u_i + (m_{ijk,k} + s_{ij} - q_{ij}) \delta \epsilon^p_{ij}] \mathtt{d}v \tag{2.4}$$

where n_i is the unit vector, normal to the surface, s, and u_i is the displacement vector. Considering the first term of the right hand side of Eq. (2.4) as the external virtual work, δw_E, and using the principle of virtual work, $\delta w_I = \delta w_E$, the last term has to vanish for arbitrary variations and two sets of equilibrium equation are obtained as

$$\begin{aligned} \sigma_{ij,j} = 0, \quad \mathtt{in} \quad v \\ m_{ijk,k} + s_{ij} - q_{ij} = 0, \quad \mathtt{in} \quad v \end{aligned} \tag{2.5}$$

By imposing the incremental version of the internal work, $\dot{w}_I$, on the second law of thermodynamics, Eq. (2.2), and using $\sigma_{ij}\dot{\epsilon}^p_{ij} = s_{ij}\dot{\epsilon}^p_{ij}$, one can show

$$\left(\sigma_{ij} - \frac{\partial \psi}{\partial \epsilon^e_{ij}}\right) \dot{\epsilon}^e_{ij} + \left(q_{ij} - \frac{\partial \psi}{\partial \epsilon^p_{ij}}\right) \dot{\epsilon}^p_{ij} + \left(m_{ijk} - \frac{\partial \psi}{\partial \epsilon^p_{ij,k}}\right) \dot{\epsilon}^p_{ij,k} \geq 0 \tag{2.6}$$

It is assumed that the free energy, ψ, depends on both elastic strains and plastic strain gradients, as

$$\psi\left(\epsilon^e_{ij}, \epsilon^p_{ij,k}\right) = \frac{1}{2} c_{ijkl} \epsilon^e_{ij} \epsilon^e_{kl} + \frac{1}{2} G L^2_* \epsilon^p_{ij,k} \epsilon^p_{ij,k} \tag{2.7}$$

where L_* is a material length scale parameter, G is the elastic shear modulus and c_{ijkl} is the isotropic tensor of the elastic moduli, defined in terms of Young's modulus, E, and Poisson's ratio, ν. Assuming that both the Cauchy stress and higher order stress can be determined directly from ψ, two constitutive equations are extracted as

$$\sigma_{ij} = \frac{\partial \psi}{\partial \epsilon^e_{ij}} = c_{ijkl} \epsilon^e_{kl}, \quad m_{ijk} = \frac{\partial \psi}{\partial \epsilon^p_{ij,k}} = G L^2_* \epsilon^p_{ij,k} \tag{2.8}$$

The second law of thermodynamics, Eq. (2.6), then reads

$$q_{ij} \dot{\epsilon}^p_{ij} \geq 0 \tag{2.9}$$

In order to be sure that the above equation is always non-negative, a dissipation potential function, $f^* = f^*(q_{ij})$, has to be defined as

$$\dot{\epsilon}^p_{ij} = \dot{\lambda} \frac{\partial f^*}{\partial q_{ij}} \tag{2.10}$$

where $\dot{\lambda}$ is a microscopic plastic multiplier. The above equation can satisfy the second law of thermodynamics if the dissipation potential function is convex. Moreover, Eq. (2.10) implies that the plastic strain increment is normal to the dissipation potential function. Here, we decide to have an associative flow rule where the plastic potential function can be substituted by the yield surface, f, see Lubliner (1990) and Tvergaard (2001), as

$$f^*(q_{ij}) = f(q_{ij}) \tag{2.11}$$

The microscopic yield surface, f, is then defined as

$$f = \sqrt{\frac{3}{2} q_{ij} q_{ij}} - \sigma_f = 0 \tag{2.12}$$

where the flow stress is given by $\sigma_f = \sigma_y + h\epsilon_e^p$, with σ_y denoting the initial yield stress, h denoting the hardening modulus and ϵ_e^p denoting the accumulated effective plastic strain as $\epsilon_e^p = \int \dot{\epsilon}_e^p d\tau$ in which τ is "pseudo-time" and $\dot{\epsilon}_e^p = \sqrt{\frac{2}{3}\dot{\epsilon}_{ij}^p \dot{\epsilon}_{ij}^p}$. Then the flow rule, which ensures the normality of the plastic strain increment to the yield surface, is obtained by

$$\dot{\epsilon}_{ij}^p = \dot{\lambda} \frac{\partial f}{\partial q_{ij}} = \frac{3}{2} \frac{q_{ij}}{q_e} \dot{\epsilon}_e^p = r_{ij} \dot{\epsilon}_e^p \tag{2.13}$$

where $q_e = \sqrt{\frac{3}{2} q_{ij} q_{ij}}$ is the effective micro stress and $r_{ij} = \frac{3}{2}\frac{q_{ij}}{q_e}$ is the flow direction.

For the numerical implementation, the evolution law of the micro stress, $\dot{q}_{ij}$, needs to be extracted. By considering $r_{ij} = \frac{3}{2}\frac{q_{ij}}{q_e}$ or equivalently $q_{ij} = \frac{2}{3} q_e r_{ij}$, one can have

$$\dot{q}_{ij} = \overline{\frac{2}{3} q_e r_{ij}}^{\cdot} = \frac{2}{3} \left(\dot{q}_e r_{ij} + q_e \dot{r}_{ij} \right) \tag{2.14}$$

where $\dot{q}_e = h\dot{\epsilon}_e^p$. Using $\dot{\epsilon}_e^p = \frac{2}{3} r_{ij} \dot{\epsilon}_{ij}^p$, the above equation is rewritten as

$$\dot{q}_{ij} = \frac{2}{3} \left(\dot{q}_e r_{ij} + q_e \dot{r}_{ij} \right) = \frac{2}{3} \left(\frac{2}{3} h r_{ij} r_{kl} \dot{\epsilon}_{kl}^p + q_e \dot{r}_{ij} \right) \tag{2.15}$$

Fig. 2.1 shows a schematic plot of the above equation. It is important to know that r_{ij} is orthogonal to $\dot{r}_{ij}$. This is shown as below

$$\begin{aligned} r_{ij} &= \frac{3}{2}\frac{q_{ij}}{q_e}, \quad \dot{r}_{ij} = \frac{3}{2}\frac{\dot{q}_{ij}}{q_e} - \frac{3}{2}\frac{q_{ij}\dot{q}_e}{q_e^2}, \\ r_{ij}\dot{r}_{ij} &= \frac{9}{4}\frac{q_{ij}\dot{q}_{ij}}{q_e^2} - \frac{9}{4}\frac{q_{ij}q_{ij}\dot{q}_e}{q_e^3} \end{aligned} \tag{2.16}$$

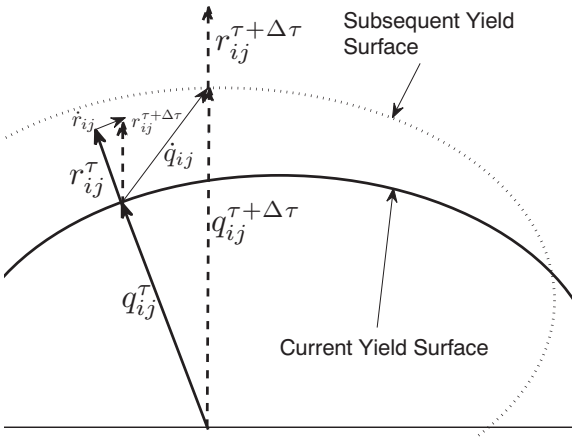

Figure 2.1 A schematic plot of the current and subsequent yield surfaces.

Using $2q_e\dot{q}_e = 3q_{ij}\dot{q}_{ij}$, one can show $r_{ij}\dot{r}_{ij} = 0$. It is seen that r_{ij} is normal to the current yield surface, while $\dot{r}_{ij}$ is tangential to it. Therefore, $\dot{q}_{ij}$ has both the normal and tangential part. Considering the flow rule, Eq. (2.13), the tangential part of the plastic work must not generate any plasticity. To ensure this, the second term of Eq. (2.15) is written in such a way that the tangential plastic strain increment vanishes, see Fredriksson et al. (2009), as

$$q_e\dot{r}_{ij} = E_0(\dot{\epsilon}_{ij}^p - \frac{2}{3}r_{ij}r_{kl}\dot{\epsilon}_{kl}^p) \tag{2.17}$$

where E_0 is the penalty factor and has to be very large compared to the hardening modulus, h. As can be seen, the plastic strain direction is forced to be normal to the current yield surface provided a large value of penalty factor is chosen. Finally, by substituting this term with the second term of Eq. (2.15), the micro stress increment can be written as

$$\dot{q}_{ij} = \frac{2}{3}\left(\frac{2}{3}(h - E_0)r_{ij}r_{kl} + E_0\delta_{ik}\delta_{jl}\right)\dot{\epsilon}_{kl}^p \tag{2.18}$$

The incremental version of the constitutive equations is completed by considering the incremental Cauchy stress and higher order stress as

$$\dot{\sigma}_{ij} = c_{ijkl}\dot{\epsilon}_{kl}^e \tag{2.19}$$

$$\dot{m}_{ijk} = GL_*^2\dot{\epsilon}_{ij,k}^p \tag{2.20}$$

2.2 Material model at the macro scale

At the macroscopic scale, the first and second law of thermodynamics must be satisfied while a conventional plasticity theory is incorporated. The first law of thermodynamics reads

$$\dot{W} = \dot{D} + \dot{\Psi} \tag{2.21}$$

where $\dot{W}$ is the rate of total energy, $\dot{D}$ is the dissipation rate and $\dot{\Psi}$ is the rate of the free energy. Again, the heat flux and entropy production terms are ignored. Constitutive descriptions must also be restricted by the second law of thermodynamics as, see Lubliner (1972) and Chaboche (1993b),

$$\dot{D} = \dot{W} - \dot{\Psi} \geq 0 \tag{2.22}$$

The rate of the total energy is written as

$$\dot{W} = \Sigma_{ij}\dot{E}_{ij} \tag{2.23}$$

As it was outlined by Benzerga et al. (2005), a part of the total work is stored and may not be recovered during the unloading. The trapped energy can be represented by an internal state variable like plastic strain, see also Rice (1971) and Rosakis et al. (2000). Here, we decide to add the plastic strain as an internal variable upon which the free energy may depend, $\Psi = \Psi(E^e_{ij}, E^p_{ij})$. The function is chosen as

$$\Psi = \frac{1}{2}C_{ijkl}E^e_{ij}E^e_{kl} + \frac{1}{2}P_{ijkl}E^p_{ij}E^p_{kl} \tag{2.24}$$

where C_{ijkl} is the elastic modulus, P_{ijkl} is a modulus which contributes the plastic strain towards the free energy ($\boldsymbol{P}$-modulus) and E^p_{ij} is the macroscopic plastic strain defined as

$$E^p_{ij} = E_{ij} - S_{ijkl}\Sigma_{kl} \tag{2.25}$$

where S_{ijkl} is the compliance tensor that relates the stress tensor to elastic strain tensor. The second term of Eq. (2.24) is the portion of the free energy which can not be recovered by elastic unloading and is trapped inside the micro structure. Imposing both Eqs. (2.23) and (2.24) on Eq. (2.22) leads to

$$\Sigma_{ij}\dot{E}_{ij} - \frac{\partial\Psi}{\partial E^e_{ij}}\dot{E}^e_{ij} - \frac{\partial\Psi}{\partial E^p_{ij}}\dot{E}^p_{ij} \geq 0 \tag{2.26}$$

Knowing $\dot{E}^e_{ij} = \dot{E}_{ij} - \dot{E}^p_{ij}$,

$$\Sigma_{ij}\dot{E}_{ij} - \frac{\partial\Psi}{\partial E^e_{ij}}(\dot{E}_{ij} - \dot{E}^p_{ij}) - \frac{\partial\Psi}{\partial E^p_{ij}}\dot{E}^p_{ij} \geq 0 \tag{2.27}$$

$$\left(\Sigma_{ij} - \frac{\partial\Psi}{\partial E^e_{ij}}\right)\dot{E}_{ij} + \left(\frac{\partial\Psi}{\partial E^e_{ij}} - \frac{\partial\Psi}{\partial E^p_{ij}}\right)\dot{E}^p_{ij} \geq 0$$

Since $\dot{E}_{ij}$ can be chosen arbitrary, a conservative way to ensure that Eq. (2.27) is always non-negative is to let the first term vanish. To accomplish this, one must have

$$\Sigma_{ij} = \frac{\partial \Psi}{\partial E^e_{ij}} = C_{ijkl} E^e_{kl} \tag{2.28}$$

It can be seen that the macroscopic Cauchy stress, Σ_{ij}, is work conjugate to the macroscopic elastic strain, E^e_{ij}. Benzerga et al. (2005) showed that there is a connection between the stored energy of cold work (Trapped energy) and the Bauschinger effect. The Bauschinger stress is then defined as, (see Rice, 1971; Chaboche, 1993b,a; Rosakis et al., 2000),

$$A_{ij} = \frac{\partial \Psi}{\partial E^p_{ij}} = P_{ijkl} E^p_{kl} \tag{2.29}$$

where A_{ij} is the Bauschinger stress. It is important to mention that the quadratic function of the plastic strain for the trapped energy, last term of Eq. (2.24), generating a linear function of the plastic strain for the Bauschinger stress, Eq. (2.29), is a constitutive choice. This choice is evaluated by the numerical data and a good agreement is achieved. The dissipation rate, Eq. (2.27), is then rewritten as

$$(\Sigma_{ij} - A_{ij}) \dot{E}^p_{ij} \geq 0 \tag{2.30}$$

In order to be sure that the above equation is always non-negative, a dissipation potential function, $\Phi^* = \Phi^*(\Sigma_{ij} - A_{ij})$, is defined as

$$\dot{E}^p_{ij} = \dot{\Lambda} \frac{\partial \Phi^*(\Sigma_{ij} - A_{ij})}{\partial (\Sigma_{ij} - A_{ij})} = \dot{\Lambda} \frac{\partial \Phi^*(\Sigma_{ij} - A_{ij})}{\partial \Sigma_{ij}} \tag{2.31}$$

where $\dot{\Lambda}$ is a macroscopic plastic multiplier. Note that A_{ij} must be inside the stress field defined by the dissipation potential function if one wants to satisfy Eq. (2.30). Here we choose A_{ij} to be the geometric center of the dissipation potential function. Adopting the principle of maximum plastic dissipation (see Lubliner, 1990), implies: (I) the dissipation potential function is convex; and (II) the plastic strain is normal to the dissipation potential function. Incorporating the Drucker's postulate, Drucker (1951), as a non-thermodynamical approach for the plastic work definition, it is seen that the yield surface is itself a plastic potential, and therefore the normality is associated with the yield criterion or, briefly, an associative flow rule. Therefore, one can have

$$\Phi^*(\Sigma_{ij} - A_{ij}) = \Phi(\Sigma_{ij} - A_{ij}) \tag{2.32}$$

where $\Phi(\Sigma_{ij} - A_{ij})$ is the macroscopic yield function. It will be shown that a modification of the Hill anisotropic yield function (Hill, 1948) is applicable to the material system analyzed. The first modification is that the Bauschinger stress, A_{ij},

is assumed to be the geometric center of the yield surface. Ignoring the terms Σ_{13} and Σ_{23}, we may express the yield function as

$$\Phi = F(\tilde{\Sigma}_{11} - \tilde{\Sigma}_{33})^2 + G(\tilde{\Sigma}_{22} - \tilde{\Sigma}_{33})^2 + H(\tilde{\Sigma}_{11} - \tilde{\Sigma}_{22})^2 + 2N\tilde{\Sigma}_{12}^2 - 1 \tag{2.33}$$

where $\tilde{\Sigma}_{ij} = \Sigma_{ij} - A_{ij}$ and F, G, H and N are the anisotropic parameters. While the above function is pressure independent, it will be shown that the yield surface for the material system considered here is not independent of pressure, but instead independent of some other linear combination of the normal components of $\tilde{\Sigma}_{ij}$. It is noted that this linear combination depends on the fiber volume fraction. Incorporating this into the yield function, we may express it as

$$\Phi = F^{\lambda}(\tilde{\Sigma}_{\lambda_1})^2 + H^{\lambda}(\tilde{\Sigma}_{\lambda_2})^2 + N^{\lambda}\tilde{\Sigma}_{\lambda_4}^2 - 1 \tag{2.34}$$

where F^{λ}, H^{λ} and N^{λ} are new anisotropic parameters and $\tilde{\Sigma}_{\lambda_4} = \Sigma_{12} - A_{12}$. The remaining $\tilde{\Sigma}_{\lambda_i}$ $(i = 1, 2, 3)$ are linearly independent combinations of the normal components of $\tilde{\Sigma}_{ij}$. In the above expression, it is assumed that the yield function is independent of $\tilde{\Sigma}_{\lambda_3}$ ($\tilde{\Sigma}_{\lambda_3}$ is parallel to the composite cylindrical axis), hence it is not included in the yield function.

In Tab. 2.1, an overview of the corresponding equations at the micro and macro scale is given.

The computational procedure for the evaluation of the macroscopic yield function, Φ, and its evolution, $\dot{\Phi}$, including the kinematic hardening and anisotropic hardening for composites with perfectly bonded parallel circular fibers distributed through the entire structure are found in [P5] and [P6].

2.3 Cohesive zone model

An extra study is also considered for the weak fiber-matrix interface. Interfacial debonding is a major failure mode in composites with certain constituents. One of the widely used method in the literature for simulation of the interfacial debonding in composites is the cohesive zone model. The idea for the cohesive model is based on the consideration that the damage analysis knows the existence of the crack in advance. Here, the model proposed by Tvergaard (1990b) which accounts for both normal and tangential separation at the interface is used. This model uses a polynomial relation between the traction and the separation. A non-dimensional parameter, λ, describing the separation of the matrix material from the fiber is defined as

$$\lambda = \sqrt{(u_n/\delta_n)^2 + (u_t/\delta_t)^2} \tag{2.35}$$

where u_n and u_t are normal and tangential separation, respectively, while δ_n and δ_t are the corresponding maximum separations at which total decohesion occurs. A function $F(\lambda)$ is introduced as

$$F(\lambda) = \frac{27}{4}\sigma_{\max}(\lambda^2 - 2\lambda + 1), \qquad 0 \leq \lambda \leq 1 \tag{2.36}$$

The normal traction, T_n, and the tangential traction, T_t, are then given by

$$\begin{aligned} T_n &= \frac{u_n}{\delta_n}F(\lambda) \\ T_t &= \alpha\frac{u_t}{\delta_t}F(\lambda) \end{aligned} \tag{2.37}$$

In pure normal separation, $u_t = 0$, the maximum stress is $\sigma_{\max}$ at $\lambda = \frac{u_n}{\delta_n} = \frac{1}{3}$. Similarly, in pure tangential separation, $u_n = 0$, the maximum stress is $\alpha\sigma_{\max}$ at $\lambda = \frac{u_t}{\delta_t} = \frac{1}{3}$. Generally, total debonding occurs when $\lambda = 1$. The model requires four damage parameters including δ_n, δ_t, $\sigma_{\max}$ and α. More details on the rate form of the above equations can be found in Tvergaard (1990b).

Equation	Micro scale	Macro scale
1st law of TD	$\dot{w} = \dot{d} + \dot{\psi}$	$\dot{W} = \dot{D} + \dot{\Psi}$
2nd law of TD	$\dot{d} = \dot{w} - \dot{\psi} \geq 0$	$\dot{D} = \dot{W} - \dot{\Psi} \geq 0$
Internal work	$\dot{w} = \sigma_{ij}\dot{\epsilon}^e_{ij} + q_{ij}\dot{\epsilon}^p_{ij} + m_{ijk}\dot{\epsilon}^p_{ij,k}$	$\dot{W} = \Sigma_{ij}\dot{E}_{ij}$
Free energy	$\psi = \frac{1}{2}c_{ijkl}\epsilon^e_{ij}\epsilon^e_{kl} + \frac{1}{2}GL^2_*\epsilon^p_{ij,k}\epsilon^p_{ij,k}$	$\Psi = \frac{1}{2}C_{ijkl}E^e_{ij}E^e_{kl} + \frac{1}{2}P_{ijkl}E^p_{ij}E^p_{kl}$
Dissipation inequality 1	$\left(\sigma_{ij} - \frac{\partial\psi}{\partial\epsilon^e_{ij}}\right)\dot{\epsilon}^e_{ij} + \left(q_{ij} - \frac{\partial\psi}{\partial\epsilon^p_{ij}}\right)\dot{\epsilon}^p_{ij} + \left(m_{ijk} - \frac{\partial\psi}{\partial\epsilon^p_{ij,k}}\right)\dot{\epsilon}^p_{ij,k} \geq 0$	$(\Sigma_{ij} - \frac{\partial\Psi}{\partial E^e_{ij}})\dot{E}_{ij} + (\frac{\partial\Psi}{\partial E^e_{ij}} - \frac{\partial\Psi}{\partial E^p_{ij}})\dot{E}^p_{ij} \geq 0$
Conventional stress	$\sigma_{ij} = \frac{\partial\psi}{\partial\epsilon^e_{ij}} = c_{ijkl}\epsilon^e_{kl}$	$\Sigma_{ij} = \frac{\partial\Psi}{\partial E^e_{ij}} = C_{ijkl}E^e_{kl}$
Non-conventional stress	$m_{ijk} = \frac{\partial\psi}{\partial\epsilon^p_{ij,k}} = GL^2_*\epsilon^p_{ij,k}$	$A_{ij} = \frac{\partial\Psi}{\partial E^p_{ij}} = P_{ijkl}E^p_{kl}$
Dissipation inequality 2	$q_{ij}\dot{\epsilon}^p_{ij} \geq 0$	$(\Sigma_{ij} - A_{ij})\,\dot{E}^p_{ij} \geq 0$
Flow potential	$\dot{\epsilon}^p_{ij} = \dot{\lambda}\frac{\partial f^*(q_{ij})}{\partial q_{ij}}$	$\dot{E}^p_{ij} = \dot{\Lambda}\frac{\partial\Phi^*(\Sigma_{ij}-A_{ij})}{\partial\Sigma_{ij}}$
General yield surface	$f(q_{ij}) = f^*(q_{ij})$	$\Phi\left(\Sigma_{ij} - A_{ij}\right) = \Phi^*\left(\Sigma_{ij} - A_{ij}\right)$
Specific yield surface 1	$f = \sqrt{\frac{3}{2}q_{ij}q_{ij}} - \sigma_f$	$\Phi = F^\lambda(\tilde{\Sigma}_{\lambda_1})^2 + H^\lambda(\tilde{\Sigma}_{\lambda_2})^2 + N^\lambda\tilde{\Sigma}^2_{\lambda_4} - 1$

Table 2.1 Material models at the micro and macro scale.

Chapter 3
Multi-scale modeling and homogenization

In this chapter multi-scale modeling is described and a certain type of which is chosen for the study. Computational homogenization as a key element of multi-scale modeling is elaborated. The homogenization connects the gradient dependent theory at the micro scale to the conventional theory at the macro scale using the governing equations extracted in Chapter 2. The chapter comprises four sections. Sec. 3.1 defines different approaches for multi-scale modeling and homogenizations. Sec. 3.2 considers the kinematics of the motion at both scales. Sec. 3.3 considers the Hill-Mandel energy condition. As a result, macroscopic quantities are finally described by the microscopic ones. Secs. 3.4 and 3.5 show the macroscopic conventional and non-conventional operators (elastic and Bauschinger moduli), respectively, using the derived macroscopic quantities.

3.1 Definition

Macroscopic properties hold the key criteria in choosing a material for a specific engineering application. The origins of material properties reside in the properties and interactions that take place at the scale of its microstructure. It is important to faithfully model macroscopic material response together with mechanisms and interactions occurring at the microstructural scale. On the other hand, if a continuum material is subjected to some load and Boundary Conditions (BCs), the resulting deformation and stresses may vary rapidly from point to point due to material heterogeneity. With a high level of heterogeneity in the material, these quantities also vary rapidly within a very small neighborhood of a given point. Thus, it is reasonable to claim that all quantities have two explicit dependences. One is on the fine scale (microscopic) and the other is on the large scale (macroscopic). The purpose of multi-scale modeling is to determine the global constitutive behavior of heterogeneous materials taking into account the effect of the microstructure. Generally, there are two different types of multi-scale modeling methods, I) Hierarchical models, and II) Concurrent models.
With hierarchical models, it is assumed that the scales are separated such that they do not affect each other. As a requirement, two assumptions are considered including I) Uniformity of macroscopic field variables, and II) Periodic Representative Volume Element (RVE). In this model, macroscopic properties are obtained by ho-

mogenizing the microscopic quantities over a RVE and they are used as an input for the large scale, see (Fish and Shek, 2000). As a result, a purely macroscopic domain (so-called level-0) with homogenized material parameters is obtained.
It has been found that the uniformity assumption is not appropriate in critical regions of large gradients like at material discontinuities and in the vicinity of interfaces and free edges. The evolution of the localized stress close to a crack can also violate the assumption of periodicity. Concurrent models have been developed to tackle these issues, (e.g. Zohdi and Wriggers, 1999; Ghosh et al., 2007). Such models not only use the so-called level-0 field but also consider two more levels (so-called level-1 and level-2) at the critical regions. The levels are described as below

Level-0) Purely macroscopic domain with homogenized material properties.

Level-1) Macro-micro domain with the micro-domain represented by a RVE.

Level-2) Purely microscopic domain without RVE.

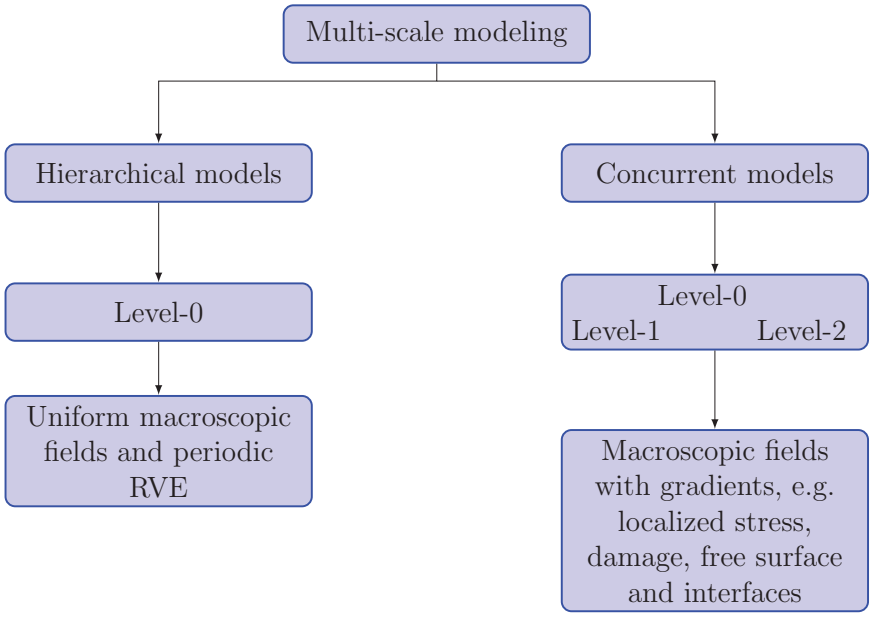

Figure 3.1 Multi-scale modeling methods.

Fig. 3.1 summarizes the multi-scale modeling methods with assumptions and requirements. More discussion is found in Ghosh et al. (2007). Fig. 3.2 schematically shows an example with different regions needing appropriate computational

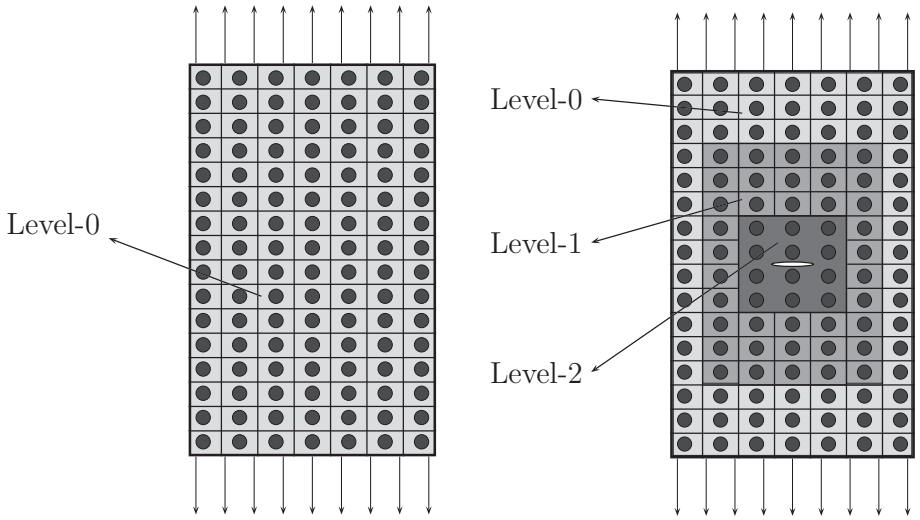

(a) Hierarchical model for the material without crack.

(b) Concurrent model for the material with crack.

Figure 3.2 Composites under simple tension and different multi-scale modeling approach.

approaches. As can be seen, a hierarchical model can be used for the composite under simple tension without any material discontinuity, while concurrent model must be considered when crack is available. The domain of each level can also be changed according to how many terms of the Taylor expansion of e.g., the displacement field, $U = \sum_{n=0}^{\infty} \frac{1}{n!} \left(\frac{\partial^n U}{\partial X^n}\right)_{X_0} (X - X_0)^n$ where U is the displacement field and $(X - X_0)$ is the distance from the crack tip, are considered. Fig. 3.3 shows schematically a crack inside the material and the change in the domain of different levels. It is seen that level-0 is expanded while level-1 is shrunk with the higher number of n in the Taylor expansion.

In this study, uniformity of macroscopic quantities is assumed, where the hierarchical model can be implemented. Moreover, the Taylor expansion of the displacement field is truncated at $n = 1$. Using these assumptions, the microscopic quantities are homogenized and saved.

Homogenization is a condensation procedure at the smaller scale which results in the evaluation of the quantities at a larger scale. On the other hand, e.g. for the conventional case, by defining the macro stress, Σ_{ij}, and macro strain, E_{ij}, finding a plausible relation between them is necessary as $\Sigma_{ij} = C_{ijkl} E_{kl}$, where C_{ijkl} is a macro constitutive operator. However, due to the contrast between the properties of the macroscopic constituent, there is no unique representation of the constitutive operator at the macro scale with different BCs. This implies that the macro constitutive operator is strictly dependent on the boundary conditions. This is not a problem at

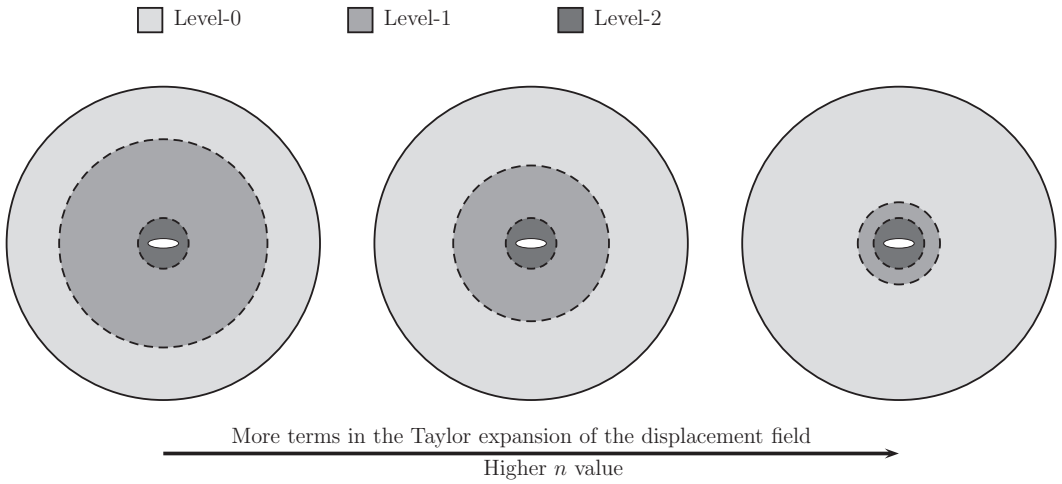

Figure 3.3

the micro scale, where the constitutive operator is assumed to be well known in advance, $\sigma_{ij} = c_{ijkl}\epsilon_{kl}$. The fact that the macro constitutive moduli strongly depends on the type of boundary condition employed was demonstrated in the linear elasticity setting by Hazanov and Huet (1994). This implies that the homogenization technique has to provide macroscopic data, which are applicable for complicated macroscopic loading. Different homogenization techniques have been proposed to estimate the overall constitutive operators at the macro scale, like effective medium approximation by Eshelby (1957), self consistent method by Hill (1965) and variational bounding methods by Hashin (1983). However, computational methods using unit cells are found to be more efficient. Several approaches have been proposed by Hashin and Shtrikman (1963), Budiansky (1965), Suquet (1985), Keller et al. (1990), Ghosh et al. (1995), Terada et al. (2000), Wieckowski (2000) and Kouznetsova et al. (2001).

By the development of strain gradient theories, the homogenization techniques have lately been extended to include such theories. Zhu et al. (1997) used strain gradient in the matrix material to obtain particle size dependent overall properties of metal matrix composites. Li et al. (2010) presented a micro-macro homogenization modeling of heterogeneous gradient-enhanced Cosserat continuum in the frame of the average-field theory. Kouznetsova et al. (2004) and Geers et al. (2010) elaborated on a computational homogenization, where the higher order stress conjugate to the full strain tensor is only available at the macro scale, while it vanishes at the micro scale.

In the next three sections, a computational homogenization method employing

a unit cell is described, where the gradient theory is used at the micro scale and conventional theory is obtained at the macro scale.

3.2 Kinematics at the micro and macro scale

Kinematics of the motion is represented in Fig. 3.4. Deformation of an undeformed macroscopic state, X_i, to the deformed state, x_i, is defined as

$$x_i = X_i + U_i \tag{3.1}$$

where U_i is the macroscopic displacement vector.

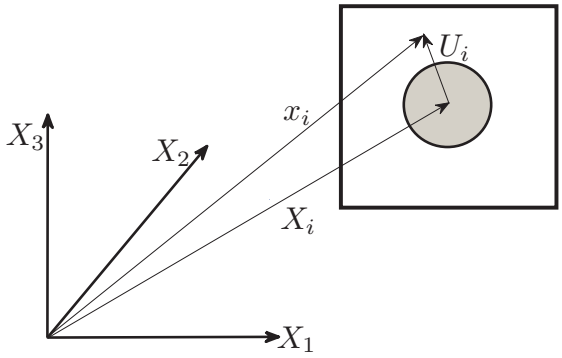

Figure 3.4 Kinematic of the motion.

Neglecting the higher order terms, the Taylor expansion about a point, X_i^0, reads

$$U_i = (U_i)_{X_i^0} + \left(\frac{\partial U_i}{\partial X_j}\right)_{X_i^0} (X_j - X_j^0) \tag{3.2}$$

where $\frac{\partial U_i}{\partial X_j}$ is the macroscopic displacement gradient at the undeformed macroscopic point, X_i^0, which can be decomposed into the symmetric and skew symmetric part as

$$\left(\frac{\partial U_i}{\partial X_j}\right)_{X_i^0} = \frac{1}{2}\left(\frac{\partial U_i}{\partial X_j} + \frac{\partial U_j}{\partial X_i}\right)_{X_i^0} + \frac{1}{2}\left(\frac{\partial U_i}{\partial X_j} - \frac{\partial U_j}{\partial X_i}\right)_{X_i^0} \tag{3.3}$$

The symmetric part of the above equation stands as the macroscopic strain tensor, E_{ij}, and the skew-symmetric part stands as the macroscopic rotation tensor, R_{ij}. Therefore,

$$\left(\frac{\partial U_i}{\partial X_j}\right)_{X_i^0} = (E_{ij} + R_{ij})_{X_i^0} \tag{3.4}$$

The microscopic displacement, u_i, is written as

$$u_i = U_i + w_i \tag{3.5}$$

where w_i is a microstructural fluctuation field which denotes a difference between microscopic and macroscopic displacements. By imposing the Taylor expansion of the macroscopic displacement, Eq. (3.2), into above equation while considering Eq. (3.4), one should have

$$u_i = (U_i)_{X_i^0} + (E_{ij} + R_{ij})_{X_i^0} (X_j - X_j^0) + w_i \tag{3.6}$$

By defining the microscopic strain tensor as $\epsilon_{ij} = \frac{1}{2}\left(\frac{\partial u_i}{\partial X_j} + \frac{\partial u_j}{\partial X_i}\right)$ and imposing on Eq. (3.6), one can show

$$\epsilon_{ij} = \frac{1}{2}(E_{ij} + R_{ij} + E_{ji} + R_{ji})_{X_i^0} + \frac{1}{2}\left(\frac{\partial w_i}{\partial X_j} + \frac{\partial w_j}{\partial X_i}\right) \tag{3.7}$$

Exploiting the properties of the symmetric strain tensor, $E_{ji} = E_{ij}$, and skew-symmetric rotation tensor, $R_{ji} = -R_{ij}$, one can have

$$\epsilon_{ij} = E_{ij} + \frac{1}{2}\left(\frac{\partial w_i}{\partial X_j} + \frac{\partial w_j}{\partial X_i}\right) \tag{3.8}$$

Volume integration is imposed on both side of the above equation as

$$\frac{1}{v}\int_v \epsilon_{ij}\mathtt{d}v = E_{ij} + \frac{1}{2v}\int_v \left(\frac{\partial w_i}{\partial X_j} + \frac{\partial w_j}{\partial X_i}\right)\mathtt{d}v \tag{3.9}$$

where v is the volume of the microstructure.
Here, it is assumed that the macroscopic strain tensor is the volume average of the microscopic strain for the perfectly bonded interface as

$$E_{ij} = \frac{1}{v}\int_v \epsilon_{ij}\mathtt{d}v \tag{3.10}$$

To survive the assumption, the second term of the right hand side of Eq. (3.9) has to vanish. To accomplish this, Gauss theorem is imposed as

$$\frac{1}{2v}\int_v \left(\frac{\partial w_i}{\partial X_j} + \frac{\partial w_j}{\partial X_i}\right)\mathtt{d}v = \frac{1}{v}\int_s w_i n_j \mathtt{d}s = 0 \tag{3.11}$$

where s is the surface of the micro volume, v. There are three conditions which can satisfy the above equation

I. $w_i = 0$, for all the microstructural points inside the volume of the unit cell. This condition suppresses any fluctuation and forces each microscopic point to deform precisely as the macroscopic one.

II. $w_i = 0$, for all the microstructural points at the surface of the unit cell. This condition prescribes a zero fluctuation at the boundary of the unit cell, while the rest of micro displacements remains undetermined.

III. $w_i n_j = 0$, for all the microstructural points at the surface of the unit cell. This condition prescribes a periodic fluctuation at the boundary of the unit cell as below

$$w_i^A(\Gamma) n_j^A(\Gamma) + w_i^B(\Gamma) n_j^B(\Gamma) = 0 \tag{3.12}$$

where A and B are the opposite sides of the unit cell and Γ is the local coordinate system on the surface. Using $n_j^A(\Gamma) = -n_j^B(\Gamma)$ as the unit vectors normal to the surface of the unit cell,

$$\left(w_i^A(\Gamma) - w_i^B(\Gamma)\right) n_j^A(\Gamma) = 0 \tag{3.13}$$

One possible way to fulfill Eq. (3.13) can be written as

$$w_i^A(\Gamma) = w_i^B(\Gamma) \tag{3.14}$$

It is seen that the only case which let us have deformation at the borders of the unit cell is the third case. Therefore, it is considered for the study known as the periodic displacement boundary conditions, consistent to the required assumption for the hierarchical multi-scale modeling.

3.3 Hill-Mandel energy condition

An extended Hill-Mandel energy condition is used which requires the microscopic volume average of the variation of the work performed on the unit cell (conventional+higher order works) to be equal to the variation of the work at the macro scale (conventional work) as

$$\frac{1}{v}\int_v [\sigma_{ij}\delta\epsilon_{ij} + (q_{ij} - s_{ij})\delta\epsilon_{ij}^p + m_{ijk}\delta\epsilon_{ij,k}^p]\mathtt{d}v = \Sigma_{ij}\delta E_{ij} \tag{3.15}$$

Using the Gauss theorem and equilibrium equation, Eq. (2.5),

$$\frac{1}{v}\int_s [\sigma_{ij} n_j \delta u_i + m_{ijk} n_k \delta\epsilon_{ij}^p]\mathtt{d}s = \Sigma_{ij}\delta E_{ij} \tag{3.16}$$

Here the variation of Eq. (3.6) is considered as

$$\delta u_i = (\delta E_{ij} + \delta R_{ij})\, X_j + \delta w_i \tag{3.17}$$

By imposing the above equation on Eq. (3.16), one can show

$$\frac{1}{v}\int_s \sigma_{ij} n_j X_k \mathtt{d}s \delta E_{ik} + \frac{1}{v}\int_s \sigma_{ij} n_j X_k \mathtt{d}s \delta R_{ik} + \frac{1}{v}\int_s \sigma_{ij} n_j \delta w_i \mathtt{d}s + \frac{1}{v}\int_s m_{ijk} n_k \delta \epsilon^p_{ij} \mathtt{d}s = \Sigma_{ij} \delta E_{ij} \tag{3.18}$$

The second term of the above equation vanishes upon application of Gauss' theorem and equilibrium, since R_{ik} is skew-symmetric. The other terms can disappear considering a certain set of the boundary conditions as

$$\begin{aligned} \int_s \sigma_{ij} n_j \delta w_i \mathtt{d}s = \int_s T_i \delta w_i \mathtt{d}s = 0, \\ \int_s m_{ijk} n_k \delta \epsilon^p_{ij} \mathtt{d}s = \int_s M_{ij} \delta \epsilon^p_{ij} \mathtt{d}s = 0 \end{aligned} \tag{3.19}$$

where $T_i = \sigma_{ij} n_j$ and $M_{ij} = m_{ijk} n_k$ are traction and higher order traction on the surface of the unit cell, respectively. One possible way to ensure that Eq. (3.19) is satisfied can be written as

$$\begin{aligned} T_i^A(\Gamma) w_i^A(\Gamma) + T_i^B(\Gamma) w_i^B(\Gamma) = 0, \quad \texttt{on} \quad s \\ M_{ij}^A(\Gamma)(\epsilon^p_{ij})^A(\Gamma) + M_{ij}^B(\Gamma)(\epsilon^p_{ij})^B(\Gamma) = 0, \quad \texttt{on} \quad s \end{aligned} \tag{3.20}$$

The above conditions are satisfied when

$$\begin{aligned} w_i^A(\Gamma) = w_i^B(\Gamma), \quad (\epsilon^p_{ij})^A(\Gamma) = (\epsilon^p_{ij})^B(\Gamma) \\ T_i^A(\Gamma) = -T_i^B(\Gamma), \quad M_{ij}^A(\Gamma) = -M_{ij}^B(\Gamma) \end{aligned} \tag{3.21}$$

It is seen from above equation, the fluctuations and plastic strains are equal at the opposite sides of the unit cell, while tractions and higher order tractions are opposite of each other. This reminds the periodic boundary conditions on the surface of the unit cell. Eq. (3.18) is then reduced to

$$\left[\frac{1}{v}\int_s \sigma_{ij} n_j X_k \mathtt{d}s\right] \delta E_{ik} = \Sigma_{ik} \delta E_{ik} \tag{3.22}$$

Using the Gauss theorem and equilibrium equation, Eq. (2.5),

$$\Sigma_{ij} = \frac{1}{v}\int_v \sigma_{ij} \mathtt{d}v \tag{3.23}$$

3.4 Macroscopic conventional operator

It is important to mention that the macroscopic conventional constitutive behavior, $\Sigma_{ij} = C_{ijkl}E_{kl}$, has not been considered as a priori. Therefore, the macroscopic conventional operator, C_{ijkl}, can be determined numerically from the relation between variation of the macroscopic free energy and variation of the macroscopic deformation at any point in the elastic regime. For the five loading trials, shown in Fig. 3.5 (Transverse and longitudinal loading, 0^o and 45^o in-plane shear and out-of-plane shear), the microscopic elastic energy is evaluated at pseudo-time τ as

$$\Psi_e^{\tau+\Delta\tau} = \Psi_e^{\tau} + \int_v \sigma_{ij}^{\tau_m} \dot{\epsilon}_{ij}^{e} dv \cdot \Delta\tau \tag{3.24}$$

where $\tau_m = \frac{2\tau+\Delta\tau}{2}$ and $\Delta\tau$ is pseudo-time increment. The components of the macro-

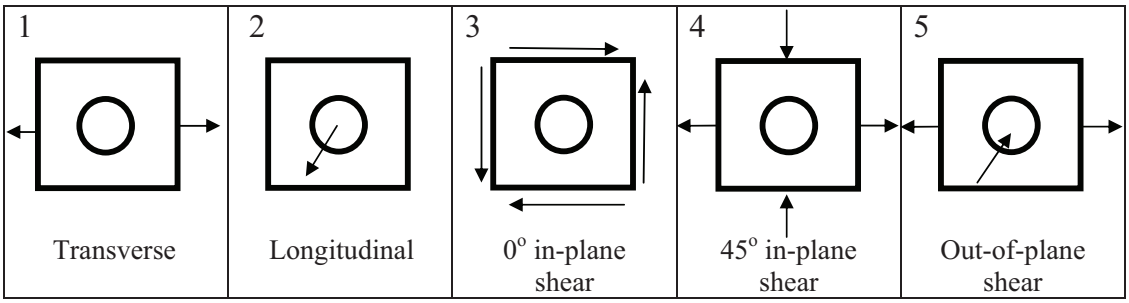

Figure 3.5 Five trial loadings used to obtain the macroscopic operators, C_{ijkl} and P_{ijkl}.

scopic conventional operator, C_{ijkl}, are solved using the relation, $\Psi_e = \frac{1}{2}C_{ijkl}E_{ij}^e E_{kl}^e$. Exploiting the material symmetries for the present problem, all moduli can be solved from the following system of equations:

$$\begin{bmatrix} \Psi_e^1 \\ \Psi_e^2 \\ \Psi_e^3 \\ \Psi_e^4 \\ \Psi_e^5 \end{bmatrix} = \begin{bmatrix} a^1 & b^1 & c^1 & d^1 & e^1 \\ a^2 & b^2 & c^2 & d^2 & e^2 \\ a^3 & b^3 & c^3 & d^3 & e^3 \\ a^4 & b^4 & c^4 & d^4 & e^4 \\ a^5 & b^5 & c^5 & d^5 & e^5 \end{bmatrix} \times \begin{bmatrix} C_{1111} \\ C_{1122} \\ C_{1133} \\ C_{3333} \\ C_{1212} \end{bmatrix} \tag{3.25}$$

where for each of the five loading trials, the constants are defined according to $a = \frac{1}{2}(E_{11}^e)^2 + \frac{1}{2}(E_{22}^e)^2$, $b = E_{11}^e E_{22}^e$, $c = (E_{11}^e + E_{22}^e)E_{33}^e$, $d = \frac{1}{2}(E_{33}^e)^2$ and $e = \frac{1}{2}(E_{12}^e)^2$. Using a reduced index notation according to $1 \approx 11$, $2 \approx 22$, $3 \approx 33$ and $4 \approx 12$, a

matrix of elastic moduli as the macroscopic conventional operator is defined as

$$\boldsymbol{C} = \begin{bmatrix} C_{11} & C_{12} & C_{13} & 0 \\ C_{12} & C_{11} & C_{13} & 0 \\ C_{13} & C_{13} & C_{33} & 0 \\ 0 & 0 & 0 & C_{44} \end{bmatrix} \tag{3.26}$$

where the decoupling between the shear component and the normal components arises due to the material symmetries. Assuming the transversely isotropic with $a = b$, results in $C_{11} = C_{22}$ and $C_{13} = C_{23}$.

3.5 Macroscopic non-conventional operator

Non-conventional macroscopic constitutive behavior described by the Bauschinger stress as a work conjugate to the plastic strain, $A_{ij} = P_{ijkl}E^p_{kl}$, has not been considered as a priori. Therefore, the non-conventional macroscopic operator, P_{ijkl}, is determined numerically from the relation between variation of the macroscopic trapped energy and variation of the macroscopic plastic strain. For the same loading trials, shown in Fig. 3.5, the microscopic trapped energy at pseudo-time τ is evaluated as suggested by Benzerga et al. (2005) according to

$$\Psi_T^{\tau+\Delta\tau} = \Psi_T^{\tau} + \frac{1}{v}\int_v [\sigma_{ij}^{\tau_m}\dot{\epsilon}^e_{ij} + m_{ijk}^{\tau_m}\dot{\epsilon}^p_{ij,k}]dv \cdot \Delta\tau - \frac{1}{2}\Sigma_{ij}^{\tau_m}S_{ijkl}\Sigma_{kl}^{\tau_m} \tag{3.27}$$

where S_{ijkl} is the macroscopic elastic compliance tensor. The components of the tensor of Bauschinger moduli, P_{ijkl}, are solved for the maximum load using the relation, $\Psi_T = \frac{1}{2}P_{ijkl}E^p_{ij}E^p_{kl}$. Exploiting the material symmetries for the present problem, all moduli can be solved from the following system of equations:

$$\begin{bmatrix} \Psi_T^1 \\ \Psi_T^2 \\ \Psi_T^3 \\ \Psi_T^4 \\ \Psi_T^5 \end{bmatrix} = \begin{bmatrix} a^1 & b^1 & c^1 & d^1 & e^1 \\ a^2 & b^2 & c^2 & d^2 & e^2 \\ a^3 & b^3 & c^3 & d^3 & e^3 \\ a^4 & b^4 & c^4 & d^4 & e^4 \\ a^5 & b^5 & c^5 & d^5 & e^5 \end{bmatrix} \times \begin{bmatrix} P_{1111} \\ P_{1122} \\ P_{1133} \\ P_{3333} \\ P_{1212} \end{bmatrix} \tag{3.28}$$

where for each of the five loading trials, the constants are defined according to $a = \frac{1}{2}(E^p_{11})^2 + \frac{1}{2}(E^p_{22})^2$, $b = E^p_{11}E^p_{22}$, $c = (E^p_{11} + E^p_{22})E^p_{33}$, $d = \frac{1}{2}(E^p_{33})^2$ and $e = \frac{1}{2}(E^p_{12})^2$. Using a reduced index notation according to $1 \approx 11$, $2 \approx 22$, $3 \approx 33$ and $4 \approx 12$, a matrix of Baushinger moduli is defined as

$$\boldsymbol{P} = \begin{bmatrix} P_{11} & P_{12} & P_{13} & 0 \\ P_{12} & P_{11} & P_{13} & 0 \\ P_{13} & P_{13} & P_{33} & 0 \\ 0 & 0 & 0 & P_{44} \end{bmatrix} \tag{3.29}$$

where the decoupling between the shear component and the normal components arises due to the material symmetries. Assuming the transversely isotropic with $a = b$, results in $P_{11} = P_{22}$ and $P_{13} = P_{23}$. Tab. 3.1 summarizes the connection between the scales.

	Micro scale	Macro scale	Connection
Displacement	u_i	U_i	$u_i = U_i + w_i$
Conventional strain	ϵ_{ij}	E_{ij}	$E_{ij} = \frac{1}{v}\int_v \epsilon_{ij} dv$
Non-conventional strain	$\epsilon^p_{ij,k}$	Not Available	Not Available
Conventional stress	σ_{ij}	Σ_{ij}	$\Sigma_{ij} = \frac{1}{v}\int_v \sigma_{ij} dv$
Non-conventional stress	m_{ijk}	A_{ij}	Not Applicable
Free energy	ψ	Ψ	$\Psi = \frac{1}{v}\int_v \psi dv$
Internal work	w	W	$W = \frac{1}{v}\int_v w dv$
Conventional operator	c_{ijkl}	C_{ijkl}	$\Psi_e = \frac{1}{2} C_{ijkl} E^e_{ij} E^e_{kl}$ $\Psi_e = \frac{1}{v}\int_v \psi_e dv$
Non conventional operator	GL^2_*	P_{ijkl}	$\Psi_T = \frac{1}{2} P_{ijkl} E^p_{ij} E^p_{kl}$ $\Psi_T = \frac{1}{v}\int_v \psi_T dv$

Table 3.1 Connection between the scales.

Chapter 4
Summary of results

In this chapter, the entire response of the composite under general loadings, e.g. macroscopic stress strain response (Σ_{ij}, E_{ij}) together with operators, microscopic plastic flow (ϵ_e^p), macroscopic yield surfaces, evolution of the yield surfaces including both anisotropic and kinematic hardening (expansion and translation) are presented. A thorough description of the macroscopic yield function (Φ) and its evolution ($\dot{\Phi}$) is presented. The chapter includes a summary of the main results of the papers [P1]-[P7], as well as additional findings.

Section 4.1 presents the response of the composite under normal loadings considering the size effect of the fiber. Two different types of unit cells, rectangular fiber [p1] and circular fiber [p2]-[p3], are studied assuming perfectly bonded interface. For the circular fiber, since only loading with the same symmetry planes as the geometry and the material itself are considered (we do not consider shear in the (x,y) coordinate system), the analyses can be carried out on a reduced unit cell containing only one quarter of a fiber. The overall stress strain curve, plastic strain distribution inside the micro structure and computational macroscopic yield surfaces are shown.
Section 4.2 presents the size-effect of the fiber on the response of the composite under simple shear loading using both rectangular and circular fibers. The simulation needs to consider both the higher order and conventional periodic boundary conditions. A thoroughly computational investigation of both the initial and subsequent yield surfaces are presented in [P4].
Section 4.3 tries to find a mathematical description of the trapped energy and corresponding Bauschinger stress for the unit cell with perfectly bonded circular fiber [p5]. Non-conventional operator is computed using the trapped energy and corresponding plastic strains. The function of trapped energy can further be used to track the kinematic hardening of the composite yield surface under general loading conditions.
Section 4.4 shows the evolution of the composite yield surface regarding the anisotropic hardening (expansion). An anisotropic pressure dependent yield function with its evolution is finally introduced [P6].
Section 4.5 follows the study in Secs. 4.1 and 4.2 for weak interfaces using the cohesive zone model of Tvergaard (1990b). The effect of the strength of fiber matrix interface on the composite behavior is investigated [P7].
The main conventional material parameters used for the matrix are $H/E_m = 0.1$,

$\sigma_y/E_m = 0.004$, $\tau_y = \sigma_y/\sqrt{3}$, $\upsilon_m = 0.3$, and for the fibers, $E_f = 5.7E_m$ and $\upsilon_f = 0.17$.

4.1 MMCs under normal loadings [p1]-[p3]

A unit cell is extracted from a composite with rectangular fibers similar to what was considered in Bittencourt et al. (2003). The geometry of the unit cell is $w = \sqrt{3}h$, $h_f = 2w_f = 0.588h$, where; w, h, w_f and h_f are the width of the unit cell, height of the unit cell, width of the fiber and height of the fiber, respectively. A fiber volume fraction of 0.2 is chosen for the study. Fig. 4.1 shows the geometry of the unit cell with rectangular fibers and both the conventional and higher order boundary conditions for normal loadings. The incremental boundary conditions are

$$\begin{array}{llllll}
\dot{u}_1 = 0, & \dot{T}_2 = 0, & \text{on} & x = -w/2, & & y \in [-h/2, h/2], \\
\dot{u}_1 = \dot{\Delta}_1, & \dot{T}_2 = 0, & \text{on} & x = w/2, & & y \in [-h/2, h/2], \\
\dot{u}_2 = 0, & \dot{T}_1 = 0, & \text{on} & x \in [-w/2, w/2], & & y = -h/2, \\
\dot{u}_2 = \dot{\Delta}_2, & \dot{T}_1 = 0, & \text{on} & x \in [-w/2, w/2], & & y = h/2, \\
\dot{\epsilon}^p_{ij} = 0, & & \text{at} & \text{all fiber matrix interfaces} & & \\
\dot{M}_{ij} = 0, & & \text{at} & x = \pm w/2, & \text{and} & y = \pm h/2,
\end{array} \tag{4.1}$$

The unit cell is loaded in the transverse direction under plain strain condition. The displacement BC are controlled such that $\Sigma_{22} = 0$ while $\Sigma_{11} \neq 0$. The method of having proportional stress loading using displacement control of the boundaries is elaborated in [P3] and Tvergaard (1976).

Fig. 4.2 shows the macroscopic stress strain curve of the unit cell loaded until $E_{11} = 2.8\epsilon_y$ affected by the material length scale, L_*/h. The macroscopic yield criterion is defined as

$$|E_{ij} - S_{ijkl}\Sigma_{kl}| \geq \epsilon_t \tag{4.2}$$

where $\epsilon_t = 0.001$ is the offset strain. Initial yield of the composite is postponed to $1.52\sigma_y$, $1.54\sigma_y$ and $1.62\sigma_y$ corresponding to $L_*/h = 0$, $L_*/h = 0.05$ and $L_*/h = 0.1$, respectively. The elastic response of the composite is shown to be independent of the size of the fibers, as could be expected. A slight enhancement of the hardening is seen with the higher material length scale.
Fig. 4.3 shows the distribution of the effective plastic strain, ϵ^p_e/ϵ_y, on the undeformed geometry. For the conventional material, the highest effective plastic strain is seen close to the fiber due to the stress concentration, $\epsilon^p_e = 3.27\epsilon_y$, while for

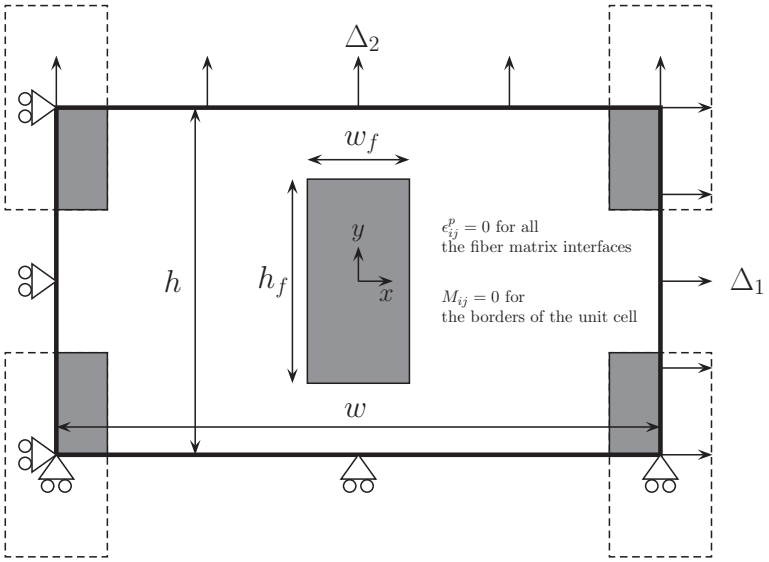

Figure 4.1 A unit cell of composite with rectangular fibers under normal loadings with $w = \sqrt{3}h$ and $h_f = 2w_f = 0.588h$.

the gradient dependent material the highest effective plastic strain is reduced to $\epsilon^p_e = 1.48\epsilon_y$ at the border of the unit cell. An overall suppression of plastic flow is observable for the gradient dependent material. This results in the enhancement of the hardening shown in Fig. 4.2. Initial and subsequent yield surfaces of the unit cell are published in [P1] for different material properties.

A composite with regular distribution of circular fibers is also studied. Fig. 4.4 shows the extracted unit cell which is further reduced to a quarter of the circular fiber due to the symmetry of the loading condition. The imposed conventional and higher order boundary conditions can be found in [P2] and [P3]. The same material properties as of the previous unit cell is studied with $V_f = 0.2$. The study is under generalized plane strain condition, where the longitudinal stress, Σ_{33}, is controlled with a constant deformation of the unit cell thickness as well as the other stress components, Σ_{11} and Σ_{22}. The numerical implementation of such a stress control is also presented in Niordson and Tvergaard (2007).

Initial tension with subsequent compression is studied and the stress strain curves are normalized by the initial yield stress and yield strain of the matrix, σ_y and $\epsilon_y = \sigma_y/E_m$, respectively. In Fig. 4.5, the unit cell is loaded in the transverse direction until $E_{11} = 3\epsilon_y$, unloaded until a stress free state and then reloaded until

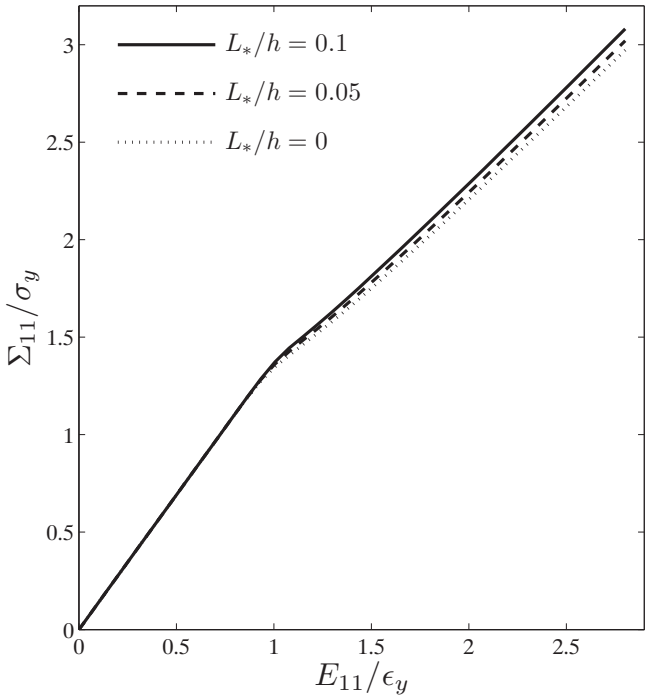

Figure 4.2 Effect of the material length scale, L_*/h, on the macroscopic stress strain curve of the unit cell with rectangular fibers loaded in transverse direction until $E_{11} = 2.8\epsilon_y$ with $V_f = 0.2$.

a compressive macroscopic strain of $E_{11} = 1.2\epsilon_y$ is achieved. The initial yield of the composite is postponed to $1.2\sigma_y$, $1.3\sigma_y$ and $1.4\sigma_y$ corresponding to $L_*/R = 0$, $L_*/R = 0.2$ and $L_*/R = 0.4$, respectively. It is concluded that the strength of composite with rectangular fibers is slightly higher than the one with circular fibers using the same fiber volume fraction, V_f.

A considerable amount of the enhanced hardening is seen for decreasing fiber size, corresponding to a larger material length scale with the current theory. These findings are consistent with experimental studies of composites by Lloyd (1994) and Yan et al. (2007), where the material hardening of the composite is observed to increase with decreasing particle size under a constant volume fraction of the reinforcement. An important observation is related to the subsequent loading, where a considerable amount of Bauschinger stress, $A_{ij} = \frac{\Sigma^f_{ij}+\Sigma^{sy}_{ij}}{2}$ (Here Σ^f_{ij} is the flow stress at the end of loading and Σ^{sy}_{ij} is the subsequent yield stress), is seen for the higher material length scale. The Bauschinger stress increases from $A_{11} = 0.033\sigma_y$ corresponding to $L_*/R = 0$ towards $A_{11} = 0.62\sigma_y$ corresponding to $L_*/R = 0.4$. The

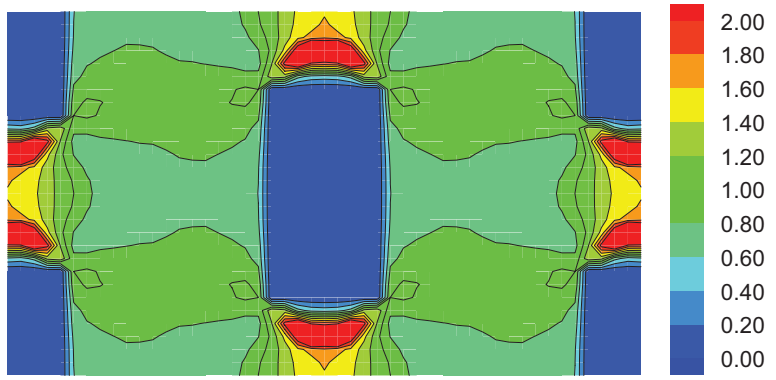

(a) $L_*/h = 0$

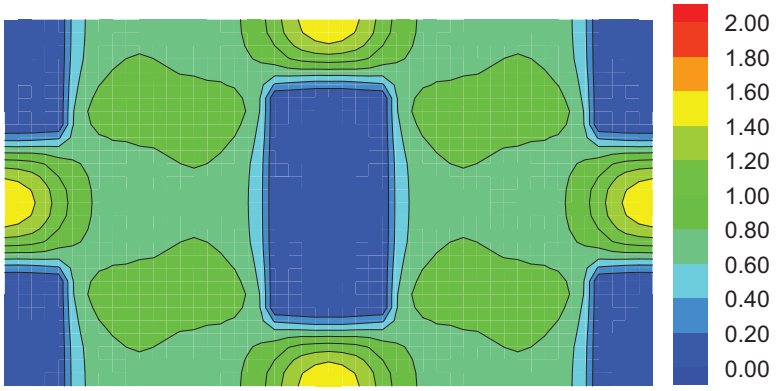

(b) $L_*/h = 0.1$

Figure 4.3 Effective plastic strain distribution, ϵ_e^p/ϵ_y, on the undeformed geometry at the end of transverse loading until $E_{11} = 2.8\epsilon_y$.

considerable amount of Bauschinger effect observed in the experiments conducted by Corbin et al. (1996) and Iyera et al. (2000) cannot be captured by conventional J2 flow theory. However, the gradient dependent analysis here captures the enhanced Bauschinger effect better.

Fig. 4.6 shows the effective plastic strain, ϵ_e^p/ϵ_y, on the undeformed geometry at the end of transverse loading shown in Fig. 4.5. A sudden jump of plastic strain from the matrix into the fiber is seen in the conventional material, while a continuous suppression of the plastic flow along the interface occurs in the gradient dependent material. The local plastic strain in conventional material can be more than $6\epsilon_y$, while in the gradient dependent material, it is around $4\epsilon_y$. Mughrabi (2001) and Fleck et al. (2003) showed that in MMCs, dislocations can not pass from matrix into the fiber and consequently pile up at the interface. This phenomenon leads to

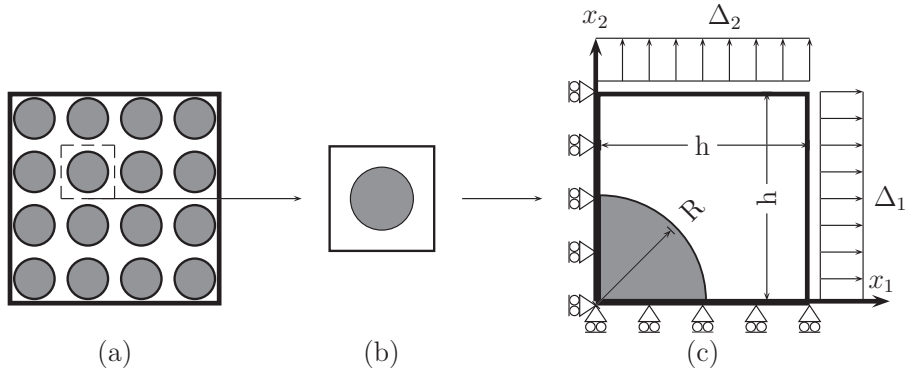

Figure 4.4 (a) Regular distribution of the circular fibers in composite. (b) Full unit cell containing one fiber. (c) Reduced unit cell containing a quarter of the fiber.

plastic strain suppression at the interfaces, which can be taken into account by the gradient theory.

Fig. 4.7 shows the corresponding Mises effective stress, $\sigma_e/\sigma_y = \sqrt{\frac{3}{2}s_{ij}s_{ij}}/\sigma_y$, at the end of transverse loading shown in Fig. 4.5. For the gradient dependent material, Fig. 4.5b, a relatively large overall load carrying capacity is seen compared to the conventional material, Fig. 4.5a, at the same macroscopic strain level, $E_{11} = 3\epsilon_y$. The concentration of stress at the interface in Fig. 4.5b is due to the suppression of plastic strain.

Effect of the fiber volume fraction, V_f, on the distribution of the effective plastic strain with $L_*/R = 0.4$ is shown in Fig. 4.8. With the higher fiber volume fraction, more suppression of the plastic flow through the matrix is accessible. The higher fiber volume fraction can increase the elastic modulus, postpone the onset of the initial yield stress, enhance the load carrying capacity after the yielding and increase the Bauschinger stress (see [P3] for more details). The details of the effect of L_*/R and V_f on the response of the composite including the longitudinal loading are found in [P2] and [P3].

Initial and subsequent yield surfaces are shown on the π-plane on which the macroscopic hydrostatic stress vanishes. In absence of the macroscopic shear stresses in the (x_1, x_2) coordinate system, the stress state is thus characterized by two stress components in the directions of $\boldsymbol{e}_p$ and $\boldsymbol{e}_q$ which are both perpendicular to the hydrostatic axis $\boldsymbol{e}_h$. With $\boldsymbol{e}_1$, $\boldsymbol{e}_2$ and $\boldsymbol{e}_3$ denoting unit vectors in the x_1, x_2 and x_3 directions, respectively the stress state can be expressed in the two equivalent forms

$$\Sigma_{11}\boldsymbol{e}_1 + \Sigma_{22}\boldsymbol{e}_2 + \Sigma_{33}\boldsymbol{e}_3 = \Sigma_h\boldsymbol{e}_h + \Sigma_p\boldsymbol{e}_p + \Sigma_q\boldsymbol{e}_q \tag{4.3}$$

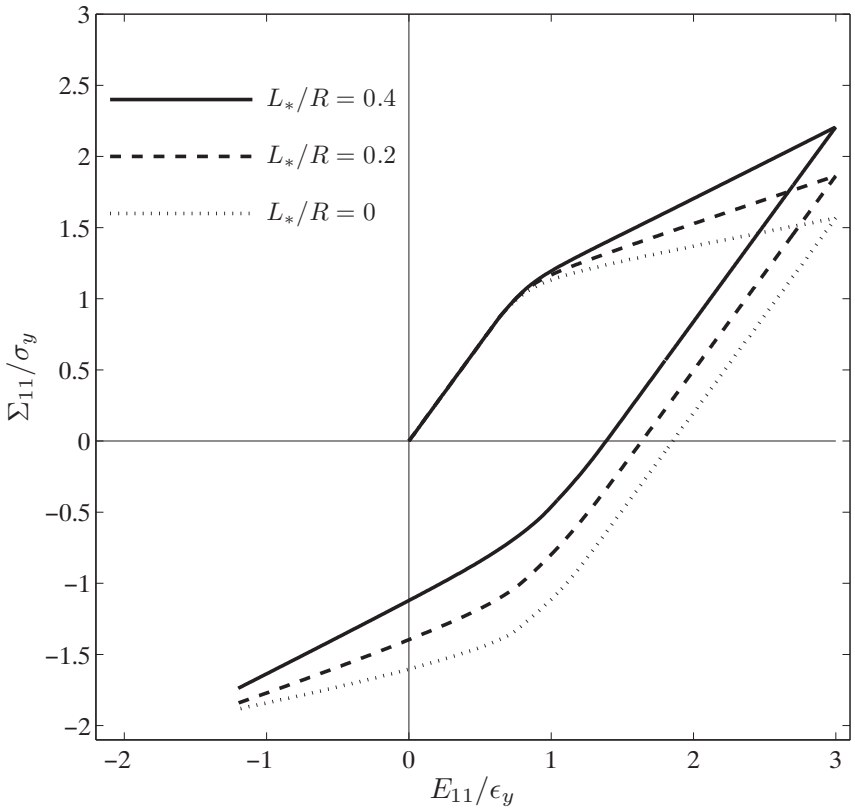

Figure 4.5 Effect of the particle size (L_*/R) on the response of the unit cell with circular fibers in transverse loading direction when $V_f = 0.2$.

where Σ_{11}, Σ_{22} and Σ_{33} are stress components in the Cartesian system, Σ_h is hydrostatic stress and Σ_p and Σ_q are stress components on the π-plane. The basis vectors on the π-plane are defined according to

$$\boldsymbol{e}_h = \frac{1}{\sqrt{3}}(1,1,1), \quad \boldsymbol{e}_p = \frac{1}{\sqrt{6}}(-1,-1,2), \quad \boldsymbol{e}_q = \frac{1}{\sqrt{2}}(1,-1,0) \tag{4.4}$$

The stress Σ_p corresponds to loading in the x_3 (longitudinal) direction with opposite loading of half magnitude in the two perpendicular directions and Σ_q corresponds to loading in the x_1 (transverse) direction with opposite loading in the x_2 direction. Fig. 4.9 shows a 3D plot of the initial yield surface of composite with $V_f = 0.2$ and $L_*/R = 0.4$, using seven different planes and 80 different initial yield points on each plane compared to the matrix yield surface. It is seen that the composite yield surface is expanded and has an almost elliptic cross section in comparison to the matrix yield surface. The cylindrical axis of the composite yield surface,

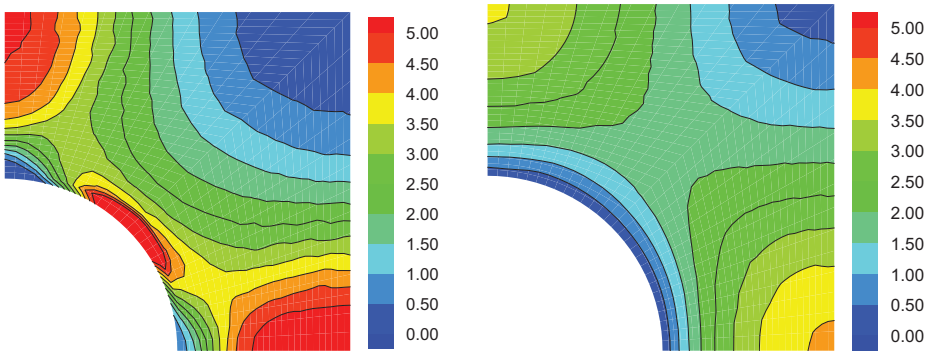

(a) $L_*/R = 0$ (b) $L_*/R = 0.4$

Figure 4.6 Effect of the material length scale on the effective plastic strain, ϵ_e^p/ϵ_y, at the end of transverse loading shown in Fig. 4.5.

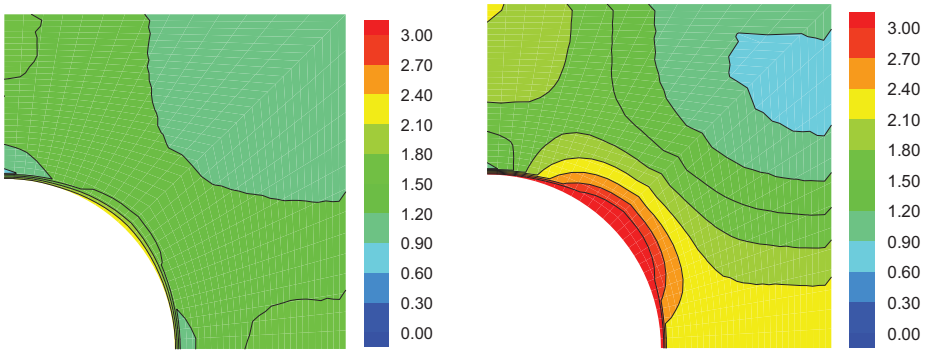

(a) $L_*/R = 0$ (b) $L_*/R = 0.4$

Figure 4.7 Effect of the material length scale on the Mises effective stress, $\sigma_e/\sigma_y = \sqrt{\frac{3}{2}s_{ij}s_{ij}}/\sigma_y$, at the end of transverse loading shown in Fig. 4.5.

$(\Sigma_{11}, \Sigma_{22}, \Sigma_{33}) = (1, 1, 1.35)$, is also deviated from the cylindrical axis of the matrix von Mises yield surface, $(\Sigma_{11}, \Sigma_{22}, \Sigma_{33}) = (1, 1, 1)$. This implies that in composites, the hydrostatic loading along the von Mises cylindrical axis, $\Sigma_{11} = \Sigma_{22} = \Sigma_{33}$, can still generate the plastic flow while hitting the wall of the composite cylinder and consequently yield the entire unit cell.

Fig. 4.10 shows the matrix yield surface, initial and subsequent yield surfaces of the composite on the π-plane for loading along e_q. The yield surface expands compared to the matrix yield surface with largest strengthening effect in e_p direction

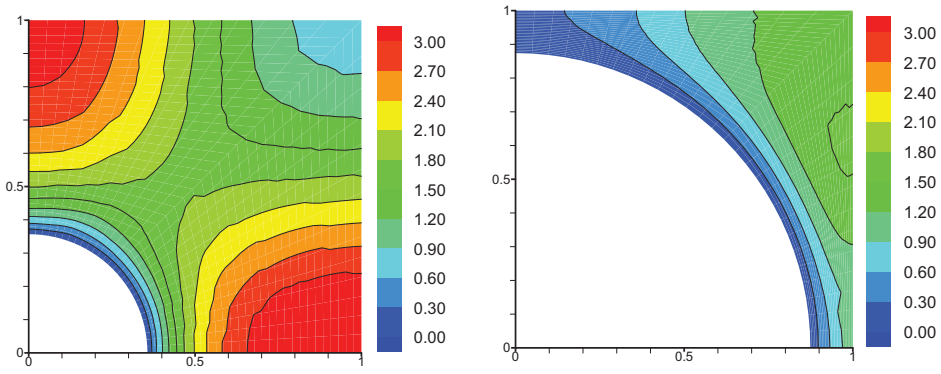

(a) $V_f = 0.1$ (b) $V_f = 0.6$

Figure 4.8 Effect of the fiber volume fraction, V_f, on the effective plastic strain, ϵ_e^p/ϵ_y, at the end of transverse loading when $L_*/R = 0.4$.

and smallest strengthening effect in e_q direction. Regarding the subsequent yield surfaces, a significant kinematic hardening with a small expansion is seen for the gradient dependent material which is opposite to the finding for the conventional material. A thoroughly computational study of both isotropic and kinematic hardening of composite yield surfaces on the π-plane can be found in [p3].

4.2 MMCs under simple shear loadings [p4]

Studying the response of composites under simple shear loading is necessary to build up the composite yield function. Two previously introduced unit cell containing rectangular and circular fibers are studied. The study excludes the out-of-plane shear loadings, $\Sigma_{13} = \Sigma_{23} = 0$. Fig. 4.11 shows both the conventional and higher order boundary conditions of simple shear imposed on the unit cell with rectangular fibers. Plastic strain is set to be zero at the fiber matrix interfaces due to plastic flow suppression shown by Mughrabi (2001). Moreover, higher order tractions vanish at the border of the unit cell (see also Bittencourt et al., 2003; Fredriksson et al., 2009). Below is the imposed boundary condition

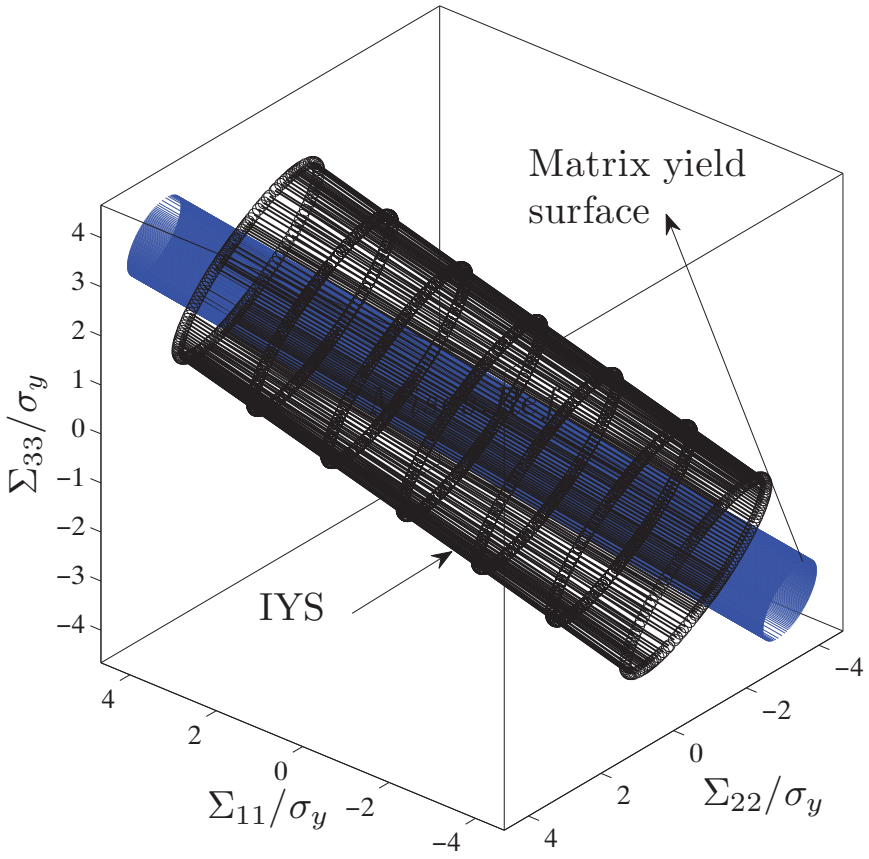

Figure 4.9 A 3D plot of the Initial Yield Surface (IYS) of the composite with $V_f = 0.2$ and $L_*/R = 0.4$ in comparison to the matrix yield surface.

$$
\begin{array}{llllll}
\dot{u}_2 = 0, & \dot{T}_1 = 0, & \text{on} & x = \pm w/2, & & y \in [-h/2, h/2], \\
\dot{u}_1 = \dot{\Delta}_3, & \dot{T}_2 = 0, & \text{on} & x \in [-w/2, w/2], & & y = h/2, \\
\dot{u}_1 = -\dot{\Delta}_3, & \dot{T}_2 = 0, & \text{on} & x \in [-w/2, w/2], & & y = -h/2, \\
\dot{\epsilon}^p_{ij} = 0, & & \text{at} & \text{all fiber matrix interfaces} & & \\
\dot{M}_{ij} = 0, & & \text{at} & x = \pm w/2, & \text{and} & y = \pm h/2,
\end{array}
\tag{4.5}
$$

Note that the above boundary condition is consistent with the requirements mentioned in Chapter 3.

Fig. 4.12 shows the response of the unit cell with rectangular fibers under simple shear loading until $E_{12} = 3.25\gamma_y$, where $\gamma_y = \tau_y/G_m$ for different value of the material length scale while $V_f = 0.2$. The macroscopic elastic shear modulus, $C_{12} = 1.24G_m$, is higher than the matrix shear modulus and it seems to be

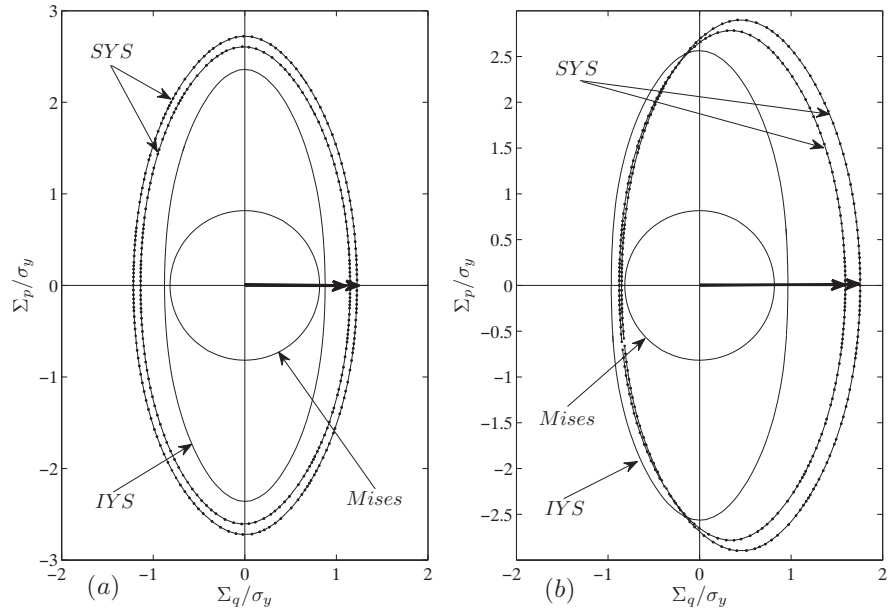

Figure 4.10 Homogenized subsequent yield surface (SYS) projected on the π-plane for two different load levels along e_q (thick arrow is the loading path). (a) $L_*/R = 0$. (b) $L_*/R = 0.4$.

unaffected by the material length scale. Initial yield stress increases from $1.08\tau_y$ corresponding to $L_*/R = 0$ towards $1.19\tau_y$ corresponding to $L_*/R = 0.4$. A considerable effect of the fiber size on the hardening is also noticeable. This has also been seen by Bittencourt et al. (2003) using the nonlocal crystal plasticity theory of Gurtin (2002). The size effect of the fiber on the effective plastic strain distribution, ϵ_e^p/ϵ_y, is shown in Fig. 4.13. A considerable amount of the plastic flow is again observable for the conventional material with concentration at the corners compared to the gradient dependent material with smooth distribution. The periodic deformation of the border is seen to be more limited for the case of gradient dependent material than the other one.

For the regularly distributed circular fibers, a unit cell with a full circle is chosen as shown in Fig. 4.14 [P4]. A complete detail of the imposed boundary condition is found in [P4].

Fig. 4.15 shows the response of the unit cell under simple shear loading with $V_f = 0.2$. Initial loading and subsequent reloading is studied, where the maximum shear strain is given by $E_{12}/\gamma_y = 1.94$ at which the load is reversed until a compressive macroscopic shear strain of $E_{12}/\gamma_y = 0.78$ is reached. As the Fig shows,

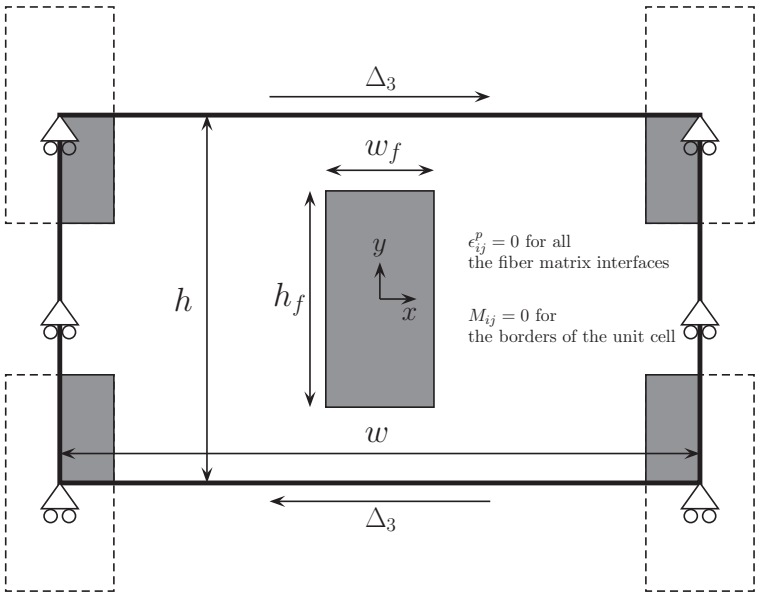

Figure 4.11 Boundary conditions and geometry of the unit cell of composite with rectangular fibers under simple shear loading with $w = \sqrt{3}h$ and $h_f = 2w_f = 0.588h$.

the stress strain curve is mainly affected after the initial yielding. The macroscopic shear modulus is $C_{12} = 1.28G_m$ and the macroscopic shear yield stress, Σ^y_{12}, has a very slight change from $1.05\tau_y$ corresponding to $L_*/R = 0$ towards $1.06\tau_y$ corresponding to $L_*/R = 0.4$. The overall hardening increases with smaller particle sizes (higher material length scale). The Bauschinger stresses also increase with smaller particle size, $A_{12} = 0, 0.017\sigma_y$ and $0.12\sigma_y$ corresponding to $L_*/R = 0, 0.2$ and 0.4, respectively. This is also observed in pure shear for strain gradient plasticity by (Anand et al., 2005; Niordson and Legarth, 2010). Regarding the initial yielding, it is concluded that composite with rectangular fibers has more strength than the one with circular fibers under simple shear loading.

Fig. 4.16 shows the distribution of the effective plastic strain, ϵ^p_e/ϵ_y, for $V_f = 0.2$ at the maximum strain loading of $E_{12} = 1.98\gamma_y$ with 30 times scaling of the displacement field. The maximum value of the effective plastic strain is higher in the conventional analysis, Fig. 4.16a, than in the gradient dependent analysis, Fig. 4.16b. With the conventional material, the plastic strain is not suppressed at the fiber matrix interface but with the gradient dependent material, the constraint on the plastic flow is observed to suppress plasticity close to the elastic fiber. It is seen that the deformation of boundaries is less wavy for the gradient dependent material

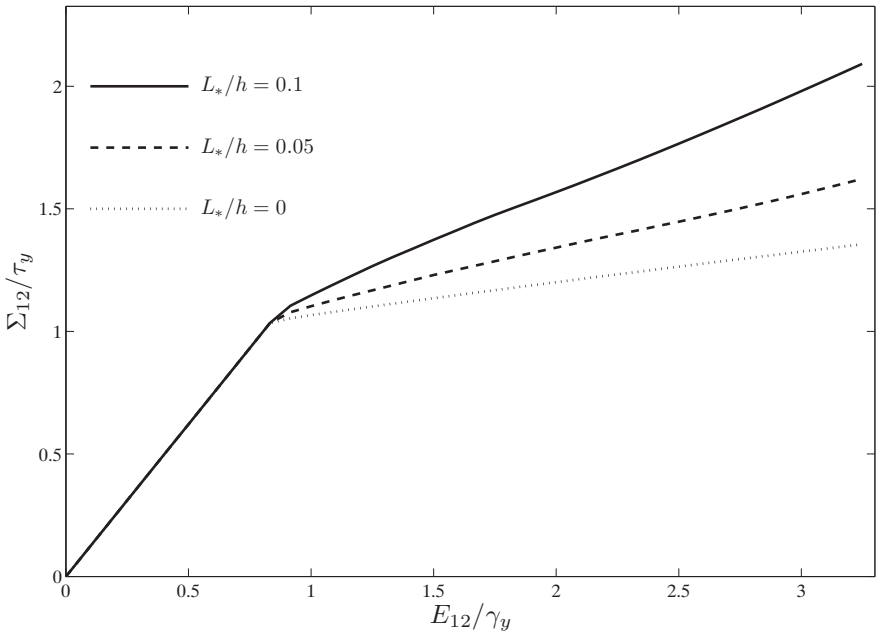

Figure 4.12 Stress strain response of the unit cell with rectangular fiber under simple shear loading until $E_{12} = 3.25\gamma_y$ affected by the material length scale, L_*/h, with $V_f = 0.2$.

than the conventional case.

Fig. 4.17 shows the corresponding effective Mises stresses, where a similar stress distribution is seen for both cases. Observing the magnitude, higher load carrying capacity at the same macroscopic shear strain is palpable for the gradient dependent material.

Fig. 4.18 shows the distribution of the normalized higher order stresses, (a) $m_{121}/(L_*\sigma_y)$ and (b) $m_{122}/(L_*\sigma_y)$, for the maximum strain loading of $E_{12}/\gamma_y = 1.98$ with $L_*/R = 0.4$. As can be seen, the higher order stress has an anti-symmetric distribution around the fiber with the maximum absolute value at the fiber matrix interface, where the gradients of the plastic strains are highest. Furthermore, they are observed to vanish at some of the boundaries in accordance to the symmetries of the problem.

Macroscopic conventional operator (elastic moduli, $\boldsymbol{C}$) is investigated according to Eq. (3.25). Since the material length scale does not affect the elastic response of composite, the study is carried out under different values of the fiber volume fraction, V_f, as shown in Tab. 4.1. It can be seen that with $V_f = 0.001$ (the composite is very close to a homogeneous material), $C_{11} = C_{22} = C_{33}$ and $C_{12} = C_{13} = C_{23}$ as it is expected. By increasing the V_f, all the components of $\boldsymbol{C}$-moduli increase, where

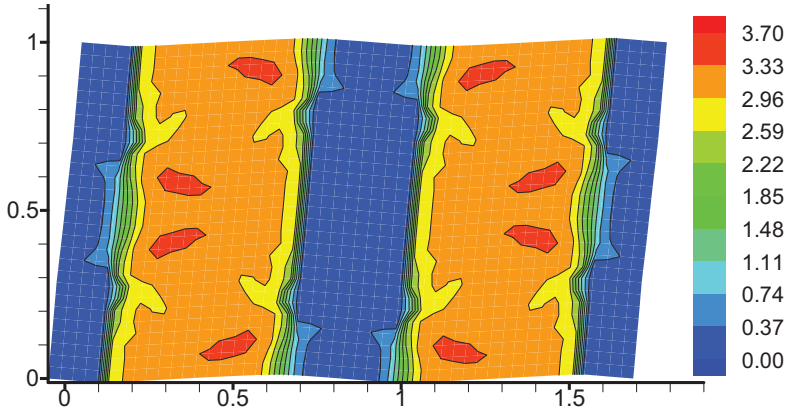

(a) $L_*/h = 0$.

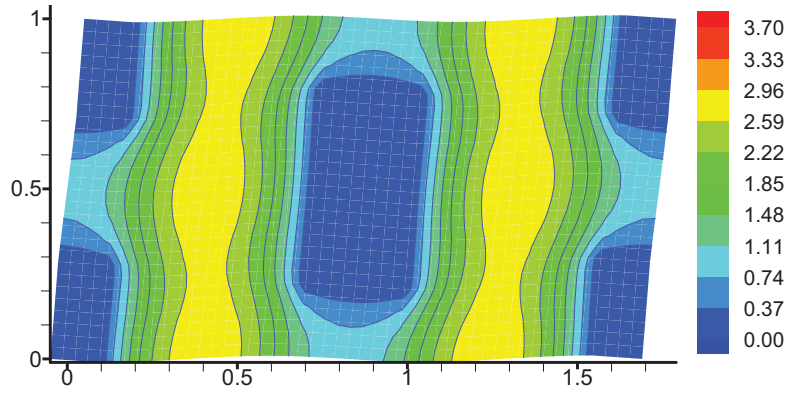

(b) $L_*/h = 0.1$.

Figure 4.13 Effective plastic strain distribution, ϵ_e^p/ϵ_y, on the deformed geometry with 5 times scaling at the end of simple shear loading until $E_{12} = 3.25\gamma_y$ while $V_f = 0.2$.

it is intense for C_{33} corresponding to the longitudinal direction, moderate for C_{11} and C_{22} corresponding to the transverse directions and small for other components. More details regarding the effect of the fiber volume fraction and matrix material hardening on the plastic deformation of composite under simple shear loading is found in [P4].

Macroscopic initial and subsequent yield surfaces are shown in Fig. 4.19 in transverse-shear (Σ_{11},Σ_{12}) coordinate system. It is seen that the composite initial yield surface is expanded most in transverse direction compared to the shear direction. The expansion is due to the suppression of the plastic deformation close to the fiber matrix interface, which tends to postpone the overall plasticity of the unit cell. This is consistent with our findings in the stress strain curves (see Figs. 4.5

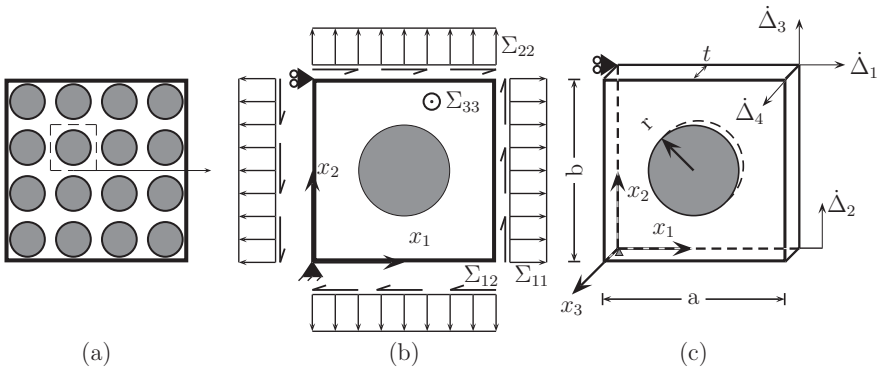

Figure 4.14 (a) Regular distribution of fibers in the composite. (b) RVE containing one fiber with traction boundary condition. (c) RVE containing one fiber with conventional displacement boundary conditions used in numerical simulation representing combined biaxial shear loading.

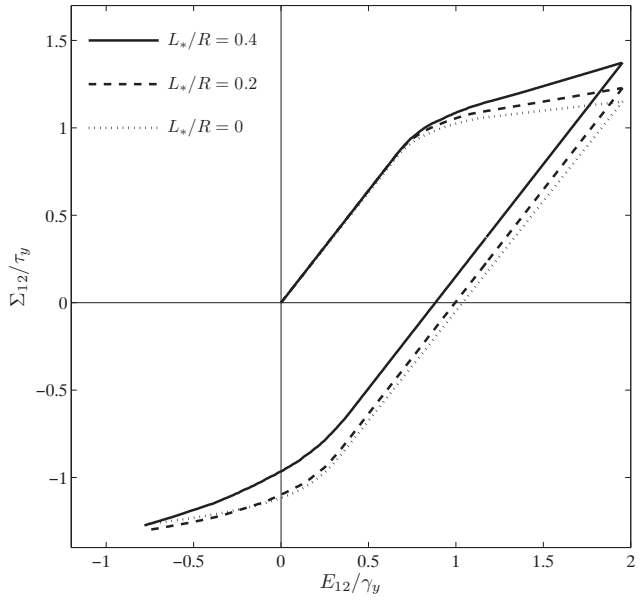

Figure 4.15 Effect of the material length scale, L_*/R, on the homogenized stress strain curve of the unit cell with circular fiber under simple shear with $V_f = 0.2$.

and 4.15). Regarding the subsequent yield surfaces, a relatively moderate expansion with a considerable kinematic hardening occurs when the unit cell is loaded in the transverse direction compared to the shear direction. Anisotropic response of

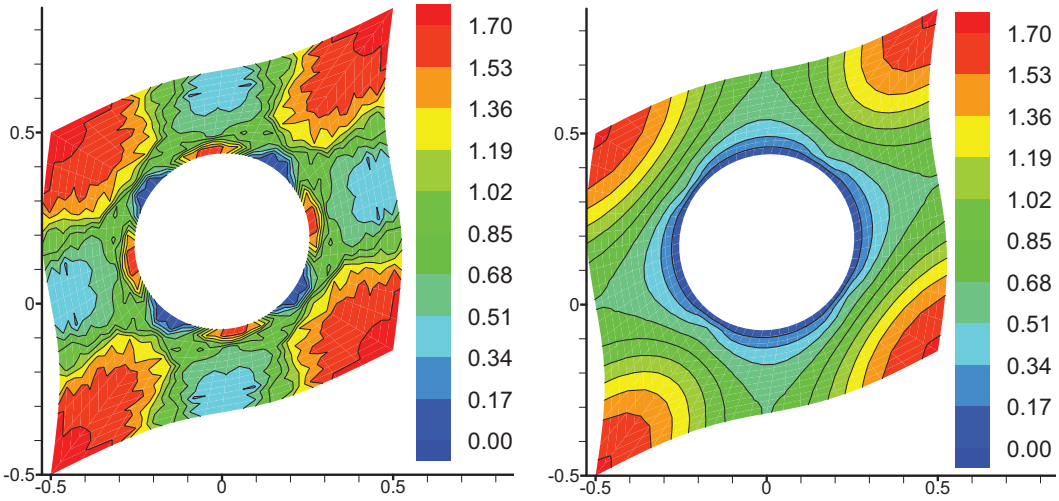

(a) $L_*/R = 0$ (b) $L_*/R = 0.4$

Figure 4.16 Effective plastic strain distribution, ϵ_e^p/ϵ_y, for simple shear with $V_f = 0.2$ at $E_{12} = 1.98\gamma_y$.

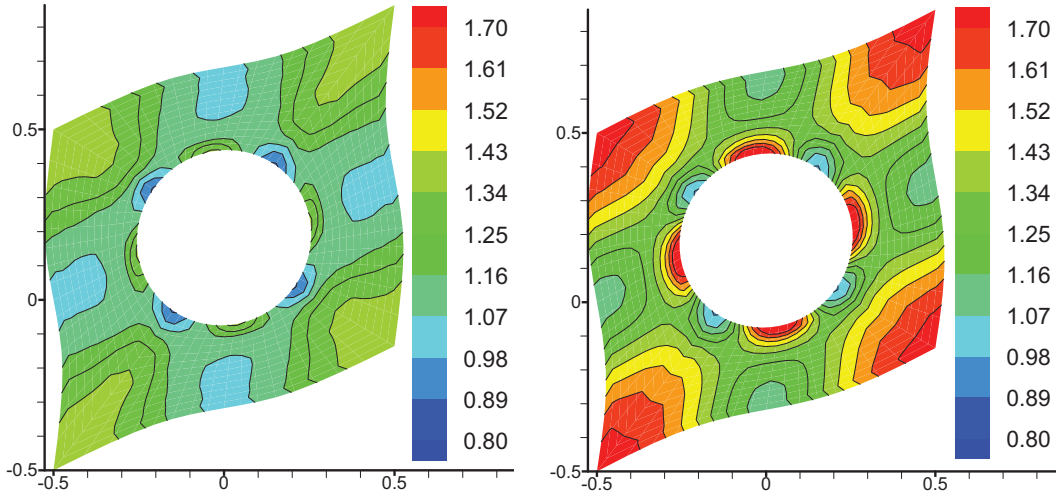

(a) $L_*/R = 0$ (b) $L_*/R = 0.4$

Figure 4.17 Effective Mises stress, $\sigma_e/\epsilon_y = \sqrt{\frac{3}{2}s_{ij}s_{ij}}/\epsilon_y$, for simple shear with $V_f = 0.2$ at $E_{12} = 1.98\gamma_y$.

the Bauschinger stress is highlighted. A thorough investigation of the initial and subsequent yield surfaces under different loading trials is found in [P4].

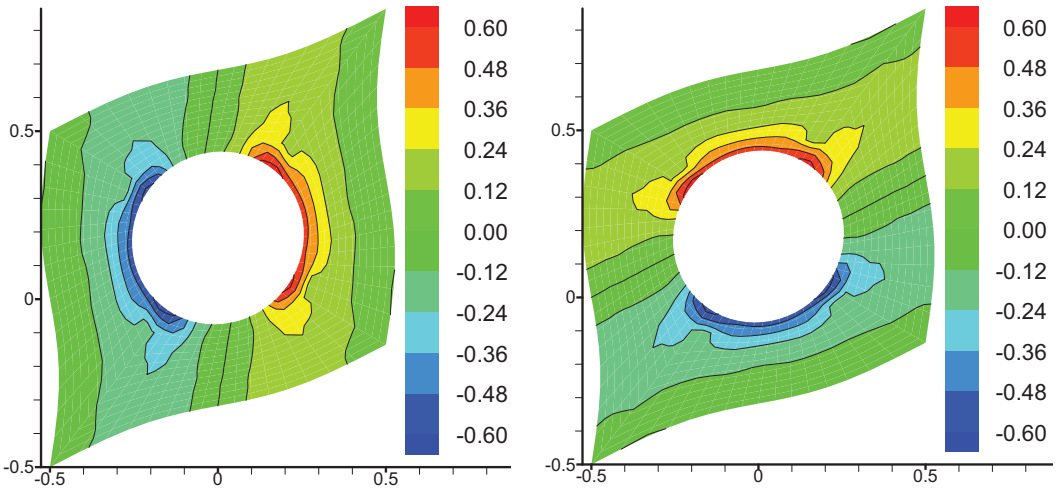

(a) $m_{121}/(L_*\sigma_y)$ (b) $m_{122}/(L_*\sigma_y)$

Figure 4.18 Higher order stresses, for simple shear with $V_f = 0.2$ at $E_{12} = 1.98\gamma_y$.

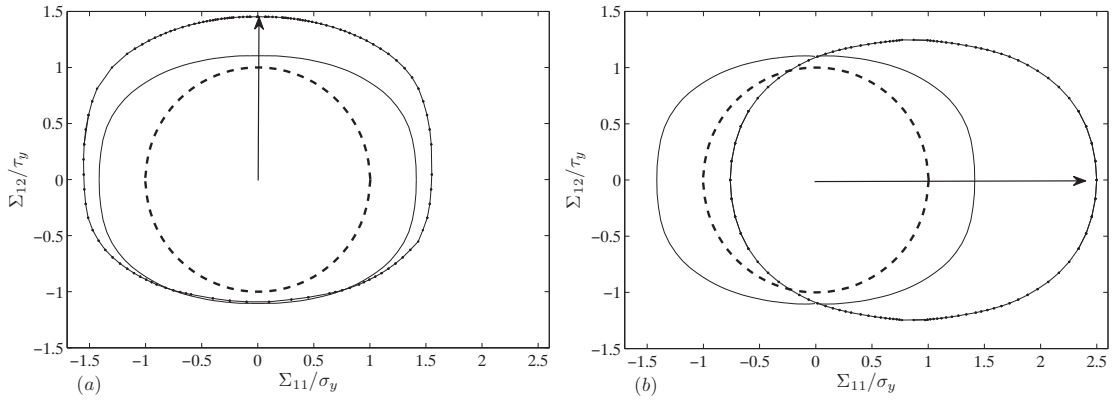

Figure 4.19 Initial and subsequent yield surface, IYS and SYS, in transverse-shear, $(\Sigma_{11}, \Sigma_{12})$, stress coordinate system with $V_f = 0.2$ and $L_*/R = 0.4$ (dashed-line: matrix yield surface, solid-line: IYS, point-line: SYS). (a) SYS with simple shear loading. (b) SYS with transverse loading.

4.3 Kinematic hardening in MMCs [p5]

The aim of this section is to establish a correlation between the trapped energy and Bauschinger stress leading to a comprehensive evaluation of the kinematic hardening in composites. The mathematical representation of the trapped energy shown in Chapter 2 facilitates the evaluation of kinematic hardening (Bauschinger stress)

	$V_f = 0.001$	$V_f = 0.2$	$V_f = 0.3$
$\frac{1}{E_m}\boldsymbol{C}$	$\begin{bmatrix} 1.35 & 0.58 & 0.58 & 0 \\ 0.58 & 1.35 & 0.58 & 0 \\ 0.58 & 0.58 & 1.35 & 0 \\ 0 & 0 & 0 & 0.38 \end{bmatrix}$	$\begin{bmatrix} 1.68 & 0.66 & 0.63 & 0 \\ 0.66 & 1.68 & 0.63 & 0 \\ 0.63 & 0.63 & 2.28 & 0 \\ 0 & 0 & 0 & 0.48 \end{bmatrix}$	$\begin{bmatrix} 1.90 & 0.69 & 0.66 & 0 \\ 0.69 & 1.90 & 0.66 & 0 \\ 0.66 & 0.66 & 2.75 & 0 \\ 0 & 0 & 0 & 0.54 \end{bmatrix}$

Table 4.1 Effect of the fiber volume fraction, V_f, on the $\boldsymbol{C}$-moduli for $L_*/R = 0.4$.

at the macroscopic scale for the sake of multi-scale modeling. Five different loading trials including transverse, longitudinal, 0^o in-plane shear, 45^o in-plane shear and out-of-plane shear are neccessary to impose on the unit cell in order to gather enough data of the trapped energy and corresponding Bauschinger stresses. The unit cell with full circular fiber is chosen for this study with the boundary condition shown in [P5].

By imposing five different loading trials, see Fig. 3.5, $\boldsymbol{P}$-moduli as the non-conventional operator, P_{ijkl} in Eqs. (2.29) and (3.28), can be computed and consequently the Bauschinger stresses are obtained. As it was shown in Fig. 4.9, the composite yield surface has an almost elliptical cross section which is expanded compared to the matrix yield surface. It is important to note that the third eigendirection of the $\boldsymbol{P}$-moduli, $\boldsymbol{v}^{\lambda_3}$, is parallel to the cylindrical axis of the composite yield surface and it deviates from the cylindrical (hydrostatic) axis of the matrix von Mises yield surface. When applying stress along this third eigendirection in the stress space, vanishing plastic strain is expected since the yield surface appears to extend to infinity. This observation can be exploited to rewrite the yield function in a reduced form on what we refer to as the Composite-plane (C-plane), which is a plane perpendicular to the third eigendirection, $\boldsymbol{v}_3^{\lambda}$. A meaningful interpretation of the Bauschinger stress as the translation is seen on just C-plane and not out of C-plane due to having a finite composite cylinder, see [P5]. Therefore, the macroscopic quantities are transformed with eigendirections of the $\boldsymbol{P}$-moduli, P_{ijkl}, as

$$\begin{bmatrix} \Omega_{\lambda_1} \\ \Omega_{\lambda_2} \\ \Omega_{\lambda_3} \\ \Omega_{\lambda_4} \end{bmatrix} = \boldsymbol{V^T} \begin{bmatrix} \Omega_{11} \\ \Omega_{22} \\ \Omega_{33} \\ \Omega_{12} \end{bmatrix}, \quad \begin{bmatrix} \Omega_{\lambda_1} \\ \Omega_{\lambda_2} \\ \Omega_{\lambda_3} \\ \Omega_{\lambda_4} \end{bmatrix} = \begin{bmatrix} v_1^{\lambda_1} & v_2^{\lambda_1} & v_3^{\lambda_1} & v_4^{\lambda_1} \\ v_1^{\lambda_2} & v_2^{\lambda_2} & v_3^{\lambda_2} & v_4^{\lambda_2} \\ v_1^{\lambda_3} & v_2^{\lambda_3} & v_3^{\lambda_3} & v_4^{\lambda_3} \\ v_1^{\lambda_4} & v_2^{\lambda_4} & v_3^{\lambda_4} & v_4^{\lambda_4} \end{bmatrix} \begin{bmatrix} \Omega_{11} \\ \Omega_{22} \\ \Omega_{33} \\ \Omega_{12} \end{bmatrix} \tag{4.6}$$

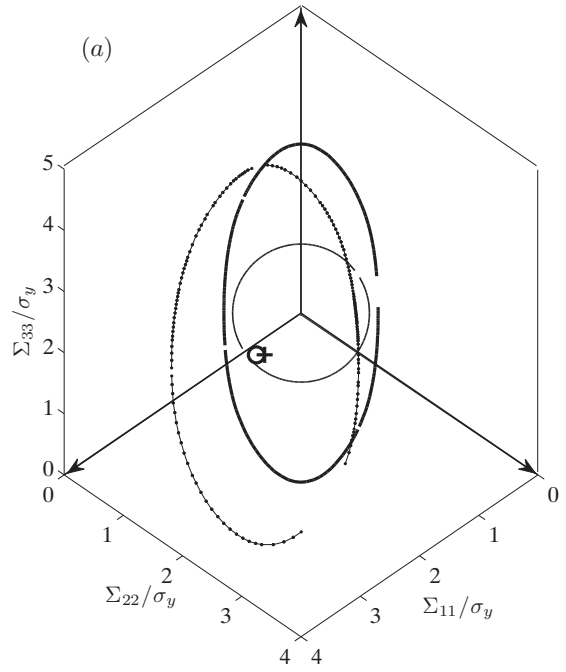

Figure 4.20 Matrix yield surface (thin line), initial yield surface (thick line) and subsequent yield surface (point line) on a plane with $\boldsymbol{v}^{\lambda_3} = \vec{e}_n = (1, 1, 1.35)$ as the normal vector and with $V_f = 0.2$ and $L_*/R = 0.4$ for loading in transverse direction till $\Sigma_{11} = 2\sigma_y$. Cross point is the geometric center of the SYS and circle point is the computed Bauschinger stress using Eq. (2.29).

where $\boldsymbol{V}$ is the matrix of eigendirections, $v_j^{\lambda_i}$ is the j_{th} component of an eigenvector of the $\boldsymbol{P}$-moduli, P_{ijkl}, in Eq. (2.24) corresponding to the i_{th} eigenvalue, λ_i, and Ω stands for any macroscopic quantity like, Σ, A and E^p.
Fig. 4.20 shows the matrix yield surface, initial yield surface and subsequent yield surface on the C-plane with $\boldsymbol{v}^{\lambda_3} = \vec{e}_n = (1, 1, 1.35)$ as the normal vector and with $V_f = 0.2$ and $L_*/R = 0.4$ for loading in transverse direction till $\Sigma_{11} = 2\sigma_y$. A good estimation of the center of the SYS using Eq. (2.29) and afterwards Eq. (4.6) is seen compared to the geometric center of the SYS. Expansion of the yield surface accompanies the translation (kinematic hardening), which will be thoroughly investigated in the next section.
Effect of the material length scale, L_*/R, on the trapped energy computed with Eq. (3.27) and the corresponding Bauschinger stresses is studied. Fig. 4.21 shows the result with $V_f = 0.2$ for (a) transverse (x_1) and (b) longitudinal (x_3) loading direction. It is seen that by decreasing the particle size (increasing the material length scale), the amount of the trapped energy increases significantly by the transverse

loading and moderately by the longitudinal loading. Deshpande et al. (2005) also showed that the stored energy associated with the dislocation (Trapped energy) is enhanced by decreasing the size. For the conventional response, the trapped energy by the transverse loading is relatively small and hardly shows a quadratic behavior, while a quadratic function is well fitted for all other curves.

In Fig. 4.22, the corresponding Bauschinger stresses using the trapped energy in

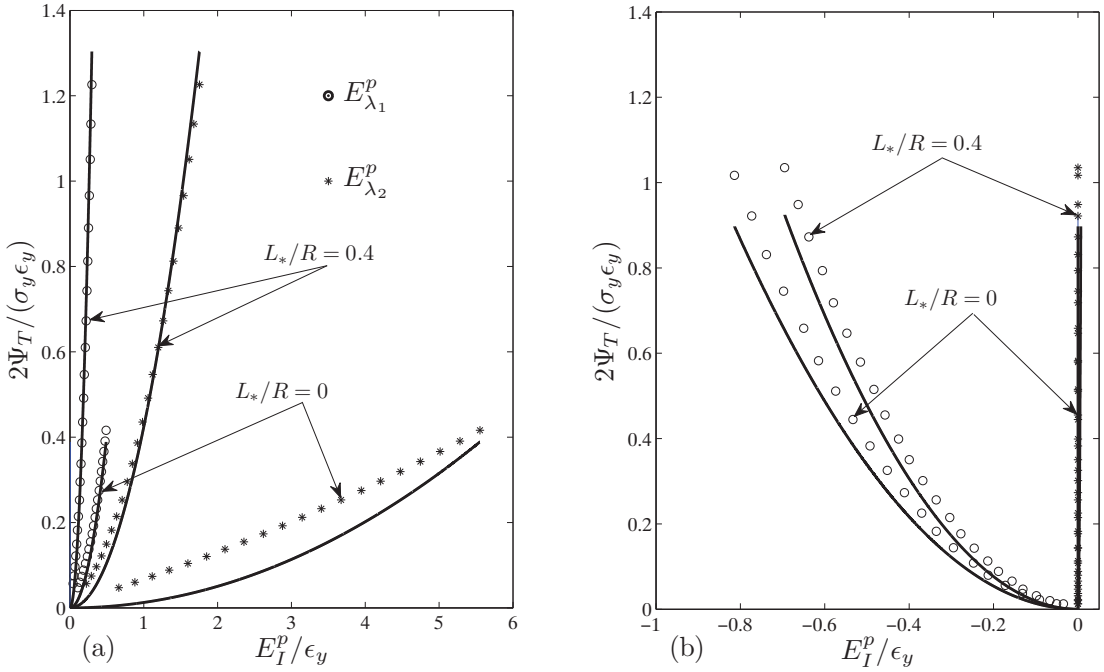

Figure 4.21 Effect of the material length scale, L_*/R, on the trapped energy, $2\Psi_T/(\sigma_y\epsilon_y)$, with $V_f = 0.2$ for (a) transverse loading (x_1). (b) longitudinal loading (x_3). Solid line is the fitting function with the parameters shown in Tab. 4.2.

Fig. 4.21 is plotted. The Fig shows that with a higher value of the material length scale, L_*/R, the transformed Bauschinger stress, A_{λ_i}, increases significantly by the transverse loading and moderately by the longitudinal loading, consistent with the behavior of the trapped energy. The solid line is the fitting function with the fitting parameters, P_{λ_i}, shown in Tab. 4.2 and the points are the geometric center of the SYS.

Fig. 4.23 is plotted to show the behavior of the unit cell under 0^o in-plane shear loading with $V_f = 0.2$. For the conventional material, Fig. 4.23a and b, an almost zero trapped energy is seen with a relatively large amount of plasticity. For the gradient dependent material, Fig. 4.23c and d, the plastic strain is suppressed close to

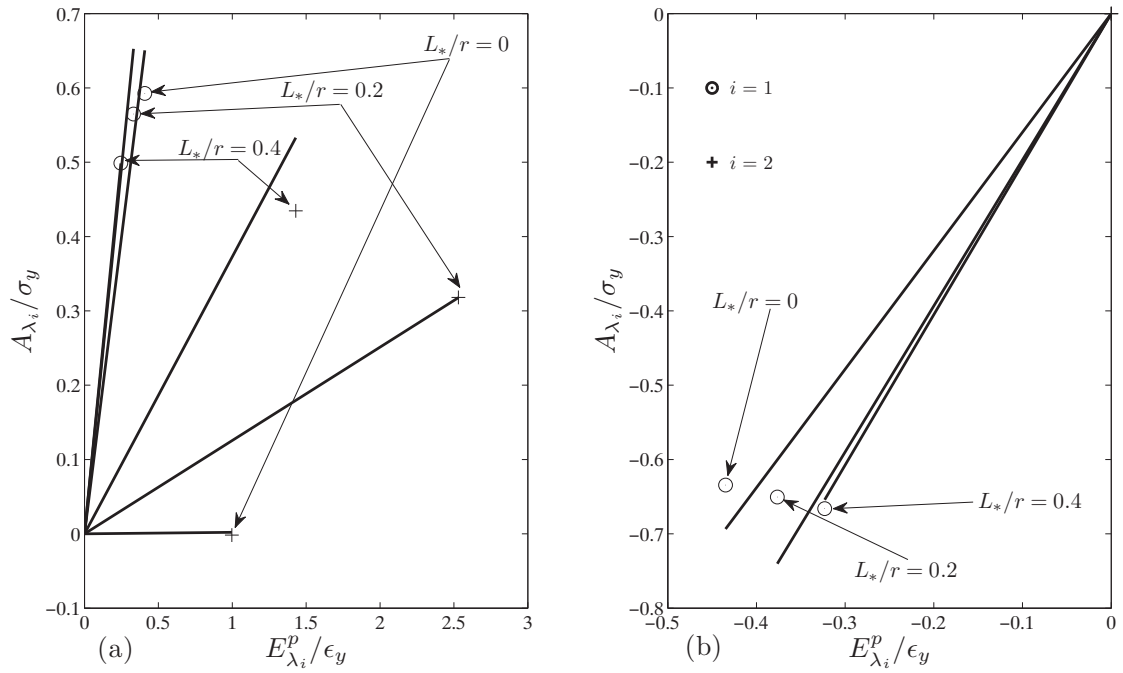

Figure 4.22 Effect of the material length scale, L_*/R, on the geometric center of the SYS in the transformed coordinate system with $V_f = 0.2$ for (a) transverse loading (x_1). (b) longitudinal loading (x_3). Solid line is the fitting function with the parameters shown in Tab. 4.2 and the points are the geometric center of the SYS.

the fiber matrix interface, where the trapped energy, $2\psi_T/(\sigma_y\epsilon_y)$, is higher compared to the other regions. The trapped energy is also available inside the fiber, where the plastic strain is zero. A smooth transition of the plastic flow from the fiber into the matrix is seen.

A quantitative study of Fig. 4.23 is plotted for the trapped energy in Fig. 4.24a and the corresponding Bauschinger stress in Fig. 4.24b. The amount of trapped energy and corresponding Bauschinger stress are almost zero for the conventional case, while it is enhanced for the gradient dependent material with $L_*/R = 0.4$. Note that due to the material symmetries assumed in the present unit cell model, 0^o in-plane shear loading trial does not generate plasticity in the $\boldsymbol{v}^{\lambda_1}$, $\boldsymbol{v}^{\lambda_2}$ and $\boldsymbol{v}^{\lambda_3}$ directions. As a result, the Bauschinger stress can be conventionally defined as (see Azizi et al., 2011b,a)

$$A_{\lambda_4} = A_{12} = \frac{(\Sigma^f_{12} + \Sigma^{sy}_{12})}{2} \tag{4.7}$$

where Σ^f_{12} is stress at the end of loading and Σ^{sy}_{12} is the stress at the subsequent yield

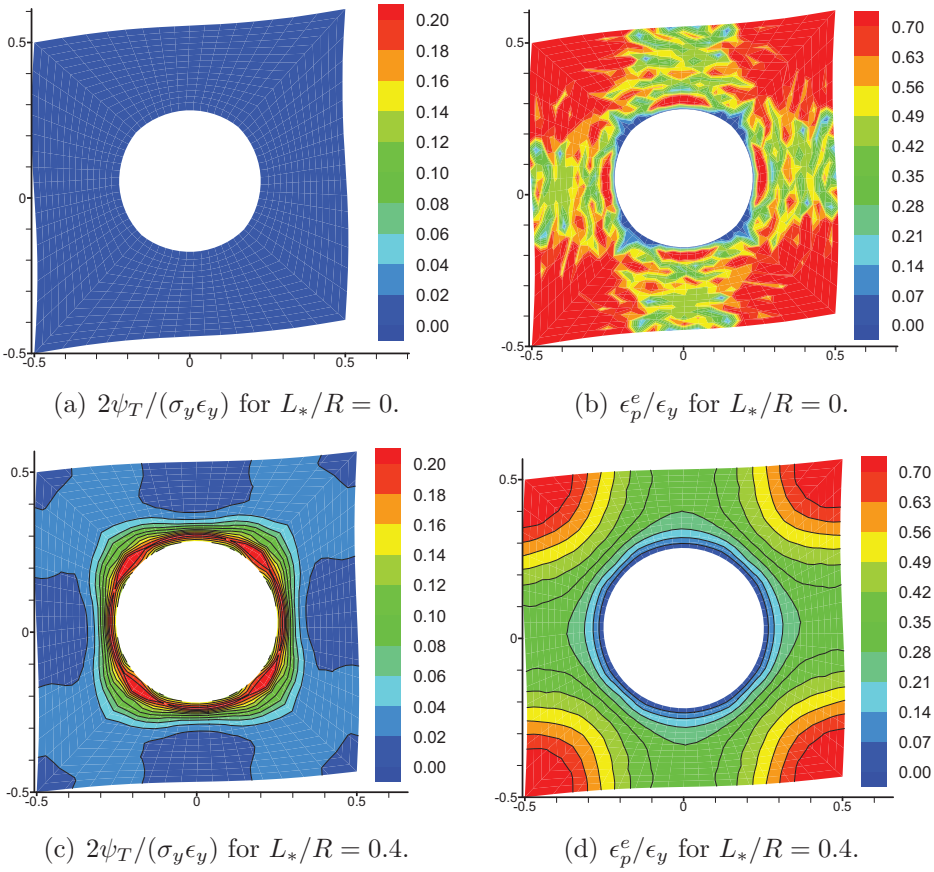

(a) $2\psi_T/(\sigma_y\epsilon_y)$ for $L_*/R = 0$. (b) ϵ_p^e/ϵ_y for $L_*/R = 0$.

(c) $2\psi_T/(\sigma_y\epsilon_y)$ for $L_*/R = 0.4$. (d) ϵ_p^e/ϵ_y for $L_*/R = 0.4$.

Figure 4.23 Trapped energy and the corresponding effective plastic strain in 0^o in-plane shear with $V_f = 0.2$.

point under reverse loading. In Fig. 4.24b, the circle points represent the geometric center of the yield surface during loading. The enhanced Bauschinger stress is in accordance with results for pure shear of a slab between rigid plates studied by Niordson and Legarth (2010). It is emphasized that the conventional definition for the Bauschinger stress, Eq. (4.7), in composite under multi-axial loadings can not represent the geometrical center of the multi-dimensional yield surface, while the definition with the current approach, Eq. (2.29), can.

As it is seen in Tab. 4.2, the material length scale does not affect the orientation of the composite cylinder, while it expands the cylinder. The expansion is represented by the eigenvalues of $\boldsymbol{P}$-matrix and the orientation is represented by the eigendirections of $\boldsymbol{P}$-matrix. However, in Tab. 4.3, the fiber volume fraction, V_f, not only expands the yield surface but also changes the orientation of it. It is seen that for a very small V_f (close to the homogeneous material), the third eigendirection,

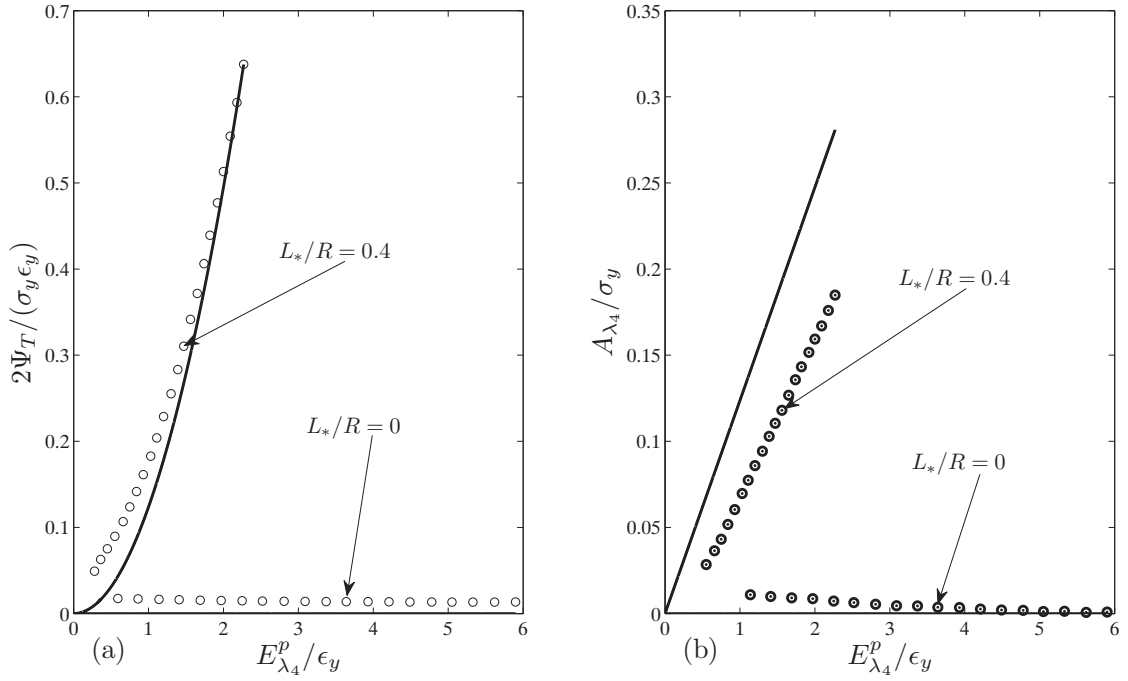

Figure 4.24 0^o in-plane shear with $V_f = 0.2$ and the effect of the material length scale, L_*/R, on (a) Trapped energy, $2\psi^T/(\sigma_y\epsilon_y)$. (b) Bauschinger stress, A_{λ_4}/σ_y. Solid line is the fitting function with the parameters shown in Tab. 4.2.

$\boldsymbol{v}^{\lambda_3}$=(0.57,0.57,0.57), is parallel to the von Mises hydrostatic pressure line as it is expected. More details of the kinematic hardening in composites can be found in [P5].

4.4 Anisotropic hardening and yield function of MMCs [p6]

As previously shown, the expansion (anisotropic hardening) accompanies the translation (kinematic hardening) of the yield surface. Knowing both types of hardening is necessary to finally develop the composite yield function. In this section, the anisotropic hardening is computationally investigated and Hill's yield function, Hill (1948), is extended to fit the numerical data (see Sec. 2.2, Chapter 2). The unit cell is chosen as of the one in the previous section for this study.

Extension of the Hill's anisotropic yield function is mainly based on the pressure dependency. It has been observed that the whole unit cell is moved to the plastic

	$L_*/R = 0$	$L_*/R = 0.2$	$L_*/R = 0.4$
$\frac{1}{E_m}\boldsymbol{P}$	$\begin{bmatrix} 206.9 & 206.9 & 282.9 & 0 \\ 206.9 & 206.9 & 282.9 & 0 \\ 282.9 & 282.9 & 390.1 & 0 \\ 0 & 0 & 0 & 0.004 \end{bmatrix}$	$\begin{bmatrix} 2420.9 & 2420.8 & 3261.7 & 0 \\ 2420.8 & 2420.9 & 3261.7 & 0 \\ 3261.7 & 3261.7 & 4398.3 & 0 \\ 0 & 0 & 0 & 0.031 \end{bmatrix}$	$\begin{bmatrix} 1307.4 & 1307.0 & 1728.3 & 0 \\ 1307.0 & 1307.4 & 1728.3 & 0 \\ 1728.3 & 1728.3 & 2288.9 & 0 \\ 0 & 0 & 0 & 0.123 \end{bmatrix}$
$\frac{1}{E_m}\boldsymbol{P}_{\lambda_i}$	$\begin{bmatrix} 1.59 & 0.002 & 802.2 & 0.004 \end{bmatrix}$	$\begin{bmatrix} 1.966 & 0.126 & 9238 & 0.030 \end{bmatrix}$	$\begin{bmatrix} 2.020 & 0.373 & 4901 & 0.123 \end{bmatrix}$
$\boldsymbol{V}$	$\begin{bmatrix} 0.49 & 0.70 & 0.50 & 0.00 \\ 0.49 & -0.70 & 0.50 & 0.00 \\ -0.71 & 0.00 & 0.69 & 0.00 \\ 0.00 & 0.00 & 0.00 & 1.00 \end{bmatrix}$	$\begin{bmatrix} 0.49 & 0.70 & 0.51 & 0.00 \\ 0.49 & -0.70 & 0.51 & 0.00 \\ -0.72 & 0.00 & 0.69 & 0.00 \\ 0.00 & 0.00 & 0.00 & 1.00 \end{bmatrix}$	$\begin{bmatrix} 0.48 & 0.70 & 0.51 & 0.00 \\ 0.48 & -0.70 & 0.51 & 0.00 \\ -0.73 & 0.00 & 0.68 & 0.00 \\ 0.00 & 0.00 & 0.00 & 1.00 \end{bmatrix}$

Table 4.2 Effect of the material length scale, L_*/R, on the $\boldsymbol{P}$-matrix, eigenvalues of the $\boldsymbol{P}$-matrix (fitting parameters) and eigendirections of $\boldsymbol{P}$-matrix (composite cylindrical axes) for $V_f = 0.2$.

regime under macroscopic hydrostatic pressure loading, $\Sigma_{11} = \Sigma_{22} = \Sigma_{33}$. To see this, the unit cell is loaded through the hydrostatic pressure line until $\Sigma_{11} = \Sigma_{22} = \Sigma_{33} = 3\sigma_y$ and the effective plastic strain distribution, ϵ_e^p/ϵ_y, is shown in Fig. 4.25. The macroscopic plasticity is generated when the stress state hits the wall of the composite cylinder shown in Fig. 4.9, while the microscopic plasticity evolves sooner than that.

Effect of the fiber volume fraction with a constant material length scale, $L_*/R = 0.4$, is also seen through Figs. 4.25a, b and c. By increasing the fiber volume fraction, the plasticity starts to grow close to the interface from a thin line distribution in Fig. 4.25a for $V_f = 0.1$ to a more clustered distribution in Fig. 4.25b for $V_f = 0.2$ and more severe clustered distribution in Fig. 4.25c for $V_f = 0.3$. This behavior reveals as the rotation of composite yield surface shown in Fig. 4.9 and Tab. 4.3. It is concluded that pressure independence of the micro-structure in composites does not result into the same behavior at the macroscopic scale.

The above observations require an extended version of the Hill's anisotropic yield function for composites. The elaborated method for this extension is found in [P6]. Here, we briefly write the composite yield function as

$$\Phi = F^{\lambda}(\tilde{\Sigma}_{\lambda_1})^2 + H^{\lambda}(\tilde{\Sigma}_{\lambda_2})^2 + N^{\lambda}(\tilde{\Sigma}_{\lambda_4})^2 - 1 \tag{4.8}$$

	$V_f = 0.001$	$V_f = 0.1$	$V_f = 0.3$
$\frac{1}{E_m}\boldsymbol{P}$	$\begin{bmatrix} 27.97 & 27.97 & 27.99 & 0 \\ 27.97 & 27.97 & 27.99 & 0 \\ 27.99 & 27.99 & 28.03 & 0 \\ 0 & 0 & 0 & 0.0001 \end{bmatrix}$	$\begin{bmatrix} 1075.1 & 1074.9 & 1260.9 & 0 \\ 1074.9 & 1075.1 & 1260.9 & 0 \\ 1260.9 & 1260.9 & 1480.0 & 0 \\ 0 & 0 & 0 & 0.032 \end{bmatrix}$	$\begin{bmatrix} 1143.8 & 1142.3 & 1749.0 & 0 \\ 1142.3 & 1143.8 & 1749.0 & 0 \\ 1749.0 & 1749.0 & 2685.1 & 0 \\ 0 & 0 & 0 & 0.40 \end{bmatrix}$
$\frac{1}{E_m}\boldsymbol{P}_{\lambda_i}$	$\begin{bmatrix} 0.004 & 0.0002 & 83.96 & 0.0001 \end{bmatrix}$	$\begin{bmatrix} 0.585 & 0.147 & 3629 & 0.032 \end{bmatrix}$	$\begin{bmatrix} 4.19 & 1.51 & 4967 & 0.40 \end{bmatrix}$
$\boldsymbol{V}$	$\begin{bmatrix} 0.41 & 0.70 & 0.57 & 0.00 \\ 0.41 & -0.70 & 0.57 & 0.00 \\ -0.81 & 0.00 & 0.57 & 0.00 \\ 0.00 & 0.00 & 0.00 & 1.00 \end{bmatrix}$	$\begin{bmatrix} 0.45 & 0.70 & 0.54 & 0.00 \\ 0.45 & -0.70 & 0.54 & 0.00 \\ -0.77 & 0.00 & 0.64 & 0.00 \\ 0.00 & 0.00 & 0.00 & 1.00 \end{bmatrix}$	$\begin{bmatrix} 0.52 & 0.70 & 0.48 & 0.00 \\ 0.52 & -0.70 & 0.48 & 0.00 \\ -0.68 & 0.00 & 0.73 & 0.00 \\ 0.00 & 0.00 & 0.00 & 1.00 \end{bmatrix}$

Table 4.3 Effect of the fiber volume fraction, V_f, on the $\boldsymbol{P}$-matrix, eigenvalues of the $\boldsymbol{P}$-matrix (fitting parameters) and eigendirections of $\boldsymbol{P}$-matrix (composite cylindrical axes) for $L_*/R = 0.4$.

where $\tilde{\Sigma}_{\lambda_i} = \Sigma_{\lambda_i} - A_{\lambda_i}$ and F^λ,H^λ and N^λ are the new anisotropic parameters. The above function represents an elliptic cross-section of the composite's cylindrically ellipsoidal yield surface. Since Σ_{λ_3} is parallel to the cylindrical axis of the composite yield surface, it is excluded from Eq. (4.8). Σ_{λ_1} and Σ_{λ_2} are the major and minor axis of the elliptic cross-section.

As an example, Fig. 4.26 is plotted (accentuating on both Σ_{λ_1} and Σ_{λ_2} while excluding Σ_{λ_3}) to show the subsequent yield surface (SYS) under longitudinal loading until $\Sigma_{33} = 3\sigma_y$ when $L_*/R = 0.4$ and $V_f = 0.2$. The figure also shows a cut of the 3D initial yield surface of the composite (Fig. 4.9). A considerable amount of the kinematic hardening together with a slight expansion is observable.
To evaluate the expansion, evolution of the anisotropic parameters of the composite yield function under longitudinal, transverse and 0^o in-plane shear loading trials is studied. Figs. 4.27 and 4.28 show the effect of the material length scale, L_*/R, on F^λ and H^λ for the longitudinal and transverse loading, respectively. They are plotted versus the macroscopic plastic strain measure, $E^p_e = \sqrt{E^p_{\lambda_i} E^p_{\lambda_i}}$, while $L_*/R = 0.4$ and $V_f = 0.2$. It is seen that for the higher material length scale, the initial and subsequent anisotropic coefficients decrease, which is a sign of both initial and sub-

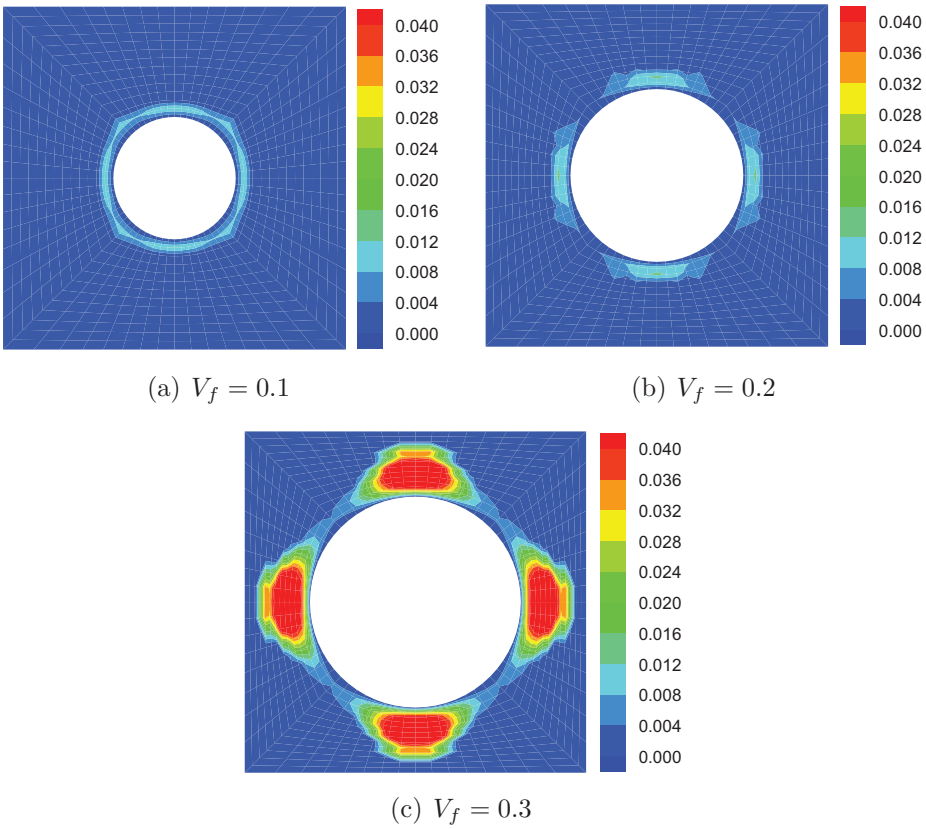

(a) $V_f = 0.1$ (b) $V_f = 0.2$

(c) $V_f = 0.3$

Figure 4.25 The effective plastic strain distribution, ϵ_e^p/ϵ_y, with hydrostatic pressure loading until $\Sigma_{11} = \Sigma_{22} = \Sigma_{33} = 3\sigma_y$ with $L_*/R = 0.4$

sequent yield surface expansion. However, the slope of the anisotropic coefficients (reduction rate) is different according to the loading condition and the material length scale. For the normal loadings, the elongation of both major and minor axes of the ellipses shown in Fig. 4.26 can be defined as

$$R^s = \sqrt{H_0^\lambda / H^\lambda} R_0^s, \quad R^l = \sqrt{F_0^\lambda / F^\lambda} R_0^l \tag{4.9}$$

where R_0^s and R_0^l are the initial length of the major and minor axes, respectively and R^s and R^l are the subsequent length of the major and minor axes, respectively. In Fig. 4.26, the minor axis is $R^s = 1.06R_0^s$, while the major axis is $R^l = 1.05R_0^l$. By studying the composite response under transverse loading [P6], it is concluded that the expansion of the ellipse is higher in the minor axis, v^{λ_2}, compared to the major axis, v^{λ_1}, for both normal loading trials.

A thorough investigation of the anisotropic hardening in composites with all the

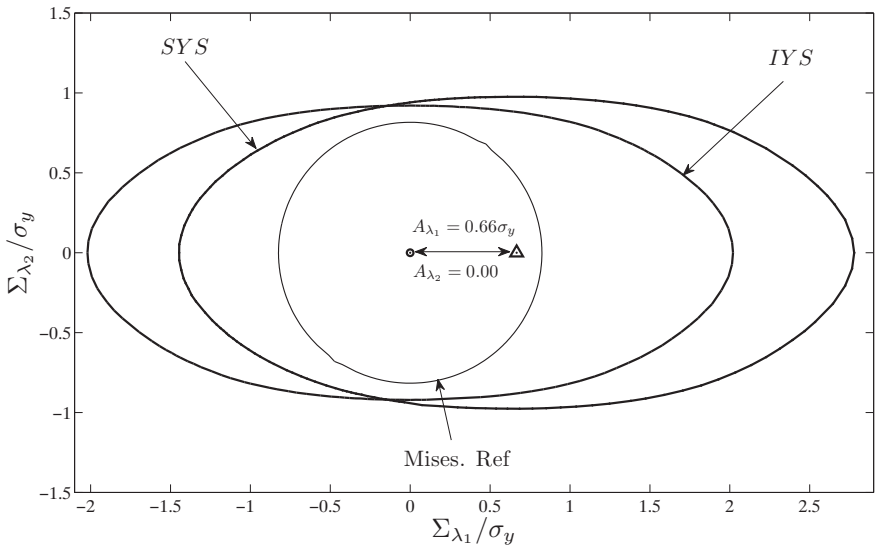

Figure 4.26 Initial and subsequent yield surface of composite with longitudinal loading until $\Sigma_{33} = 3\sigma_y$ when $L_*/R = 0.4$ and $V_f = 0.2$.

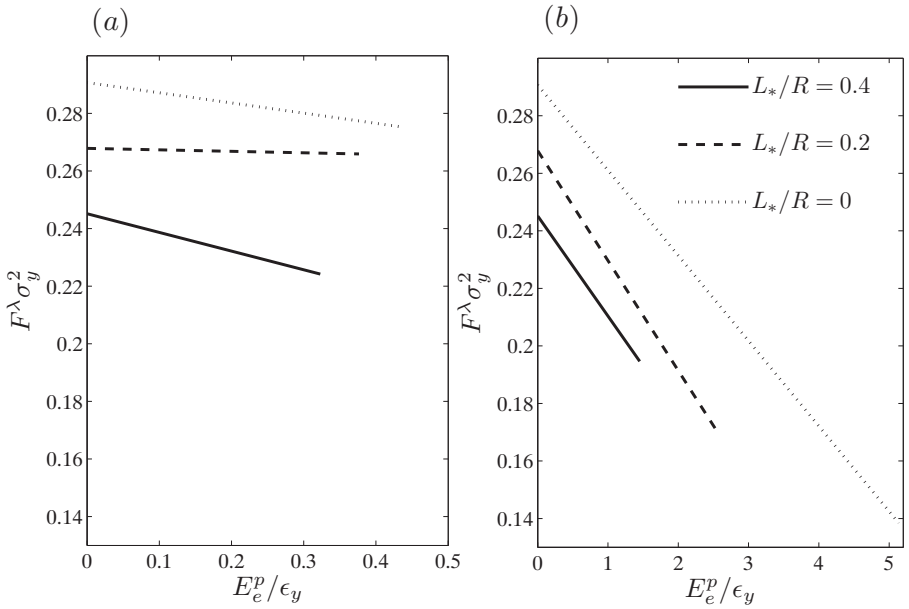

Figure 4.27 Effect of the material length scale on F^λ for (a) Longitudinal loading until $\Sigma_{33} = 3\sigma_y$. (b) Transverse loading until $\Sigma_{11} = 2\sigma_y$.

required loading trials is found in [P6]. As the result of the study, the anisotropic hardening coefficients at the macroscopic scale affected by the material length scale are introduced. By knowing the hardening coefficients [P6] and the Bauschinger stress and tangent operators [P5], one can use the defined anisotropic pressure dependent yield function in Eq. (4.8) to model a problem at the macro scale using hierarchical method in multi-scale modeling.

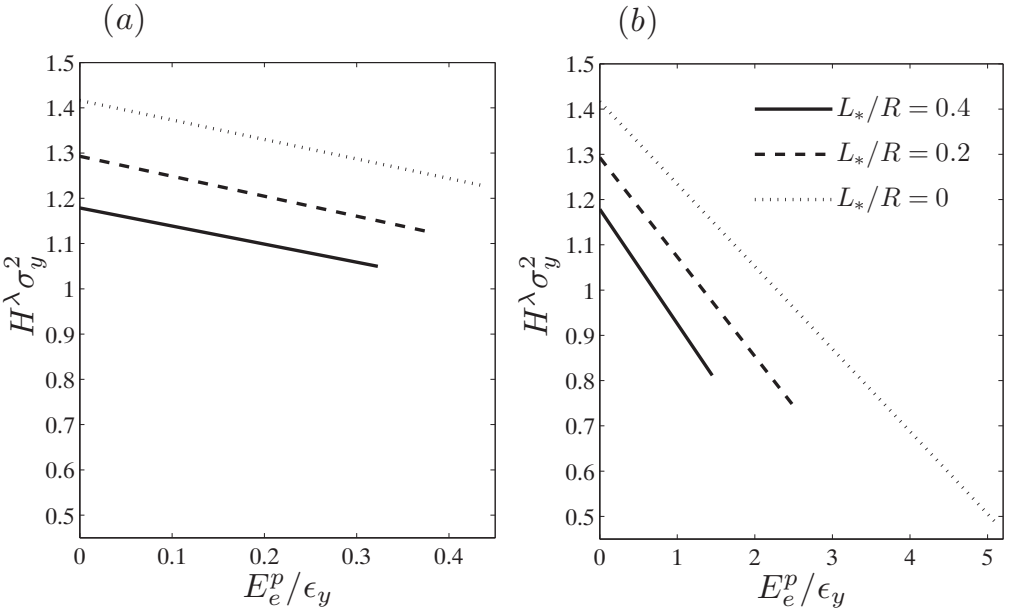

Figure 4.28 Effect of the material length scale on H^λ for (a) Longitudinal loading until $\Sigma_{33} = 3\sigma_y$. (b) Transverse loading until $\Sigma_{11} = 2\sigma_y$.

4.5 Debonding failure in MMCs [p7]

A weak interface is analyzed under uniaxial loading in the transverse direction. The unit cell with circular fiber is loaded until the maximum deformation of $E_{11} = 5\epsilon_y$ is achieved.

Fig. 4.29 shows the effect of the material length scale, L_*/R, on the stress strain curve with $\sigma_{max} = \sigma_y$ and $\delta_n = \delta_t = \delta = 0.03R$. It is seen that the material length scale does not affect the elastic modulus but it can slightly increase the yield point and hardening as was found experimentally by Nan and Clarke (1996). The stress drops due to the interface debonding at $\Sigma_{11} = 1.27\sigma_y$ corresponding to $L_*/R = 0$, at $\Sigma_{11} = 1.39\sigma_y$ corresponding to $L_*/R = 0.2$ and at $\Sigma_{11} = 1.46\sigma_y$ corresponding

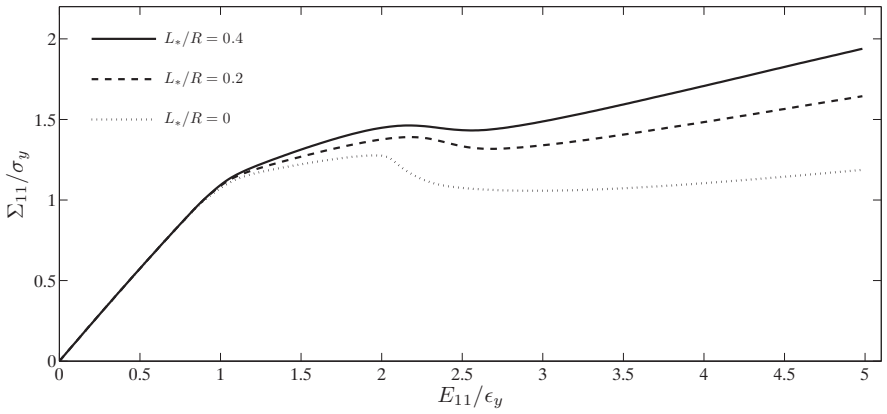

Figure 4.29 Effect of the material length scale, L_*/R, on the stress strain curve of uniaxial tension with $\sigma_{max} = \sigma_y$ and $\delta_n = \delta_t = \delta = 0.03R$.

to $L_*/R = 0.4$. After failure by debonding, the load carrying capacity is almost constant for the conventional material, where an enhancement is seen for the strain gradient dependent material.

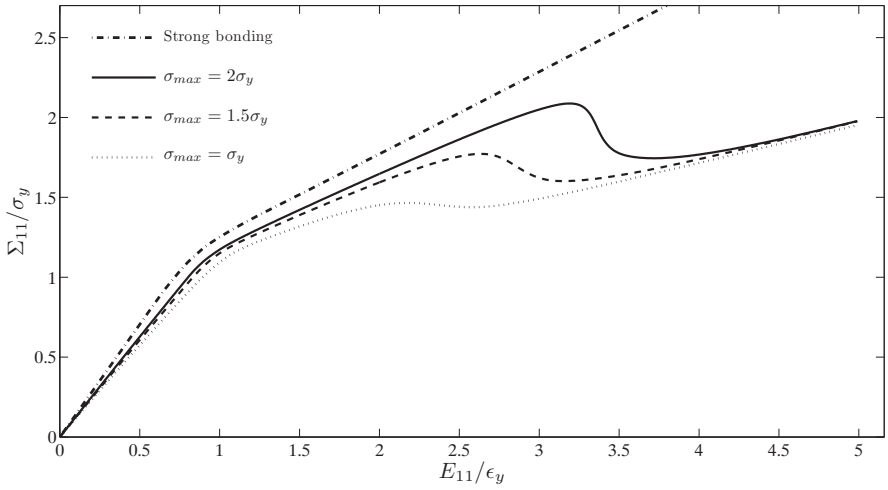

Figure 4.30 Effect of the maximum stress carried by the interface, σ_{max}, on the stress strain curve of the uniaxial tension with $\delta = 0.03R$ and $L_*/R = 0.4$.

Fig. 4.30 shows the effect of the maximum stress carried by the interface, σ_{max}, on the stress strain curve with $\delta = 0.03R$ and $L_*/R = 0.4$. Both elastic modulus

and yield stress increase slightly. The onset of debonding is significantly postponed from $\Sigma_{11} = 1.46\sigma_y$ corresponding to $\sigma_{max} = \sigma_y$ towards $\Sigma_{11} = 2.08\sigma_y$ corresponding to $\sigma_{max} = 2\sigma_y$. The stress-drop occurs more sudden for the higher value of σ_{max}. Thereafter, the hardening is seen to be the same for all the cases. Similar behavior has been shown by Xu and Needleman (1993), Needleman et al. (2010) and Zhang et al. (2005).

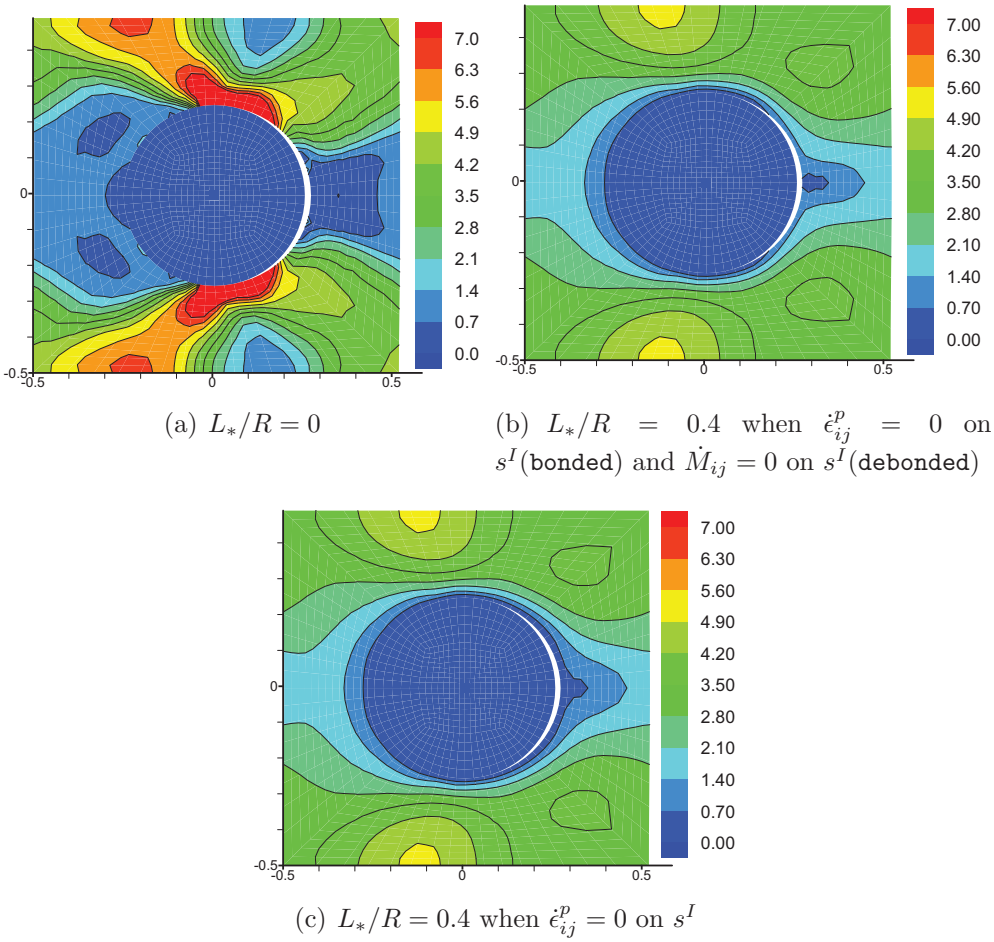

(a) $L_*/R = 0$

(b) $L_*/R = 0.4$ when $\dot{\epsilon}^p_{ij} = 0$ on s^I(`bonded`) and $\dot{M}_{ij} = 0$ on s^I(`debonded`)

(c) $L_*/R = 0.4$ when $\dot{\epsilon}^p_{ij} = 0$ on s^I

Figure 4.31 Accumulative plastic strain, ϵ^p_e/ϵ_y, for uniaxial tension with $\delta = 0.03R$ and $\sigma_{max} = \sigma_y$ at the end of loading where $E_{11} = 5\epsilon_y$ with real deformation field.

Fig. 4.31 shows the effect of the length scale, L_*/R, on the effective plastic strain, ϵ^p_e/ϵ_y, with $\delta = 0.03R$ and $\sigma_{max} = \sigma_y$. For the case of conventional material, Fig. 4.31a, a significant amount of the plasticity is observable at the crack tip, see also Ghassemieh (2002) and Zhang et al. (2005), where the suppression of the plastic

strain at the crack tip is noticeable for the gradient dependent material, Fig. 4.31b and c. A smooth transition of the plastic strain from the fiber towards the matrix is highlighted for the gradient dependent material as it was shown by Legarth and Niordson (2010). This smooth transition pushes the maximum plastic strain towards the borders. For the second set of the higher order boundary conditions, Fig. 4.31c is plotted. Suppression of the plastic strain close to the debonded void is seen, which is not the case for the first set, Fig. 4.31b. An elaborated study of the weak interface is found in [P7].

Chapter 5
Concluding remarks

The goal of the present work is to deliver a comprehensive dataset of composites behavior at the large scale (macro), while knowing the material properties at the lower scale (micro). More specifically, the study uses a gradient dependent yield function at the micro scale, while a conventional description of the yield surface and its evolution are developed at the macroscopic scale. Seven papers [P1]-[P7] have been included in the thesis.
Among the gradient theories, a rate independent higher order strain gradient plasticity theory proposed by Gudmundson (2004) is considered. Numerical studies are carried out using a finite element cell model, where the components of the plastic strain tensor appear as free variables in addition to the displacement variables. The free energy has contributions from both elastic strains and plastic strain gradients. Micro-macro homogenization is used, where the Hill-Mandel energy condition is satisfied. As a result of the homogenization, higher order boundary condition is imposed such that macroscopic higher order energy vanishes and conventional response is accessible.

In [P1], [P2] and [P3], elasto-plastic behavior of MMCs are studied. Two different types of the unit cell including rectangular fiber [p1] and circular fiber [p2]-[p3] are studied assuming a perfectly bonded interface. In [P3], since only loading with the same symmetry planes as the geometry and the material itself are considered, the analyses can be carried out on a reduced unit cell containing only one quarter of a fiber. Results for different combinations of normal loading in the longitudinal and transverse directions are presented. It is shown that the elastic modulus, yield stress and Bauschinger effect increase in both loading directions with higher fiber volume fraction. Furthermore, it is seen that for higher fiber volume fractions the overall plastic flow is suppressed at a given load-level and, as a result, the initial yield surface expands. It is concluded that V_f is the most important conventional parameter leading to the Bauschinger effect in both loading directions.
The effect of a constitutive length scale in the matrix material is analyzed. The results show that the length scale serves as to increase the overall hardening of the composite. Consequently, the initial yield surface expands in all directions. The Bauschinger effect is also found to increase with L_*/R which results in additional kinematic hardening. It is shown that the material model is capable of accounting for Baushinger effects under reversed loading, due to the back stresses originating from the plastic gradient accommodated by the free energy.

In [P4], the elasto-plastic behavior of MMCs is studied under more general loading conditions including the simple shear. Such a comprehensive analysis needs to have a unit cell with the whole fiber represented. Periodic boundary conditions are considered for both displacement and plastic strain fields.
It is shown that the elastic modulus, yield stress and Bauschinger effect increase for in-plane shear loading with the higher fiber volume fraction. The expansion of the composite yield surface in shear-transverse stress coordinate system shows an anisotropic growth, where it is significant in the transverse direction and small in the shear direction.
The Bauschinger effect is found to be large in longitudinal direction, moderate in the transverse direction and small in shear direction, which is almost opposite to the finding for the expansion of the yield surface. It is also seen that the Bauschinger stress increases with smaller particle size results in an additional kinematic hardening due to the residual higher order stresses. It is concluded that the inclusion of the constitutive material length scale results in an isotropic growth of the initial yield surface and anisotropic expansion and translation of the subsequent yield surface upon loading in different directions.

In [P5] different loading trials are imposed on the unit cell with one circular fiber using generalized plain strain condition. The goal is to characterize the kinematic hardening of the composite yield surface. The thermodynamically consistent model at the macro scale showed a relationship between the amount of trapped energy and the Bauschinger stress. This fact is investigated and a mathematical representation of the numerically computed trapped energy is introduced such that the Bauschinger stresses can be extracted. It is found that a quadratic function of plastic strains can be considered for the trapped energy during the plastic deformation. As a result, a linear function of plastic strains is derived for the Bauschinger stresses. The eigendirections of the Bauschinger modulus ($\boldsymbol{P}$-modulus) are found to be the cylindrical and planar axes of the composite yield surface.
Effect of the material length scale, L_*/R, on the trapped energy, Bauschinger stress and plastic strain is investigated. A considerable enhancement of the trapped energy and corresponding Baushinger stress with higher L_*/R can be seen. The computed Bauschinger stresses are also compared with the geometric center of the subsequent yield surface and an adequate agreement with the current approach is found for all loading trials. It is emphasized that the conventional definition for the Bauschinger stress, Eq. (4.7), in composite under multi-axial loadings can not represent the geometrical center of the multi-dimensional yield surface, while the definition with the current approach, Eq. (2.29), can. It is highlighted that the material length scale does not change the orientation of the composite cylinder, whereas it can expand it. The fiber volume fraction as a conventional parameter can both expand and deviate the orientation of composite cylinder.

In [P6] a conventional anisotropic hydrostatic pressure dependent yield function is finally introduced. By drawing the 3D yield surface of the composite, $(\Sigma_{11}, \Sigma_{22}, \Sigma_{33})$, an elliptically cylindrical yield surface is seen. As was mentioned, the eigendirections of the $\boldsymbol{P}$-modulus (P_{ijkl}), are parallel to the cylindrical axes. Exploiting this, a transformation matrix, $\boldsymbol{V}$, is built and all of the macroscopic quantities including the Cauchy stress, Σ_{ij}, Bauschinger stress, A_{ij}, and plastic strain, E^p_{ij}, are transformed. Using the transformed quantities, Σ_{λ_i}, A_{λ_i} and $E^p_{\lambda_i}$, the yield surface properties like pressure dependency, expansion and translation are considered by extending the Hill anisotropic yield function. It is observed that by hydrostatic pressure loading, plastic deformation evolves inside the micro structure, which can be captured by the extended Hill anisotropic yield function.
Effect of the material length scale on the yield function is sought. It is seen that with higher material length scale both initial and subsequent anisotropic parameters, F^λ,H^λ and N^λ, decrease with different rate which is a sign of an anisotropic expansion of both initial and subsequent yield surface. Finally, the macroscopic hardening coefficients, f_i,h_i and n_i, needed to track the expansion of the yield surface are calculated and introduced. The function is now ready to be used at the large scale.

An extra study is conducted in [P7] considering the weak interface of the fiber-matrix interface using cohesive zone model. The effect of both critical separation distances (work of separation per unit interface area), $\delta_n = \delta_t = \delta$, and maximum stress carried by the interface, σ_{max}, on the stress strain curve are investigated. It is shown that by increasing of both of those parameters, the stress-drop corresponding to the onset of debonding is postponed. However, the effect of σ_{max} is much more intense on the strength of interface compared to the effect of δ. Comparing to the strong interface, it is also observed that the elastic modulus for the material with weak interface is lower than the one with strong interface. This is due to the cohesive zone model, where traction-displacement curve is loosening the strength of material before the onset of debonding at $\lambda = 1/3$.

Bibliography

Acharya, A., Bassani, J. L., 2000. Lattice incompatibility and a gradient theory of crystal plasticity. Journal of the Mechanics and Physics of Solids 48, 1565–1595.

Anand, L., Gurtin, M., Lele, S., Gething, C., 2005. A one-dimensional theory of strain-gradient plasticity: Formulation, analysis, numerical results. Journal of the Mechanics and Physics of Solids 53, 1789–1826.

Asaro, R., Needleman, A., 1985. Texture development and strain hardening in rate dependent polycrystals. Acta Metall. 33 (6), 923–953.

Azizi, R., Niordson, C., Legarth, B., 2011a. On homogenization of metal matrix composites using strain gradient plasticity. Submitted.

Azizi, R., Niordson, C., Legarth, B., 2011b. Size-effects on yield surfaces for micro reinforced composites. International Journal of Plasticity 27, 1817–1832.

Bao, G., Hutchinson, J. W., McMeeking, R. M., 1991. Particle reinforcement of ductile matrices against plastic flow and creep. Acta Metallurgica et Materialia 39 (8), 1871–1882.

Barlat, F., Lege, D., Brem, J., 1991. A six-component yield function for anisotropic materials. Int. J. Plast 7, 693–712.

Bassani, J. L., 2001. Incompatibility and a simple gradient theory of plasticity. Journal of the Mechanics and Physics of Solids 49, 1983–1996.

Benzerga, A. A., Brechet, Y., Needleman, A., Van der Giessen, E., 2005. The stored energy of cold work: Predictions from discrete dislocation plasticity. Acta Materialia 53, 4765–4779.

Bittencourt, E., Needleman, A., Gurtin, M., Van der giessen, E., 2003. A comparison of nonlocal continuum and discrete dislocation plasticity predictions. J.Mech.Phys.Solids 51, 281–310.

Budiansky, B., 1965. On elastic moduli of some heterogeneous materials. Journal of The Mechanics and Physics of Solids 13, 223–227.

Chaboche, J., 1993a. Cyclic viscoplastic constitutive equations. J. App. Mech. 60, 822–828.

Chaboche, J., 1993b. Cyclic viscoplastic constitutive equations- i: a thermodynamically consistent formulation. J. Appl. Mech. 60, 813–821.

Chung, K., Ryou, H., 2009. Development of viscoelastic/rate-sensitive-plastic constitutive law for fiber-reinforced composites and its applications. part i: Theory and material characterization. Composites Science and Technology 69, 284–291.

Corbin, S., Wilkinson, D., Embury, J., 1996. The bauschinger effect in a particulate reinforced al alloy. Materials Science and Engineering A207, 1–11.

Deshpande, V., Needleman, A., Van der Giessen, E., 2005. Size dependence of energy storage and dissipation in a discrete dislocation plasticity analysis of static friction. Materials Science and Engineering A 400-401, 393–396.

Deshpande, V. S., Fleck, N. A., Ashby, M. F., 2001. Effective properties of the octet-truss lattice material. Journal of the Mechanics and Physics of Solids 49 (8), 1747–1769.

Drucker, D., 1951. A more fundamental approach to stress-strain relations. Proc. 1^st U.S.Nat. Congr. of Appl. Mech., ASME 487.

Drucker, D. C., Prager, W., 1952. Soil mechanics and plastic analysis for limit design. Quarterly of Applied Mathematics 10 (2), 157–165.

Dvorak, G., Rao, M., Tarn, J., 1973. Yielding in unidirectional composites under external loads and temperature changes. J Compos Mater 7, 194–216.

Eshelby, J. D., 1957. The determination of the field of an ellipsoidal inclusion and related problems. Proc. R. Soc. Lond A 241, 376–396.

Feyel, F., 1999. Multiscale fe2 elastoviscoplastic analysis of composite structures. Comput Mater Sci 16, 344–354.

Feyel, Chaboche, J., 2000. Fe2 multiscale approach for modelling the elastoviscoplastic behavior of long fibre sic/ti composite materials. Comput. Meth. Appl. Mech. Eng. 183, 309–330.

Fish, J., Shek, K., 2000. Multiscale analysis of composite materials and structures. Comput. Sci. Technol. 60, 2547–2556.

Fleck, N. A., Ashby, M., Hutchinson, J. W., 2003. The role of geometrically necessary dislocations in giving material strengthening. Scripta Materialia 48, 179–183.

Fleck, N. A., Hutchinson, J. W., 1997. Strain gradient plasticity. In: Hutchinson, J. W., Wu, T. Y. (Eds.), Advances in Applied Mechanics. Vol. 33. Academic Press, pp. 295–361.

Fleck, N. A., Hutchinson, J. W., 2001. A reformulation of strain gradient plasticity. Journal of the Mechanics and Physics of Solids 49, 2245–2271.

Fleck, N. A., Willis, J. R., 2009a. A mathematical basis for strain-gradient plasticity theory - Part I: Scalar plastic multiplier. Journal of the Mechanics and Physics of Solids 57, 161–177.

Fleck, N. A., Willis, J. R., 2009b. A mathematical basis for strain-gradient plasticity theory - Part II: Tensorial plastic multiplier. Journal of the Mechanics and Physics of Solids, 57, 1045–1057.

Fredriksson, P., Gudmundson, P., L.P., M., 2009. Finite element implementation and numerical issues of strain gradient plasticity with application to metal matrix composites. International Journal of Solids and Structures 46, 3977–3987.

Gao, H., Huang, Y., 2003. Geometrically necessary dislocation and size-dependent plasticity. Scripta Materialia 48, 113–118.

Gao, H., Huang, Y., Nix, W. D., Hutchinson, J. W., 1999. Mechanism-based strain gradient plasticity - I. Theory. Journal of the Mechanics and Physics of Solids 47 (6), 1239–1263.

Geers, M., Kouznetsova, V., Brekelmans, W., 2010. Multi-scale computational homogenization: Trends and challenges. Journal of Computational and Applied Mathematics 234, 2175–2182.

Ghassemieh, E., 2002. Micro-mechanical analysis of bonding failure in a particle-filled composite. Composites Science and Technology 62, 67–82.

Ghosh, S., Bai, J., Raghavan, P., 2007. Concurrent multi-level model for damage evolution in microstructurally debonding composites. Mechanics of Materials 39, 241–266.

Ghosh, S., Lee, K., Moorthy, S., 1995. Multiple scale analysis of heterogeneous elastic structures using homogenization theory and voronoi cell finite element method. International Journal of Solids and Structures 32 (1), 27–62.

Gudmundson, P., 2004. A unified treatment of strain gradient plasticity. Journal of the Mechanics and Physics of Solids 52 (6), 1379–1406.

Gupta, N., H.A., L., 1983. A study of yield surface upon reversal of loading under biaxial stress. ZAMM 63, 497–504.

Gurtin, M. E., 2002. A gradient theory of single-crystal viscoplasticity that accounts for geometrically necessary dislocations. Journal of the Mechanics and Physics of Solids 50 (1), 5–32.

Gurtin, M. E., Anand, L., 2005. A theory of strain-gradient plasticity for isotropic, plastically irrotational materials. Part I: Small deformations. Journal of the Mechanics and Physics of Solids 53 (7), 1624–1649.

Hashin, Z., 1983. Analysis of composite materials. a survey. J. Appl. Mech. 50, 481–505.

Hashin, Z., Shtrikman, S., 1963. A variational approach to the theory of the elastic behaviour of multiphase materials. Journal of the Mechanics and Physics of Solids 11 (2), 127–140.

Hazanov, S., Huet, C., 1994. Order relationships for boundary conditions effect in heterogeneous bodies smaller than the representative volume. J. Mech. Phys. Solids 42, 1995–2011.

Hill, R., 1948. A theory of the yielding and plastic flow of anisotropic metals. Proceedings of the Royal Society of London A193, 281–297.

Hill, R., 1965. A self-consistent mechanics of composite materials. Journal of The Mechanics and Physics of Solids 13, 213–222.

Iyera, S., Lissendena, C., Arnoldb, S., 2000. Local and overall flow in composites predicted by micromechanics. Composites Part B:Engineering 31, 327–343.

Jansson, S., 1992. Homogenized nonlinear constitutive properties and local stress concentrations for composites with periodic internal structure. Int. J. Solids Sturctures 29, 2181–2200.

Jansson, S., 1995. Non-linear constitutive equations for strongly bonded fibre-reinforced metal matrix composites. Composites 26, 415–124.

Keller, R. R., Phelps, J. M., Read, D. T., 1990. Preprocessing and postprocessing for materials based on the homogenization method with adaptive finite element methods. Computer methods in applied mechanics and engineering 83, 143–198.

Kouznetsova, V., Brekelmans, W. A. M., Baaijens, F. P. T., 2001. An approach to micro-macro modeling of heterogeneous materials. Comput. Mech. 27, 37–48.

Kouznetsova, V., Geers, M., Brekelmans, W., 2004. Multi-scale second-order computational homogenization of multi-phase materials: a nested finite element solution strategy. Comput. Methods Appl. Mech. Engrg 193, 5525–5550.

Kowalsky, U., Ahrens, H., Dinkler, D., 1999. Distorted yield surfaces - modelling by higher order anisotropic hardening tensors. Computational Materials Science 16, 81–88.

Lee, M., Kim, D., Chung, K., Youn, J., Kang, T., 2004. Combined isotropic-kinematic hardening laws with anisotropic back-stress evolution for orthotropic fiber-reinforced composites. POLYMERS and POLYMER COMPOSITES 12, 225–233.

Legarth, B. N., 2003. Debonding of particles in anisotropic materials. International Journal of Mechanical Sciences 45, 1119–1133.

Legarth, B. N., Kuroda, M., 2004. Particle debonding using different yield criteria. European Journal of Mechanics - A/Solids 23 (5), 737–751.

Legarth, B. N., Niordson, C. F., 2010. Debonding failure and size effects in micro-reinforced composites. International journal of plasticity 26 (1), 149–165.

Lele, S. P., Anand, L., 2008. A small-deformation strain-gradient theory for isotropic viscoplastic materials. Philosophical Magazine 88 (30), 1478–6435.

Li, X., Zhang, J., Zhang, X., 2010. Micro-macro homogenization of gradient-enhanced cosserat media. European Journal of Mechanics A/Solids.

Lissenden, 2010. Experimental investigation of initial and subsequent yield surfaces for laminated metal matrix composites. International Journal of Plasticity 26, 1606–1628.

Liu, C., Huang, Y., Stout, M. G., 1997. On the asymmetric yield surface of plastically orthotropic materials: A phenomenological study. Acta Materialia 45 (6), 2397–2406.

Lloyd, D. J., 1994. Particle reinforced aluminium and magnesium matrix composites. International Materials Reviews 39 (1), 1–23.

Lubliner, J., 1972. On the thermodynamic foundations of non-linear solid mechanics. J. Non-Linear Mech. 7, 237.

Lubliner, J., 1990. Plasticity theory. Pearson Education, Inc.

McDanels, D., 1985. Analysis of stress-strain, fracture, and ductility behavior of aluminum matrix composites containing discontinuous silicon carbide reinforcement. Metallurgical Transactions A (Physical Metallurgy and Materials Science) 16A (6), 1105–1115.

Mughrabi, H., 2001. The effect of geometrically necessary dislocations on the flow stress of deformed crystals containing a heterogeneous dislocation distribution. Materials Science and Engineering, 139–143.

Nan, C., Clarke, D., 1996. The influence of particle size and particle fracture on the elastic/plastic deformation of metal matrix composites. Acta mater 44, 3801–3811.

Needleman, A., Borders, T., Brinson, L., Flores, V., Schadler, L., 2010. Effect of an interphase region on debonding of a cnt reinforced polymer composite. Composites Science and Technology 70, 2207–2215.

Niordson, C. F., Legarth, B. N., 2010. Strain gradient effecits on cyclic plasticity. Journal of the Mechanics and Physics of Solids 58, 542–557.

Niordson, C. F., Tvergaard, V., 2001. Nonlocal plasticity effects on the tensile properties of a metal matrix composite. European Journal of Mechanics - A/Solids 20 (4), 601–613.

Niordson, C. F., Tvergaard, V., 2002. Nonlocal plasticity effects on fibre debonding in a whisker-reinforced metal. European Journal of Mechanics - A/Solids 21 (2), 239–248.

Niordson, C. F., Tvergaard, V., 2007. Size-effects in porous metals. Mater. Sci. Eng. 15, 51–60.

Phillips, A., Juh-Ling, T., 1972. The effect of loading path on the yield surface at elevated temperatures. Internat. J. Solids Struct. 8, 463–474.

Rice, J., 1971. Inelastic constitutive relations for solids: An internal-variable theory and its application to metal plasticity. Journal of the Mechanics and Physics of Solids 19, 433–455.

Rosakis, P., Rosakis, A., Ravichandran, G., Hodowan, J., 2000. A thermodynamic internal variable model for the partition of plastic work into heat and stored energy in metals. Journal of the Mechanics and Physics of Solids 48, 581–607.

Suquet, P. M., 1985. Local and global aspects in the mathematical theory of plasticity. Plasticity todays: modelling, methods and applications, 279–310.

Tamma, K., Chung, P., 1999. Woven fabric composites: developments in engineering bounds, homogenization and applications. Int. J. Numer. Meth. Eng. 45, 1757–1790.

Terada, K., Hori, M., Kyoya, T., Kikuchi, N., 2000. Simulation of the multi-scale convergence in computational homogenization approaches. Journal of Solids and Structures 37, 2285–2311.

Tvergaard, V., 1976. Effect of thickness inhomogeneities in internally pressurized elastic-plastic spherical shells. Journal of the Mechanics and Physics of Solids 24, 291–304.

Tvergaard, V., 1990a. Analysis of tensile properties for a whisker-reinforced metal-matrix composite. Acta Metallurgica 38 (2), 185–194.

Tvergaard, V., 1990b. Effect of fibre debonding in a whisker-reinforced metal. Materials Science & Engineering A: Structural Materials: Properties, Microstructure and Processing A125 (2), 203–213.

Tvergaard, V., 1995. Fibre debonding and breakage in a whisker-reinforced metal. Materials Science and Engineering: A 190, 215–222.

Tvergaard, V., 2001. Plasticity and creep in structural materials. Department of Mechanical Engineering, Solid Mechanics, Technical University of Denmark.

Vemaganti, K., Oden, J., 2001. Estimation of local modeling error and goal-oriented adaptive modeling of heterogeneous materials, part ii: a computational environment for adaptive modeling of heterogeneous elastic solids. Comput. Meth. Appl. Mech. Eng. 190, 6029–6214.

Wieckowski, Z., 2000. Dual finite element methods in homogenization for elastic-plastic fibrous composite material. International Journal of Plasticity 16, 199–221.

Xu, X.-P., Needleman, A., 1993. Void nucleation by inclusion debonding in a crystal matrix. Modelling and Simulation in Materials Science and Engineering 1, 111–132.

Yan, Y., Geng, L., Li, A., 2007. Experimental and numerical studies of the effect of particle size on the deformation behavior of the metal matrix composites. Materials Science and Engineering 448, 315–325.

Zhang, H., Ramesh, K., Chin, E., 2005. Effects of interfacial debonding on the rate-dependent response of metal matrix composites. Acta Materialia 53, 4687–4700.

Zhu, H., Zbib, H. M., Aifantis, E., 1997. Strain gradients and continuum modeling of size effect in metal matrix composites. Acta Mech 121, 165–176.

Zohdi, T., Wriggers, P., 1999. A domain decomposition method for bodies with heterogeneous microstructure based on material regularization. Int. J. Solids Struct 36, 2507–2525.

Publication [P1]

Effects of back stress in metal matrix composite due to the plastic strain gradients

X International Conference on Computational Plasticity
COMPLAS X
E. Oñate and D. R. J. Owen (Eds)

Effects of back stress in metal matrix composite due to the plastic strain gradients

Reza Azizi *

* Department of Mechanical Engineering
Technical University of Denmark, 2800 Kgs. Lyngby, Denmark
e-mail: reaz@mek.dtu.dk

Key words: Back stress, composites, strain gradient plasticity

Summary. The overall properties of micron to sub-micron scale reinforced metal matrix composites are studied. The focus of the study is on effective yield surfaces and the overall hardening behavior. A recent strain gradient plasticity theory, based on energetic contributions due to the gradient of the plastic strain tensor, is employed to model relevant size-effects in the matrix material. Numerical studies are carried out using a finite element method, where the components of the plastic strain tensor appear as free variables in addition to the displacement variables. Due to the higher order nature of the theory, higher order boundary conditions must be imposed. These non-conventional boundary conditions give enhanced modeling capabilities, that are important to micron scale applications such as micron reinforced materials, and in the present study they are used to model dislocation blocking at the interface between fibers and the matrix material. The results show increased hardening for micron scale reinforcement, compared to that predicted by conventional models. The results are in accordance with experimental observations, which cannot be modeled by conventional scale independent plasticity theories. It is shown that the material model is capable of accounting for Baushinger effects under reversed loading, due to back stresses originating from the plastic gradient contributions to the free energy.

1 INTRODUCTION

Size effect in metal matrix composites during plastic deformation can be modeled using strain gradient plasticity. Fibers in the matrix can suppress the plastic flow intensely. An explanation is that if a glide path of a dislocation encounter a fiber surface, the dislocation cannot pass the fiber. This behavior cannot be considered by conventional plasticity since no size effects exist. Theories of strain gradient of plasticity have the capabilities to consider this fact.

Gudmundson [1] introduced a new formulation to avoid negative energy dissipation during plastic deformation. A full form of strain gradient plasticity with positive energy dissipation has been developed by Fleck [2]. A conservative way to have positive energy dissipation is to extract the gradient of plastic strain from elastic energy. This was done by Gudmundson and Fredriksson [3]. Recently, Lele and Anand developed a complete description of higher order theory for viscoplastic material [4]. In this paper, the energetic higher order theory of SGP proposed by Gudmundson[1] will be implemented for a metal matrix composite under general

plane strain loading. The overall behavior of the metal matrix composite will be evaluated based on a micro model.

2 FORMULATIONS

2.1 Constitute equations

Under small strain, one can separate the plastic and elastic strain as below:

$$\dot{\varepsilon}_{ij} = \dot{\varepsilon}^e_{ij} + \dot{\varepsilon}^p_{ij} \tag{1}$$

Free energy is assumed to have contributions from the gradient of plastic strain in addition to the conventional elastic strain [3].

$$\psi = \frac{1}{2} D_{ijkl} \varepsilon^e_{ij} \varepsilon^e_{kl} + \frac{1}{2} L_*^2 G \varepsilon^p_{ij,k} \varepsilon^p_{ij,k} \tag{2}$$

where L_* is a constitutive length parameter, G is the shear modulus, and D_{ijkl} is the tensor of elastic moduli.

The conventional stress and higher order stress, work conjugate to the plastic strain gradient, can be derived from the potential ψ as follows:

$$\begin{cases} \sigma_{ij} = \dfrac{\partial \psi}{\partial \varepsilon^e_{ij}} = D_{ijkl} \varepsilon^e_{kl} \\ m_{ijk} = \dfrac{\partial \psi}{\partial \varepsilon^p_{ij,k}} = G L_*^2 \varepsilon^p_{ij,k} \end{cases} \tag{3}$$

The increment of plastic strain is taken to be co-rotational with a micro stress q_{ij}.

$$\dot{\varepsilon}^p_{ij} = \frac{3}{2} \frac{q_{ij}}{q_e} \dot{\varepsilon}^p_e \tag{4}$$

where, $q_e = \sqrt{\frac{3}{2} q_{ij} q_{ij}}$ and $\dot{\varepsilon}^p_e = \sqrt{\frac{2}{3} \dot{\varepsilon}^p_{ij} \dot{\varepsilon}^p_{ij}}$

and q_{ij} satisfies the higher order equilibrium equation:

$$m_{ijk,k} + s_{ij} - q_{ij} = 0, \tag{5}$$

where s_{ij} is the deviatoric part of the Cauchy stress.

It can be seen that the micro stress q_{ij}, is in general different from S_{ij} when higher order stress exist. Since the yield condition is specified in terms of q_e ($f = \sqrt{3/2 q_{ij} q_{ij}} - \left(\sigma_y + H \varepsilon^p_e\right)$), this suggests that energetic strain gradient effects may lead to kinematic hardening effects for non-homogeneous deformation states.

2.2 Effective strain and yield condition in composite

In this paper, strain based averaging has been used to evaluate the yield surface. Equations (6) shows the macroscopic effective strain of a composite.

$$\dot{E}^M = \frac{1}{V}\int_V \dot{\varepsilon}_e^m \, dV \tag{6}$$

In order to consider both the initial and subsequent yield surfaces, a macroscopic yield condition should be considered. This has been done by considering the change in macroscopic reloading slope as below:

$$\left|C_i - C_{reload}\right| < 0.7 C_{reload} \tag{7}$$

Where, C_i is current slope and C_{reload} is the elastic modulus during reloading.

3. RESULTS

A metal-matrix composite has been simulated with $w = \sqrt{3}h$, $w_f = 2h_f$, and $h_f = 0.588h$ which is shown in Fig.1a Normalized matrix properties are $E = 78.6 \times H$, $\sigma_Y = H/18.35$, $H = \partial\sigma_f / \partial\varepsilon_p$ and $E_f = 6.43 \times E_M$ is the Young's modulus of fibers. To compute the initial yield surface under overall proportional loading a method employing a linear combination of two deformation status has been used as shown in Fig.1b:

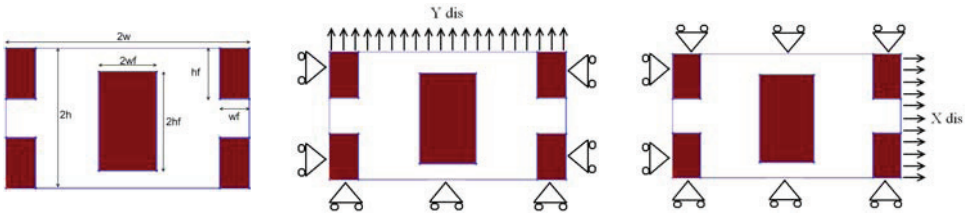

Figure 1: a) Metal matrix geometry b) Metal matrix boundary conditions

Fig.2 reveals the initial yield surface both for matrix and metal-matrix. As the figure shows, there is a considerable expansion of the yield surface for overall behavior of metal-matrix. The figure also shows that yield surface with energetic strain gradient theory of plasticity is a little larger than conventional plasticity which is expected due to the higher order boundary condition. The length parameter (L^*) has very small effect on the initial yield surface but it has a considerable effect on subsequent yield surface which will be shown. It can be seen that yield surface has deviation from mises yield surface because of the anisotropic effect of fibers.

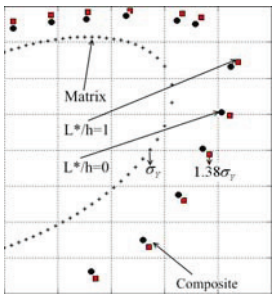

Figure 2: Initial yield surface

A subsequent yield surface has been evaluated with biaxial loading with $\Delta_2 = \Delta_1 = h\Gamma$, in which Δ_2, Δ_1 are displacements in two perpendicular axes and $\Gamma = 0.009$. Fig.3 shows the subsequent yield surfaces. It can be seen that pure isotropic hardening is not completely satisfied when L*/h=0. This is due to the existence of fibers which increases the level of residual stress and acts as a kinematic hardening. By increasing the length scale value, significant kinematic hardening occurs. As mentioned above, this is due to the higher order stress which exists during loading and gives a back-stress effect. It can be seen that the stress states are larger for larger values of the length scale.

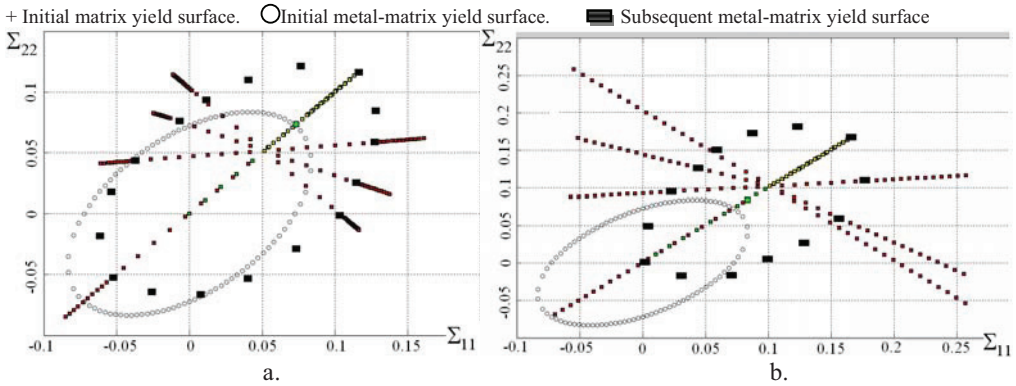

Figure 3: a) L*/h=1 b) L*/h=0

4 CONCLUSIONS

In this paper, energetic strain gradient plasticity was employed to model the size effects in a metal-matrix composite. The relationship between macro and micro for yielding has been discussed. A metal matrix was simulated and both initial and subsequent yield surfaces were computed. It was shown that the material model is capable of accounting for Baushinger effects under reversed loading, due to back-stresses originating from the plastic gradient contributions to the free energy.

REFERENCES

[1] Gudmundson, P., 2004. A unified treatment of strain gradient plasticity. Journal of the Mechanics and Physics of Solids 52 (2004) 1379 – 1406

[2] Fleck, N.A., 2008. A mathematical basis for strain gradient plasticity theory. Part I:scalar plastic multiplier. Journal of the Mechanics and Physics of Solids. In press

[3] Gudmundson P., Fredriksson, P,. Finite element implementation and numerical issues of strain gradient plasticity with application to metal matrix composites. PhD thesis, KTH Engineering Sciences, Royal institute of technology.

[4] Suvrat P.Lele, Lallit Anand, 2008. A large-deformation strain-gradient theory for isotropic viscoplastic materials. International Journal of Plasticity. In Press.

[5] Bao, G. Hutchinson, J.W. Mcmeeking, R. M, 1991. Particle reinforcement of ductile materials against plastic flow and creep

Corrected Caption for figure number 3:

Figure 3: a) L*/h=0 b) L*/h=1

Publication [P2]

Metal matrix composite with size-effects

Second African Conference on Computational Mechanics - An International Conference - AfriCOMP11
January 5 - 8, 2011, Cape Town, South Africa
A.G. Malan, P. Nithiarasu and B.D. Reddy (Eds.)

Metal matrix composite with size-effects

Reza Azizi[⋆], Christian F. Niordson[⋆⋆] and Brian N. Legarth[⋆⋆⋆]
[⋆]Department of Mechanical Engineering, Solid Mechanics, Technical University of Denmark, DK-2800 Kgs. Lyngby, Denmark, reaz@mek.dtu.dk
[⋆⋆]Department of Mechanical Engineering, Solid Mechanics, Technical University of Denmark, DK-2800 Kgs. Lyngby, Denmark, cn@mek.dtu.dk
[⋆⋆⋆]Department of Mechanical Engineering, Solid Mechanics, Technical University of Denmark, DK-2800 Kgs. Lyngby, Denmark, bnl@mek.dtu.dk

SUMMARY

Size effects in composites are studied using a rate independent higher order strain gradient plasticity theory, where strain gradient effects are incorporated in the stored energy of the material. Numerical studies are carried out using a finite element method, where the components of the plastic strain tensor appear as free variables in addition to the displacement variables. Non-conventional boundary conditions are applied at material interfaces to model a constraint on plastic flow due to dislocation blocking. Unit cell calculations are carried out under generalized plane strain conditions. The homogenized response of a material with cylindrical reinforcing fibers is analyzed for different values of the internal material length scale. The effect of fiber volume fraction (V_f) and the length scale parameter (L_*) will be shown.

Key Words: Metal matrix composite, strain gradient plasticity, unit cell

1 INTRODUCTION

Reinforcement of metals by stiff elastic fibers is used to obtain increased stiffness, strength and creep resistance, but often on the cost of decreased ductility and fracture properties. A significant amount of research has analyzed how geometry and material parameters affect the overall properties of the composite material. These studies are based on conventional gradient independent plasticity models, and hence predict no effect of reinforcement size, see ([1],[2]). Conventional theories of plasticity lack the ability to model size-effects, as no constitutive length parameters are used. Some of the proposed strain gradient plasticity models are of lower order nature, retaining the structure of a conventional boundary value problem in solid mechanics, but most of the proposed theories are of higher order nature, employing higher order stress-measures as work-conjugates to strain gradients [3],[4]. These models demand non-conventional higher order boundary conditions.

In this paper, size-effects on the homogenized properties of composites for which the matrix material can be modeled by strain gradient plasticity theory is studied. The energetic higher order strain gradient plasticity theory proposed in [4] and [5] has been implemented in a generalized plane strain setting, and numerical finite element cell model analyses have been carried out to study the material response under plane normal loading conditions. The results are presented in terms of overall response curves.

2 Material model, problem formulation, and results

The fibers are assumed to be isotropic and linear elastic with Young's modulus E_f and Possion's ratio ν_f, while the matrix material is assumed to follow a gradient enhanced isotropic elasto-plastic material model.

The material model applied for the matrix material is the rate independent energetic strain gradient plasticity model proposed in [4] which accounts for gradients of the full plastic strain tensor. The theory is based on the incremental principle of virtual work on the following form

$$\int_V [\dot{\sigma}_{ij}\delta\dot{\epsilon}_{ij} + (\dot{q}_{ij} - \dot{s}_{ij})\delta\dot{\epsilon}^p_{ij} + \dot{m}_{ijk}\delta\dot{\epsilon}^p_{ij,k}]\mathrm{d}V = \int_S [\dot{T}_i\delta\dot{u}_i + \dot{M}_{ij}\delta\dot{\epsilon}^p_{ij}]\mathrm{d}S \tag{1}$$

where the increment of a given quantity is denoted by a superposed dot, $\dot{(\ )}$ and V is the volume of the body analysed, while S is the surface of the body. The stress tensor is denoted by σ_{ij} and $s_{ij} = \sigma_{ij} - \frac{1}{3}\delta_{ij}\sigma_{kk}$ is the stress deviator. The total strain, ϵ_{ij}, is the sum of the elastic strain, ϵ^e_{ij}, and the plastic strain, ϵ^p_{ij}, while $\epsilon^p_{ij,k}$ denotes the gradients of the plastic strain tensor. The micro stress, q_{ij}, and the higher order stress, m_{ijk}, are work conjugate stress-measures to the plastic strain and the plastic strain gradient, respectively. The traction, T_i, and higher order traction, M_{ij}, are surface quantities work-conjugate to the displacement, u_i, and the plastic strain tensor, ϵ^p_{ij}, respectively.

The free energy per unit volume, ψ, of the strain gradient dependent material is assumed to be on the form $\psi = \psi(\epsilon^e_{ij}, \epsilon^p_{ij,k})$. Hence, no free energy is stored due to the plastic strain tensor itself and the increment of dissipation per unit volume is given by $q_{ij}\dot{\epsilon}^p_{ij}$. Following [5] we take the following specific form of the free energy

$$\psi\left(\epsilon^e_{ij}, \epsilon^p_{ij}\right) = \frac{1}{2}D_{ijkl}\epsilon^e_{ij}\epsilon^e_{kl} + \frac{1}{2}L^2_* G\epsilon^p_{ij,k}\epsilon^p_{ij,k} \tag{2}$$

Here, L_* is a material length scale parameter introduced for dimensional consistency, G is the elastic shear modulus and D_{ijkl} is the isotropic tensor of elastic moduli, all defined in terms of Young's modulus, E_m, and Poisson's ratio, ν_m, of the matrix. By derivation of the free energy with respect to the elastic strain and the gradient of plastic strain, the stress and the higher order stress are found as

$$\sigma_{ij} = \frac{\partial\psi}{\partial\epsilon^e_{ij}} = D_{ijkl}\epsilon^e_{kl} \quad , \quad m_{ijk} = \frac{\partial\psi}{\partial\epsilon^p_{ij,k}} = GL^2_*\epsilon^p_{ij,k} \tag{3}$$

The yield condition for the matrix material is given in terms of the micro stress, q_{ij}, as

$$f\left(q_{ij}, \sigma_f\right) = \sqrt{\frac{3}{2}q_{ij}q_{ij}} - \sigma_f = q_e - \sigma_f \tag{4}$$

where yielding occurs for $f = 0$. The effective micro stress has been introduced as $q_e = \sqrt{\frac{3}{2}q_{ij}q_{ij}}$ and the instantaneous flow stress is denoted σ_f. Here, linear hardening is considered with the instantaneous flow stress given by $\sigma_f = \sigma_y + H\epsilon^p_e$, where σ_y denotes the initial yield stress, H denotes the hardening modulus and ϵ^p_e denotes the accumulated effective plastic strain, defined incrementally through the relation $\dot{\epsilon}^p_e = \sqrt{\frac{2}{3}\dot{\epsilon}^p_{ij}\dot{\epsilon}^p_{ij}}$, i.e. $\epsilon^p_e = \int \dot{\epsilon}^p_e \mathrm{d}\tau$, where τ is "time".

The flow rule for the plastic strain is given by the relation

$$\dot{\epsilon}^p_{ij} = \frac{3}{2}\frac{q_{ij}}{q_e}\dot{\epsilon}^p_e = r_{ij}\dot{\epsilon}^p_e \tag{5}$$

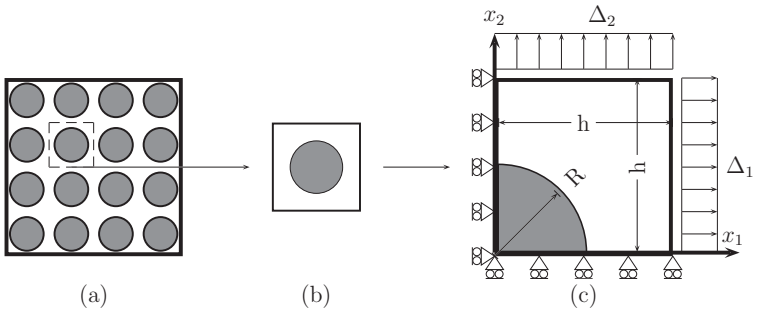

Figure 1: Representative volume element with boundary conditions

which ensures normality of the plastic strain increment with respect to the yield surface. In this expression $r_{ij} = \frac{3}{2}\frac{q_{ij}}{q_e}$ is the direction of the plastic strain increment.

We model a composite with a regular distribution of long parallel cylindrical fibers of circular cross section(see Fig. 1a). The loading is characterised by macroscopic normal loading, such that the composite deforms under generalized plane strain conditions. Thus, a unit cell containing a single fiber may be extracted as shown in Fig. 1b. Furthermore, since only loading with the same symmetry planes as the geometry and the material itself are considered, the analyses can be carried out on a reduced unit cell containing only one quarter of a fiber (Fig. 1c). At the exterior of the cell appropriate symmetry conditions are applied. In addition to demanding that the conventional shear traction must vanish, these symmetry conditions also imply that $M_{ij} = 0$ for $i = j$ and $\epsilon^p_{ij} = 0$ for $i \neq j$ at the exterior of the elastic-plastic part of the cell. Imposing this, the incremental boundary conditions can be summarized as follows

$$
\begin{array}{llllll}
\dot{u}_1 = 0, & \dot{T}_2 = 0 & \text{on} & x_1 = 0, & x_2 \in [0,h] \\
\dot{\epsilon}^p_{12} = 0, & \dot{M}_{11} = \dot{M}_{22} = 0 & \text{on} & x_1 = 0, & x_2 \in [R,h] \\
\dot{u}_1 = \dot{\Delta}_1, & \dot{T}_2 = 0 & \text{on} & x_1 = h, & x_2 \in [0,h] \\
\dot{\epsilon}^p_{12} = 0, & \dot{M}_{11} = \dot{M}_{22} = 0 & \text{on} & x_1 = h, & x_2 \in [0,h] \\
\dot{u}_2 = 0, & \dot{T}_1 = 0 & \text{on} & x_1 \in [0,h], & x_2 = 0 \\
\dot{\epsilon}^p_{12} = 0, & \dot{M}_{11} = \dot{M}_{22} = 0 & \text{on} & x_1 \in [R,h], & x_2 = 0 \\
\dot{u}_2 = \dot{\Delta}_2, & \dot{T}_1 = 0, & \text{on} & x_1 \in [0,h], & x_2 = h \\
\dot{\epsilon}^p_{12} = 0, & \dot{M}_{11} = \dot{M}_{22} = 0 & \text{on} & x_1 \in [0,h], & x_2 = h \\
\dot{\epsilon}^p_{11} = \dot{\epsilon}^p_{22} = \dot{\epsilon}^p_{12} = 0 & & \text{on} & x_1^2 + x_2^2 = R^2 &
\end{array}
\tag{6}
$$

Here, $\dot{\Delta}_1$ and $\dot{\Delta}_2$ are displacement increments to be determined to ensure prescribed macroscopic stresses as described later, $\dot{T}_i = \dot{\sigma}_{ij} n_j$ and $\dot{M}_{ij} = \dot{m}_{ijk} n_k$ are the increments of the traction vector and the higher order traction, respectively, with n_i denoting the outward unit normal vector.

The results presented focus on the response of the composite under different plane loading conditions. Conventional material parameters used for the matrix are $\sigma_y/E_m = 0.004$, $\nu_m = 0.3$, and H/E_m=0.1. For the fibers that are considered elastic the material parameters are given by $E_f/E_m = 5.7$, and $\nu_f = 0.17$. These parameters apply well for SiC reinforced aluminum.

In Fig. 2a homogenized stress-strain curves are shown for simple tension in the longitudinal direction (Σ_L,E_L) as well as in the transverse direction (Σ_T,E_T) for three different values of the fiber volume fraction, $V_f = \frac{\pi R^2}{4h^2} = 0.013$, 0.08 and 0.13. The results are for a conventional matrix material without strain gradient effects ($L_* = 0$). As expected the composite has a stiffer response

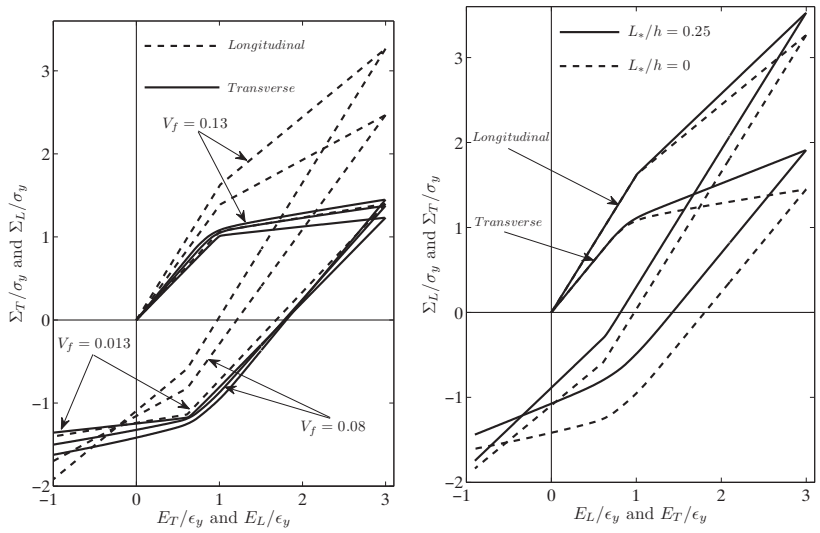

Figure 2: Stress strain relationship for simple tension

in the longitudinal direction as compared to the transverse direction, and a stiffening effect is observed in both loading directions with increasing fiber volume fraction, V_f.

In Fig. 2b the effect of the constitutive length scale of the matrix material is analyzed. Homogenized response curves are shown in the transverse and in the longitudinal directions for material length scales of $L_*/h = 0$ and 0.25. The results show that the length scale parameter causes an increase on the overall hardening of the composite.

3 CONCLUSIONS

This study shows how the stiffness of micron scale reinforced composites is increased when compared to conventional predictions. Furthermore, it was shown that the only conventional material parameter that has a significant influence on both elastic response and hardening for the composites studied here, is the fiber volume fraction, V_f, specially for loading in the longitudinal direction.

REFERENCES

[1] Tvergaard, V., Fibre debonding and breakage in a whisker-reinforced metal. Materials Science and Engineering: A 190, 215-222, 1995.

[2] Legarth, B. N., Debonding of particles in anisotropic materials. International Journal of Mechanical Sciences 45, 1119-1133, 2003.

[3] Fleck, N. A., Hutchinson, J. W., A reformulation of strain gradient plasticity. Journal of the Mechanics and Physics of Solids 49, 2245-2271, 2001.

[4] Gudmundson, P., A unified treatment of strain gradient plasticity. Journal of the Mechanics and Physics of Solids 52, 1379-1406, 2004.

[5] Fredriksson, P., Gudmundson, P., L.P., M., Finite element implementation and numerical issues of strain gradient plasticity with application to metal matrix composites. International Journal of Solids and Structures 46, 3977-3987, 2009.

Publication [P3]

Size-effects on yield surfaces for micro reinforced composites

International Journal of Plasticity 27 (2011) 1817–1832

Contents lists available at ScienceDirect

International Journal of Plasticity

journal homepage: www.elsevier.com/locate/ijplas

Size-effects on yield surfaces for micro reinforced composites

Reza Azizi *, Christian F. Niordson, Brian Nyvang Legarth

Department of Mechanical Engineering, Solid Mechanics, Technical University of Denmark, DK-2800 Kgs. Lyngby, Denmark

ARTICLE INFO

Article history:
Received 4 October 2010
Received in final revised form 11 May 2011
Available online 24 May 2011

ABSTRACT

Size effects in heterogeneous materials are studied using a rate independent higher order strain gradient plasticity theory, where strain gradient effects are incorporated in the free energy of the material. Numerical studies are carried out using a finite element method, where the components of the plastic strain tensor appear as free variables in addition to the displacement variables. Non-conventional boundary conditions are applied at material interfaces to model a constraint on plastic flow due to dislocation blocking. Unit cell calculations are carried out under generalized plane strain conditions. The homogenized response of a material with cylindrical reinforcing fibers is analyzed for different values of the internal material length scale and homogenized yield surfaces are presented. While the main focus is on initial yield surfaces, subsequent yield surfaces are also presented. The center of the yield surface is tracked under uniaxial loading both in the transverse and longitudinal directions and an anisotropic Bauschinger effect is shown to depend on the size of the fibers. Results are compared to conventional predictions, and size-effects on the kinematic hardening are accentuated.

1. Introduction

Reinforcement of metals by stiff elastic fibers is used to obtain increased stiffness, strength and creep resistance, but often on the cost of decreased ductility and fracture properties (see McDanels, 1985). A significant amount of research has analyzed how geometry and material parameters affect the overall properties of the composite material (see Christman et al., 1989; Bao et al., 1991; Tvergaard, 1990, 1995; Ltissenden et al., 2000; Legarth, 2003, 2004, 2005). These studies are based on conventional gradient independent plasticity models, and hence predict no effect of reinforcement size.

Recent interests in size-effects in metals have confirmed experimentally that 'smaller is stronger'. This has been shown for different materials and under different loading conditions such as bending (Stölken and Evans, 1998; Haque and Saif, 2003; Lou et al., 2005), torsion (Fleck et al., 1994), indentation and contact compression (Ma and Clarke, 1995; Swadener et al., 2002; Wang et al., 2006). For metal matrix composites, a non-trivial size-effect was observed by Lloyd (1994) who compared tests for two different SiC particle sizes in aluminum, 16 μm and 7.5 μm, while keeping the volume fraction constant. Shu and Barlow (2000) have compared an experimentally obtained TEM map of the lattice misorientation with computed deformation fields around a whisker, obtained using a strain gradient crystal plasticity model in a plane strain cell model of the composite. It was found that a classical crystal formulation tends to over-predict deformation gradients near whiskers, while a strain gradient crystal plasticity model predicted a more smooth field with lower gradients that correlated better with the measurements.

Conventional theories of plasticity lack the ability to model size-effects, as no constitutive length parameters are used. Based on the experimental evidence on size-effects in metals, various size-dependent strain gradient plasticity theories have been proposed. Aifantis (1984) proposed one of the earliest models that accounts for size effects in the plastic regime by

* Corresponding author.
E-mail addresses: reaz@mek.dtu.dk (R. Azizi), cn@mek.dtu.dk (C.F. Niordson), bnl@mek.dtu.dk (B.N. Legarth).

0749-6419/$ - see front matter © 2011 Elsevier Ltd. All rights reserved.
doi:10.1016/j.ijplas.2011.05.006

introducing gradients of the plastic strain in the yield condition. Some of the proposed strain gradient plasticity models are of lower order nature (see Acharya and Bassani, 2000; Bassani, 2001), retaining the structure of a conventional boundary value problem in solid mechanics, but most of the proposed theories are of higher order nature, employing higher order stress-measures as work-conjugates to strain gradients. These models demand non-conventional higher order boundary conditions (e.g. Fleck and Hutchinson, 1997, 2001; Gao et al., 1999; Gurtin, 2002; Gudmundson, 2004; Gurtin and Anand, 2005; Lele and Anand, 2008; Fleck and Willis, 2009a,b). Within the context of size-effects in composites, strain gradient plasticity theories have been used to model stiffening and damage (e.g. Niordson and Tvergaard, 2001, 2002; Niordson, 2003; Huang and Li, 2005; Borg et al., 2006; Legarth and Niordson, 2010), as well as to quantify size-effects in TRIP-steels (Mazzoni-Leduc et al., 2008, 2010). Recently, Barai and Weng (2011) showed that with a perfect interface contact, decreasing the fiber radius would enhance the overall stiffness and plastic strength, but with an imperfect interface the size effect is reversed.

The present paper is an initial step towards solving the complicated problem of obtaining homogenized properties of composites when accounting for material size-effects. It is the aim to study size-effects on the homogenized properties of composites for which the matrix material can be modeled by strain gradient plasticity theory. The energetic higher order strain gradient plasticity theory proposed by Gudmundson (2004) and Fredriksson et al. (2009) has been implemented in a generalized plane strain setting, and numerical finite element cell model analyses have been carried out to study the material response under different loading conditions. The results are presented in terms of overall response curves, contour-plots of stress quantities, as well as initial and subsequent yield surfaces.

2. Material model

The fibers are assumed to be isotropic and linear elastic with Young's modulus E_f and Possion's ratio ν_f, while the matrix material is assumed to follow a gradient enhanced isotropic elasto-plastic material model.

The material model applied for the matrix material is the rate independent energetic strain gradient plasticity model proposed by Gudmundson (2004) which accounts for gradients of the full plastic strain tensor. The theory is based on the incremental principle of virtual work on the following form:

$$\int_V \left[\dot{\sigma}_{ij}\delta\dot{\epsilon}_{ij} + (\dot{q}_{ij} - \dot{s}_{ij})\delta\dot{\epsilon}^p_{ij} + \dot{m}_{ijk}\delta\dot{\epsilon}^p_{ij,k}\right]\mathrm{d}V = \int_S \left[\dot{T}_i\delta\dot{u}_i + \dot{M}_{ij}\delta\dot{\epsilon}^p_{ij}\right]\mathrm{d}S, \tag{1}$$

where the increment of a given quantity is denoted by a superposed dot, $\dot{(\cdot)}$ and V is the volume of the body analyzed, while S is the surface of the body. The stress tensor is denoted by σ_{ij} and $s_{ij} = \sigma_{ij} - \frac{1}{3}\delta_{ij}\sigma_{kk}$ is the stress deviator. The total strain, ϵ_{ij}, is the sum of the elastic strain, ϵ^e_{ij}, and the plastic strain, ϵ^p_{ij}, while $\epsilon^p_{ij,k}$ denotes the gradient of the plastic strain tensor. The micro stress, q_{ij}, and the higher order stress, m_{ijk}, are work conjugate stress-measures to the plastic strain and the plastic strain gradient, respectively. The traction, T_i, and higher order traction, M_{ij}, are surface quantities work-conjugate to the displacement, u_i, and the plastic strain tensor, ϵ^p_{ij}, respectively.

The free energy per unit volume, ψ, of the strain gradient dependent material is assumed to be on the form $\psi = \psi\left(\epsilon^e_{ij}, \epsilon^p_{ij,k}\right)$. Hence, no free energy is stored due to the plastic strain tensor itself and the increment of dissipation per unit volume is given by $q_{ij}\dot{\epsilon}^p_{ij}$. Following Fredriksson et al. (2009) we take the following specific form of the free energy

$$\psi\left(\epsilon^e_{ij}, \epsilon^p_{ij}\right) = \frac{1}{2}D_{ijkl}\epsilon^e_{ij}\epsilon^e_{kl} + \frac{1}{2}L_*^2 G\epsilon^p_{ij,k}\epsilon^p_{ij,k}. \tag{2}$$

Here, L_* is a material length scale parameter introduced for dimensional consistency, G is the elastic shear modulus and D_{ijkl} is the isotropic tensor of elastic moduli, defined in terms of Young's modulus, E_m, and Poisson's ratio, ν_m, for the matrix. By derivation of the free energy with respect to the elastic strain and the gradient of plastic strain, the stresses and the higher order stresses are found as

$$\sigma_{ij} = \frac{\partial\psi}{\partial\epsilon^e_{ij}} = D_{ijkl}\epsilon^e_{kl}, \quad m_{ijk} = \frac{\partial\psi}{\partial\epsilon^p_{ij,k}} = GL_*^2\epsilon^p_{ij,k}. \tag{3}$$

The yield condition for the matrix material is given in terms of the micro stress, q_{ij}, as

$$f(q_{ij}, \sigma_f) = \sqrt{\frac{3}{2}q_{ij}q_{ij}} - \sigma_f = q_e - \sigma_f, \tag{4}$$

where yielding occurs for $f = 0$. The effective micro stress has been introduced as $q_e = \sqrt{\frac{3}{2}q_{ij}q_{ij}}$ and the instantaneous flow stress is denoted σ_f. Here, linear hardening is considered with the instantaneous flow stress given by $\sigma_f = \sigma_y + H\epsilon^p_e$, where σ_y denotes the initial yield stress, H denotes the hardening modulus and ϵ^p_e denotes the accumulated effective plastic strain, defined incrementally through the relation $\dot{\epsilon}^p_e = \sqrt{\frac{2}{3}\dot{\epsilon}^p_{ij}\dot{\epsilon}^p_{ij}}$, i.e. $\epsilon^p_e = \int \dot{\epsilon}^p_e \mathrm{d}\tau$, where τ is "pseudo-time".

The flow rule is given by the relation

$$\dot{\epsilon}^p_{ij} = \frac{3}{2}\frac{q_{ij}}{q_e}\dot{\epsilon}^p_e = r_{ij}\dot{\epsilon}^p_e, \tag{5}$$

which ensures normality of the plastic strain increment with respect to the yield surface. In this expression $r_{ij} = \frac{3}{2}\frac{q_{ij}}{q_e}$ is the direction of the plastic strain increment.

The constitutive equation for the micro stress, q_{ij}, can be written on the incremental form

$$\dot{q}_{ij} = \dot{\overline{\frac{2}{3}q_e r_{ij}}} = \frac{2}{3}\left(\dot{q}_e r_{ij} + q_e \dot{r}_{ij}\right). \tag{6}$$

At the point of yielding, where $f = 0$, Eq. (4) gives $q_e = \sigma_f = \sigma_y + H\epsilon_e^p$, i.e. $\dot{q}_e = H\dot{\epsilon}_e^p$, and we may rewrite Eq. (6) to obtain

$$\dot{q}_{ij} = \frac{2}{3}\left(\frac{2}{3}H r_{ij} r_{kl}\dot{\epsilon}_{kl}^p + q_e \dot{r}_{ij}\right), \tag{7}$$

where the identity $r_{kl}r_{kl} = \frac{3}{2}$ has been used. Following Fredriksson et al. (2009) this equation is reformulated using a penalty method ensuring normality of the plastic flow

$$\dot{q}_{ij} = \frac{2}{3}\left(\frac{2}{3}(H - E_0) r_{ij} r_{kl} + E_0 \delta_{ik}\delta_{jl}\right)\dot{\epsilon}_{kl}^p. \tag{8}$$

Here, the penalty factor, E_0, must be large compared to the hardening modulus, H, but small enough to ensure a well-conditioned system of equations.

3. Problem formulation

Assume that the composite can be modeled by a regular distribution of long parallel cylindrical fibers of circular cross section, see Fig. 1a. The loading is characterized by macroscopic tri-axial loading, such that the composite deforms under generalized plane strain conditions. Thus, a unit cell containing a single fiber may be extracted as shown in Fig. 1b. Furthermore, since only loading with the same symmetry planes as the geometry and the material itself are considered (we do not consider shear in the (x_1,x_2) coordinate system), the analyses can be carried out on a reduced unit cell containing only one quarter of a fiber, Fig. 1c. At the center of the fiber a reference right-hand Cartesian coordinate system, x_i, is located and aligned with the sides of the cell. The positive direction of the third axis, x_3 (not shown), points in the out-of-plane direction normal to the (x_1,x_2)-plane. As tri-axial loading is studied with only normal strains imposed along the coordinate axes, the cell sides will remain straight during the deformation. The dimensions of the reduced unit cell is specified by the length of the sides, h, and the radius of the fiber, R, according to Fig. 1c. The fibers are modeled as linear elastic, whereas the matrix material is modeled using the energetic strain gradient plasticity theory described in the previous section. The higher order material model for the matrix material needs higher order boundary conditions on either the plastic flow or on the higher order traction. Since dislocations are assumed not to pass from the matrix into the fiber and consequently pile up at the interface, plastic flow is suppressed by specifying $\epsilon_{ij}^p = 0$ at the interface, see also Hutchinson (2000). Macroscopic homogeneous deformations are considered such that an appropriate symmetry conditions are applied at the exterior of the cell. In addition to demanding that the conventional shear traction must vanish, these symmetry conditions also imply that $M_{ij} = 0$ for $i = j$ and $\epsilon_{ij}^p = 0$ for $i \neq j$ at the exterior of the elastic–plastic part of the cell (see also Legarth and Niordson, 2010). The incremental boundary conditions can be summarized as follows:

$$\begin{array}{llllll}
\dot{u}_1 = 0, & \dot{T}_2 = 0, & \text{on} & x_1 = 0, & x_2 \in [0,h], \\
\dot{\epsilon}_{12}^p = 0, & \dot{M}_{11} = \dot{M}_{22} = 0, & \text{on} & x_1 = 0, & x_2 \in [R,h], \\
\dot{u}_1 = \dot{\Delta}_1, & \dot{T}_2 = 0, & \text{on} & x_1 = h, & x_2 \in [0,h], \\
\dot{\epsilon}_{12}^p = 0, & \dot{M}_{11} = \dot{M}_{22} = 0, & \text{on} & x_1 = h, & x_2 \in [0,h], \\
\dot{u}_2 = 0, & \dot{T}_1 = 0, & \text{on} & x_1 \in [0,h], & x_2 = 0, \\
\dot{\epsilon}_{12}^p = 0, & \dot{M}_{11} = \dot{M}_{22} = 0, & \text{on} & x_1 \in [R,h], & x_2 = 0, \\
\dot{u}_2 = \dot{\Delta}_2, & \dot{T}_1 = 0, & \text{on} & x_1 \in [0,h], & x_2 = h, \\
\dot{\epsilon}_{12}^p = 0, & \dot{M}_{11} = \dot{M}_{22} = 0, & \text{on} & x_1 \in [0,h], & x_2 = h, \\
\dot{\epsilon}_{11}^p = \dot{\epsilon}_{22}^p = \dot{\epsilon}_{12}^p = 0, & & \text{on} & x_1^2 + x_2^2 = R^2, &
\end{array} \tag{9}$$

Here, $\dot{\Delta}_1$ and $\dot{\Delta}_2$ are displacement increments to be determined to give prescribed macroscopic stresses as described later, and $\dot{T}_i = \dot{\sigma}_{ij}n_j$ and $\dot{M}_{ij} = \dot{m}_{ijk}n_k$ are the increments of traction vector and higher order traction, respectively, with n_i denoting the outward unit normal vector. The out-of-plane plastic strain, ϵ_{33}^p, is given in terms of in-plane plastic strain components by plastic incompressibility, $\epsilon_{ii}^p = 0$. Similarly, M_{33} is given in terms of the in-plane components M_{11} and M_{22}, where $M_{ii} = m_{iik}n_k = 0$. Finally, out-of-plane deformation is controlled by specifying a constant out-of-plane normal strain increment, $\dot{\epsilon}_{33} = \dot{\Delta}_3/t$, with t denoting the reference thickness of the computational unit cell. Here, one side of the unit-cell is fixed on the (x_1,x_2)-plane, while the other side has the prescribed displacement increment, $\dot{\Delta}_3$. It is emphasized that this generalized plane strain problem formulation only includes a single out-of-plane degree of freedom, namely the displacement $\dot{u}_3$.

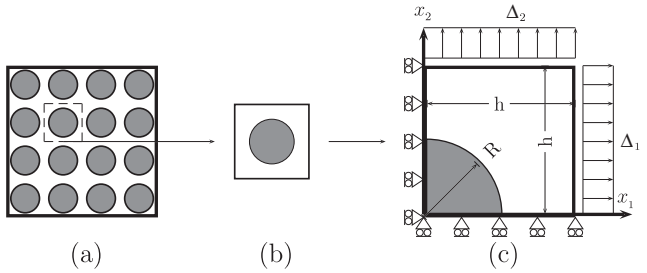

Fig. 1. (a) Regular distribution of fibers in the composite. (b) Full unit cell containing one fiber. (c) Reduced unit cell containing a quarter of a fiber.

4. Homogenization and macroscopic yield criterion

4.1. Homogenization

The overall macroscopic behavior of the analyzed composite depends on the micro-structural response of the unit cell. It is obtained by appropriate volume averaging of stress and strain data at the unit cell scale (see, e.g. Terada et al., 2000; Drago and Pindera, 2007; Alfaro, 2008). The overall macroscopic stress increment, $\dot{\Sigma}_{ij}$, is then evaluated as

$$\dot{\Sigma}_{ij} = \frac{1}{V}\int_V \dot{\sigma}_{ij}\mathrm{d}V, \tag{10}$$

while the overall macroscopic strain increment for perfect bonding between fiber and matrix is evaluated similarly by

$$\dot{E}_{ij} = \frac{1}{V}\int_V \dot{\epsilon}_{ij}\mathrm{d}V. \tag{11}$$

By applying the divergence theorem and using the conventional equilibrium equation, $\sigma_{ij,i} = 0$, one can obtain

$$\dot{\Sigma}_{ij} = \frac{1}{V}\int_S \dot{\sigma}_{ik} n_k x_j \mathrm{d}S, \tag{12}$$

where, n_k is the outward unit normal vector, x_j is the position vector and S is the boundary surface of unit cell. It is emphasized that since only one quarter of a fiber is investigated, see Fig. 1c, the volume averaging in Eq. (12) will result in non-vanishing in-plane shear components which is canceled by the mirrored quarter unit-cells. On the other hand, when modeling the full fiber, see Fig. 1b, the volume averaging would deliver zero in-plane shear components as expected for the loading considered here.

4.2. Macroscopic yield criterion

In order to establish initial and subsequent yield surfaces for the composite material, a macroscopic yield condition will be defined. At the level of the unit cell, the yield surface is of von Mises type, see Eq. (4), given in terms of the micro stress, q_{ij}. On the macroscopic scale, however, the overall higher order stress will average out, due to the symmetries of the problem. Hence, the macroscopic yield condition should be stated in terms of the conventional macroscopic stress, Σ_{ij}, and strain, E_{ij}, quantities alone. Here, a strain based macroscopic yield condition is defined as the point where the overall effective plastic strain has exceeded some threshold value, ϵ_t, according to the inequality

$$\left\| E_{ij} - C^{-1}_{ijkl}\Sigma_{kl} - E^{res}_{ij} \right\| \geqslant \epsilon_t. \tag{13}$$

The overall macroscopic tensor of elastic moduli, C_{ijkl}, for the composite is defined according to the numerical differentiation of the macroscopic quantities as

$$C_{ijkl} = \frac{\partial \Sigma_{ij}}{\partial E_{kl}} = \frac{\Sigma^{t+1}_{ij} - \Sigma^{t}_{ij}}{E^{t+1}_{kl} - E^{t}_{kl}}, \tag{14}$$

where t is the load increment and E^{res}_{ij} is the macroscopic residual strains defined as the components of the plastic strain after unloading. Note that the residual strain is zero for initial yielding and that the 2-norm is used in Eq. (13).

4.3. Macroscopic yield surface

In order to be able to determine yield surfaces for any combination of normal stresses with respect to the Cartesian reference coordinate system, x_i in Fig. 1c, a generalized plane strain analysis has been carried out. This allows for control of the

out-of-plane stress so that analyses of the yield surface at different values of the overall stress state can be considered. In terms of the overall stress quantities the yield condition can generally be stated as $F = 0$, with

$$F = F\left(\Sigma_{11}, \Sigma_{22}, \Sigma_{33}, \Sigma_f^T, \Sigma_f^L\right), \tag{15}$$

where Σ_f^T and Σ_f^L are composite yield strengths in the transverse and longitudinal direction, respectively. It is emphasized, that this study excludes the macroscopic shear stress, i.e. $\Sigma_{12} = 0$. Proportionality of the macroscopic stresses, Σ_{11}, Σ_{22} and Σ_{33}, is imposed such that

$$\kappa_1 = \frac{\Sigma_{22}}{\Sigma_{11}} \quad \text{and} \quad \kappa_2 = \frac{\Sigma_{33}}{\Sigma_{11}} \tag{16}$$

are constants for any single analysis. The method used to prescribe these ratios is based on constructing the solution as a linear combination of the three different trial-solutions shown in Fig. 2, while imposing the conditions in Eq. (16) (see Niordson and Tvergaard, 2007). The higher order boundary conditions for these three trial-solutions are identical to what is stated in Eq. (9). However the conventional boundary conditions have to be revised according to

$$\begin{aligned}
\text{Fig. 2(a)} \quad & \dot{u}_1(0,x_2,x_3) = 0, \quad \dot{u}_1(h,x_2,x_3) = \dot{\Delta}_1, \\
& \dot{u}_2(x_1,0,x_3) = 0, \quad \dot{u}_2(x_1,h,x_3) = 0, \\
& \dot{u}_3(x_1,x_2,0) = 0, \quad \dot{u}_3(x_1,x_2,t) = 0, \\
\text{Fig. 2(b)} \quad & \dot{u}_1(0,x_2,x_3) = 0, \quad \dot{u}_1(h,x_2,x_3) = 0, \\
& \dot{u}_2(x_1,0,x_3) = 0, \quad \dot{u}_2(x_1,h,x_3) = \dot{\Delta}_2, \\
& \dot{u}_3(x_1,x_2,0) = 0, \quad \dot{u}_3(x_1,x_2,t) = 0, \\
\text{Fig. 2(c)} \quad & \dot{u}_1(0,x_2,x_3) = 0, \quad \dot{u}_1(h,x_2,x_3) = 0, \\
& \dot{u}_2(x_1,0,x_3) = 0, \quad \dot{u}_2(x_1,h,x_3) = 0, \\
& \dot{u}_3(x_1,x_2,0) = 0, \quad \dot{u}_3(x_1,x_2,t) = \dot{\Delta}_3,
\end{aligned} \tag{17}$$

where t is the thickness of the unit cell and $\dot{\Delta}_i$ are the prescribed displacement increments. The homogenized macroscopic stress increments for each trial-solution $\left(\dot{\Sigma}_{ij}^A, \dot{\Sigma}_{ij}^B \text{ and } \dot{\Sigma}_{ij}^C\right)$ are used to express the combined homogenized stress increments as the following linear combination

$$\dot{\Sigma}_{ij} = \dot{\Sigma}_{ij}^A + C_1\dot{\Sigma}_{ij}^B + C_2\dot{\Sigma}_{ij}^C, \tag{18}$$

which together with the prescribed stress ratios, Eq. (16), allows for the solution of C_1 and C_2. With C_1 and C_2 known, any kind of incremental stress, strain or displacement data, $\dot{\Lambda}$, may be calculated as a similar linear combination

$$\dot{\Lambda} = \dot{\Lambda}^A + C_1\dot{\Lambda}^B + C_2\dot{\Lambda}^C. \tag{19}$$

5. Numerical implementation

The incremental version of virtual work stated in Eq. (1) is used as a basis for the finite element method as outlined by Fredriksson et al. (2009). In the present context a generalized plane strain numerical solution method is treated. Quadrilateral elements with eight nodes have been used for in-plane displacement interpolation generating functions for total strains of second order. Since comparable orders of interpolation is desirable for both total and plastic strains (and consequently for elastic strains), bilinear four node elements are used to interpolate the plastic strain components. For the plastic strain interpolation, three unknowns are treated, $\dot{\epsilon}_{11}^p$, $\dot{\epsilon}_{22}^p$ and $\dot{\epsilon}_{12}^p$, and the out-of-plane component is calculated by plastic incompressibility as $\dot{\epsilon}_{33}^p = -(\dot{\epsilon}_{11}^p + \dot{\epsilon}_{22}^p)$. For the displacement degrees of freedom (DOF), two in-plane displacements are used at all nodes in the model, and a single extra DOF for the entire finite element model is used to control the out-of-plane strain, which is

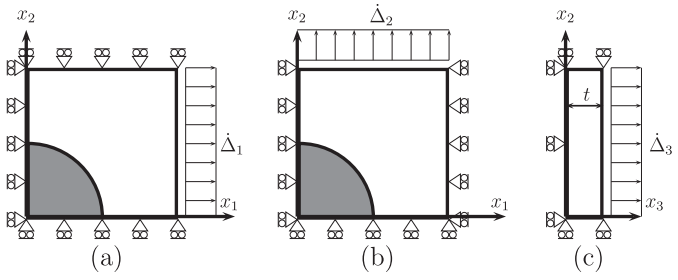

Fig. 2. The unit cell with applied boundary conditions for the three different trial cases.

constant throughout the computational domain. Hence, in total five local DOFs are used at corner nodes and two at non-corner nodes, in addition to one extra out-of-plane DOF for the entire finite element model.

Nodal interpolation is stated as follows:

$$\dot{u}_i = \sum_{n=1}^{2k} N_i^n \dot{U}^n, \quad \dot{\epsilon}_{ij}^p = \sum_{m=1}^{3l} P_{ij}^m \dot{\epsilon}_m^p, \tag{20}$$

where N_i^n and P_{ij}^m are shape function matrices for the displacements and plastic strain components, respectively, and $k = 8$ and $l = 4$ are the number of nodes used for the different interpolation schemes. The nodal unknowns are arranged in the vectors $\dot{U}^n$ and $\dot{\epsilon}_m^p$. The relevant derivatives of the displacement field and the plastic strain field can be expressed as

$$\dot{\epsilon}_{ij} = \sum_{n=1}^{2k} B_{ij}^n \dot{U}^n, \quad \dot{\epsilon}_{ij,k}^p = \sum_{m=1}^{3l} Q_{ijk}^m \dot{\epsilon}_m^p, \tag{21}$$

where, $B_{ij}^n = (N_{i,j}^n + N_{j,i}^n)/2$ and $Q_{ijk}^m = P_{ij,k}^m$ contain appropriate spatial derivatives of the shape functions. The discretized system of equations can then be expressed in the matrix form

$$\begin{bmatrix} \boldsymbol{K}_u & -\boldsymbol{K}_{up} \\ -\boldsymbol{K}_{up}^{\mathrm{T}} & -\boldsymbol{K}_p \end{bmatrix} \begin{bmatrix} \dot{\boldsymbol{U}} \\ \dot{\boldsymbol{\epsilon}}^p \end{bmatrix} = \begin{bmatrix} \dot{\boldsymbol{f}}_u \\ \dot{\boldsymbol{f}}_p \end{bmatrix}, \tag{22}$$

where $\dot{\boldsymbol{f}}_u = \int_S \boldsymbol{N}^{\mathrm{T}} \dot{\boldsymbol{T}} \mathrm{d}S$ is the incremental nodal force vector and $\dot{\boldsymbol{f}}_p = \int_S \boldsymbol{P}^{\mathrm{T}} \dot{\boldsymbol{M}} \mathrm{d}S$ is the incremental higher order nodal force vector. The element matrices are given by

$$\boldsymbol{K}_u = \int_v \boldsymbol{B}^{\mathrm{T}} \boldsymbol{D}_e \boldsymbol{B} \mathrm{d}V, \tag{23}$$

$$\boldsymbol{K}_p = \int_v \left[\boldsymbol{P}^{\mathrm{T}} (\boldsymbol{D}_e + \boldsymbol{D}_p) \boldsymbol{P} + \boldsymbol{Q}^{\mathrm{T}} \boldsymbol{D}_h \boldsymbol{Q} \right] \mathrm{d}V, \tag{24}$$

$$\boldsymbol{K}_{up} = \int_v \boldsymbol{B}^{\mathrm{T}} \boldsymbol{D}_e \boldsymbol{P} \mathrm{d}V, \tag{25}$$

where $\boldsymbol{D}_e$ is the isotropic elastic stiffness matrix, $\boldsymbol{D}_p$ contains the plastic moduli, and $\boldsymbol{D}_h$ contains the higher order moduli. Thus,

$$\boldsymbol{D}_e = \frac{E}{(1+\upsilon)(1-2\upsilon)} \begin{bmatrix} 1-\upsilon & \upsilon & \upsilon & 0 \\ \upsilon & 1-\upsilon & \upsilon & 0 \\ \upsilon & \upsilon & 1-\upsilon & 0 \\ 0 & 0 & 0 & \frac{1-2\upsilon}{2} \end{bmatrix} \tag{26}$$

$$\boldsymbol{D}_p = \frac{2}{3} \left(\frac{2}{3} (H - E_0) \boldsymbol{r}\boldsymbol{r}^{\mathrm{T}} + E_0 \boldsymbol{I}_p \right) \tag{27}$$

$$\boldsymbol{D}_h = G L_*^2 \boldsymbol{I} \tag{28}$$

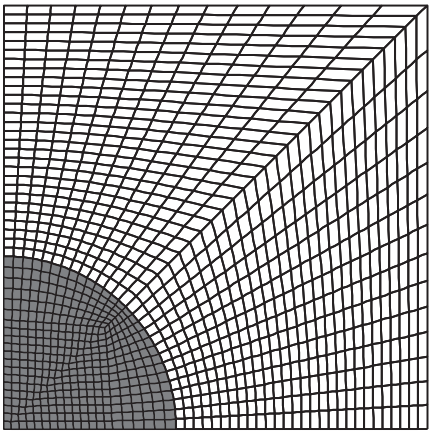

Fig. 3. An example of finite element mesh used in the numerical computations.

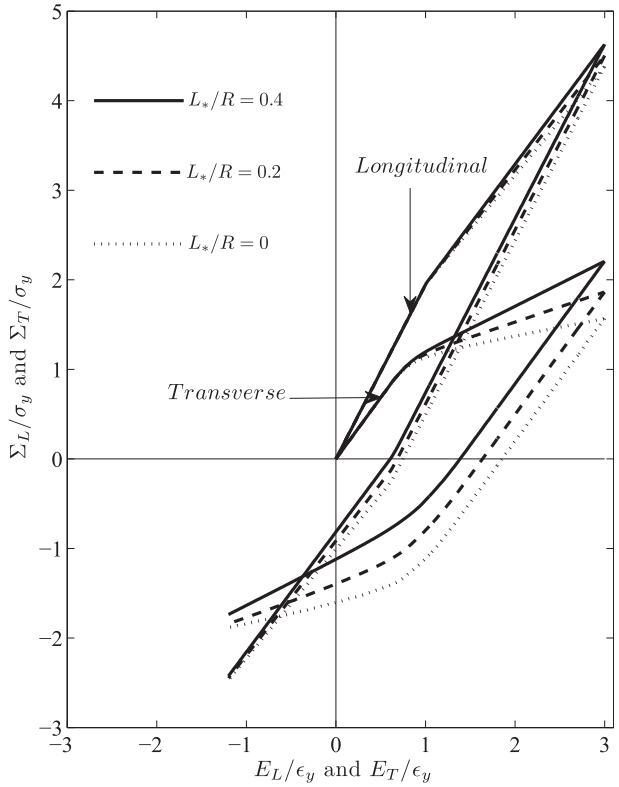

Fig. 4. Effect of the particle size (L_*/R) in uniaxial loading in both transverse and longitudinal directions with $H/E_m = 0.1$ and $V_f = 0.2$.

Table 1
Bauschinger stress in the composite for the two different loading directions (transverse, A_T, and longitudinal, A_L, see Fig. 4) with $H/E_m = 0.1$ and $V_f = 0.2$.

	$L_*/R = 0$	$L_*/R = 0.2$	$L_*/R = 0.4$
A_T/σ_y	0.033	0.29	0.62
A_L/σ_y	1.49	1.55	1.85

where E_0 is the penalty factor introduced to ensure normality of the plastic flow, $\boldsymbol{r} = (r_{11}, r_{22}, r_{33}, r_{12})^{\mathrm{T}}$, $\boldsymbol{I}_p = \mathrm{diag}(1,1,1,1/2)$, and $\boldsymbol{I}$ is the 8×8 identity matrix. In Eq. (26) E and v is taken as the fiber or matrix moduli in the corresponding elements.

Fig. 3 shows an example of a finite element mesh with 1148 elements used in the numerical computations. Load integration is performed using the forward Euler method with a large number of small load increments. In the elastic regime, the plastic stiffness matrix suppresses plastic deformation, since a large value of the hardening modulus is used. In the limit of conventional plasticity this would lead to an artificial boundary layer effect with a width scaling with the element size. Hence, when using the computational method in the conventional limit, the plastic stiffness matrix has instead been defined by $\boldsymbol{K}_p = 10^{-8} E \boldsymbol{I}_{12\times 12}$ (with E being either E_m or E_f) and the coupling matrix $\boldsymbol{K}_{up} = \boldsymbol{0}$ for elastic integration points, while plastic strain quantities are only updated in integration points that are in the plastic regime.

6. Results

The first part of the results focuses on the response of the composite under uniaxial loading in the fiber direction (x_3-direction; longitudinal) and perpendicular to the fiber direction (x_1-direction; transverse). The second part focuses on the yield surface of the composite.

Conventional material parameters used for the matrix are $\sigma_y/E_m = 0.004$, $v_m = 0.3$, with the two different values of the hardening modulus $H/E_m = 0.01$ and 0.1. For the fibers that are considered elastic the material parameters are given by $E_f/E_m = 5.7$ and $v_f = 0.17$. These parameters apply well for SiC reinforced aluminum. The penalty factor is taken to be $E_o = 100H$ for the results presented. The number of load increments is chosen to be 900 giving a good solution convergence. Higher numbers of load increments have been tried and it is found that is costly and hardly affects the solution.

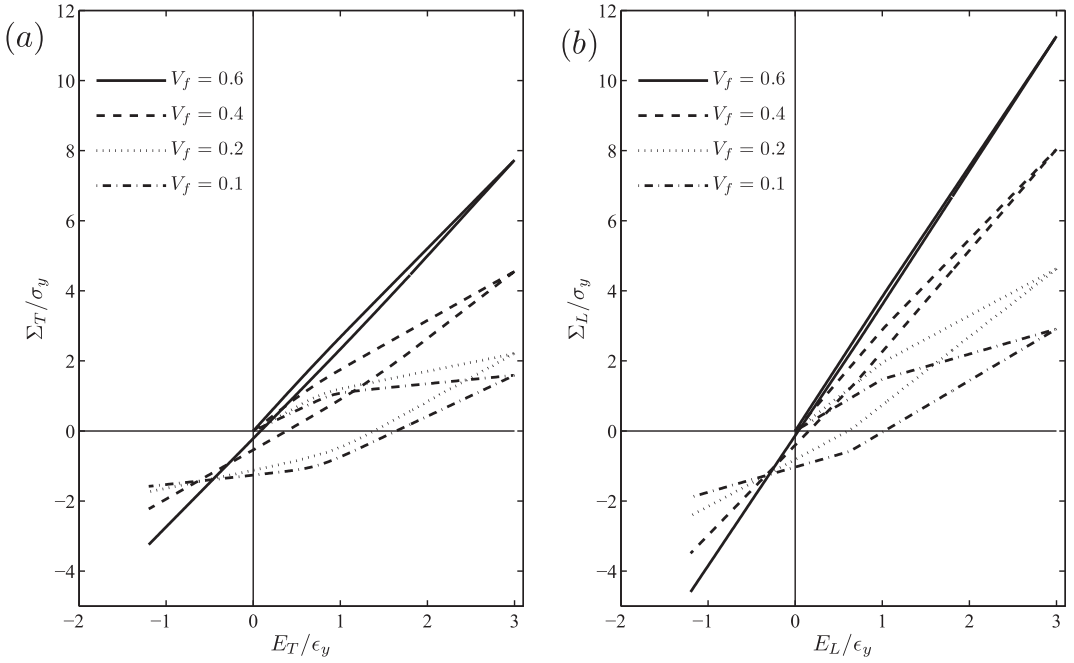

Fig. 5. Effect of the fiber volume fraction for uniaxial loading with $L_*/R = 0.4$ and $H/E_m = 0.1$. (a) Transverse loading. (b) Longitudinal loading.

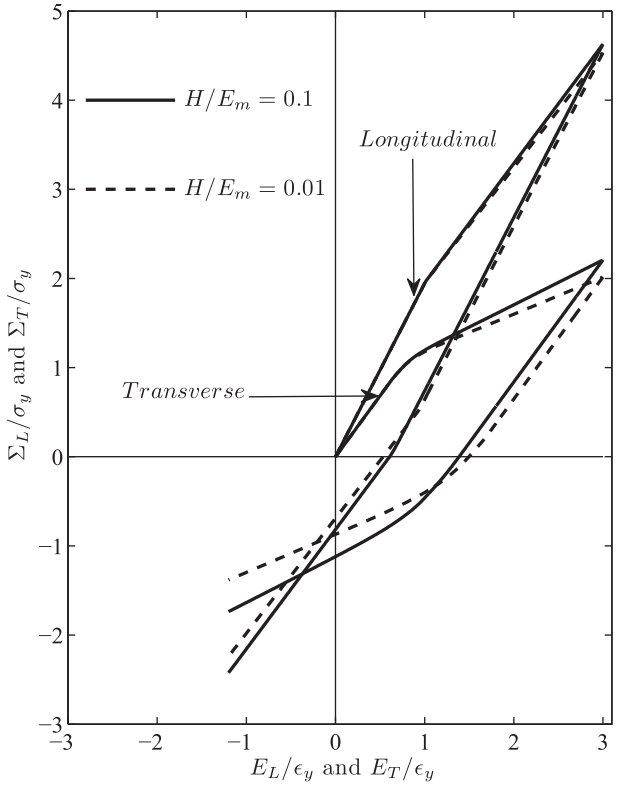

Fig. 6. Effect of the hardening in uniaxial loading in both transverse and longitudinal direction with $L_*/R = 0.4$ and $V_f = 0.2$.

Lloyd (1994) showed that the response of composites with the same volume fraction of SiC particles depends on the size of the particles. Investigations by a number of authors, e.g. Hutchinson (2000) have shown that for specimens with sizes falling in the range from roughly a fraction of a micron to ten microns a size-effect exists which cannot be captured by

Table 2
Bauschinger stress in the composite for two different loading directions (transverse, A_T, and longitudinal, A_L, see Fig. 6) with $L_*/R = 0.4$ and $V_f = 0.2$.

	$H/E_m = 0.01$	$H/E_m = 0.1$
A_T/σ_y	0.74	0.62
A_L/σ_y	1.85	1.59

Table 3
The qualitative impact of the different material parameters on the Bauschinger effect of the composite in the two different loading directions considered (transverse and longitudinal).

	Fig. 4 Effect of L_* on Bauschinger effect (with $V_f > 0$)	Fig. 5 Effect of V_f on Bauschinger effect	Fig. 6 Effect of H on Bauschinger effect (with $V_f > 0$)
Transverse	Large	Large	Small
Longitudinal	Small	Large	Small

conventional plasticity. Furthermore, it was argued that the material length scale for metals is in the range 0.25–1 μm for a slightly different but related model. For a micron scale length parameter of $L_* = 1$ μm in the present model, we analyse cases for $L_*/R = 0$, $L_*/R = 0.2$ and 0.4 which corresponds to large fibers, fibers with $R = 5$ μm and $R = 2.5$ μm, respectively.

6.1. Uniaxial loading

Fig. 4 shows the effect of the particle size for a fiber volume fraction of $V_f = (\pi R^2)/(4h^2) = 0.2$ and $H/E_m = 0.1$. Homogenized stress–strain curves are shown in the transverse, (Σ_T, E_T), and in the longitudinal, (Σ_L, E_L), directions for different particle size of $L_*/R = 0$, 0.2 and 0.4. Initial tension with subsequent compression is studied and the stress–strain curves are normalized by the initial yield stress and yield strain of the matrix, σ_y and $\epsilon_y = \sigma_y/E_m$, respectively. The composite is seen to have a stiffer response in the longitudinal direction as compared to the transverse direction. The results also show that the length scale in

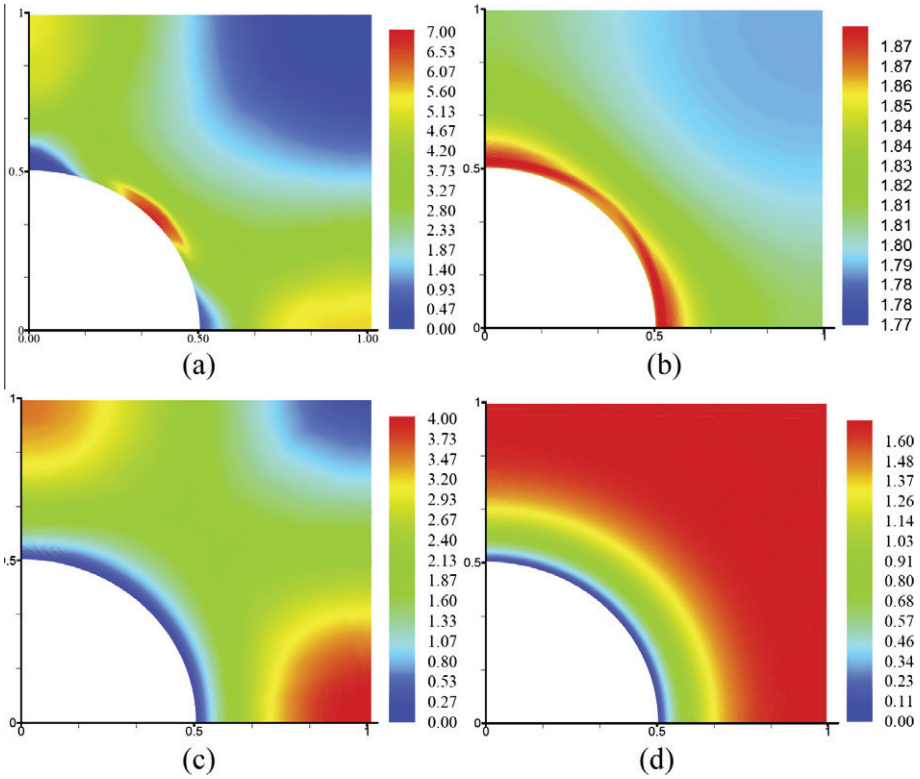

Fig. 7. Effective plastic strain distribution $(\epsilon_e^p/\epsilon_y)$ for $V_f = 0.2$ and $H/E_m = 0.1$ at the end of uniaxial tension. (a) Transverse direction (x_1) with $L_*/R = 0$. (b) Longitudinal direction (x_3) with $L_*/R = 0$. (c) Transverse direction with $L_*/R = 0.4$. (d) Longitudinal direction with $L_*/R = 0.4$.

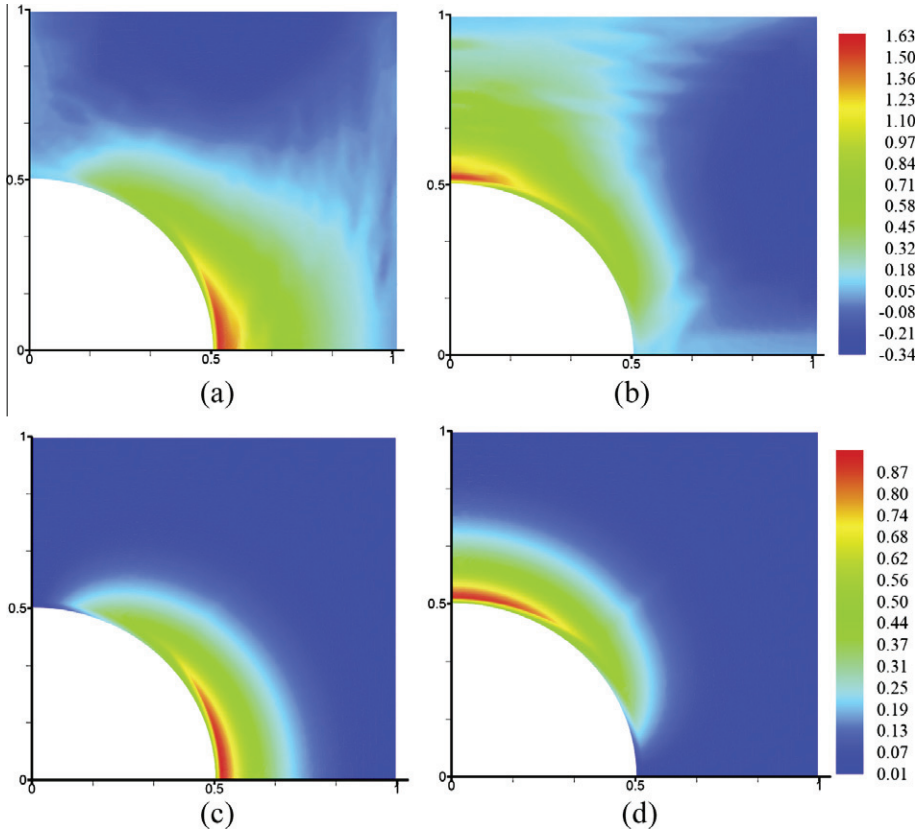

Fig. 8. Higher order stress distribution for $L_*/R = 0.4$, $V_f = 0.2$ and $H/E_m = 0.1$ at the end of uniaxial tension, see Fig. 7c and d. (a) $m_{111}/(L_*\sigma_y)$ in transverse direction (x_1). (b) $m_{112}/(L_*\sigma_y)$ in transverse direction (x_1). (c) $m_{331}/(L_*\sigma_y)$ in longitudinal direction (x_3). (d) $m_{332}/(L_*\sigma_y)$ in longitudinal direction (x_3).

the present strain gradient formulation serves as to increase the overall hardening of the composite while the particle size is decreasing in accordance with earlier studies using strain gradient plasticity (Anand et al., 2005; Legarth and Niordson, 2010). These findings are consistent with experimental studies of composites by Yan et al. (2007) and Lloyd (1994) where material hardening of the composite is observed to increase with decreasing particle size under a constant volume fraction of the reinforcement. The maximum strain in Fig. 4 is given by three times the yield strain in uniaxial tension for the matrix material at which the load is reversed until a compressive macroscopic strain of $1.2\epsilon_y$ is reached in the direction of the load.

Defining the Bauschinger stress by

$$A = \left(\Sigma^f + \Sigma^Y_{syp}\right)\Big/2, \tag{29}$$

where Σ^f is stress at the end of loading and Σ^Y_{syp} is subsequent yield stress, Table 1 shows the value of the Bauschinger stress for different particle sizes in both transverse and longitudinal directions. Upon load reversal, the Bauschinger stress is observed from Fig. 4 and Table 1 to be higher in the longitudinal direction than in the transverse direction for all fiber sizes considered. However, the relative increase of the Bauschinger stress with increasing L_*/R is higher in the transverse than in the longitudinal direction. In Fig. 5 homogenized stress–strain curves are shown for uniaxial loading in the transverse direction (Fig. 5a) and longitudinal direction (Fig. 5b) for four different values of the fiber volume fraction, $V_f = 0.1$, 0.2, 0.4 and 0.6. The results are for strain gradient dependent materials with $L_*/R = 0.4$. A stiffening effect is observed in both loading directions with increasing fiber volume fraction, V_f, as also observed experimentally by Corbin et al. (1996) for SiC/A356. This behavior has also been seen by Barai and Weng (2011) which was compared with experimental data of Kim et al. (2006). The considerable amount of Bauschinger effect observed in the experiments conducted by Corbin et al. (1996) and Lissenden (2010) cannot be captured by conventional J2 flow theory. However, the gradient dependent analysis here captures the enhanced Bauschinger effect better. Fig. 5 shows a moderate Bauschinger effect in the transverse direction, whereas a significant Bauschinger effect is noted when loading in the longitudinal direction. For $V_f = 0.6$, the responses are basically linear especially for longitudinal loading (Fig. 5b). The higher Bauschinger stress with higher fiber volume fraction has also been shown by Brassart et al. (2010) in the transverse direction.

The effect of the matrix material hardening is analyzed in Fig. 6 where homogenized stress–strain curves are shown in both the longitudinal and transverse loading directions for the hardening moduli $H/E_m = 0.01$ and 0.1 when $L_*/R = 0.4$ and

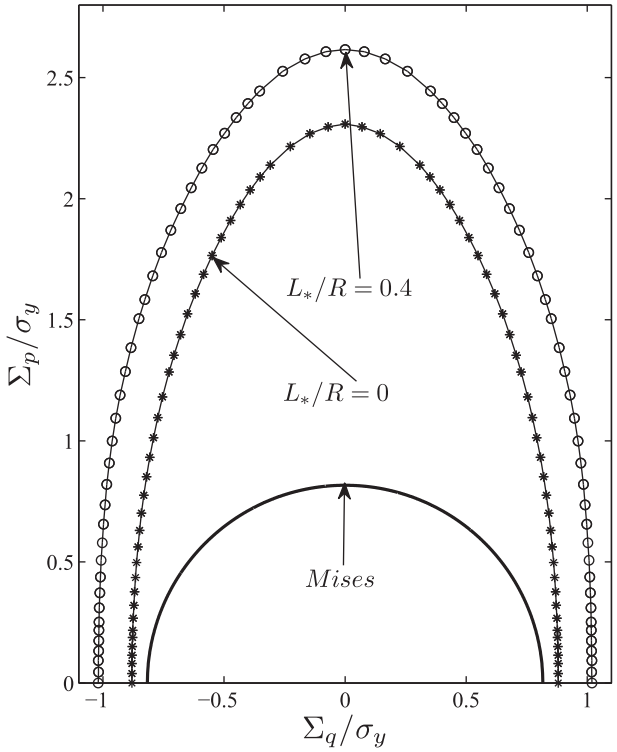

Fig. 9. Effect of the length scale (L_*/R) on homogenized initial yield surface (IYS) projected on the π-plane with $V_f = 0.2$, $H/E_m = 0.1$ and $\Sigma_h = 0$.

$V_f = 0.2$. For both levels of the matrix material hardening a Bauschinger effect is observed which again is larger in the longitudinal direction. Furthermore, Fig. 6 and the corresponding quantitative data in Table 2 show that the Bauschinger effect decreases with increasing matrix material hardening.

The main findings on the influence of the different material parameters on the Bauschinger effect are qualitatively summarized in Table 3. We conclude that the only conventional material parameter that has a significant influence on the Bauschinger effect is the fiber volume fraction, V_f, and most so in the longitudinal direction. However, the non-standard energetic material length parameter, L_*, has a significant influence on the Bauschinger effect in the transverse direction.

Fig. 7 shows the effective plastic strain distribution at the maximum level of deformation studied in Fig. 4. Conventional results ($L_*/R = 0$) for loading in the transverse and longitudinal direction are shown in Fig. 7 a and b, respectively. Fig. 7 c and d shows corresponding results for a size-dependent material with $L_*/R = 0.4$. The constraint on the plastic flow is observed to suppress plasticity close to the elastic fiber. Shu and Barlow (2000) used a finite-deformation strain gradient crystal plasticity formulation together with a classical crystal formulation to characterize the deformation of the matrix in a unit cell. They found that while a classical crystal formulation tends to over-predict the spatial gradient of the deformation, the strain gradient formulation is able to predict a more smooth field consistent with experimental finding. This is confirmed in Fig. 7 where the gradient dependent material has a smooth transition from zero plastic flow in the fiber in contrast to the conventional material which has an abrupt change.

The distribution of the appropriate higher order stress is seen in Fig. 8 where the components m_{111} (Fig. 8a) and m_{112} (Fig. 8b) are shown at the maximum tensile load in the transverse direction and m_{331} (Fig. 8c) and m_{332} (Fig. 8d) for tension at the maximum tensile load in the longitudinal direction. As can be seen, the higher order stresses are significant at the fiber–matrix interface where the gradients of the plastic strains are higher and vanish on the surface. The existence of the higher order stresses leads to an increased Bauschinger effect due to the higher order equilibrium equation that must be satisfied (see Gudmundson, 2004)

$$s_{ij} = q_{ij} - m_{ijk,k}, \tag{30}$$

From this relation it is observed that the divergence of the higher order stress has the role of a back stress, which leads to an increased Bauschinger effect when higher order stresses arise. This is also observed in pure shear for energetic strain gradient plasticity by Anand et al. (2005) and Niordson and Legarth (2010).

6.2. Yield surface

Eighty points on the yield surface for different value of κ_1 are computed using $\epsilon_t = 0.002$ in Eq. (13). Yield surfaces are shown on the π plane on which the macroscopic hydrostatic stress vanishes, so that $\kappa_1 + \kappa_2 = -1$. In absence of the macroscopic shear

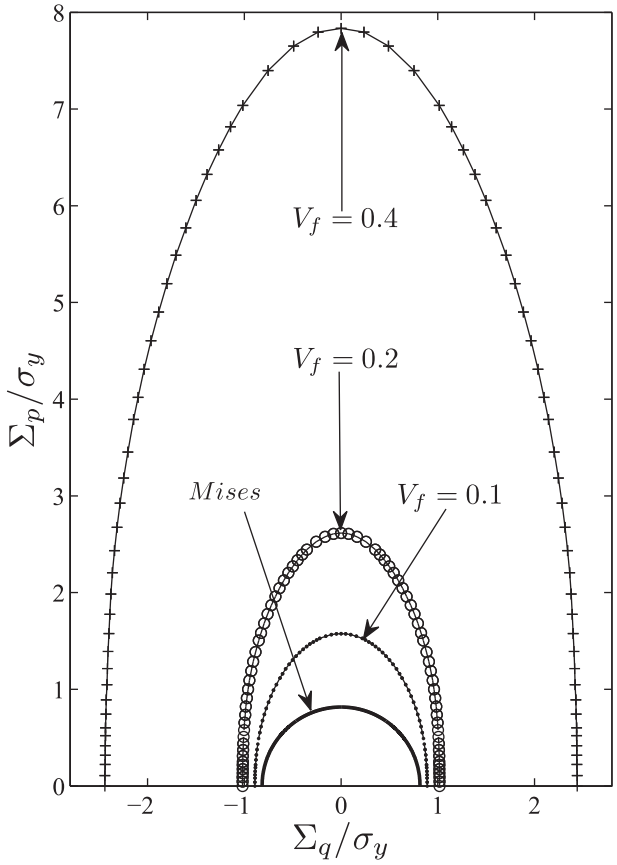

Fig. 10. Effect of the fiber volume fraction, V_f, on homogenized initial yield surface (IYS) projected on the π-plane with $L_*/R = 0.4$ and $H/E_m = 0.1$.

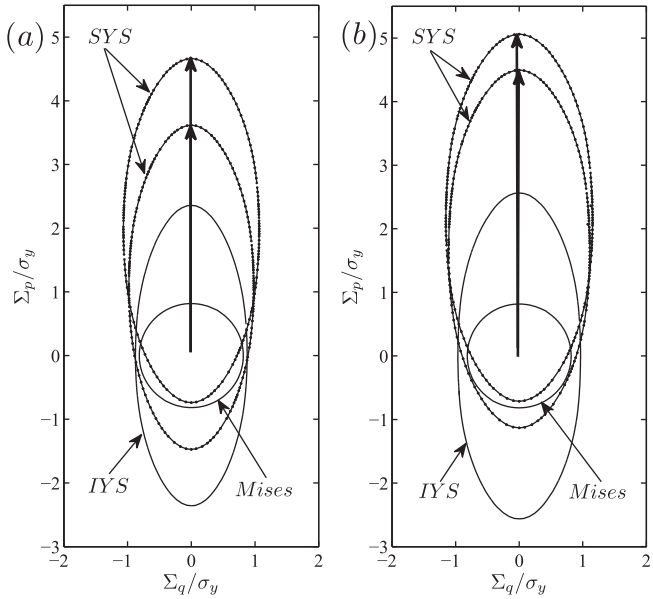

Fig. 11. Homogenized subsequent yield surface (SYS) projected on the π-plane for two different load levels along e_p with $H/E_m = 0.1$ (Thick arrow is the loading path). (a) $L_*/R = 0$. (b) $L_*/R = 0.4$.

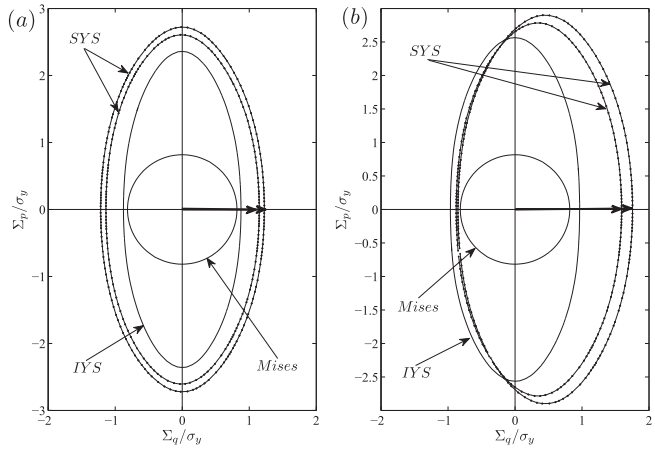

Fig. 12. Homogenized subsequent yield surface (SYS) projected on the π-plane for two different load levels along e_q with $H/E_m = 0.1$ (thick arrow is the loading path). (a) $L_*/R = 0$. (b) $L_*/R = 0.4$.

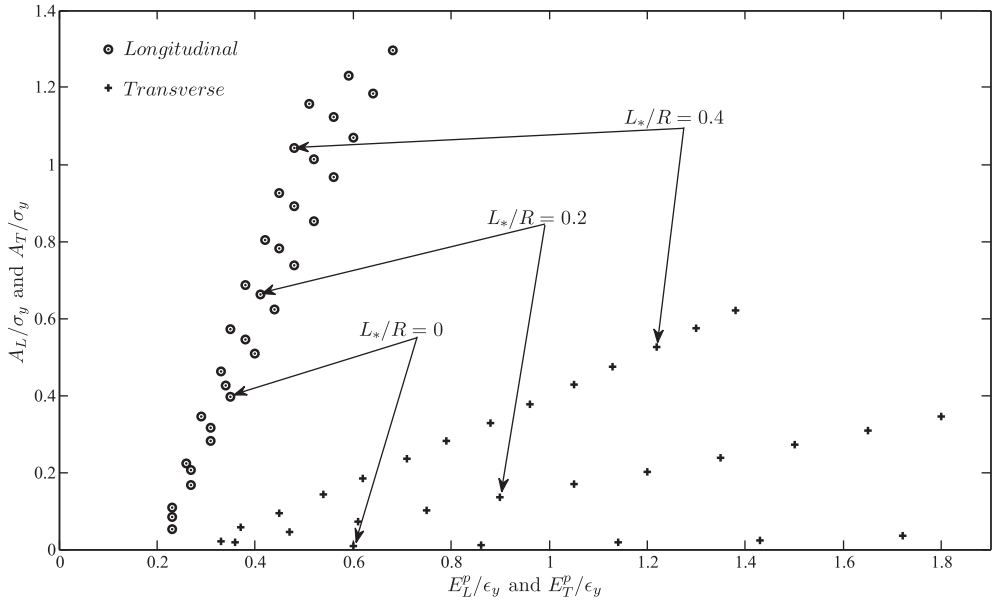

Fig. 13. Bauschinger stress for $H/E_m = 0.1$ and $V_f = 0.2$ for both transverse (x_1) and longitudinal (x_3) directions.

stresses in the (x_1,x_2) coordinate system shown in Fig. 1c, the stress state is thus characterized by two stress components in the directions of $\boldsymbol{e}_p$ and $\boldsymbol{e}_q$ which are both perpendicular to the hydrostatic axis $\boldsymbol{e}_h$. With $\boldsymbol{e}_1$, $\boldsymbol{e}_2$ and $\boldsymbol{e}_3$ denoting unit vectors in the x_1, x_2 and x_3 directions, respectively the stress state can be expressed in the two equivalent forms

$$\Sigma_{11}\boldsymbol{e}_1 + \Sigma_{22}\boldsymbol{e}_2 + \Sigma_{33}\boldsymbol{e}_3 = \Sigma_h\boldsymbol{e}_h + \Sigma_p\boldsymbol{e}_p + \Sigma_q\boldsymbol{e}_q, \tag{31}$$

where Σ_{11}, Σ_{22} and Σ_{33} are stress components in the Cartesian system, Σ_h is hydrostatic stress and Σ_p and Σ_q are stress components on the π plane. The base vectors in the π-plane are defined according to

$$\boldsymbol{e}_h = \frac{1}{\sqrt{3}}(1,1,1), \quad \boldsymbol{e}_p = \frac{1}{\sqrt{6}}(-1,-1,2), \quad \boldsymbol{e}_q = \frac{1}{\sqrt{2}}(1,-1,0). \tag{32}$$

With these definitions the stress Σ_p corresponds to loading in the x_3 (longitudinal) direction with opposite loading of half magnitude in the two perpendicular directions and Σ_q corresponds to loading in the x_1 (transverse) direction with opposite loading in the x_2 direction.

The effect of the material length scale on the initial yield surface (IYS) is shown in Fig. 9 with $V_f = 0.2$, $H/E_m = 0.1$ and $\Sigma_h = 0$. For comparison the isotropic Mises yield surface for the matrix material is included in the figure. It is seen that a

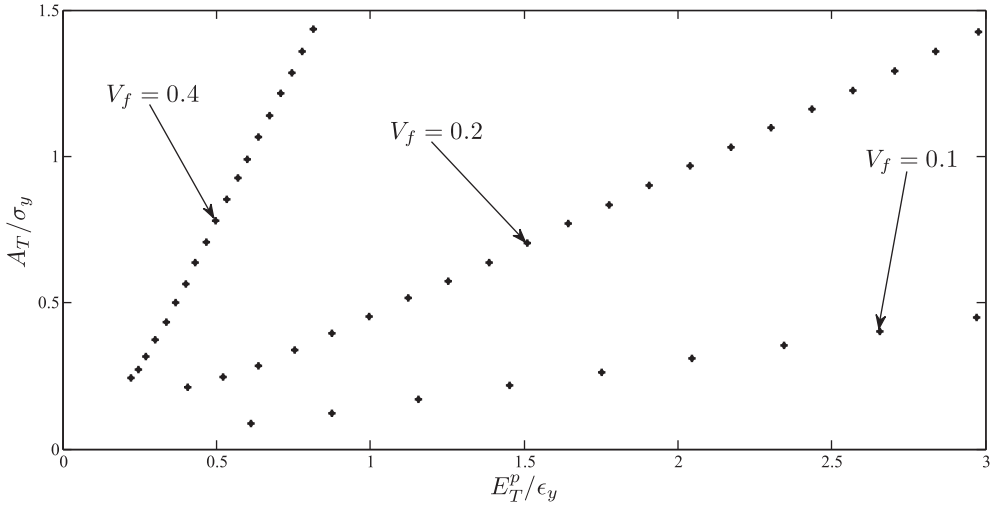

Fig. 14. Bauschinger stress for $H/E_m = 0.1$ and $L_*/R = 0.4$ in transverse direction (x_1).

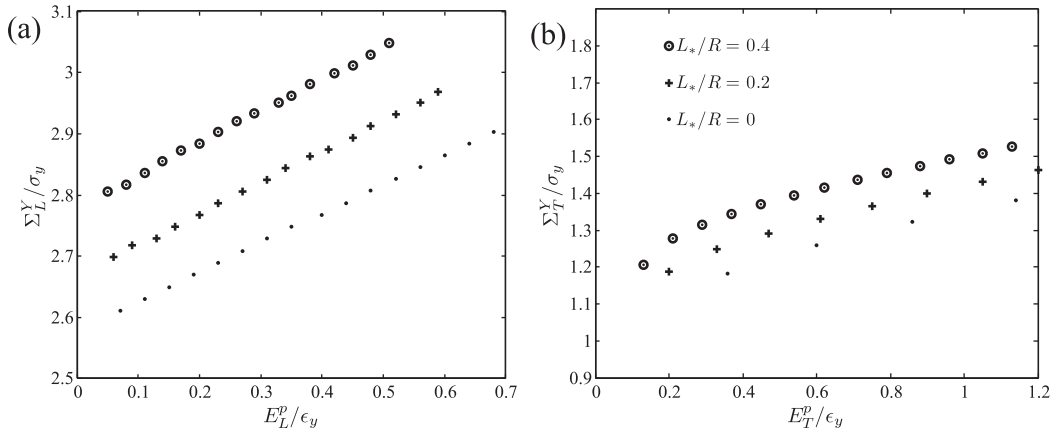

Fig. 15. Macroscopic yield stress with $H/E_m = 0.1$, $V_f = 0.2$ and $\epsilon_t = 0.001$. (a) Transverse (x_1) direction. (b) Longitudinal (x_3) direction.

homogeneous expansion in all directions occurs which increases with decreasing particle size. It is also noted that the yield surface of the composite material exceeds that of the pure matrix material.

Fig. 10 shows the IYS for $\Sigma_h = 0$ and different values of the fiber volume fraction, V_f, with $L_*/R = 0.4$. It is seen that the yield surface expands with increasing fiber volume fraction. The largest strengthening effects are observed when $\Sigma_q = 0$ corresponding to loading in the longitudinal direction with opposite loading of half magnitude in the two perpendicular directions. On the other hand, the smallest strengthening effect is observed for $\Sigma_p = 0$, which corresponds to macroscopic in-plane loading in the (x_1,x_2)-plane with equal and opposite loading in the x_1 and x_2 transverse directions. The conventional results are in agreement with findings of Seifert and Schmidt (2009).

In Fig. 11a and b multiple subsequent yield surfaces (SYS) are shown for uniaxial loading along $\boldsymbol{e}_p$ with $V_f = 0.2$ and when $L_*/R = 0$ and $L_*/R = 0.4$, respectively. The yield surface of the pure matrix material is also presented. First the load is increased to the amount of $3.6\sigma_y$ and $4.65\sigma_y$ for $L_*/R = 0$ and $4.5\sigma_y$ and $5\sigma_y$ for $L_*/R = 0.4$ then decreased to half the amount of loading. From this point the yield surface is probed in 80 different directions. A moderate isotropic expansion of the yield surface is observed with a significant kinematic hardening. Fig. 12 a and b show the corresponding yield surface for loading along $\boldsymbol{e}_q$ when $L_*/R = 0$ and $L_*/R = 0.4$, respectively. For this case, a significant isotropic expansion of the yield surface is observed, together with some kinematic hardening. It is seen that the Bauschinger effect is clearly anisotropic in the composites.

In Fig. 13 the Bauschinger stress (the center of yield surfaces according to Eq. (29)) is plotted as a function of the macroscopic plastic strain, E_T^p and E_L^p evaluated by Eq. (13), for both loading directions (transverse and longitudinal) when $V_f = 0.2$ and $H/E_m = 0.1$. It can be seen that the Bauschinger stress increases linearly with the macroscopic plastic strain for both loading cases. Note that the linear behavior of the Bauschinger stress versus plastic strain cannot be inferred for small levels of plastic deformation ($\left\|E_{ij}^p\right\| \cong \epsilon_t$).

Fig. 14 shows the effect of the fiber volume fraction, V_f, on Bauschinger stress with $L_*/R = 0.4$ in transverse direction. A significant effect of V_f on the Bauschinger stress is observed as discussed in connection with Table 3.

Expansion of the yield surface of the composite accompanies the kinematic hardening as it was seen in Figs. 11 and 12. Fig. 15 is plotted to show the amount of the macroscopic yield stress in both transverse and longitudinal directions as a function of the macroscopic plastic strain during the loading. The macroscopic yield stress is defined as

$$\Sigma^Y = \frac{|\Sigma^f| + |\Sigma^Y_{syp}|}{2}. \tag{33}$$

It is seen from the figure that the macroscopic yield stress increases almost linearly in both directions independent of the fiber size and that the increase is higher for the small particles.

7. Conclusion

In this paper, a rate independent higher order strain gradient plasticity theory has been used to investigate the overall behavior of heterogeneous materials under generalized plane strain condition. The elasto-plastic behavior of metal matrix composites has been studied and compared using both conventional and strain gradient plasticity theories. A unit cell containing one quarter of a circular fiber has been used for numerical investigations. Results for different combinations of normal loading in the longitudinal and transverse directions have been presented.

It is shown that the elastic modulus, yield stress and Bauschinger effect increase in both loading directions with higher fiber volume fraction. Furthermore, it is seen that for higher fiber volume fractions the overall plastic flow is suppressed at a given load-level and, as a result, the initial yield surface on the π-plane expands. It is concluded that V_f is the most important conventional parameter leading to a Bauschinger effect in both loading directions.

The effect of a constitutive length scale in the matrix material has been analyzed. The results show that the length scale, which is included energetically in the present strain gradient formulation, serves as to increase the overall hardening of the composite. Mainly, this occurs due to the fact that the gradient dependent material has a smooth transition from zero plastic flow at the fiber interface in contrast to the conventional material which has an abrupt change. As a result, the initial yield surface expands in all directions. The Bauschinger effect is also found to increase with L_*/R which results in additional kinematic hardening. It is concluded that the Bauschinger stress is significantly anisotropic in the composite.

Acknowledgment

This work is supported by the Danish Research Council for Technology and Production Sciences in a project entitled Plasticity Across the Scales. The computational resources have been provided by a hardware grant from the Danish Center of Scientific Computing (DCSC).

References

Acharya, A., Bassani, J.L., 2000. Lattice incompatibility and a gradient theory of crystal plasticity. Journal of the Mechanics and Physics of Solids 48, 1565–1595.

Aifantis, E.C., 1984. On the microstructural origin of certain inelastic models. Transactions of the ASME. Journal of Engineering Materials and Technology 106 (4), 326–330.

Alfaro, M., 2008. Multiscale analyses of fiber metal laminates. Ph.D. thesis, Delft University of Technology.

Anand, L., Gurtin, M., Lele, S., Gething, C., 2005. A one-dimensional theory of strain-gradient plasticity: formulation, analysis, numerical results. Journal of the Mechanics and Physics of Solids 53, 1789–1826.

Bao, G., Hutchinson, J.W., McMeeking, R.M., 1991. Particle reinforcement of ductile matrices against plastic flow and creep. Acta Metallurgica et Materialia 39 (8), 1871–1882.

Barai, P., Weng, G., 2011. A theory of plasticity for carbon nanotube reinforced composites. International Journal of Plasticity 27, 539–559.

Bassani, J.L., 2001. Incompatibility and a simple gradient theory of plasticity. Journal of the Mechanics and Physics of Solids 49, 1983–1996.

Borg, U., Niordson, C.F., Fleck, N.A., Tvergaard, V., 2006. A viscoplastic strain gradient analysis of materials with voids or inclusions. International Journal of Solids and Structures 43 (16), 4906–4916.

Brassart, L., Doghri, I., D. L., 2010. Homogenization of elasto-plastic composites coupled with a nonlinear finite element analysis of the equivalent inclusion problem. International Journal of Solids and Structures 47, 716–729.

Christman, T., Needleman, A., Suresh, S., 1989. An experimental and numerical study of deformation in metal–ceramic composites. Acta Metallurgica et Materialia 37 (11), 3029–3050.

Corbin, S., Wilkinson, D., Embury, J., 1996. The bauschinger effect in a particulate reinforced al alloy. Materials Science and Engineering A207, 1–11.

Drago, A., Pindera, M.-J., 2007. Micro-macromechanical analysis of heterogeneous materials: macroscopically homogeneous vs periodic microstructure. Composites Science Technology 67, 1243–1263.

Fleck, N.A., Hutchinson, J.W., 1997. Strain gradient plasticity. In: Hutchinson, J.W., Wu, T.Y. (Eds.), Advances in Applied Mechanics, vol. 33. Academic Press, pp. 295–361.

Fleck, N.A., Hutchinson, J.W., 2001. A reformulation of strain gradient plasticity. Journal of the Mechanics and Physics of Solids 49, 2245–2271.

Fleck, N.A., Muller, G.M., Ashby, M.F., Hutchinson, J.W., 1994. Strain gradient plasticity: theory and experiment. Acta Metallurgica et Materialia 42 (2), 475–487.

Fleck, N.A., Willis, J.R., 2009a. A mathematical basis for strain-gradient plasticity theory – Part I: Scalar plastic multiplier. Journal of the Mechanics and Physics of Solids 57, 161–177.

Fleck, N.A., Willis, J.R., 2009b. A mathematical basis for strain-gradient plasticity theory – Part II: Tensorial plastic multiplier. Journal of the Mechanics and Physics of Solids 57, 1045–1057.

Fredriksson, P., Gudmundson, P., L.P., M., 2009. Finite element implementation and numerical issues of strain gradient plasticity with application to metal matrix composites. International Journal of Solids and Structures 46, 3977–3987.

Gao, H., Huang, Y., Nix, W.D., Hutchinson, J.W., 1999. Mechanism-based strain gradient plasticity – I. Theory. Journal of the Mechanics and Physics of Solids 47 (6), 1239–1263.
Gudmundson, P., 2004. A unified treatment of strain gradient plasticity. Journal of the Mechanics and Physics of Solids 52 (6), 1379–1406.
Gurtin, M.E., 2002. A gradient theory of single-crystal viscoplasticity that accounts for geometrically necessary dislocations. Journal of the Mechanics and Physics of Solids 50 (1), 5–32.
Gurtin, M.E., Anand, L., 2005. A theory of strain-gradient plasticity for isotropic, plastically irrotational materials. Part I: Small deformations. Journal of the Mechanics and Physics of Solids 53 (7), 1624–1649.
Haque, M.A., Saif, M.T.A., 2003. Strain gradient effect in nanoscale thin films. Acta Materialia 51 (11), 3053–3061.
Huang, M., Li, Z., 2005. Size effects on stress concentration induced by a prolate ellipsoidal particle and void nucleation mechanism. International Journal of Plasticity 21 (8), 1568–1590.
Hutchinson, J.W., 2000. Plasticity at the micron scale. International Journal of Solids and Structures 37 (1–2), 225–238.
Kim, K., Cha, S., Hong, S., Hong, S., 2006. Microstructure and tensile behavior of carbon nanotubes reinforced cu matrix nanocomposites. Materials Science and Engineering 430, 27–33.
Legarth, B.N., 2003. Debonding of particles in anisotropic materials. International Journal of Mechanical Sciences 45, 1119–1133.
Legarth, B.N., 2004. Unit cell debonding analyses for arbitrary orientations of plastic anisotropy. International Journal of Solids and Structures 41 (26), 7267–7285.
Legarth, B.N., 2005. Effects of geometrical anisotropy on failure in a plastically anisotropic metal. Engineering Fracture Mechanics 72 (18), 2792–2807.
Legarth, B.N., Niordson, C.F., 2010. Debonding failure and size effects in micro-reinforced composites. International journal of plasticity 26 (1), 149–165.
Lele, S.P., Anand, L., 2008. A small-deformation strain-gradient theory for isotropic viscoplastic materials. Philosophical Magazine 88 (30), 1478–6435.
Lissenden, 2010. Experimental investigation of initial and subsequent yield surfaces for laminated metal matrix composites. International Journal of Plasticity 26, 1606–1628.
Ltissenden, C.J., Arnold, S.M., I. S. K., 2000. Flow/damage surfaces for fiber–reinforced metals having different periodic microstructures. International Journal of Plasticity 16, 1049–1074
Lloyd, D.J., 1994. Particle reinforced aluminium and magnesium matrix composites. International Materials Reviews 39 (1), 1–23.
Lou, J., Shrotriya, P., Soboyejo, W.O., 2005. A cyclic microbend study on LIGA Ni microelectromechanical systems thin films. Transactions of the ASME. Journal of Engineering Materials and Technology 127 (1), 16–22.
Ma, Q., Clarke, D.R., 1995. Size dependent hardness of silver single crystals. Journal of Materials Research 10, 853–863.
Mazzoni-Leduc, L., Pardoen, T., Massart, T., 2008. Strain gradient plasticity analysis of transformation induced plasticity in multiphase steels. International Journal of Solids and Structures 45 (20), 5397–5418.
Mazzoni-Leduc, L., Pardoen, T., Massart, T., 2010. Analysis of size effects associated to the transformation strain in trip steels with strain gradient plasticity. European Journal of Mechanics – A/Solids 29 (2), 132–142.
McDanels, D., 1985. Analysis of stress–strain, fracture, and ductility behavior of aluminum matrix composites containing discontinuous silicon carbide reinforcement. Metallurgical Transactions A (Physical Metallurgy and Materials Science) 16A (6), 1105–1115.
Niordson, C.F., 2003. Strain gradient plasticity effects in whisker–reinforced metals. Journal of the Mechanics and Physics of Solids 51 (10), 1863–1883.
Niordson, C.F., Legarth, B.N., 2010. Strain gradient effecits on cyclic plasticity. Journal of the Mechanics and Physics of Solids 58, 542–557.
Niordson, C.F., Tvergaard, V., 2001. Nonlocal plasticity effects on the tensile properties of a metal matrix composite. European Journal of Mechanics – A/Solids 20 (4), 601–613.
Niordson, C.F., Tvergaard, V., 2002. Nonlocal plasticity effects on fibre debonding in a whisker–reinforced metal. European Journal of Mechanics – A/Solids 21 (2), 239–248.
Niordson, C.F., Tvergaard, V., 2007. Size-effects in porous metals. Materials Science and Engineering 15, 51–60.
Seifert, T., Schmidt, I., 2009. Plastic yielding in cyclically loaded porous materials. International Journal of Plasticity 25 (12), 2435–2453.
Shu, J.Y., Barlow, C.Y., 2000. Strain gradient effects on microscopic strain field in a metal matrix composite. International Journal of Plasticity 16, 563–591.
Stölken, J.S., Evans, A.G., 1998. A microbend test method for measuring the plasticity length scale. Acta Materialia 46 (14), 5109–5115.
Swadener, J.G., George, E.P., Pharr, G.M., 2002. The correlation of the indentation size effect measured with indenters of various shapes. Journal of the Mechanics and Physics of Solids 50, 681–694.
Terada, K., Hori, M., Kyoya, T., Kikuchi, N., 2000. Simulation of the multi-scale convergence in computational homogenization approaches. Journal of Solids and Structures 37, 2285–2311.
Tvergaard, V., 1990. Effect of fibre debonding in a whisker–reinforced metal. Materials Science and Engineering A125, 203–213.
Tvergaard, V., 1995. Fibre debonding and breakage in a whisker–reinforced metal. Materials Science and Engineering A190, 215–222.
Wang, J., Lian, J., Greer, J.R., Nix, W.D., Kim, K.-S., 2006. Size effect in contact compression of nano- and microscale pyramid structures. Acta Materialia 54 (15), 3973–3982.
Yan, Y., Geng, L., Li, A., 2007. Experimental and numerical studies of the effect of particle size on the deformation behavior of the metal matrix composites. Materials Science and Engineering 448, 315–325.

Publication [P4]

On homogenization of metal matrix composites using strain gradient theory

On homogenization of metal matrix composites using strain gradient plasticity

Reza Azizi*, Christian F. Niordson, Brian N. Legarth

Department of Mechanical Engineering, Solid Mechanics, Technical University of Denmark, DK-2800 Kgs. Lyngby, Denmark

Abstract

The homogenized response of Metal Matrix Composites (MMCs) is studied using strain gradient plasticity. The material model employed is a rate independent formulation of energetic strain gradient plasticity at the micro scale and conventional rate independent plasticity at the macro scale. Free energy inside the micro structure is included due to the elastic strains and plastic strain gradients. A unit cell containing a circular elastic fiber is analyzed under macroscopic simple shear in addition to transverse and longitudinal loading. The analyses are carried out under generalized plane strain condition. Micro-Macro homogenization is performed observing the Hill-Mandel energy condition, and overall loading is considered such that the homogenized higher order terms vanish. The results highlight the intrinsic size-effects as well as the effect of fiber volume fraction on the overall response curves, plastic strain distributions and homogenized yield surfaces under different loading conditions. It is concluded that composites with smaller reinforcement size have larger initial yield surfaces and furthermore, they exhibit more kinematic hardening.

Keywords: Metal matrix composite, strain gradient plasticity, homogenization, size-effects

*Corresponding Author

Email addresses: reaz@mek.dtu.dk (Reza Azizi*), cn@mek.dtu.dk (Christian F. Niordson), bnl@mek.dtu.dk (Brian N. Legarth)

1. Introduction

Metal Matrix Composites (MMC) comprised of hard elastic fibers in a ductile metal matrix introduce a class of materials which are desirable in many applications. High termostability and high stiffness with low weight are recognized characters of MMC together with deficiencies like low ductility and fracture toughness (see McDanels, 1985).

A conventional modeling approach for evaluating the mechanical behavior of MMC has been considered by several authors including Tvergaard (1990), Bao et al. (1991), Tvergaard (1995), Legarth (2003) and Legarth and Kuroda (2004). Research on the intrinsic size-effect in MMC with micron scale fibers has been carried out starting with the experimental study by Lloyd (1994), who showed that the response of composites, with the same volume fraction of SiC particles, depends on the size of the particles, with smaller being stiffer. Mughrabi (2001), Fleck et al. (2003) and Gao and Huang (2003) showed that in MMC, dislocations can not pass from the matrix into the fiber and consequently pile up at the interface leading to plastic strain suppression at the interfaces. Investigations by a number of authors, e.g. Hutchinson (2000) have shown in some generality, that for problems with lengths falling in the range from roughly a fraction of a micron to tens of microns a size-effect exists which conventional plasticity cannot capture.

Strain gradient plasticity theories have been developed to model such size-effects, through incorporation of constitutive material length parameters and even use of non-conventional stress and strain terms. While some of these are of lower-order nature retaining the structure of conventional boundary value problems (see Acharya and Bassani, 2000; Bassani, 2001), most of the proposed theories are of higher order nature, employing higher order stress-measures as work-conjugates to strain gradients, thus demanding non-conventional higher order boundary conditions (e.g. Fleck and Hutchinson, 1997, 2001; Gao et al., 1999; Gurtin, 2002; Gudmundson, 2004; Gurtin and Anand, 2005; Lele and Anand, 2008; Fleck and Willis, 2009a,b).

In this paper, the energetic higher order strain gradient plasticity proposed by Gudmundson (2004) is used at the micro scale while a conventional homogenized response at the macro scale is sought. Different homogenization techniques have been proposed to estimate the overall macroscopic properties like effective medium approximation by Eshelby (1957) and Budiansky (1965), the self consistent method by Hill (1965) and variational bounding methods by Hashin (1983). Here, a computational unit cell method is em-

ployed. Within this context several homogenization approaches have been proposed (see Hashin and Shtrikman, 1963; Suquet, 1985; Keller et al., 1990; Ghosh et al., 1995; Terada et al., 2000; Wieckowski, 2000; Kouznetsova et al., 2001). Niordson and Tvergaard (2001), Niordson and Tvergaard (2002) and Niordson (2003) used strain gradient plasticity theory to model the matrix material in order to predict the particle size dependent overall properties of metal matrix composites. Kouznetsova et al. (2004) developed second order computational homogenization, where the higher order stress conjugate to the full strain gradient tensor is available at the macro scale, while using a conventional model at the micro scale.

In the present paper, a study of a metallic matrix with long parallel fibers is presented. The Hill-Mandel energy condition (Hill, 1963) is considered under the assumption that the material at the micro scale is gradient dependent, while at the macro scale it is conventional. This restricts considerations to macroscopically homogeneous deformation with periodic boundary conditions imposed on the unit cell for both the displacements and the plastic strain fields.

Our previous work, Azizi et al. (2011), is extended now also modeling the macroscopic simple shear in addition to transverse and longitudinal loading. Results on the overall response curves as well as energy apportionment in elastic, plastic and higher order parts are shown in addition to plastic strain and higher order stress distributions. Using an engineering definition for the onset of macro plasticity, the shapes of the macroscopic initial and subsequent yield surfaces are investigated for the strain gradient plasticity model as well as a conventional plasticity model. It is shown that the material length scale and fiber volume fraction tend to expand the macroscopic initial yield surface and increase the macroscopic kinematic hardening.

2. Material model

The fibers are modeled as isotropic elastic with Young's modulus, E_f, and Poisson's ratio, ν_f. The matrix is governed by a rate independent isotropic gradient enhanced elasto-plastic material model, in which gradient contributions to the free energy are accounted for, as laid out by Gudmundson (2004). The internal virtual work for the volume of the unit cell containing fiber-matrix interfaces is written as

$$\delta w_i = \int_v [\sigma_{ij}\delta\epsilon_{ij} + (q_{ij} - s_{ij})\delta\epsilon^p_{ij} + m_{ijk}\delta\epsilon^p_{ij,k}]dv + \int_{s^I} M^I_{ij}\delta(\epsilon^p_{ij})^I ds^I \quad (1)$$

where v is the volume of the unit cell, s^I is the surface of the fiber-matrix interfaces, σ_{ij} is the Cauchy stress tensor with $s_{ij} = \sigma_{ij} - \frac{1}{3}\delta_{ij}\sigma_{kk}$ denoting the stress deviator. The total strain, ϵ_{ij}, is the summation of the plastic strain, ϵ^p_{ij}, and elastic strain, ϵ^e_{ij}, and $\epsilon^p_{ij,k}$ is the gradient of plastic strain. The micro stress, q_{ij}, and the higher order stress, m_{ijk}, are work conjugate to the plastic strain and the gradient of plastic strain, respectively. The higher order traction at the interface, M^I_{ij}, is work-conjugate to the plastic strain at the interface, $(\epsilon^p_{ij})^I$. By application of Gauss' theorem we obtain

$$\delta w_i = \int_s [\sigma_{ij}n_j\delta u_i + m_{ijk}n_k\delta\epsilon^p_{ij}]ds + \int_{s^I} M^I_{ij}\delta(\epsilon^p_{ij})^I ds^I - \int_v [\sigma_{ij,j}\delta u_i + (m_{ijk,k} + s_{ij} - q_{ij})\delta\epsilon^p_{ij}]dv \quad (2)$$

where s is the surface of the unit cell, n is the outward unit vector normal to the surface, s. The conventional traction, $T_i = \sigma_{ij}n_j$, is work-conjugate to the displacement, u_i. From Eq. (2) two sets of equilibrium equation and a surface condition can be extracted as

$$\begin{aligned} \sigma_{ij,j} &= 0, && \texttt{in} && v \\ m_{ijk,k} + s_{ij} - q_{ij} &= 0, && \texttt{in} && v \\ M^I_{ij} + m_{ijk}p_k &= 0 && \texttt{on} && s^I \end{aligned} \quad (3)$$

where p_k denotes the outward unit normal to the fiber-matrix interfaces, s^I.

The free energy in the present formulation, $\psi = \psi(\epsilon^e_{ij}, \epsilon^p_{ij,k})$, is assumed to depend on the elastic strain and the plastic strain gradient. This implies that the work due to the plastic strain gradients, $m_{ijk}\dot{\epsilon}^p_{ij,k}$, is stored and the dissipation rate is given by $q_{ij}\dot{\epsilon}^p_{ij}$. The free energy is taken according to Fredriksson et al. (2009) as

$$\psi\left(\epsilon^e_{ij}, \epsilon^p_{ij}\right) = \frac{1}{2}D_{ijkl}\epsilon^e_{ij}\epsilon^e_{kl} + \frac{1}{2}GL^2_*\epsilon^p_{ij,k}\epsilon^p_{ij,k} \quad (4)$$

where L_* is a material length scale parameter, G is the elastic shear modulus and D_{ijkl} is the isotropic tensor of elastic moduli, defined in terms of

Young's modulus, E_m, and Poisson's ratio, ν_m, of the matrix. The Cauchy and moment stresses can be extracted by derivation of the free energy with respect to the elastic strain and the gradient of plastic strain,

$$\sigma_{ij} = \frac{\partial \psi}{\partial \epsilon^e_{ij}} = D_{ijkl}\epsilon^e_{kl}, \quad m_{ijk} = \frac{\partial \psi}{\partial \epsilon^p_{ij,k}} = GL_*^2 \epsilon^p_{ij,k} \tag{5}$$

The yield surface, f, depends on the micro stress, q_{ij}, through

$$f\left(q_{ij}, \sigma_f\right) = \sqrt{\frac{3}{2} q_{ij} q_{ij}} - \sigma_f = 0 \tag{6}$$

where the flow stress is given by the linear hardening relation, $\sigma_f = \sigma_y + H\epsilon^p_e$, with σ_y denoting the initial yield stress, H denoting the hardening modulus and ϵ^p_e denoting the accumulated effective plastic strain defined as $\epsilon^p_e = \int \dot{\epsilon}^p_e d\tau$ where τ is "pseudo-time" and $\dot{\epsilon}^p_e = \sqrt{\frac{2}{3}\dot{\epsilon}^p_{ij}\dot{\epsilon}^p_{ij}}$.

The flow rule which enforces normality of the plastic strain increment to the flow surface is given by

$$\dot{\epsilon}^p_{ij} = \dot{\lambda}\frac{\partial f}{\partial q_{ij}} = \frac{3}{2}\frac{q_{ij}}{q_e}\dot{\epsilon}^p_e = r_{ij}\dot{\epsilon}^p_e \tag{7}$$

where $\dot{\lambda}$ is the plastic multiplier, $q_e = \sqrt{\frac{3}{2} q_{ij} q_{ij}}$ is the effective micro stress, and $r_{ij} = \frac{3}{2}\frac{q_{ij}}{q_e}$ is the direction of the plastic strain increment. For the numerical implementation, an expression for $\dot{q}_{ij}$ ensuring the coaxiality between q_{ij} and $\dot{\epsilon}^p_{ij}$ has to be established. The evolution law for the micro stress is obtained by considering $r_{ij} = \frac{3}{2}\frac{q_{ij}}{q_e}$ or equivalently $q_{ij} = \frac{2}{3} q_e r_{ij}$. The incremental micro stress can be written as

$$\dot{q}_{ij} = \dot{\overline{\frac{2}{3} q_e r_{ij}}} = \frac{2}{3}\left(\dot{q}_e r_{ij} + q_e \dot{r}_{ij}\right) \tag{8}$$

where $\dot{q}_e = H\dot{\epsilon}^p_e$. Using $\dot{\epsilon}^p_e = \frac{2}{3} r_{ij}\dot{\epsilon}^p_{ij}$ and inserting into Eq. (8), we get

$$\dot{q}_{ij} = \frac{2}{3}\left(\dot{q}_e r_{ij} + q_e \dot{r}_{ij}\right) = \frac{2}{3}\left(\frac{2}{3} H r_{ij} r_{kl}\dot{\epsilon}^p_{kl} + q_e \dot{r}_{ij}\right) \tag{9}$$

The last term on the right hand side of the above equation depends on $\dot{q}_{ij}$ through $\dot{r}_{ij}$. Since this relation does not give $\dot{q}_{ij}$ explicitly, it can not be

readily used in the constitutive framework. The last term defines the part of $\dot{q}_{ij}$ tangent to the yield surface, and the first term defines the part of $\dot{q}_{ij}$ normal to the yield surface. The correct magnitude of $\dot{\epsilon}^p_{ij}$ is obtained from the first term alone and the second term has the sole function of ensuring co-coaxiality between q_{ij} and $\dot{\epsilon}^p_{ij}$. Therefore, the second term is removed and replaced by a penalty term ensuring normality of the plastic strain increment to the yield surface as proposed by Fredriksson et al. (2009). The penalty term is expressed as

$$E_0 \left(\dot{\epsilon}^p_{ij} - \frac{2}{3} r_{ij} r_{kl} \dot{\epsilon}^p_{kl} \right) \tag{10}$$

where the penalty factor, E_0, has to be large compared to the hardening modulus, H. Hence, the flow rule for the micro stress can be rewritten as

$$\dot{q}_{ij} = \frac{2}{3} \left(\frac{2}{3}(H - E_0) r_{ij} r_{kl} + E_0 \delta_{ik} \delta_{jl} \right) \dot{\epsilon}^p_{kl} \tag{11}$$

thus, penalizing any component of the plastic strain increment tangent to the yield surface. Fig. 1 shows a schematic plot of the current and subsequent yield surfaces including the directions.

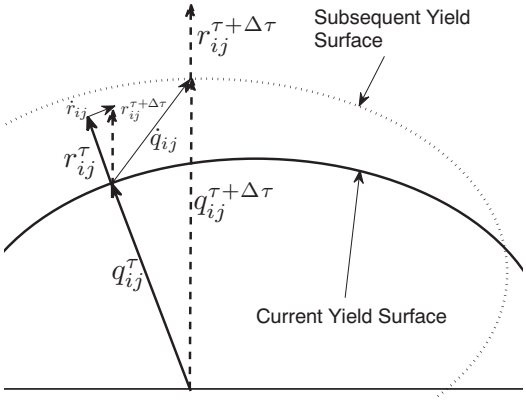

Figure 1: A schematic plot of the current and subsequent yield surfaces.

The incremental version of the constitutive equations is completed by considering the incremental Cauchy stress and higher order stress as

$$\dot{\sigma}_{ij} = D_{ijkl} \dot{\epsilon}^e_{kl} \tag{12}$$

$$\dot{m}_{ijk} = GL_*^2 \dot{\epsilon}^p_{ij,k} \tag{13}$$

3. Homogenization and macroscopic yield criterion

At the micro scale, the matrix material is governed by strain gradient plasticity, while at the macro scale conventional material response is sought. To link the scales, micro-macro homogenization is established based on the Hill-Mandel energy condition, which ensures that the work expended at the micro scale equals that of the macro scale, see Hill (1963) and Suquet (1985). It will be shown that this reduction of the strain gradient dependent material at the micro scale to the conventional response at the macro scale sets limits to the kind of boundary conditions that must be imposed on the unit cell.

Kinematic variables representing the deformation at the various scales are now introduced. The displacement of a material point, X_i, in the undeformed state to a point, x_i, in the deformed state is defined as $x_i = X_i + U_i$, where U_i is the macroscopic displacement vector. Considering a macroscopic homogeneous deformation state, the displacement field can be expressed by the first term in the Taylor expansion about any point, X_i^0, as

$$U_i = (U_i)_{X_i^0} + \left(\frac{\partial U_i}{\partial X_j}\right)_{X_i^0} (X_j - X_j^0) \tag{14}$$

where $\frac{\partial U_i}{\partial X_j}$ is the macroscopic displacement gradient. The microscopic displacement, u_i, is then defined in terms of the macroscopic displacement, U_i, and a microstructural fluctuation field, w_i, as follows

$$u_i = U_i + w_i \tag{15}$$

Introducing the macroscopic strain tensor, $E_{ij} = \frac{1}{2}\left(\frac{\partial U_i}{\partial X_j} + \frac{\partial U_j}{\partial X_i}\right)_{X_i^0}$, and rotation tensor, $R_{ij} = \frac{1}{2}\left(\frac{\partial U_i}{\partial X_j} - \frac{\partial U_j}{\partial X_i}\right)_{X_i^0}$, Eq. (15) can be expressed as

$$u_i = (U_i)_{X_i^0} + (E_{ij} + R_{ij})(X_j - X_j^0) + w_i \tag{16}$$

Defining the microscopic strain tensor by $\epsilon_{ij} = \frac{1}{2}\left(\frac{\partial u_i}{\partial X_j} + \frac{\partial u_j}{\partial X_i}\right)$ and evaluating the volume average, we obtain

$$\frac{1}{v}\int_v \epsilon_{ij} dv = E_{ij} + \frac{1}{2v}\int_v \left(\frac{\partial w_i}{\partial X_j} + \frac{\partial w_j}{\partial X_i}\right) dv \tag{17}$$

Under the assumption of periodic displacement boundary conditions, the last term in Eq. (17) vanishes upon application of Gauss' theorem. Hence, we conclude that the macroscopic strain equals the volume average of microscopic strain as

$$E_{ij} = \frac{1}{v}\int_v \epsilon_{ij} dv \tag{18}$$

The Hill-Mandel energy condition is used to extract the appropriate macroscopic work-conjugate to the macroscopic strain. The microscopic volume average of the variation of the work performed on the unit cell is assumed to be equal to the variation of the internal work at the macro scale as expressed by

$$\frac{1}{v}\int_v [\sigma_{ij}\delta\epsilon_{ij} + (q_{ij} - s_{ij})\delta\epsilon^p_{ij} + m_{ijk}\delta\epsilon^p_{ij,k}]dv + \frac{1}{v}\int_{s^I} M^I_{ij}\delta(\epsilon^p_{ij})^I ds^I = \Sigma_{ij}\delta E_{ij} \tag{19}$$

Using Gauss theorem and the equilibrium equations, Eq. (3), we obtain

$$\frac{1}{v}\int_s [\sigma_{ij}n_j\delta u_i + m_{ijk}n_k\delta\epsilon^p_{ij}]ds + \frac{1}{v}\int_{s^I} M^I_{ij}\delta(\epsilon^p_{ij})^I ds^I = \Sigma_{ij}\delta E_{ij} \tag{20}$$

Taking the variation of Eq. (16), $\delta u_i = (\delta E_{ij} + \delta R_{ij})\, X_j + \delta w_i$, and inserting it in Eq. (20), we get

$$\begin{aligned}\frac{1}{v}\int_s \sigma_{ij}n_j X_k ds\delta E_{ik} + \frac{1}{v}\int_s \sigma_{ij}n_j X_k ds\delta R_{ik} + \frac{1}{v}\int_s \sigma_{ij}n_j\delta w_i ds + \\ \frac{1}{v}\int_s m_{ijk}n_k\delta\epsilon^p_{ij}ds + \frac{1}{v}\int_{s^I} M^I_{ij}\delta\epsilon^{pI}_{ij}ds^I = \Sigma_{ij}\delta E_{ij}\end{aligned} \tag{21}$$

The second term of the above equation vanishes upon application of Gauss' theorem and equilibrium, since R_{ik} is skew-symmetric. Under the assumption of periodic boundary conditions for the unit cell, the third and fourth term vanish:

$$\frac{1}{v}\int_s \sigma_{ij}n_j\delta w_i ds = \quad \tfrac{1}{v}\textstyle\int_s T_i\delta w_i ds = 0 \tag{22}$$

$$\frac{1}{v}\int_s m_{ijk}n_k\delta\epsilon^p_{ij}ds = \quad \tfrac{1}{v}\textstyle\int_s M_{ij}\delta\epsilon^p_{ij}ds = 0 \tag{23}$$

where $T_i = \sigma_{ij}n_j$ and $M_{ij} = m_{ijk}n_k$ are traction and higher order traction on the surface of the unit cell. Assuming that we have no plasticity on the

fiber matrix interface ($\epsilon_{ij}^{pI} = 0$), the fifth term also disappears.

$$\frac{1}{v}\int_{s^I} M_{ij}^I \delta\epsilon_{ij}^{pI} ds^I = 0 \tag{24}$$

Hence, the macroscopic stress which is work conjugate to E_{ij}, is obtained from

$$\left[\frac{1}{v}\int_s \sigma_{ij} n_j X_k ds\right] \delta E_{ik} = \Sigma_{ik}\delta E_{ik} \tag{25}$$

Using Gauss' theorem and the equilibrium, we can express the macroscopic stress as the volume average of microscopic stress

$$\Sigma_{ij} = \frac{1}{v}\int_v \sigma_{ij} dv \tag{26}$$

A strain based yield criterion at the macro scale is used where an overall effective plastic strain (here calculated as the 2-norm) exceeds some threshold value, ϵ_t, according to

$$\left|E_{ij} - C_{ijkl}^{-1}\Sigma_{kl} - E_{ij}^{res}\right| \geq \epsilon_t \tag{27}$$

where the overall macroscopic tensor of elastic moduli, C_{ijkl}, is defined according to the numerical differentiation of the macroscopic quantities as

$$C_{ijkl} = \frac{\partial\Sigma_{ij}}{\partial E_{kl}} = \frac{\Sigma_{ij}^{\tau+\Delta\tau} - \Sigma_{ij}^{\tau}}{E_{kl}^{\tau+\Delta\tau} - E_{kl}^{\tau}} \tag{28}$$

Here, τ is the pseudo time when the entire unit cell is in the elastic regime and E_{ij}^{res} is the macroscopic residual strains. Note that the residual strain is zero for initial yielding.

Macroscopic yield surfaces will be presented in $(\Sigma_{11}, \Sigma_{22})$, $(\Sigma_{11}, \Sigma_{33})$ and $(\Sigma_{11}, \Sigma_{12})$ stress coordinate systems. To find the yield surfaces, proportionality of the macroscopic stresses is imposed such that

$$\kappa_1 = \frac{\Sigma_{22}}{\Sigma_{11}}, \qquad \kappa_2 = \frac{\Sigma_{33}}{\Sigma_{11}} \qquad \text{and} \qquad \kappa_3 = \frac{\Sigma_{12}}{\Sigma_{11}} \tag{29}$$

are constant for any single analysis. Details on the numerical implementation are found in Azizi et al. (2011).

4. Problem Formulation

MMC with parallel circular fibers distributed through the entire structure has been considered (see Fig. 2a). Loading including both macroscopic tri-axial normal stress under generalized plane strain condition and in-plane shear stress (excluding out-of-plane shear stresses) are studied. A unit cell is extracted as shown in Fig. 2(b), where both macroscopic normal stresses and in-plane shear stress are indicated. At the left-bottom corner of the unit cell a reference Cartesian coordinate system, x_i, is located and aligned with the sides of the cell. The positive direction of the third axis, x_3, points out of (x_1, x_2)-plane. Fig. 2(c) shows the displacement boundary conditions and the dimensions of the unit cell. The radius of the fibers is denoted by r, the dimensions of the unit cell in the direction of the coordinate axes (perpendicular to the fiber direction) are denoted by a and b, while the thickness of the unit cell is denoted by t.

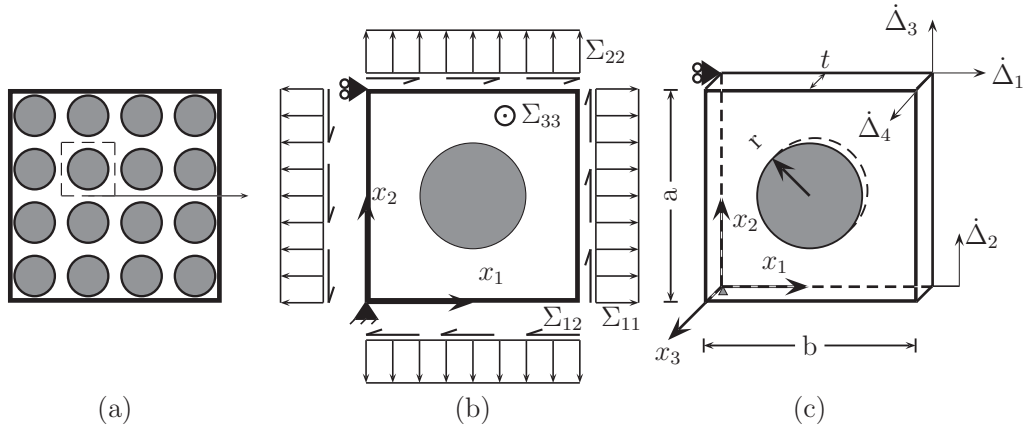

Figure 2: (a) Regular distribution of fibers in the composite. (b) Unit cell containing one fiber with traction boundary condition. (c) Unit cell containing one fiber with conventional displacement boundary conditions used in numerical simulation representing combined biaxial shear loading as shown in (*b*).

Fibers are considered to be purely elastic whereas the matrix exhibits an elasto-plastic behavior with gradients effects as described in Section 2. Since plastic strain-gradients are of higher order nature, higher-order boundary conditions must be prescribed in addition to the conventional conditions on

displacements and surface tractions. At the exterior of the cell periodic boundary conditions are used, see also Borg et al. (see 2008); Hussein et al. (see 2008),

$$\begin{array}{llll} \dot{u}_1^b = \dot{u}_1^t & \text{and} & \dot{u}_2^b = \dot{u}_2^t - [\dot{\Delta}_3 - \dot{\Delta}_2] \\ \dot{T}_1^b = -\dot{T}_1^t & \text{and} & \dot{T}_2^b = -\dot{T}_2^t \\ \dot{u}_1^l = \dot{u}_1^r - \dot{\Delta}_1 & \text{and} & \dot{u}_2^l = \dot{u}_2^r - \dot{\Delta}_2 \\ \dot{T}_1^r = -\dot{T}_1^l & \text{and} & \dot{T}_2^r = -\dot{T}_2^l \\ \dot{M}_{ij}^b = -\dot{M}_{ij}^t & \text{and} & \dot{M}_{ij}^r = -\dot{M}_{ij}^l \\ [\dot{\epsilon}_{ij}^p]^b = [\dot{\epsilon}_{ij}^p]^t & \text{and} & [\dot{\epsilon}_{ij}^p]^r = [\dot{\epsilon}_{ij}^p]^l \end{array} \tag{30}$$

In the above equations the super-scripts b, t, l and r refer to bottom, top, left and right of the unit cell, respectively. In addition to the periodic boundary condition on the displacements, tractions, plastic strains and higher order tractions, the following conditions are also imposed

$$\begin{array}{lll} \dot{u}_1 = \dot{u}_2 = 0, & \text{at} & (x_1, x_2) = (0, 0) \\ \dot{u}_2 = \dot{\Delta}_2, & \text{at} & (x_1, x_2) = (a, 0) \\ \dot{u}_1 = \dot{\Delta}_1,\ \dot{u}_2 = \dot{\Delta}_3, & \text{at} & (x_1, x_2) = (a, b) \\ \dot{u}_3 = 0 & \text{at} & x_3 = 0 \\ \dot{u}_3 = \dot{\Delta}_4 & \text{at} & x_3 = t \\ \dot{\epsilon}_{ij}^p = 0, & \text{at} & (x_1^2 + x_2^2 = r^2) \end{array} \tag{31}$$

where $\dot{\Delta}_1$, $\dot{\Delta}_2$, $\dot{\Delta}_3$ and $\dot{\Delta}_4$ are prescribed displacement increment quantities. The out-of-plane plastic strain, ϵ_{33}^p, is given in terms of in-plane plastic strain components by plastic incompressibility, $\epsilon_{ii}^p = 0$. Similarly, M_{33} is given in terms of the in-plane components M_{11} and M_{22} where $M_{ii} = 0$. Finally, out-of-plane deformation is controlled by specifying a constant out-of-plane normal strain increment, $\dot{\epsilon}_{33} = \dot{\Delta}_4/t$, with t denoting the reference thickness of the unit cell. In summary, the problem in its general form has one material length parameter, L_*, and four geometrical length parameters, $[a, b, r, t]$ in addition to the conventional material parameters.

5. Numerical implementation

For the purpose of numerical implementation, the incremental version of the principle of virtual work is used as

$$\int_v [\dot{\sigma}_{ij}\delta\dot{\epsilon}_{ij} + (\dot{q}_{ij} - \dot{s}_{ij})\delta\dot{\epsilon}^p_{ij} + \dot{m}_{ijk}\delta\dot{\epsilon}^p_{ij,k}]dv + \int_{s^I} \dot{M}^I_{ij}\delta(\dot{\epsilon}^p_{ij})^I ds^I = \int_s [\dot{T}_i\delta\dot{u}_i + \dot{M}_{ij}\delta\dot{\epsilon}^p_{ij}]ds, \tag{32}$$

where $\dot{T}_i$ and $\dot{M}_{ij}$ are traction increments and moment traction increments, respectively. Quadrilateral elements with eight nodes are used for in-plane displacement interpolation, while bilinear four node elements are used to interpolate the plastic strain components. Considering both elements at the same time, each corner node has five degrees of freedom (two for displacements and three for plastic strains) and each middle node has two degrees of freedom for displacement. Moreover, an extra degree of freedom is added for the entire elements to control the thickness of the unit cell. Nodal interpolation is defined according to

$$\dot{u}_i = \sum_{n=1}^{2k} N^n_i \dot{U}_n, \quad \dot{\epsilon}^p_{ij} = \sum_{m=1}^{3l} P^m_{ij}\dot{\epsilon}^p_m \tag{33}$$

where N^n_i and P^m_{ij} are shape functions for the displacements and plastic strain components, respectively, and k and l are the number of nodes used for the different interpolation schemes, see Appendix. A. The appropriate derivatives of the displacement field and the plastic strain field can be expressed as

$$\dot{\epsilon}_{ij} = \sum_{n=1}^{2k} B^n_{ij}\dot{U}_n, \quad \dot{\epsilon}^p_{ij,k} = \sum_{m=1}^{3l} Q^m_{ijk}\dot{\epsilon}^p_m \tag{34}$$

where, $B^n_{ij} = (N^n_{i,j} + N^n_{j,1})/2$ and $Q^m_{ijk} = P^m_{ij,k}$, (see Appendix A). The discretized equation obtained from the principle of virtual work is

$$\begin{bmatrix} \mathbf{K}_u & -\mathbf{K}_{up} \\ -\mathbf{K}^T_{up} & \mathbf{K}_p \end{bmatrix} \begin{bmatrix} \dot{\mathbf{U}} \\ \dot{\boldsymbol{\epsilon}}^p \end{bmatrix} = \begin{bmatrix} \dot{\mathbf{f}}_u \\ \dot{\mathbf{f}}_p \end{bmatrix} \tag{35}$$

where $\dot{\mathbf{f}}_u = \int_s \mathbf{N}^T\dot{\mathbf{T}}ds$ is incremental nodal force vector and $\dot{\mathbf{f}}_p = \int_s \mathbf{P}^T\dot{\mathbf{M}}ds$ is the incremental higher order nodal force. Stiffness matrices are given by

$$\mathbf{K}_u = \int_v \mathbf{B}^T\mathbf{D}_e\mathbf{B}dv \tag{36}$$

$$\mathbf{K}_p = \int_v [\mathbf{P}^T(\mathbf{D}_e + \mathbf{D}_p)\mathbf{P} + \mathbf{Q}^T\mathbf{D}_h\mathbf{Q}]dv \tag{37}$$

$$\mathbf{K}_{up} = \int_v \mathbf{B}^T \mathbf{D}_e \mathbf{P} dv \tag{38}$$

where $\mathbf{D}_e$ is the isotropic elastic moduli, $\mathbf{D}_p$ is the plastic moduli and $\mathbf{D}_h$ is higher order moduli defined by

$$\mathbf{D}_e = \frac{E}{(1+\upsilon)(1-2\upsilon)} \begin{bmatrix} 1-\upsilon & \upsilon & \upsilon & 0 \\ \upsilon & 1-\upsilon & \upsilon & 0 \\ \upsilon & \upsilon & 1-\upsilon & 0 \\ 0 & 0 & 0 & \frac{1-2\upsilon}{2} \end{bmatrix} \tag{39}$$

$$\mathbf{D}_p = \frac{2}{3}\left(\frac{2}{3}(H - E_0)\mathbf{r}\mathbf{r}^T + E_0 \mathbf{I}_p\right) \tag{40}$$

$$\mathbf{D}_h = G L_*^2 \boldsymbol{I} \tag{41}$$

where E_0 is the penalty factor, G is the shear modulus, $\boldsymbol{I}_{(8\times 8)}$ is the identity matrix, $\boldsymbol{I}_p$=diag(1 1 1 1/2) and $\mathbf{r} = (r_{11}, r_{22}, r_{33}, r_{12})^T$. The values of Young's modulus and Poisson's ratio are taken as the relevant values for the fiber or matrix in the corresponding elements.

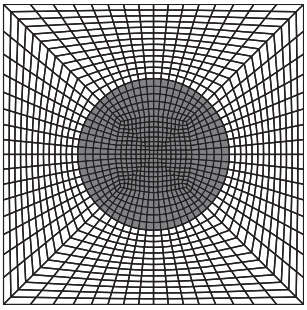

Figure 3: An example of finite element mesh used in the numerical computation.

Fig. 3 shows an example of the finite element mesh with 1408 elements used in numerical computations. Numerical integration is performed using the forward Euler method with sufficiently small load increments, so that convergence is assured. To avoid plastic flow in the elastic regime, the plastic stiffness is chosen to be large as suggested by Fredriksson et al. (2009). However, in the limit of conventional plasticity this would lead to an artificial boundary layer effect with a width scaling with the element size. Hence,

when using the computational method in the conventional limit, the plastic stiffness matrix has instead been defined by $\mathbf{K}_p = 10^{-8} E_m \boldsymbol{I}_{(12\times12)}$ and the coupling matrix $\mathbf{K}_{up} = \mathbf{0}$ for elastic integration points. Plastic strain quantities are only updated in integration points that are in the plastic regime.

6. Results

The conventional material parameters used for the matrix are $H/E_m = 0.01$ and 0.1, $\epsilon_y = \sigma_y/E_m = 0.004$, $\upsilon_m = 0.3$, and for the fibers, $E_f = 5.7E_m$ and $\upsilon_f = 0.17$. The penalty factor is taken to be $E_0 = 1000H$ for the case of simple shear and $E_0 = 100H$ for the case of uniaxial loadings due to numerical stability. The unit cell is taken to be quadratic ($a = b$). For both loading and reloading, $\dot{\Delta}_i = \frac{h}{2}\epsilon_y \dot{\Gamma}$ is considered in which $\dot{\Gamma} = 0.02$. Each numerical computation includes 1408 elements with 300 increments at each step of loading, unloading and reloading.

Lloyd (1994) showed that the response of composites with the same volume fraction of SiC particles depends on the size of the particles. Investigations by a number of authors, e.g. Hutchinson (2000) have shown that for problems with lengths falling in the range from roughly a fraction of a micron to ten microns a size-effect exists but conventional plasticity cannot capture it, and it was shown that the material length scale for metals is in the range of $0.25\mu m$ to $1\mu m$ for a slightly different but related model. For a micron scale length parameter of $L = 1\mu m$ in the present model, we analyze cases for $L_*/r = 0$, $L_*/r = 0.2$ and $L_*/r = 0.4$ which corresponds to large fibers, fibers with $r = 5\mu m$ and $r = 2.5\mu m$, respectively.

6.1. Simple shear

For simple shear, all values of κ is set to zero except for $\kappa_3 = 1000$. This value ensures that the macro shear stress, Σ_{12}, is large compared to Σ_{11} and other components of the macro stresses are small such that it is very close to pure shear loading.

	$L_*/r = 0$	$L_*/r = 0.2$	$L_*/r = 0.4$
A_{12}/σ_y	0.007	0.017	0.120

Table 1: Bauschinger stress in the composite for simple shear loading, $\kappa_1 = \kappa_2 = 0$ and $\kappa_3 = 1000$, with $V_f = 0.2$ and $H/E_m = 0.1$, see Fig. 4.

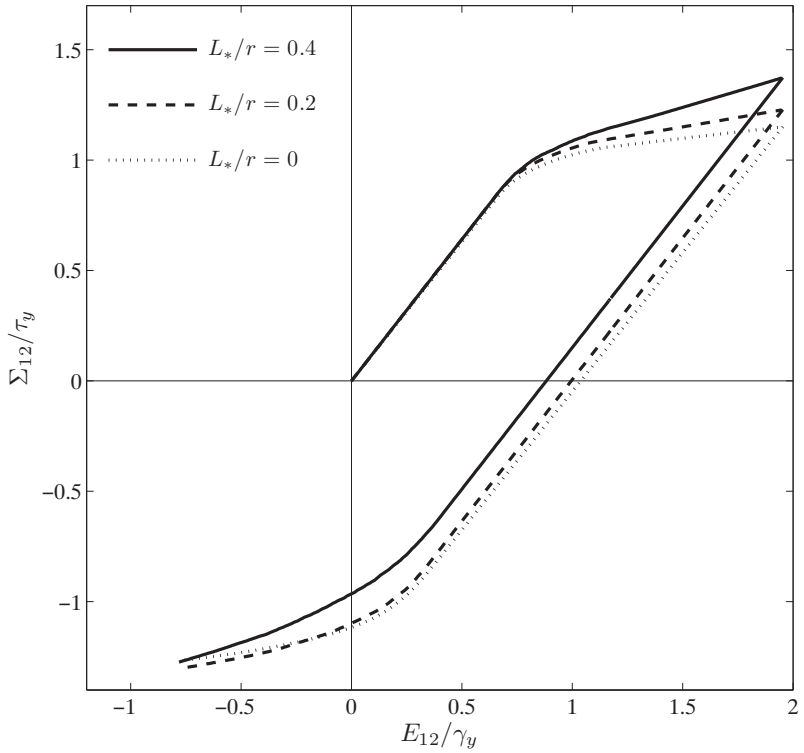

Figure 4: Effect of the material length scale, L_*/r, on the homogenized stress strain curve for simple shear, $\kappa_1 = \kappa_2 = 0$ and $\kappa_3 = 1000$, with $V_f = 0.2$ and $H/E_m = 0.1$.

Fig. 4 shows the effect of the constitutive length scale of the matrix material, L_*/r, on the homogenized stress-strain curve with $V_f = \frac{\pi r^2}{a^2} = 0.2$ and $H/E_m = 0.1$. Initial loading and subsequent reloading is studied where the maximum shear strain is given by $E_{12}/\gamma_y = 1.94$, $\gamma_y = \tau_y/G$ with $\tau_y = \sigma_y/\sqrt{3}$, at which the load is reversed until a compressive macroscopic shear strain of $E_{12}/\gamma_y = 0.78$ is reached. The result shows that the overall hardening of the composite increases with smaller particle sizes (higher length scale). Bauschinger stress is defined according to, (see Taya et al., 1990),

$$A_{ij} = (\Sigma^f_{ij} + \Sigma^{syp}_{ij})/2 \tag{42}$$

where Σ^f_{ij} is the stress at the end of loading and Σ^{syp}_{ij} is subsequent yield stress

during the reloading. Tab. 1 shows the values of the Bauschinger stress for different particle sizes. As can be seen, the Bauschinger stress increases with decreasing particle size. A similar trend is observed in pure shear between rigid platens by Anand et al. (2005) and Niordson and Legarth (2010).
In Fig. 5 the effect of the fiber volume fraction, V_f, on the homogenized stress-strain curve with $L_*/r = 0.4$ and $H/E_m = 0.1$ is shown. It is seen that higher fiber volume fraction increases the shear modulus significantly and the yield point moderately in accordance to findings by Choi and Jang (2011). After yielding, a significant enhancement of the hardening is observed. Upon load reversal, the Bauschinger stress is calculated and presented in Tab. 2, from which it is seen that the Bauschinger stress increases with the higher fiber volume fraction. This behavior has also been reported by Barai and Weng (2011), where it was found to be in accordance with experimental data of Kim et al. (2006).

	$V_f = 0.1$	$V_f = 0.2$	$V_f = 0.4$	$V_f = 0.6$
A_{12}/σ_y	0.016	0.120	0.692	1.081

Table 2: Bauschinger stress in the composite for simple shear loading, $\kappa_1 = \kappa_2 = 0$ and $\kappa_3 = 1000$, with $L_*/r = 0.4$ and $H/E_m = 0.1$, see Fig. 5.

The effect of the matrix material hardening for simple shear is analyzed in Fig. 6 for $L_*/r = 0.4$ and $V_f = 0.2$ using two different hardening moduli specified by $H/E_m = 0.01$ and $H/E_m = 0.1$. Tab. 3 shows the Bauschinger stress for the two hardening moduli, where it is smaller for the case of higher hardening.

	$H/E_m = 0.01$	$H/E_m = 0.1$
A_{12}/σ_y	0.182	0.120

Table 3: Bauschinger stress in the composite for simple shear loading, $\kappa_1 = \kappa_2 = 0$ and $\kappa_3 = 1000$, with $L_*/r = 0.4$ and $V_f = 0.2$, see Fig. 6.

The distribution of the normalized effective plastic strain, ϵ_e^p/ϵ_y, is shown in the contour plots of Fig. 7, for $V_f = 0.2$ and $H/E = 0.1$ at the maximum deformation of $E_{12}/\gamma_y = 1.98$. Fig. 7(a) shows contours for a conventional

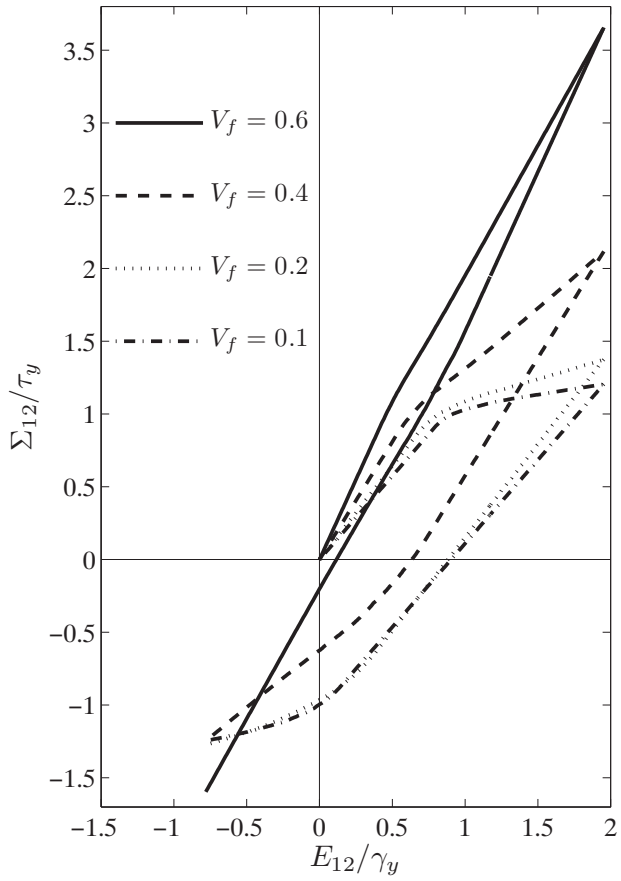

Figure 5: Effect of the fiber volume fraction, V_f, on the homogenized stress strain curve for simple shear, $\kappa_1 = \kappa_2 = 0$ and $\kappa_3 = 1000$, with $L_*/r = 0.4$ and $H/E_m = 0.1$.

material, while Fig. 7(b) shows results for the gradient dependent material with $L_*/r = 0.4$ and thirty times scaling of the displacement field. The maximum value of the effective plastic strain is significantly higher in the conventional analysis, Fig. 7(a), compared to the gradient dependent analysis, Fig. 7(b). This is due to a general suppression of plastic strain throughout the unit cell due to the constraint on plastic strain at the fiber-matrix interface.

Fig. 8 shows the distribution of the normalized higher order stresses, (a) $m_{121}/(L_*\sigma_y)$ and (b) $m_{122}/(L_*\sigma_y)$, for the maximum strain loading of

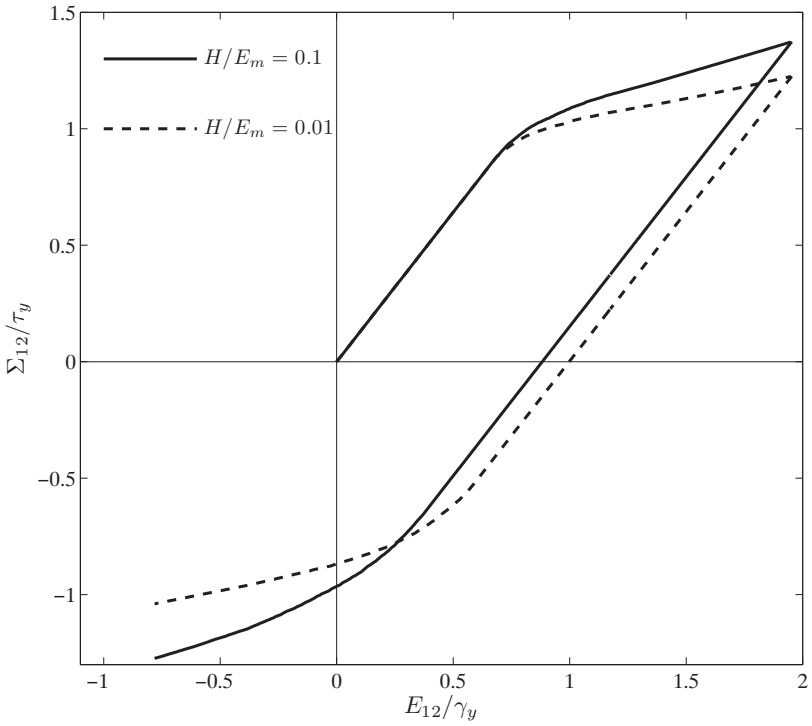

Figure 6: Effect of the matrix hardening, H, on the homogenized stress-strain curve for simple shear, $\kappa_1 = \kappa_2 = 0$ and $\kappa_3 = 1000$, with $L_*/r = 0.4$ and $V_f = 0.2$.

$E_{12}/\gamma_y = 1.98$ with $L_*/r = 0.4$ and $H/E_m = 0.1$. As can be seen, the higher order stress has an anti-symmetric distribution around the fiber with the maximum absolute value at the fiber matrix interface, where the gradients of the plastic strains are highest. Furthermore, they are observed to vanish at some of the boundaries in accordance to the symmetries of the problem.

Through the loading history including loading, unloading and reloading, the total energy density, W, supplied to the system can be split into three parts; a part is stored as elastic energy and a part as higher order energy, while the rest is dissipated. Fig. 9 shows the exchange of the energy throughout the loading history. The elastic energy is denoted by Ψ, the higher order energy is denoted by O and the dissipation by D. Loading until $E_{12}/\gamma_y = 1.98$ ($\tau = 300$) is followed by unloading until zero macroscopic stress ($\tau = 600$).

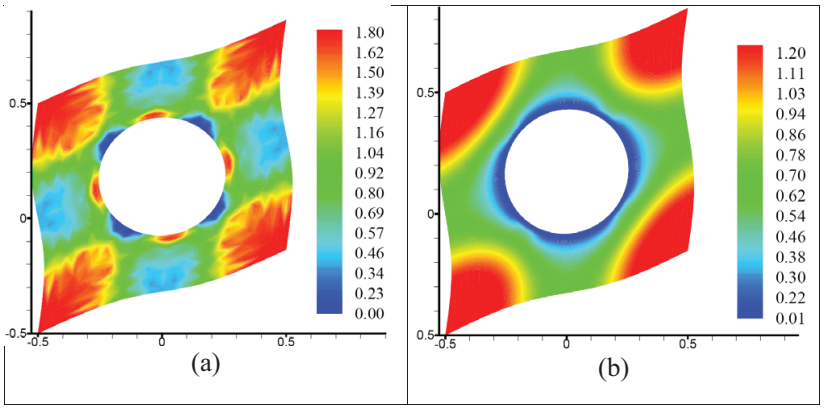

Figure 7: Effective plastic strain distribution, ϵ_e^p/ϵ_y, for simple shear, $\kappa_1 = \kappa_2 = 0$ and $\kappa_3 = 1000$, with $V_f = 0.2$ and $H/E_m = 0.1$. (a) $L_*/r = 0$. (b) $L_*/r = 0.4$. see Fig. 4 at $E_{12}/\gamma_y = 1.98$.

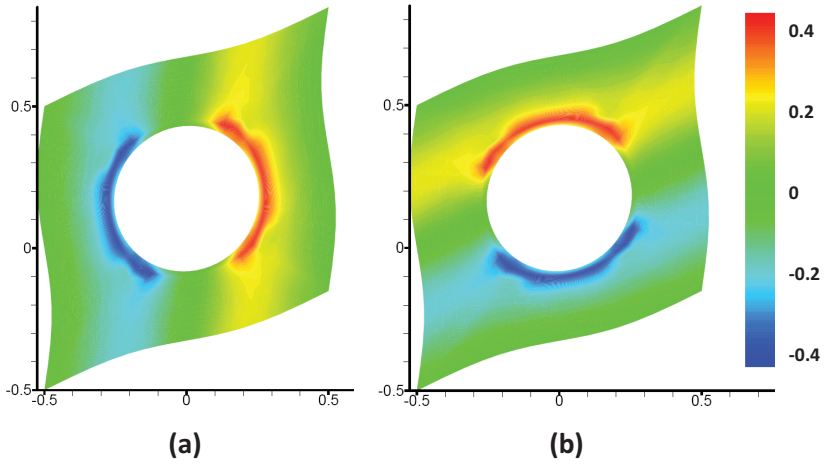

Figure 8: Higher order stress distribution for simple shear, $\kappa_1 = \kappa_2 = 0$ and $\kappa_3 = 1000$, with $V_f = 0.2$ and $H/E = 0.1$. (a) $m_{121}/(L_*\sigma_y)$. (b) $m_{122}/(L_*\sigma_y)$. see Fig. 4 at $E_{12}/\gamma_y = 1.98$.

Finally, the unit cell is loaded in reverse until the macroscopic shear strain of $E_{12}/\gamma_y = -0.78$ ($\tau = 900$). The material parameters used are $V_f = 0.2$, $H/E_m = 0.1$ and $L_*/r = 0.4$. The figure shows that the higher order energy

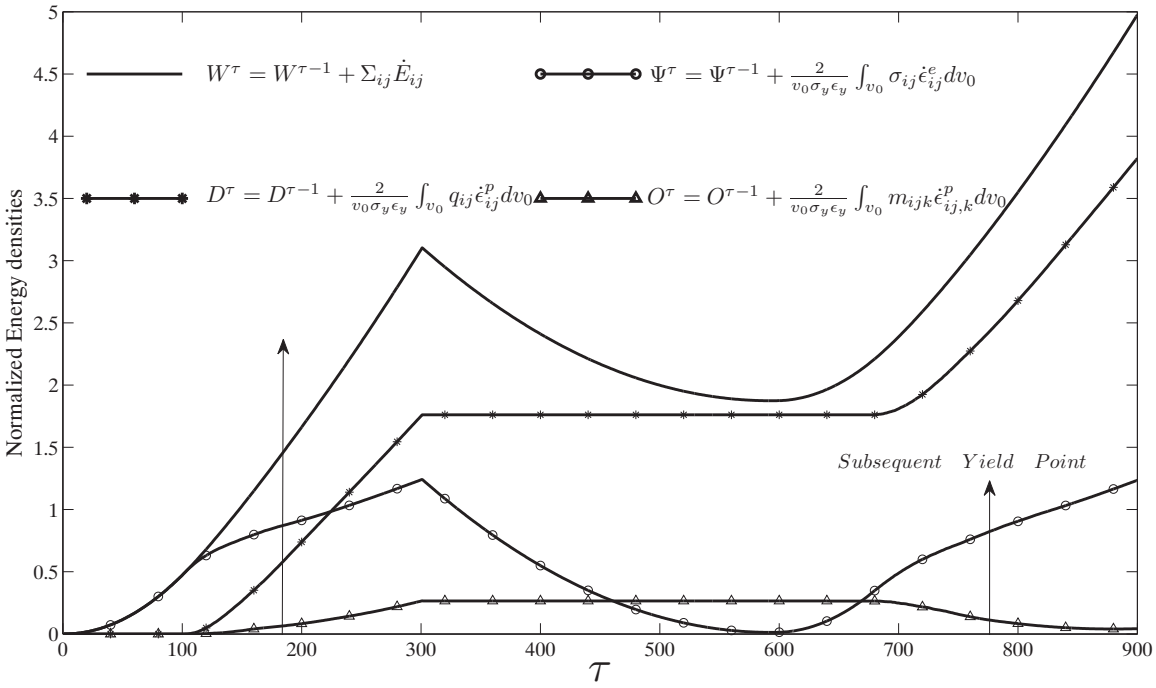

Figure 9: Densities of elastic energy, $2\Psi/(\sigma_y\epsilon_y)$, dissipation, $2D/(\sigma_y\epsilon_y)$, higher order energy, $2O/(\sigma_y\epsilon_y)$, and total energy, $2W/(\sigma_y\epsilon_y)$, during the loading, unloading and reloading for simple shear, $\kappa_1 = \kappa_2 = 0$ and $\kappa_3 = 1000$, with $V_f = 0.2$, $H/E_m = 0.1$ and $L_*/r = 0.4$, see Fig. 4.

starts to increase close to the macroscopic initial yield point along with the dissipation. During the unloading, the elastic energy decreases to a small value, while both the dissipation and higher order energy remain constant. During reverse loading, the higher order energy which was stored in the present setting is partially recovered.

6.2. Uniaxial loading

Uniaxial loading in both the transverse and longitudinal directions is now analyzed. For transverse uniaxial loading, all of the values of κ are set to zero, $\kappa_1 = \kappa_2 = \kappa_3 = 0$, which results in just one non-zero stress component, Σ_{11}. For longitudinal loading, $\kappa_1 = 1$, $k_2 = 1000$ and $\kappa_3 = 0$ ensure a

non-zero value for Σ_{33}, while suppressing all other stress components in the solution.

Fig. 10 shows the distribution of normalized effective plastic strain, ϵ_e^p/ϵ_y, on the deformed unit cell with thirty times scaling of the displacement, at the maximum macroscopic tensile strain of $3\epsilon_y$, with the material specified by $V_f = 0.2$ and $H/E_m = 0.1$. For the conventional material loaded in both the transverse direction (a) and the longitudinal direction (b), a considerable amount of the plastic deformation takes place at the fiber matrix interface, whereas in the gradient dependent material (c) and (d) the plastic deformation is suppressed. Shu and Barlow (2000) used a finite-deformation strain gradient crystal plasticity formulation together with a classical crystal formulation to characterize the deformation of the matrix in the unit cell. They found that while a classical crystal formulation tends to over-predict the spatial gradient of the deformation, the strain gradient formulation is able to predict a more smooth field consistent with experimental findings. This is confirmed in Fig. 10, where the gradient dependent material has a smooth transition from zero plastic flow in the fiber-matrix interface compared to the conventional material with an abrupt change in plastic flow across the fiber-matrix interface. Note that the periodic boundary conditions imposed lead to straight unit cell boundaries in accordance with the symmetries of the present problem.

For uniaxial transverse loading, Fig. 11 shows a breakup plot of the energy density in the system as was presented for pure shear in Fig. 9. At first the unit cell is loaded to the macroscopic tensile strain of $E_{11}/\epsilon_y = 3$ ($\tau = 300$), after which it is unloaded until zero macroscopic tensile stress ($\tau = 600$). Finally, reverse loading takes place until the macroscopic compressive strain of $E_{11}/\epsilon_y = -1.64$. The material parameters employed are $V_f = 0.2$, $H/E_m = 0.1$ and $L_*/r = 0.4$. As fore pure shear, both the higher order energy and dissipation start to increase before the initial macroscopic yield point, defined according to Eq. 27. During unloading the higher order energy and the dissipation remain constant, until the elastic energy descends to a minimum value at zero macroscopic strain. During reverse loading, the trapped elastic energy speed up the onset of the subsequent yield point and gives rise to the Bauschinger effect in the composite. The higher order energy is seen to be released with the reversed loading, close to the macro subsequent yield point. An important difference when comparing with Fig. 9 is that the free energy at the end of unloading (trapped energy) is relatively higher for the case of transverse loading than for pure shear.

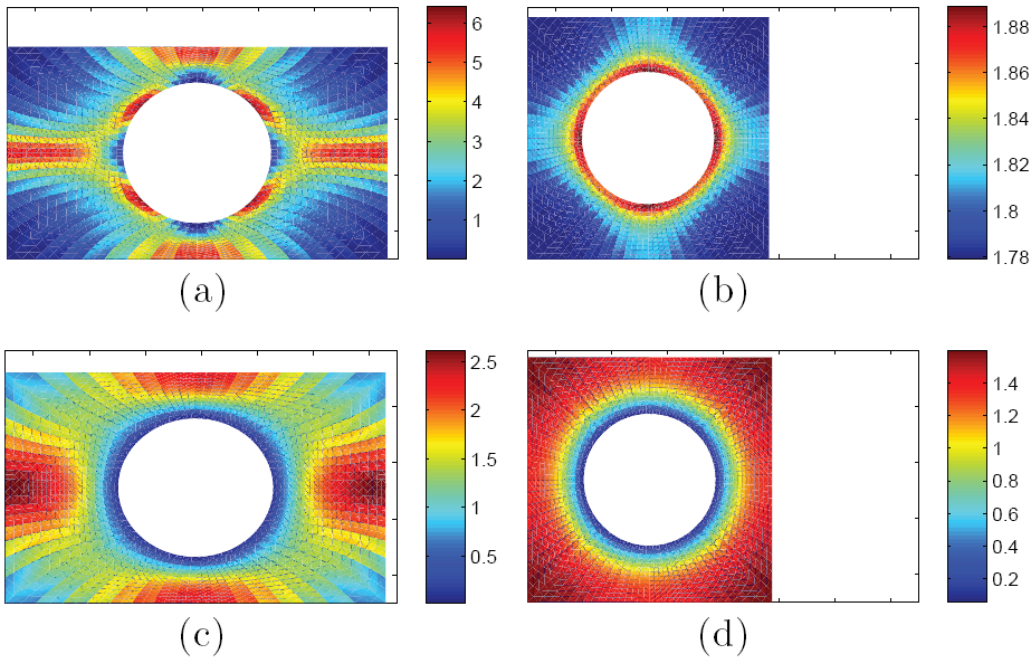

Figure 10: Effective plastic strain distribution, ϵ_e^p/ϵ_y, for in-plane tension at the maximum macroscopic tensile strain of $3\epsilon_y$ with $V_f = 0.2$ and $H/E_m = 0.1$. (a) $L_*/r = 0$ in transverse direction (x_1). (b) $L_*/r = 0$ in longitudinal direction (x_3). (c) $L_*/r = 0.4$ in transverse direction (x_1). (d) $L_*/r = 0.4$ in longitudinal direction (x_3).

6.3. Yield surfaces

In order to study the effect of different parameters on the composite yield surface, macroscopic initial and subsequent yield surfaces are plotted in different stress coordinate systems as done by Lissenden and Arnold (1998) for conventional materials. The present study includes the effect of the material length scale, L_*/r, and fiber volume fraction, V_f, on the three following representations of the yield surfaces:

- Transverse-Transverse (Σ_{11},Σ_{22}) by varying κ_1 while setting $\kappa_2 = \kappa_3 = 0$
- Transverse-Longitudinal (Σ_{11},Σ_{33}) by varying κ_2 while setting $\kappa_1 =$

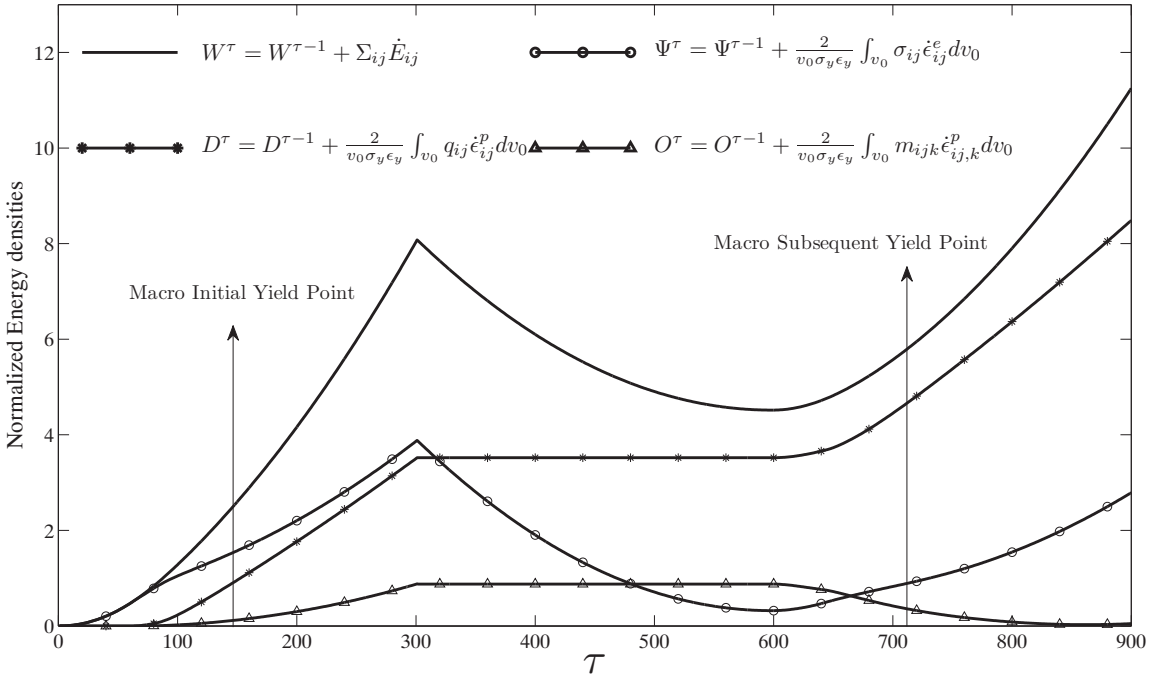

Figure 11: Densities of elastic energy, $2\Psi/(\sigma_y\epsilon_y)$, dissipation, $2D/(\sigma_y\epsilon_y)$, higher order energy, $2O/(\sigma_y\epsilon_y)$, and total energy, $2W/(\sigma_y\epsilon_y)$, during the uniaxial loading, unloading and reloading in transverse direction, $\kappa_1 = \kappa_2 = \kappa_3 = 0$, with $V_f = 0.2$, $H/E_m = 0.1$ and $L_*/r = 0.4$, see Fig. 10.

$\kappa_3 = 0$

- Transverse-Shear (Σ_{11},Σ_{12}) by varying κ_3 while setting $\kappa_1 = \kappa_2 = 0$

Similar probings of the yield surfaces on the π-plane are presented in Azizi et al. (2011). The yield tolerance in Eq. (27) is set to $\epsilon_t = 0.002$ for the subsequent analyzes.

The effect of the material length scale on the initial yield surfaces with $V_f = 0.2$ and $H/E_m = 0.1$ are plotted in Figs. 12, 13 and 14 on the stress coordinate system of Transverse-Transverse (Σ_{11},Σ_{22}), Transverse-Longitudinal (Σ_{11},Σ_{33}) and Transverse-Shear (Σ_{11},Σ_{12}), respectively. It can be seen that

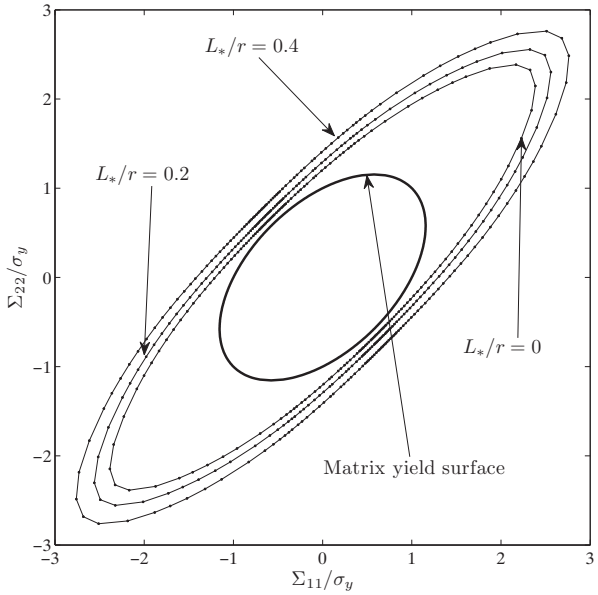

Figure 12: Effect of the material length scale on initial yield surface in Transverse-Transverse, $(\Sigma_{11}, \Sigma_{22})$, stress coordinate system with $V_f = 0.2$ and $H/E_m = 0.1$.

the effect of the material length scale is to expand the corresponding initial yield surface computed for the conventional case in all directions. This can be explained by the suppression of the plastic deformation close to the fiber matrix interface (Figs. 7 and 10), which tends to postpone the overall plasticity of the unit cell at the macro scale. This is consistent with the experimental investigation by Yan et al. (2007), where an enhancement of the yield stress of composite is observed with decreasing particle size.

Figs. 15, 16 and 17 show the effect of the fiber volume fraction, V_f, on the initial yield surfaces for a gradient dependent material with $L_*/r = 0.4$ and $H/E_m = 0.1$ on the Transverse-Transverse (Σ_{11},Σ_{22}), Transverse-Longitudinal (Σ_{11},Σ_{33}) and Transverse-Shear (Σ_{11},Σ_{12}) stress coordinate systems, respectively. It is seen that the effect of V_f on the initial yield surfaces is a significant expansion. In Fig. 15, the maximum expansion takes place when $\Sigma_{11} = \Sigma_{22}$ and the minimum expansion takes place when $\Sigma_{11} = -\Sigma_{22}$. Fig. 16 shows that when V_f is increased, the major axis of the yield surface

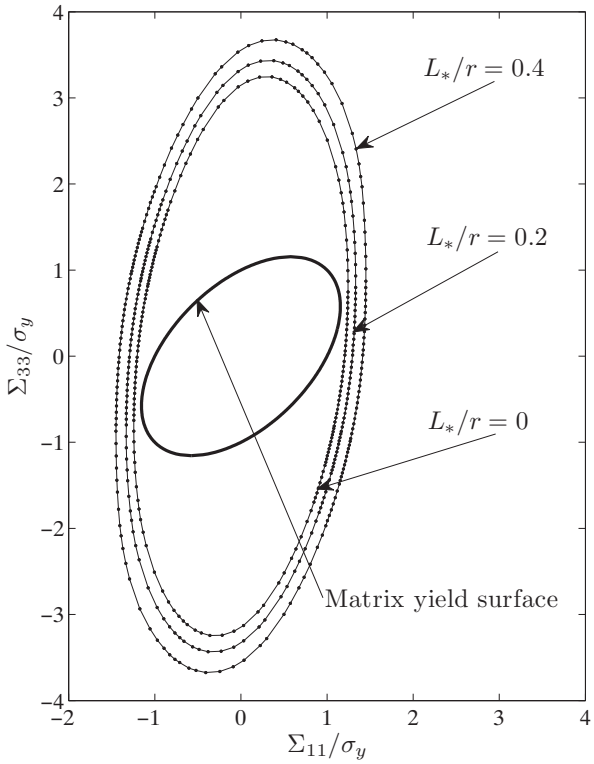

Figure 13: Effect of the material length scale on initial yield surface in Transverse-Longitudinal, $(\Sigma_{11}, \Sigma_{33})$, stress coordinate system with $V_f = 0.2$ and $H/E_m = 0.1$.

starts to increase and rotate toward the longitudinal direction. Thereby, the unit cell is significantly stiffer in the longitudinal direction than in the transverse direction. Similar results have been reported by Lissenden and Arnold (1998) for conventional material behavior. In Fig. 17, Transverse-Shear (Σ_{11},Σ_{12}) yield surfaces are shown, where the expansion is significant in the transverse direction but limited in the shear direction which is in agreement with the results reported in Fig. 5.

Subsequent yield surfaces are now analyzed in order to investigate the kinematic hardening (Bauschinger effect) as well as the anisotropic hardening (subsequent expansion). For the material parameters $L_*/r = 0.4$, $V_f = 0.2$ and $H/E_m = 0.1$ initial and subsequent yield surfaces are plotted

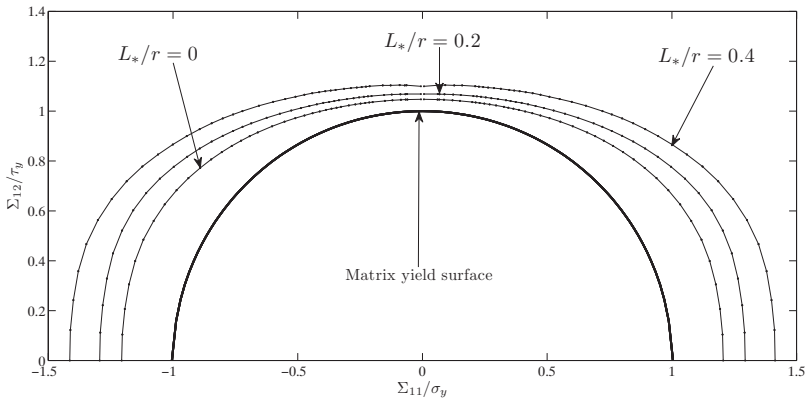

Figure 14: Effect of the material length scale on initial yield surface in Transverse-Shear, $(\Sigma_{11}, \Sigma_{12})$, stress coordinate system with $V_f = 0.2$ and $H/E_m = 0.1$.

in Fig. 18 in the Transverse-Transverse coordinate system (Σ_{11},Σ_{22}). Figs. 18(a) and (b) show the subsequent yield surface upon transverse loading in the x_1- and the x_2-directions, respectively. Fig. 18(c) shows subsequent yield surfaces upon in-plane equi-biaxial loading. The effect of loading in the x_1- and the x_2-directions are observed to be identical in accordance with the material symmetries. It is seen that a moderate anisotropic hardening (subsequent expansion) and kinematic hardening (translation) occur for loadings in both x_1- and x_2-directions, while a small anisotropic hardening (subsequent expansion) and large kinematic hardening (translation) occur in in-plane equi-biaxial loading.

For the same material, the initial and subsequent yield surfaces are shown in Fig. 19 in the Transverse-Longitudinal coordinate system (Σ_{11},Σ_{33}). Fig. 19(a) shows results for transverse loading, while Fig. 19(b) shows results for longitudinal loading. Fig. 19(c) shows results for out-of-plane equi-biaxial loading ($\Sigma_{11} = \Sigma_{33}$). As can be seen in Figs. 19(a) and (b), the Bauschinger stress (translation) is higher when loading in the longitudinal direction compared to loading in the transverse direction. For the out-of-plane equi-biaxial loading, Bauschinger stress is also considerable, and for all three loading cases there is a moderate anisotropic hardening (subsequent expansion).

In Fig. 19 initial and subsequent yield surfaces are shown in the Transverse-Shear coordinate system (Σ_{11},Σ_{12}). A relatively moderate anisotropic hard-

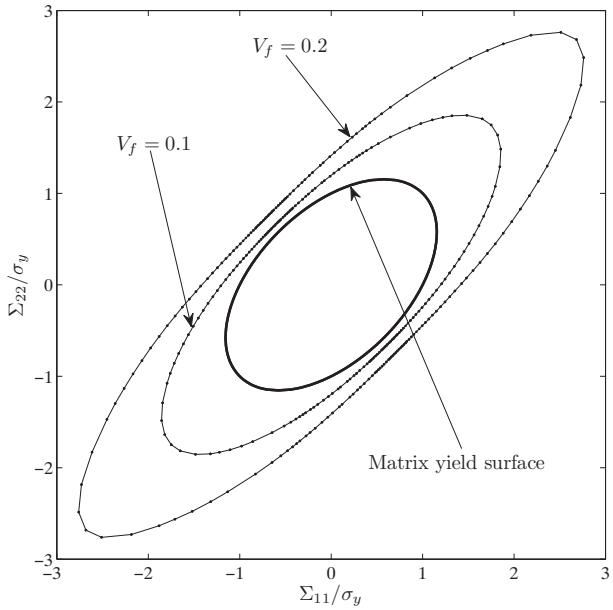

Figure 15: Effect of the fiber volume fraction on initial yield surface in Transverse-Transverse, $(\Sigma_{11}, \Sigma_{22})$, stress coordinate system with $L_*/r = 0.4$ and $H/E_m = 0.1$.

	Fig. 18	Fig. 18	Fig. 19	Fig. 20
Loadings	Transverse $\kappa_2 = \kappa_3 = 0$ $\kappa_1 = 0$	Transverse $\kappa_2 = \kappa_3 = 0$ $\kappa_1 = 1$	Longitudinal $\kappa_1 = 1$, $\kappa_3 = 0$ $\kappa_2 = 1000$	Shear $\kappa_1 = \kappa_2 = 0$ $\kappa_3 = 1000$
Anisotropic hardening	Moderate	Small	Small	Large
Kinematic hardening	Moderate	Large	Large	Small

Table 4: Qualitative comparison of both the kinematic and anisotropic hardening in the composite (Figs. 18, 19 and 20).

ening with a considerable kinematic hardening occurs when the unit cell is loaded in the transverse direction, which is opposite to the finding in the shear direction. As a result of Figs. 18, 19 and 20, the Bauschinger stress shows a significant anisotropic growth. Tab. 4 summarizes qualitatively the amount of both kinematic and anisotropic hardening based on different types

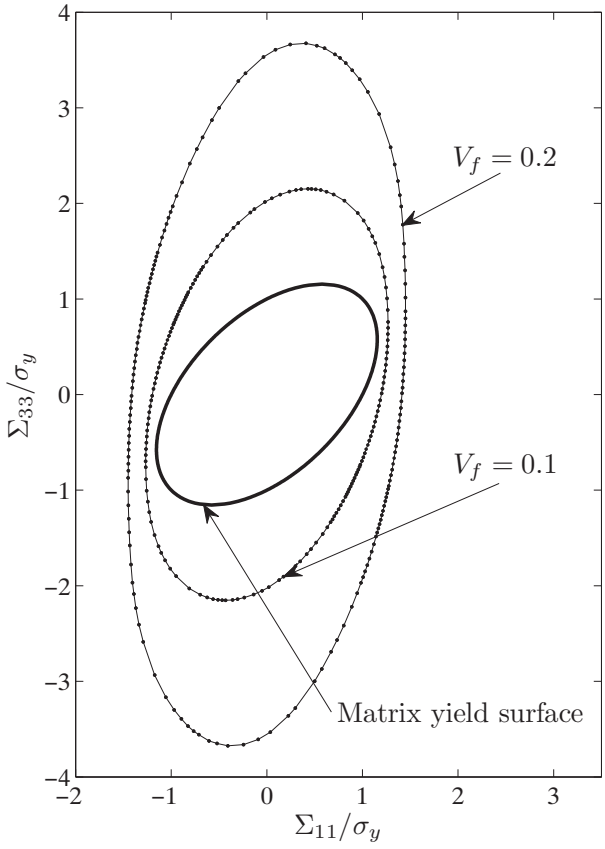

Figure 16: Effect of the fiber volume fraction on the initial yield surface in Transverse-Longitudinal, $(\Sigma_{11}, \Sigma_{33})$, stress coordinate system with $L_*/r = 0.4$ and $H/E_m = 0.1$.

of the loading discussed above.

7. Conclusion

The macroscopic response of metal matrix composites with long circular unidirectional fibers is studied, using a rate independent higher order strain gradient plasticity theory for the matrix and an elastic model for the fiber. The macroscopic elasto-plastic behavior of composite is compared with conventional predictions. Micro-macro homogenization is carried out under the

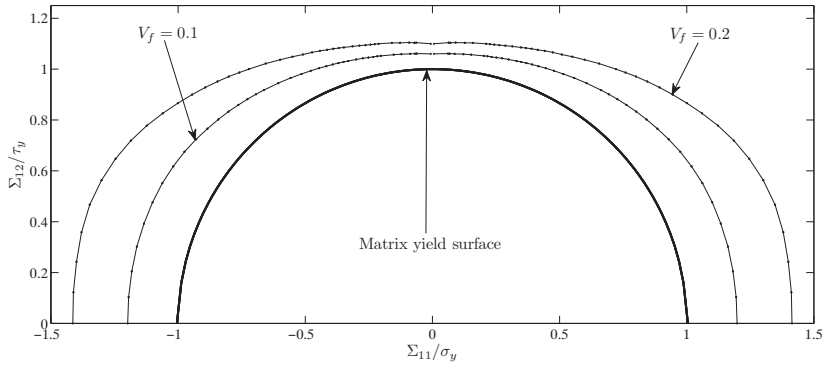

Figure 17: Effect of the fiber volume fraction on the initial yield surface in Transverse-Shear, $(\Sigma_{11}, \Sigma_{12})$, stress coordinate system with $L_*/r = 0.4$ and $H/E_m = 0.1$.

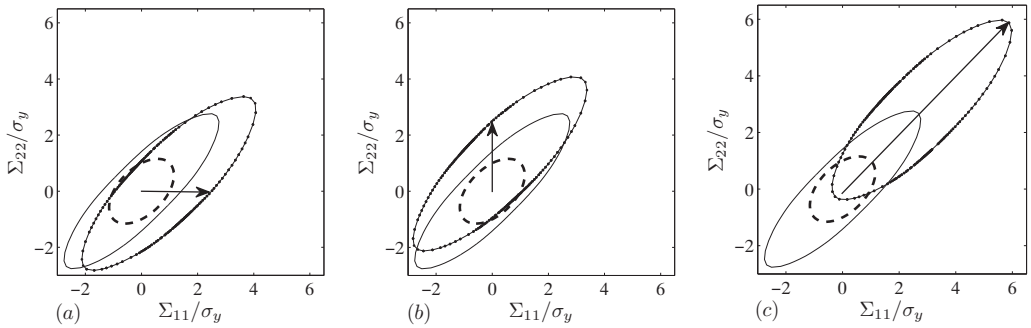

Figure 18: Subsequent yield surface in Transverse-Transverse, $(\Sigma_{11}, \Sigma_{22})$, stress coordinate system with $V_f = 0.2$, $L_*/r = 0.4$ and $H/E_m = 0.1$ (Dashed-line: Matrix yield surface, Solid-line: Initial yield surface, point-line: Subsequent yield surface). (a) $\kappa_1 = \kappa_2 = \kappa_3 = 0$ (Transverse loading). (b) $\kappa_2 = \kappa_3 = 0$ and $\kappa_1 = 1000$ (Transverse loading). (c) $\kappa_2 = \kappa_3 = 0$ and $\kappa_1 = 1$ (In-plane equi-biaxial loading).

assumption of macroscopically homogeneous loading such that the macroscopic material model employed is of conventional nature. Analyzes have been carried out for simple shear and uniaxial loading in the transverse and longitudinal direction under generalized plane strain condition.

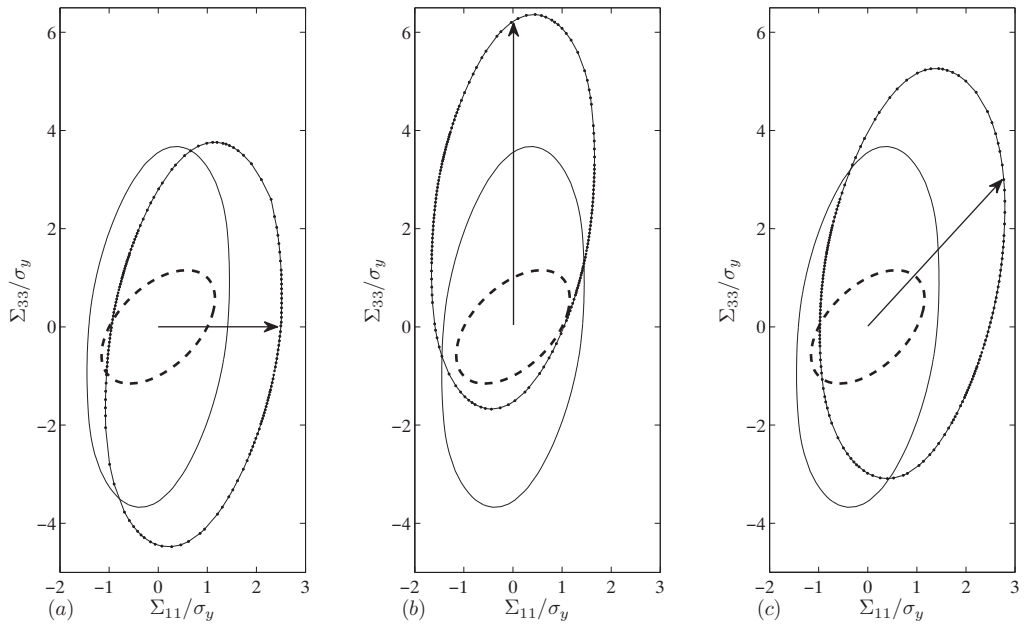

Figure 19: Subsequent yield surface in Transverse-Longitudinal, $(\Sigma_{11}, \Sigma_{33})$, stress coordinate system with $V_f = 0.2$, $L_*/r = 0.4$ and $H/E_m = 0.1$ (Dashed-line: Matrix yield surface, Solid-line: Initial yield surface, point-line: Subsequent yield surface). (a) $\kappa_1 = \kappa_2 = \kappa_3 = 0$ (Transverse loading). (b) $\kappa_1 = 1$, $\kappa_3 = 0$ and $\kappa_2 = 1000$ (Longitudinal loading). (c) $\kappa_1 = \kappa_3 = 0$ and $\kappa_2 = 1$ (Out-of-plane Biaxial loading).

It is shown that the elastic modulus, the yield stress and the Bauschinger effect increase for simple shear loading with higher fiber volume fraction. Furthermore, it is seen that for increasing fiber volume fraction, the overall plastic flow is suppressed and, as a result, the initial yield surface expands. The expansion exhibits anisotropic growth, where it is large in the longitudinal direction and small in the shear direction. It is concluded that V_f is the most important conventional parameter leading to expansion of the initial yield surface as well as anisotropic hardening (subsequent expansion) and kinematic hardening (translation) of the subsequent yield surface in all loading directions.

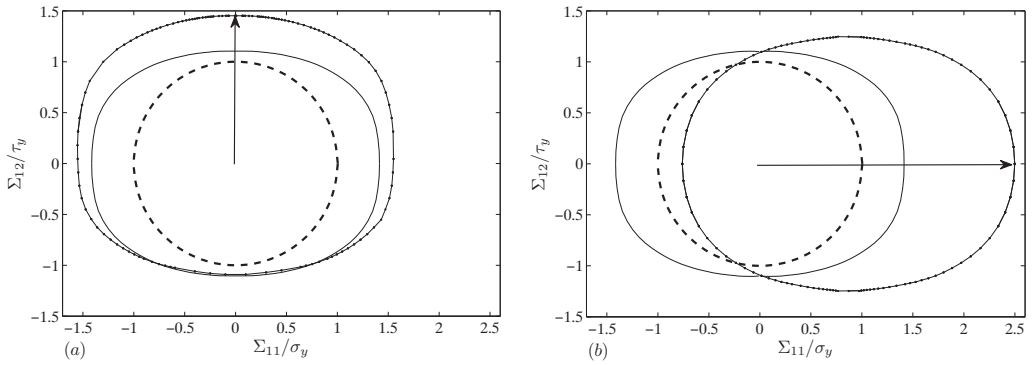

Figure 20: Subsequent yield surface in Transverse-Shear, $(\Sigma_{11}, \Sigma_{12})$, stress coordinate system with $V_f = 0.2$, $L_*/r = 0.4$ and $H/E_m = 0.1$ (Dashed-line: Matrix yield surface, Solid-line: Initial yield surface, point-line: Subsequent yield surface). (a) $\kappa_1 = \kappa_2 = 0$ and $\kappa_3 = 1000$ (Simple shear loading). (b) $\kappa_1 = \kappa_2 = \kappa_3 = 0$ (Transverse loading).

The effect of fiber size has also been analyzed. The results show that the material length scale, which is included energetically in the present strain gradient formulation, serves as to expand the initial yield surface and increase the overall hardening of the composite, due to storage of free energy in the material through plastic strain gradients. Furthermore, it is shown that the Bauschinger stress increases with decreasing particle size, meaning that more kinematic hardening is observed for micron scale fibers than for large fibers. The study of subsequent yield surfaces shows that the Bauschinger effect (translation) is largest in the longitudinal direction (as well as in in-plane equi-biaxial), moderate in the transverse direction and small in the shear direction, and conversely for the anisotropic hardening (subsequent expansion). It is concluded that the inclusion of the constitutive material length scale in the present model results in an isotropic growth of the initial yield surface and anisotropic expansion and translation of the subsequent yield surface upon loading in different directions.

Acknowledgment

This work was supported by the Danish Research Council for Technology and Production Sciences in a project entitled Plasticity Across the Scales. The computational resources have been provided by a hardware grant from the Danish Center of Scientific Computing (DCSC).

A. Appendix. Matrices in Finite element method

In this section, the numerical method is described. Eight node quadrilateral elements with two degrees of freedom for the displacement field at each node and four node quadrilateral elements with three degrees of freedom for plastic strains at each node are used. The generalized plane strain assumption requires an additional degree of freedom for the displacement in the longitudinal (out-of-plane) direction, W, and is common for all elements. Within each element, the displacement field , $\dot{\mathbf{U}}_n$, and the plastic strain field, $\dot{\boldsymbol{\epsilon}}^p_m$, shown in Eq. (33), are expressed in an array

$$\dot{\mathbf{U}}_n = \begin{bmatrix} \dot{U}_1 & \dot{V}_1 & ... & \dot{U}_8 & \dot{V}_8 & \dot{W} \end{bmatrix}^{\mathrm{T}} \tag{A.1}$$

$$\dot{\boldsymbol{\epsilon}}^p_m = \begin{bmatrix} \dot{\epsilon}^{p1}_{11} & \dot{\epsilon}^{p1}_{22} & \dot{\gamma}^{p1}_{12} & ... & \dot{\epsilon}^{p4}_{11} & \dot{\epsilon}^{p4}_{22} & \dot{\gamma}^{p4}_{12} \end{bmatrix}^{\mathrm{T}} \tag{A.2}$$

where $\dot{U}_I$, $\dot{V}_I$ and $\dot{W}$ are displacement increments at node I in the X_1, X_2 and X_3 directions, respectively, and $\dot{\epsilon}^{pI}_{ij}$ is plastic strain increments at node I. Note that $\dot{\gamma}^{pI}_{12} = 2\dot{\epsilon}^{pI}_{12}$.

The interpolation functions for displacement, $\mathbf{N}^n$, and plastic strain field, $\mathbf{P}^m$, is written as

$$\mathbf{N}^n = \begin{bmatrix} N_1 & 0 & N_2 & 0 & ... & N_8 & 0 & 0 \\ 0 & N_1 & 0 & N_2 & ... & 0 & N_8 & 0 \\ 0 & 0 & 0 & 0 & ... & 0 & 0 & 1 \end{bmatrix}_{(3\times 17)} \tag{A.3}$$

$$\mathbf{P}^m = \begin{bmatrix} P_1 & 0 & 0 & ... & P_4 & 0 & 0 \\ 0 & P_1 & 0 & ... & 0 & P_4 & 0 \\ -P_1 & -P_1 & 0 & ... & -P_4 & -P_4 & 0 \\ 0 & 0 & P_1 & ... & 0 & 0 & P_4 \end{bmatrix}_{(4\times 12)} \tag{A.4}$$

where plastic incompressibility, $\dot{\epsilon}^p_{ii} = 0$, is used in $\mathbf{P}^m$. Nodal interpolation is obtained from

$$\begin{bmatrix} \dot{u}_1 \\ \dot{u}_2 \\ \dot{w} \end{bmatrix}_{(3\times 1)} = \begin{bmatrix} N_1 & 0 & N_2 & 0 & ... & N_8 & 0 & 0 \\ 0 & N_1 & 0 & N_2 & ... & 0 & N_8 & 0 \\ 0 & 0 & 0 & 0 & ... & 0 & 0 & 1 \end{bmatrix}_{(3\times 17)} \times \begin{bmatrix} \dot{U}_1 \\ \dot{V}_1 \\ \cdot \\ \cdot \\ \cdot \\ \dot{U}_8 \\ \dot{V}_8 \\ \dot{W} \end{bmatrix}_{(17\times 1)} \tag{A.5}$$

where $\dot{w}$ is the longitudinal length increase of the domain. Similarly,

$$\begin{bmatrix} \dot{\epsilon}^p_{11} \\ \dot{\epsilon}^p_{22} \\ \dot{\epsilon}^p_{33} \\ \dot{\gamma}^p_{12} \end{bmatrix}_{(4\times1)} = \begin{bmatrix} P_1 & 0 & 0 & ... & P_4 & 0 & 0 \\ 0 & P_1 & 0 & ... & 0 & P_4 & 0 \\ -P_1 & -P_1 & 0 & ... & -P_4 & -P_4 & 0 \\ 0 & 0 & P_1 & ... & 0 & 0 & P_4 \end{bmatrix}_{(4\times12)} \times \begin{bmatrix} \dot{\epsilon}^{p1}_{11} \\ \dot{\epsilon}^{p1}_{22} \\ \dot{\gamma}^{p1}_{12} \\ . \\ . \\ . \\ \dot{\epsilon}^{p4}_{11} \\ \dot{\epsilon}^{p4}_{22} \\ \dot{\gamma}^{p4}_{12} \end{bmatrix}_{(12\times1)} \tag{A.6}$$

Strain and plastic strain gradients are computed by the appropriate derivatives of the displacement and plastic strain fields according to

$$\mathbf{B}^n = \begin{bmatrix} N_{1,1} & 0 & N_{2,1} & 0 & ... & N_{8,1} & 0 & 0 \\ 0 & N_{1,2} & 0 & N_{2,2} & ... & 0 & N_{8,2} & 0 \\ 0 & 0 & 0 & 0 & 0 & 0 & 0 & \frac{1}{t} \\ N_{1,2} & N_{1,1} & N_{2,2} & N_{2,1} & ... & N_{8,2} & N_{8,1} & 0 \end{bmatrix}_{4\times17} \tag{A.7}$$

where t is the thickness (in the out-of-plane x_3-direction) of the unit cell.

$$\mathbf{Q}^m = \begin{bmatrix} P_{1,1} & 0 & 0 & ... & P_{4,1} & 0 & 0 \\ P_{1,2} & 0 & 0 & ... & P_{4,2} & 0 & 0 \\ 0 & P_{1,1} & 0 & ... & 0 & P_{4,1} & 0 \\ 0 & P_{1,2} & 0 & ... & 0 & P_{4,2} & 0 \\ -P_{1,1} & -P_{1,1} & 0 & ... & -P_{4,1} & -P_{4,1} & 0 \\ -P_{1,2} & -P_{1,2} & 0 & ... & -P_{4,2} & -P_{4,2} & 0 \\ 0 & 0 & P_{1,1} & ... & 0 & 0 & P_{4,1} \\ 0 & 0 & P_{1,2} & ... & 0 & 0 & P_{4,2} \end{bmatrix}_{8\times12} \tag{A.8}$$

Also here, plastic incompressibility $\dot{\epsilon}^p_{ii,k} = 0$ is exploited.

The interpolated strain and plastic strain gradient can be shown as

$$\begin{bmatrix}\dot{\epsilon}_{11}\\ \dot{\epsilon}_{22}\\ \dot{\epsilon}_{33}\\ \dot{\gamma}_{12}\end{bmatrix}_{4\times1} = \begin{bmatrix}N_{1,1} & 0 & N_{2,1} & 0 & ... & N_{8,1} & 0 & 0\\ 0 & N_{1,2} & 0 & N_{2,2} & ... & 0 & N_{8,2} & 0\\ 0 & 0 & 0 & 0 & 0 & 0 & 0 & \frac{1}{t}\\ N_{1,2} & N_{1,1} & N_{2,2} & N_{2,1} & ... & N_{8,2} & N_{8,1} & 0\end{bmatrix}_{4\times17} \times \begin{bmatrix}\dot{U}_1\\ \dot{V}_1\\ .\\ .\\ .\\ \dot{U}_8\\ \dot{V}_8\\ \dot{W}\end{bmatrix}_{(17\times1)} \tag{A.9}$$

where $\dot{\gamma}_{ij} = 2\dot{\epsilon}_{ij}$. Similarly,

$$\begin{bmatrix}\dot{\epsilon}^p_{11,1}\\ \dot{\epsilon}^p_{11,2}\\ \dot{\epsilon}^p_{22,1}\\ \dot{\epsilon}^p_{22,2}\\ \dot{\epsilon}^p_{33,1}\\ \dot{\epsilon}^p_{33,2}\\ \dot{\gamma}^p_{12,1}\\ \dot{\gamma}^p_{12,2}\end{bmatrix}_{8\times1} = \begin{bmatrix}P_{1,1} & 0 & 0 & ... & P_{4,1} & 0 & 0\\ P_{1,2} & 0 & 0 & ... & P_{4,2} & 0 & 0\\ 0 & P_{1,1} & 0 & ... & 0 & P_{4,1} & 0\\ 0 & P_{1,2} & 0 & ... & 0 & P_{4,2} & 0\\ -P_{1,1} & -P_{1,1} & 0 & ... & -P_{4,1} & -P_{4,1} & 0\\ -P_{1,2} & -P_{1,2} & 0 & ... & -P_{4,2} & -P_{4,2} & 0\\ 0 & 0 & P_{1,1} & ... & 0 & 0 & P_{4,1}\\ 0 & 0 & P_{1,2} & ... & 0 & 0 & P_{4,2}\end{bmatrix}_{8\times12} \times \begin{bmatrix}\dot{\epsilon}^{p1}_{11}\\ \dot{\epsilon}^{p1}_{22}\\ \dot{\gamma}^{p1}_{12}\\ .\\ .\\ .\\ \dot{\epsilon}^{p4}_{11}\\ \dot{\epsilon}^{p4}_{22}\\ \dot{\gamma}^{p4}_{12}\end{bmatrix}_{(12\times1)} \tag{A.10}$$

The stress increment, $\dot{\sigma}_{ij}$, the micro stress increment, $\dot{q}_{ij}$, and the higher order stress increment, $\dot{m}_{ijk}$, are evaluated according to

$$\begin{bmatrix}\dot{\sigma}_{11}\\ \dot{\sigma}_{22}\\ \dot{\sigma}_{33}\\ \dot{\sigma}_{12}\end{bmatrix}_{4\times1} = \frac{E}{(1+\upsilon)(1-2\upsilon)} \begin{bmatrix}1-\upsilon & \upsilon & \upsilon & 0\\ \upsilon & 1-\upsilon & \upsilon & 0\\ \upsilon & \upsilon & 1-\upsilon & 0\\ 0 & 0 & 0 & \frac{1-2\upsilon}{2}\end{bmatrix}_{4\times4} \times \begin{bmatrix}\dot{\epsilon}_{11}\\ \dot{\epsilon}_{22}\\ \dot{\epsilon}_{33}\\ \dot{\gamma}_{12}\end{bmatrix}_{4\times1} \tag{A.11}$$

$$\begin{bmatrix} \dot{q}_{11} \\ \dot{q}_{22} \\ \dot{q}_{33} \\ \dot{q}_{12} \end{bmatrix}_{4\times 1} = \Bigg\{ \frac{4}{9}(H - E_0) \begin{bmatrix} r_{11}^2 & r_{11}r_{22} & r_{11}r_{33} & r_{11}r_{12} \\ r_{11}r_{22} & r_{22}^2 & r_{22}r_{33} & r_{22}r_{12} \\ r_{11}r_{33} & r_{22}r_{33} & r_{33}^2 & r_{12}r_{33} \\ r_{11}r_{12} & r_{22}r_{12} & r_{33}r_{12} & r_{12}^2 \end{bmatrix}_{4\times 4} + \frac{2}{3}E_0 \begin{bmatrix} 1 & 0 & 0 & 0 \\ 0 & 1 & 0 & 0 \\ 0 & 0 & 1 & 0 \\ 0 & 0 & 0 & 1/2 \end{bmatrix}_{4\times 4} \Bigg\} \times \begin{bmatrix} \dot{\epsilon}_{11}^p \\ \dot{\epsilon}_{22}^p \\ \dot{\epsilon}_{33}^p \\ \dot{\gamma}_{12}^p \end{bmatrix}_{4\times 1} \tag{A.12}$$

$$\begin{bmatrix} \dot{m}_{111} \\ \dot{m}_{112} \\ \dot{m}_{221} \\ \dot{m}_{222} \\ \dot{m}_{331} \\ \dot{m}_{332} \\ \dot{m}_{121} \\ \dot{m}_{122} \end{bmatrix}_{8\times 1} = GL_*^2 \begin{bmatrix} 1 & 0 & 0 & 0 & 0 & 0 & 0 & 0 \\ 0 & 1 & 0 & 0 & 0 & 0 & 0 & 0 \\ 0 & 0 & 1 & 0 & 0 & 0 & 0 & 0 \\ 0 & 0 & 0 & 1 & 0 & 0 & 0 & 0 \\ 0 & 0 & 0 & 0 & 1 & 0 & 0 & 0 \\ 0 & 0 & 0 & 0 & 0 & 1 & 0 & 0 \\ 0 & 0 & 0 & 0 & 0 & 0 & 1 & 0 \\ 0 & 0 & 0 & 0 & 0 & 0 & 0 & 1 \end{bmatrix}_{8\times 8} \times \begin{bmatrix} \dot{\epsilon}_{11,1}^p \\ \dot{\epsilon}_{11,2}^p \\ \dot{\epsilon}_{22,1}^p \\ \dot{\epsilon}_{22,2}^p \\ \dot{\epsilon}_{33,1}^p \\ \dot{\epsilon}_{33,2}^p \\ \dot{\gamma}_{12,1}^p \\ \dot{\gamma}_{12,2}^p \end{bmatrix}_{8\times 1} \tag{A.13}$$

References

Acharya, A., Bassani, J. L., 2000. Lattice incompatibility and a gradient theory of crystal plasticity. Journal of the Mechanics and Physics of Solids 48, 1565–1595.

Anand, L., Gurtin, M., Lele, S., Gething, C., 2005. A one-dimensional theory of strain-gradient plasticity: Formulation, analysis, numerical results. Journal of the Mechanics and Physics of Solids 53, 1789–1826.

Azizi, R., Niordson, C., Legarth, B., 2011. Size-effects on yield surfaces for micro reinforced composites. International Journal of Plasticity 27, 1817–1832.

Bao, G., Hutchinson, J. W., McMeeking, R. M., 1991. Particle reinforcement of ductile matrices against plastic flow and creep. Acta Metallurgica et Materialia 39 (8), 1871–1882.

Barai, P., Weng, G., 2011. A theory of plasticity for carbon nanotube reinforced composites. International Journal of Plasticity 27, 539–559.

Bassani, J. L., 2001. Incompatibility and a simple gradient theory of plasticity. Journal of the Mechanics and Physics of Solids 49, 1983–1996.

Borg, U., Niordson, C., Kysar, J., 2008. Size effects on void growth in single crystals with distributed voids. International Journal of Plasticity 24, 688–701.

Budiansky, B., 1965. On elastic moduli of some heterogeneous materials. Journal of The Mechanics and Physics of Solids 13, 223–227.

Choi, H. S., Jang, Y. H., 2011. Micro-mechanical behavior of a unidirectional composite subjected to transverse shear loading. Appl Compos Mater 18, 127–148.

Eshelby, J. D., 1957. The determination of the field of an ellipsoidal inclusion and related problems. Proc. R. Soc. Lond A 241, 376–396.

Fleck, N. A., Ashby, M., Hutchinson, J. W., 2003. The role of geometrically necessary dislocations in giving material strengthening. Scripta Materialia 48, 179–183.

Fleck, N. A., Hutchinson, J. W., 1997. Strain gradient plasticity. In: Hutchinson, J. W., Wu, T. Y. (Eds.), Advances in Applied Mechanics. Vol. 33. Academic Press, pp. 295–361.

Fleck, N. A., Hutchinson, J. W., 2001. A reformulation of strain gradient plasticity. Journal of the Mechanics and Physics of Solids 49, 2245–2271.

Fleck, N. A., Willis, J. R., 2009a. A mathematical basis for strain-gradient plasticity theory - Part I: Scalar plastic multiplier. Journal of the Mechanics and Physics of Solids 57, 161–177.

Fleck, N. A., Willis, J. R., 2009b. A mathematical basis for strain-gradient plasticity theory - Part II: Tensorial plastic multiplier. Journal of the Mechanics and Physics of Solids, doi:10.1016/j.jmps.2009.03.007.

Fredriksson, P., Gudmundson, P., L.P., M., 2009. Finite element implementation and numerical issues of strain gradient plasticity with application to metal matrix composites. International Journal of Solids and Structures 46, 3977–3987.

Gao, H., Huang, Y., 2003. Geometrically necessary dislocation and size-dependent plasticity. Scripta Materialia 48, 113–118.

Gao, H., Huang, Y., Nix, W. D., Hutchinson, J. W., 1999. Mechanism-based strain gradient plasticity - I. Theory. Journal of the Mechanics and Physics of Solids 47 (6), 1239–1263.

Ghosh, S., Lee, K., Moorthy, S., 1995. Multiple scale analysis of heterogeneous elastic structures using homogenization theory and voronoi cell finite element method. International Journal of Solids and Structures 32 (1), 27–62.

Gudmundson, P., 2004. A unified treatment of strain gradient plasticity. Journal of the Mechanics and Physics of Solids 52 (6), 1379–1406.

Gurtin, M. E., 2002. A gradient theory of single-crystal viscoplasticity that accounts for geometrically necessary dislocations. Journal of the Mechanics and Physics of Solids 50 (1), 5–32.

Gurtin, M. E., Anand, L., 2005. A theory of strain-gradient plasticity for isotropic, plastically irrotational materials. Part I: Small deformations. Journal of the Mechanics and Physics of Solids 53 (7), 1624–1649.

Hashin, Z., 1983. Analysis of composite materials. a survey. J. Appl. Mech. 50, 481–505.

Hashin, Z., Shtrikman, S., 1963. A variational approach to the theory of the elastic behaviour of multiphase materials. Journal of the Mechanics and Physics of Solids 11 (2), 127–140.

Hill, R., 1963. Elastic properties of reinforced solids: some theoretical principles. Journal of the Mechanics and Physics of Solids 11, 357–372.

Hill, R., 1965. A self-consistent mechanics of composite materials. Journal of The Mechanics and Physics of Solids 13, 213–222.

Hussein, M., Borg, U., Niordson, C., Deshpande, V., 2008. Plasticity size effects in voided crystals. Journal of the Mechanics and Physics of Solids 56, 114–131.

Hutchinson, J. W., 2000. Plasticity at the micron scale. International Journal of Solids and Structures 37 (1-2), 225–238.

Keller, R. R., Phelps, J. M., Read, D. T., 1990. Preprocessing and postprocessing for materials based on the homogenization method with adaptive finite element methods. COMPUTER METHODS IN APPLIED MECHANICS AND ENGINEERING 83, 143–198.

Kim, K., Cha, S., Hong, S., Hong, S., 2006. Microstructure and tensile behavior of carbon nanotubes reinforced cu matrix nanocomposites. Mater. Sci. Eng. 430, 27–33.

Kouznetsova, V., Brekelmans, W. A. M., Baaijens, F. P. T., 2001. An approach to micro-macro modeling of heterogeneous materials. Comput. Mech. 27, 37–48.

Kouznetsova, V., Geers, M., Brekelmans, W., 2004. Multi-scale second-order computational homogenization of multi-phase materials: a nested finite element solution strategy. Comput. Methods Appl. Mech. Engrg 193, 5525–5550.

Legarth, B. N., 2003. Debonding of particles in anisotropic materials. International Journal of Mechanical Sciences 45, 1119–1133.

Legarth, B. N., Kuroda, M., 2004. Particle debonding using different yield criteria. European Journal of Mechanics - A/Solids 23 (5), 737–751.

Lele, S. P., Anand, L., 2008. A small-deformation strain-gradient theory for isotropic viscoplastic materials. Philosophical Magazine 88 (30), 1478–6435.

Lissenden, C., Arnold, S., 1998. Effect of microstructural architecture on flow/damage surfaces for metal matrix composites. Damage Mechanics in Engineering Materials, 385–400.

Lloyd, D. J., 1994. Particle reinforced aluminium and magnesium matrix composites. International Materials Reviews 39 (1), 1–23.

McDanels, D., 1985. Analysis of stress-strain, fracture, and ductility behavior of aluminum matrix composites containing discontinuous silicon carbide reinforcement. Metallurgical Transactions A (Physical Metallurgy and Materials Science) 16A (6), 1105–1115.

Mughrabi, H., 2001. The effect of geometrically necessary dislocations on the flow stress of deformed crystals containing a heterogeneous dislocation distribution. Materials Science and Engineering, 139–143.

Niordson, C. F., 2003. Strain gradient plasticity effects in whisker-reinforced metals. Journal of the Mechanics and Physics of Solids 51 (10), 1863 – 1883.

Niordson, C. F., Legarth, B. N., 2010. Strain gradient effecits on cyclic plasticity. Journal of the Mechanics and Physics of Solids 58, 542–557.

Niordson, C. F., Tvergaard, V., 2001. Nonlocal plasticity effects on the tensile properties of a metal matrix composite. European Journal of Mechanics - A/Solids 20 (4), 601–613.

Niordson, C. F., Tvergaard, V., 2002. Nonlocal plasticity effects on fibre debonding in a whisker-reinforced metal. European Journal of Mechanics - A/Solids 21 (2), 239–248.

Shu, J. Y., Barlow, C. Y., 2000. Strain gradient effects on microscopic strain field in a metal matrix composite. International Journal of Plasticity 16, 563–591.

Suquet, P. M., 1985. Local and global aspects in the mathematical theory of plasticity. Plasticity todays: modelling, methods and applications, 279–310.

Taya, M., Lualy, K., Wakashima, K., Lloyd, D., 1990. Bauschinger effect in particulate sic-6061 aluminum composites. Material science and engineering 124, 103–111.

Terada, K., Hori, M., Kyoya, T., Kikuchi, N., 2000. Simulation of the multi-scale convergence in computational homogenization approaches. Journal of Solids and Structures 37, 2285–2311.

Tvergaard, V., 1990. Analysis of tensile properties for a whisker-reinforced metal-matrix composite. Acta Metallurgica 38 (2), 185–194.

Tvergaard, V., 1995. Fibre debonding and breakage in a whisker-reinforced metal. Materials Science and Engineering: A 190, 215–222.

Wieckowski, Z., 2000. Dual finite element methods in homogenization for elastic-plastic fibrous composite material. International Journal of Plasticity 16, 199–221.

Yan, Y., Geng, L., Li, A., 2007. Experimental and numerical studies of the effect of particle size on the deformation behavior of the metal matrix composites. Materials Science and Engineering 448, 315–325.

Publication [P5]

On the Bauschinger effect and kinematic hardening in metal matrix composites modeled by strain gradient plasticity

On the Bauschinger effect and kinematic hardening in metal matrix composites modeled by strain gradient plasticity

R. Azizi [a,*], C.F. Niordson [a], M.G.D. Geers [b], R.H.J. Peerlings [b], B.N. Legarth [a]

[a] *Department of Mechanical Engineering, Solid Mechanics, Technical University of Denmark, DK-2800 Kgs. Lyngby, Denmark*
[b] *Department of Mechanical Engineering, Eindhoven University of Technology, P.O. Box 513, 5600 MB Eindhoven, The Netherlands*

Abstract

The Bauschinger effect in Metal Matrix Composites (MMCs) is studied using a thermodynamically consistent model of energetic higher order strain gradient plasticity, for a reinforcement size ranging from the micron scale and up. Micro-macro homogenization is employed subject to the Hill-Mandel energy condition. As the result, a conventional constitutive model for the macroscopic response is obtained. The study is carried out using a unit cell method of a single cylindrical fiber with periodic boundary conditions under generalized plane strain conditions. The interrelation between the Baushinger effect and the trapped free energy due to residual stresses and higher order stresses is quantified using five different loading paths, including transverse and longitudinal loading as well as in-plane shears and out-of-plane shear. A mathematical representation of the numerically computed trapped energy is introduced, through which the kinematic hardening can be quantified at the macroscopic level. The results are presented in the form of a trapped energy and a Bauschinger stress versus the related plastic strain. The computed Bauschinger stress is compared with the displaced geometric center of the subsequent yield surfaces and a good agreement is found.

*Corresponding Author

Email addresses: reaz@mek.dtu.dk (R. Azizi [a,*]), cn@mek.dtu.dk (C.F. Niordson [a]), M.G.D.Geers@tue.nl (M.G.D. Geers [b]), r.h.j.peerlings@tue.nl (R.H.J. Peerlings [b]), bnl@mek.dtu.dk (B.N. Legarth [a])

Keywords: Metal matrix composite, strain gradient plasticity, kinematic hardening, Bauschinger effect, trapped energy

1. Introduction

Materials like Metal Matrix Composites (MMCs) present enhanced properties like thermostability and stiffness yet at the price of having poor ductility. Generally, these materials contain an elasto-plastic metallic matrix with embedded elastic fibers like Carbon Nano Tubes (CNTs). More details of the properties can be found in McDanels (1985), where aluminum matrix composites are evaluated containing discontinuous silicon carbide reinforcement.

When MMCs are deformed, a portion of the imposed energy related to the plastic deformation, W_p, is dissipated as heat in the micro structure. The rest of this energy, known as the stored energy or trapped energy, Ψ_T, remains available. Knowing the accurate portion of the total work which is dissipated as heat in the microstructure is important for evaluation of properties like thermal softening, which promotes mechanical instabilities, e.g., necking and shear banding. Since the trapped energy is associated with an internal stress state, there is a direct connection with the Bauschinger effect. Therefore, the partitioning of the plastic working, W_p, into heat generation, D, and trapped energy, Ψ_T, is of general interest. There have been several experimental attempts to measure the trapped energy of different materials during plastic deformation, e.g., Oliferuk et al. (1996) and Kapoor and Nemat Nasser (1998). Kuhlmann-Wilsdorf (1970) compared two different types of calorimetric evaluation of the trapped energy implemented by Wolfenden (1970). She asserts that the results of two different experimental measurements affect maximum and minimum values.

Continuum frameworks with internal variables also incorporate the trapped energy (e.g. Rice, 1971; Rosakis et al., 2000; Benzerga et al., 2005). They confirmed a relationship between the trapped energy and Bauschinger stress by presenting the trapped energy as a function of internal parameters like plastic strain, $\Psi_T = \Psi_T(E^p_{ij})$. Chaboche (1993b) used the experimental data of stored energy and considered the constitutive equations in a framework of time-independent thermoplasticity, where he determined the response analytically in the case of uniaxial tension-compression. Benzerga et al. (2005) outlined a theoretical calculation of the trapped energy for planar single crystals under tensile loading with plastic deformation occurring through

dislocation glide. Oliferuk and Maj (2009) compared the experimentally determined stored energy during tensile deformation of austenitic steels and titanium with the part calculated from the stress strain curve.

The aim of the present work is to establish a correlation between the trapped energy and Bauschinger stress in MMCs. The mathematical representation of the trapped energy facilitates the evaluation of kinematic hardening at the macroscopic scale. Studying the size effect of the fiber on the Bauschinger stress is also of interest in this work. Lloyd (1994) showed that the response of composites with the same volume fraction of SiC particles depends on the size of the particles. Further investigations on the elastoplastic behavior of MMCs by Hutchinson (2000), Mughrabi (2001), Fleck et al. (2003) and Gao and Huang (2003) showed that dislocations can not pass from the matrix into the fiber (plastic strain suppression at the fiber-matrix interface) and consequently pile up at the interface.

Non-local plasticity has the capability to reproduce these effects, since it can capture observed size-effects and incorporate non-conventional boundary conditions. Several non local plasticity theories have been developed to face these issues. While some of these are of lower-order nature (see Acharya and Bassani, 2000; Bassani, 2001), most of the proposed theories are of higher order nature, employing higher order stress-measures as work-conjugates to strain gradients, demanding non-conventional higher order boundary conditions (e.g. Fleck and Hutchinson, 1997, 2001; Gao et al., 1999; Gurtin, 2002; Gudmundson, 2004; Gurtin and Anand, 2005; Lele and Anand, 2008; Fleck and Willis, 2009a,b).

In this paper, the energetic higher order strain gradient plasticity theory proposed by Gudmundson (2004) is considered for the matrix material, while a macroscopically conventional response is desirable. For such a connection between the scales, the Hill-Mandel energy condition (Hill, 1963) is considered for the homogenization, where periodic boundary conditions are assumed on the unit cell.

A unit cell is chosen and a finite element cell model under generalized plane strain condition is investigated. The macroscopic trapped energy is evaluated and analyzed during the plastic deformation. Five different loading paths including transverse, longitudinal, 0^o in-plane shear, 45^o in-plane shear and out-of-plane shear are necessary to be considered in order to gather enough data on the trapped energy and the corresponding Bauschinger stresses. A comprehensive fitting function is introduced to represent the numerical data of the trapped energy, which can further be used to evaluate

the Bauschinger stress. The computed Bauschinger stress is also compared with the displaced geometric center of the subsequent yield surfaces.

2. Material models

The matrix material is described by a strain gradient plasticity theory at the micro scale with embedded elastic fibers, while a conventional material model augmented by a free energy depending on the macroscopic plastic strain, is considered at the macro scale.

2.1. Material model at the micro scale

For the matrix, the rate independent energetic strain-gradient plasticity theory proposed by Gudmundson (2004) is used, while the fibers are taken purely elastic. Strong interface is considered for the fiber-matrix interface. For the isothermal problem studied here, the first law of the thermodynamics can be expressed by

$$\dot{w} = \dot{d} + \dot{\psi} \tag{1}$$

where $\dot{w}$ is the rate of total work, $\dot{d}$ is the dissipation rate and $\dot{\psi}$ is the rate of the free energy. The second law of thermodynamics states that dissipation must be non-negative;

$$\dot{d} = \dot{w} - \dot{\psi} \geq 0 \tag{2}$$

At the microscopic scale the variation of the internal virtual work, δw_I, is assumed to be

$$\delta w_I = \int_v [\sigma_{ij}\delta\epsilon_{ij} + (q_{ij} - s_{ij})\delta\epsilon^p_{ij} + m_{ijk}\delta\epsilon^p_{ij,k}]dv \tag{3}$$

where v is the volume and ϵ_{ij} is the total strain, defined as the sum of the elastic strain, ϵ^e_{ij}, and the plastic strain, ϵ^p_{ij}. The Cauchy stress, the deviatoric part of the Cauchy stress, the micro stress (work conjugate to the plastic strain) and the higher order stress (work conjugate to the plastic strain gradients) are denoted by σ_{ij}, s_{ij}, q_{ij} and m_{ijk}, respectively. By application of Gauss' theorem we obtain

$$\delta w_I = \int_s [\sigma_{ij}n_j\delta u_i + m_{ijk}n_k\delta\epsilon^p_{ij}]ds - \tag{4}$$
$$\int_v [\sigma_{ij,j}\delta u_i + (m_{ijk,k} + s_{ij} - q_{ij})\delta\epsilon^p_{ij}]dv$$

where n_i is the unit vector, normal to surface, s, of the volume considered, and u_i is the displacement vector. Assuming that the first term of the right hand side of Eq. (4) equals the external virtual work, δw_E, and using the principle of virtual work, $\delta w_I = \delta w_E$, the last integral must vanish and two sets of equilibrium equations are obtained as

$$\begin{aligned} \sigma_{ij,j} = 0, \quad \text{in} \quad v \\ m_{ijk,k} + s_{ij} - q_{ij} = 0, \quad \text{in} \quad v \end{aligned} \tag{5}$$

Adopting the weak form of the internal work, $\dot{w}_I$, in the second law of the thermodynamics, Eq. (2), and using $\sigma_{ij}\dot{\epsilon}^p_{ij} = s_{ij}\dot{\epsilon}^p_{ij}$, we obtain

$$\left(\sigma_{ij} - \frac{\partial \psi}{\partial \epsilon^e_{ij}}\right)\dot{\epsilon}^e_{ij} + \left(q_{ij} - \frac{\partial \psi}{\partial \epsilon^p_{ij}}\right)\dot{\epsilon}^p_{ij} + \left(m_{ijk} - \frac{\partial \psi}{\partial \epsilon^p_{ij,k}}\right)\dot{\epsilon}^p_{ij,k} \geq 0 \tag{6}$$

It is assumed that the free energy, ψ, is stored due to both elastic strains and plastic strain gradients (see Fredriksson et al., 2009) according to

$$\psi\left(\epsilon^e_{ij}, \epsilon^p_{ij,k}\right) = \frac{1}{2}c_{ijkl}\epsilon^e_{ij}\epsilon^e_{kl} + \frac{1}{2}GL^2_*\epsilon^p_{ij,k}\epsilon^p_{ij,k} \tag{7}$$

where L_* is a material length scale parameter, G is the elastic shear modulus and c_{ijkl} is the isotropic tensor of elastic moduli, defined in terms of Young's modulus, E, and Poisson's ratio, ν. Assuming that both the Cauchy stress and the higher order stress are purely energetic, two constitutive equations are extracted as

$$\sigma_{ij} = \frac{\partial \psi}{\partial \epsilon^e_{ij}} = c_{ijkl}\epsilon^e_{kl}, \quad m_{ijk} = \frac{\partial \psi}{\partial \epsilon^p_{ij,k}} = GL^2_*\epsilon^p_{ij,k} \tag{8}$$

The second law of thermodynamics, Eq. (6), then reads

$$q_{ij}\dot{\epsilon}^p_{ij} \geq 0 \tag{9}$$

In order to ensure that the dissipation is always non-negative according to the above inequality, a dissipation potential function, $f^* = f^*(q_{ij})$, is introduced and a flow rule is defined as

$$\dot{\epsilon}^p_{ij} = \dot{\lambda}\frac{\partial f^*}{\partial q_{ij}} \tag{10}$$

where $\dot{\lambda}$ is a microscopic plastic multiplier. The above equation implies that the plastic strain increment is normal to the dissipation potential function, and it satisfies positive dissipation if the dissipation potential is convex. We now assume an associated flow rule, where the plastic potential function can be substituted by the yield surface, f, (see Lubliner, 1990), according to

$$f^*(q_{ij}) = f(q_{ij}) \tag{11}$$

The microscopic yield surface, f, is defined as

$$f = \sqrt{\frac{3}{2} q_{ij} q_{ij}} - \sigma_f = 0 \tag{12}$$

and a linearly hardening material behaviour is assumed with the flow stress given by $\sigma_f = \sigma_y + h\epsilon_e^p$. Here, σ_y denotes the initial yield stress, h denotes the hardening modulus and ϵ_e^p denotes the accumulated effective plastic strain defined as $\epsilon_e^p = \int \dot{\epsilon}_e^p d\tau$ where τ is "pseudo-time" and $\dot{\epsilon}_e^p = \sqrt{\frac{2}{3}\dot{\epsilon}_{ij}^p \dot{\epsilon}_{ij}^p}$. Then the flow rule, which ensures the normality of the plastic strain increment to the yield surface, is obtained by

$$\dot{\epsilon}_{ij}^p = \dot{\lambda}\frac{\partial f}{\partial q_{ij}} = \frac{3}{2}\frac{q_{ij}}{q_e}\dot{\epsilon}_e^p = r_{ij}\dot{\epsilon}_e^p \tag{13}$$

where $q_e = \sqrt{\frac{3}{2} q_{ij} q_{ij}}$ is the effective micro stress and $r_{ij} = \frac{3}{2}\frac{q_{ij}}{q_e}$ is the direction of the plastic strain increment. For the numerical implementation, a constitutive relation between the micro stress, $\dot{q}_{ij}$, and the plastic strain must be specified. By considering $r_{ij} = \frac{3}{2}\frac{q_{ij}}{q_e}$ or equivalently $q_{ij} = \frac{2}{3} q_e r_{ij}$, we obtain

$$\dot{q}_{ij} = \dot{\overline{\frac{2}{3} q_e r_{ij}}} = \frac{2}{3}\left(\dot{q}_e r_{ij} + q_e \dot{r}_{ij}\right) \tag{14}$$

from which the increment of the micro stress is defined implicitly. The last term on the right hand side of the above equation depends on $\dot{q}_{ij}$ through $\dot{r}_{ij}$. Since this relation does not give $\dot{q}_{ij}$ explicitly, it can not be readily used in the constitutive framework. The last term defines the part of $\dot{q}_{ij}$ tangent to the yield surface, and the first term defines the part of $\dot{q}_{ij}$ normal to the yield surface. The correct magnitude of $\dot{\epsilon}_{ij}^p$ is obtained from the first term alone and the second term has the sole function of ensuring co-coaxiality between q_{ij} and $\dot{\epsilon}_{ij}^p$. Therefore, the second term is removed and replaced by a penalty

term ensuring normality of the plastic strain increment to the yield surface as proposed by Fredriksson et al. (2009). The penalty term is expressed as

$$E_0 \left(\dot{\epsilon}^p_{ij} - \frac{2}{3} r_{ij} r_{kl} \dot{\epsilon}^p_{kl} \right) \tag{15}$$

where the penalty factor, E_0, has to be large compared to the hardening modulus, h. Hence, the flow rule for the micro stress can be rewritten as

$$\dot{q}_{ij} = \frac{2}{3} \left(\frac{2}{3}(h - E_0) r_{ij} r_{kl} + E_0 \delta_{ik} \delta_{jl} \right) \dot{\epsilon}^p_{kl} \tag{16}$$

thus, penalizing any component of the plastic strain increment tangent to the yield surface. Fig. 1 shows a schematic plot of the current and subsequent yield surfaces including the directions.

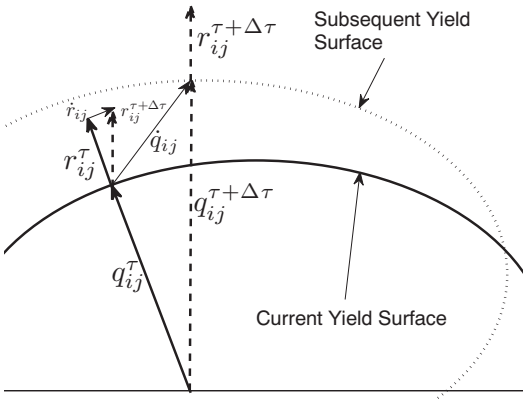

Figure 1: A schematic plot of the current and subsequent yield surfaces.

The incremental version of the constitutive equations is completed by considering the incremental Cauchy stress and higher order stress as

$$\dot{\sigma}_{ij} = D_{ijkl} \dot{\epsilon}^e_{kl} \tag{17}$$

$$\dot{m}_{ijk} = G L_*^2 \dot{\epsilon}^p_{ij,k} \tag{18}$$

2.2. Material model at the macro scale

At the macroscopic scale, the first law of thermodynamics is expressed as

$$\dot{W} = \dot{D} + \dot{\Psi} \tag{19}$$

where $\dot{W}$ is the total work rate, $\dot{D}$ is the dissipation rate and $\dot{\Psi}$ is the rate of the free energy. Non-negative dissipation (see also Coleman and Noll, 1963; Lubliner, 1972; Chaboche, 1993b) is expressed by

$$\dot{D} = \dot{W} - \dot{\Psi} \geq 0 \tag{20}$$

The macroscopic plastic strain is defined by

$$E^p_{ij} = E_{ij} - C^{-1}_{ijkl}\Sigma_{kl} \tag{21}$$

where E_{ij} is the total macroscopic strain, Σ_{kl} is the macroscopic stress and C_{ijkl} is the macroscopic tensor of elastic moduli. The rate of total work in the conventional macroscopic setting is defined by

$$\dot{W} = \Sigma_{ij}\dot{E}_{ij} \tag{22}$$

As explained by Benzerga et al. (2005), a part of the total work may be trapped as unrecoverable stored energy even upon unloading. This trapped energy can be represented by an internal state variable like plastic strain as shown by Rice (1971) and Rosakis et al. (2000). Here, the macroscopic plastic strain tensor is used as an internal variable through which the free energy is stored;

$$\Psi = \frac{1}{2}C_{ijkl}E^e_{ij}E^e_{kl} + \frac{1}{2}P_{ijkl}E^p_{ij}E^p_{kl} \tag{23}$$

Here, P_{ijkl} is a tensor of moduli which defines how plastic strain contributes to the free energy. The first term on the right hand side represents the conventional elastic energy, and the second term represents trapped energy on the microscopic level, which is due to residual stresses as well as residual higher order stresses. Inserting Eqs. (22) and (23) into Eq. (20) gives

$$\Sigma_{ij}\dot{E}_{ij} - \frac{\partial\Psi}{\partial E^e_{ij}}\dot{E}^e_{ij} - \frac{\partial\Psi}{\partial E^p_{ij}}\dot{E}^p_{ij} \geq 0 \tag{24}$$

and considering the macroscopic elastic strain increment as $\dot{E}^e_{ij} = \dot{E}_{ij} - \dot{E}^p_{ij}$, one can have

$$(\Sigma_{ij} - \frac{\partial\Psi}{\partial E^e_{ij}})\dot{E}_{ij} + (\frac{\partial\Psi}{\partial E^e_{ij}} - \frac{\partial\Psi}{\partial E^p_{ij}})\dot{E}^p_{ij} \geq 0 \tag{25}$$

Since $\dot{E}_{ij}$ can be chosen arbitrarily, the first term must vanish as a conservative choice. This means that the macroscopic stress can be derived from the free energy as follows

$$\Sigma_{ij} = \frac{\partial \Psi}{\partial E^e_{ij}} = C_{ijkl} E^e_{kl} \tag{26}$$

Benzerga et al. (2005) showed that in the presence of trapped energy, a Bauschinger effect is expected. A Bauschinger stress, A_{ij}, is now defined as the derivative of free energy with respect to plastic strain (see also Rice, 1971; Chaboche, 1993b,a; Rosakis et al., 2000) as follows

$$A_{ij} = \frac{\partial \Psi}{\partial E^p_{ij}} = P_{ijkl} E^p_{kl} \tag{27}$$

The dissipation inequality, Eq. (25), can now be rewritten as

$$(\Sigma_{ij} - A_{ij}) \dot{E}^p_{ij} \geq 0 \tag{28}$$

In order to ensure non-negative dissipation, the plastic strain rate is derived from a convex dissipation potential, $\Phi^* = \Phi^*(\Sigma_{ij} - A_{ij})$, according to

$$\dot{E}^p_{ij} = \dot{\Lambda} \frac{\partial \Phi^*(\tilde{\Sigma}_{ij})}{\partial \tilde{\Sigma}_{ij}} = \dot{\Lambda} \frac{\partial \Phi^*(\tilde{\Sigma}_{ij})}{\partial \Sigma_{ij}} \tag{29}$$

where $\tilde{\Sigma}_{ij} = \Sigma_{ij} - A_{ij}$ and $\dot{\Lambda}$ is a macroscopic plastic multiplier. Adopting the principle of maximum plastic dissipation (see Lubliner, 1990), implies: (I) the dissipation potential function is convex; and (II) the plastic strain is normal to the dissipation potential function. Incorporating Drucker's postulates (see Drucker, 1951), as a non-thermodynamical approach for the plastic work definition, the yield surface itself is a plastic potential. Hence, normality is associated with the yield criterion or in other words an associative flow rule is obtained as

$$\Phi^*(\tilde{\Sigma}_{ij}) = \Phi(\tilde{\Sigma}_{ij}) \tag{30}$$

where $\Phi(\tilde{\Sigma}_{ij})$ is the macroscopic yield function. It will be shown that a modification of the Hill anisotropic yield function (Hill, 1948) is applicable to the material system analyzed. The first modification is that the Bauschinger stress, A_{ij}, determines the geometrical center of the yield surface. Due to the assumption of having long unidirectional fiber, the shear terms Σ_{13} and Σ_{23} are ignored where we may express the yield function as

$$\Phi = F(\tilde{\Sigma}_{11} - \tilde{\Sigma}_{33})^2 + G(\tilde{\Sigma}_{22} - \tilde{\Sigma}_{33})^2 + H(\tilde{\Sigma}_{11} - \tilde{\Sigma}_{22})^2 + 2N\tilde{\Sigma}^2_{12} - 1 \tag{31}$$

where F, G, H and N are the anisotropic parameters. While the above function is pressure independent, it will be shown that the yield surface for the material system considered here is not independent of pressure, but instead independent of some other linear combination of the normal components of $\tilde{\Sigma}_{ij}$, depending on the fiber volume fraction. Incorporating this into the yield function, Eq. (31), results in

$$\Phi = F^{\lambda}(\tilde{\Sigma}_{\lambda_1})^2 + H^{\lambda}(\tilde{\Sigma}_{\lambda_2})^2 + N^{\lambda}\tilde{\Sigma}^2_{\lambda_4} - 1 \tag{32}$$

where F^{λ}, H^{λ} and N^{λ} are new anisotropic parameters and $\tilde{\Sigma}_{\lambda_4} = \Sigma_{12} - A_{12}$. The remaining $\tilde{\Sigma}_{\lambda_i}$ $(i = 1, 2, 3)$ are linearly independent combinations of the normal components of $\tilde{\Sigma}_{ij}$. In the above expression, it is assumed that the yield function is independent of $\tilde{\Sigma}_{\lambda_3}$, hence it is not included in the yield function.

In Tab. 1 an overview of the corresponding equations at the micro and macro scales is given.

3. Homogenization

The matrix material is governed by strain gradient plasticity at the micro scale, while a conventional material response is to be recovered at the macro scale. The micro-macro homogenization is based on the Hill-Mandel energy condition, which ensures that the work per unit of volume expended at the micro scale equals that of the macro scale, see Hill (1963) and Suquet (1985).

Kinematic variables representing the deformation at the various scales are now introduced. The displacement of a material point, X_i, in the undeformed state to a point, Y_i, in the deformed state is defined as $Y_i = X_i + U_i$, where U_i is the macroscopic displacement vector. Considering a macroscopically homogeneous deformation state, the displacement field can be expressed by the first term in the Taylor expansion about any point, X_i^0, as

$$U_i = (U_i)_{X_i^0} + \left(\frac{\partial U_i}{\partial X_j}\right)_{X_i^0} (X_j - X_j^0) \tag{33}$$

where $\frac{\partial U_i}{\partial X_j}$ is the macroscopic displacement gradient. The microscopic displacement, u_i, is then defined in terms of the macroscopic displacement, U_i, and a microstructural fluctuation field, w_i, as follows

$$u_i = U_i + w_i \tag{34}$$

Equation	Micro scale	Macro scale
1st law of TD	$\dot{w} = \dot{d} + \dot{\psi}$	$\dot{W} = \dot{D} + \dot{\Psi}$
2nd law of TD	$\dot{d} = \dot{w} - \dot{\psi} \geq 0$	$\dot{D} = \dot{W} - \dot{\Psi} \geq 0$
Internal work	$\dot{w} = \sigma_{ij}\dot{\epsilon}^e_{ij} + q_{ij}\dot{\epsilon}^p_{ij} + m_{ijk}\dot{\epsilon}^p_{ij,k}$	$\dot{W} = \Sigma_{ij}\dot{E}_{ij}$
Free energy	$\psi = \frac{1}{2}c_{ijkl}\epsilon^e_{ij}\epsilon^e_{kl} + \frac{1}{2}GL^2_*\epsilon^p_{ij,k}\epsilon^p_{ij,k}$	$\Psi = \frac{1}{2}C_{ijkl}E^e_{ij}E^e_{kl} + \frac{1}{2}P_{ijkl}E^p_{ij}E^p_{kl}$
Dissipation inequality 1	$\left(\sigma_{ij} - \frac{\partial\psi}{\partial\epsilon^e_{ij}}\right)\dot{\epsilon}^e_{ij} + \left(q_{ij} - \frac{\partial\psi}{\partial\epsilon^p_{ij}}\right)\dot{\epsilon}^p_{ij} + \left(m_{ijk} - \frac{\partial\psi}{\partial\epsilon^p_{ij,k}}\right)\dot{\epsilon}^p_{ij,k} \geq 0$	$(\Sigma_{ij} - \frac{\partial\Psi}{\partial E^e_{ij}})\dot{E}_{ij} + (\frac{\partial\Psi}{\partial E^e_{ij}} - \frac{\partial\Psi}{\partial E^p_{ij}})\dot{E}^p_{ij} \geq 0$
Conventional stress	$\sigma_{ij} = \frac{\partial\psi}{\partial\epsilon^e_{ij}} = c_{ijkl}\epsilon^e_{kl}$	$\Sigma_{ij} = \frac{\partial\Psi}{\partial E^e_{ij}} = C_{ijkl}E^e_{kl}$
Nonconventional stress	$m_{ijk} = \frac{\partial\psi}{\partial\epsilon^p_{ij,k}} = GL^2_*\epsilon^p_{ij,k}$	$A_{ij} = \frac{\partial\Psi}{\partial E^p_{ij}} = P_{ijkl}E^p_{kl}$
Dissipation inequality 2	$q_{ij}\dot{\epsilon}^p_{ij} \geq 0$	$(\Sigma_{ij} - A_{ij})\,\dot{E}^p_{ij} \geq 0$
Flow potential	$\dot{\epsilon}^p_{ij} = \dot{\lambda}\frac{\partial f^*(q_{ij})}{\partial q_{ij}}$	$\dot{E}^p_{ij} = \dot{\Lambda}\frac{\partial\Phi^*(\Sigma_{ij}-A_{ij})}{\partial\Sigma_{ij}}$
General yield surface	$f(q_{ij}) = f^*(q_{ij})$	$\Phi\left(\Sigma_{ij} - A_{ij}\right) = \Phi^*\left(\Sigma_{ij} - A_{ij}\right)$
Specific yield surface 1	$f = \sqrt{\frac{3}{2}q_{ij}q_{ij}} - \sigma_f$	$\Phi = F^\lambda(\tilde{\Sigma}_{\lambda_1})^2 + H^\lambda(\tilde{\Sigma}_{\lambda_2})^2 + N^\lambda\tilde{\Sigma}^2_{\lambda_4} - 1$

Table 1: Material models at the micro- and macroscales.

Introducing the macroscopic strain tensor, $E_{ij} = \frac{1}{2}\left(\frac{\partial U_i}{\partial X_j} + \frac{\partial U_j}{\partial X_i}\right)_{X^0_i}$, and rotation tensor, $R_{ij} = \frac{1}{2}\left(\frac{\partial U_i}{\partial X_j} - \frac{\partial U_j}{\partial X_i}\right)_{X^0_i}$, Eq. (34) can be expressed as

$$u_i = (U_i)_{X^0_i} + (E_{ij} + R_{ij})\,(X_j - X^0_j) + w_i \tag{35}$$

Defining the microscopic strain tensor by $\epsilon_{ij} = \frac{1}{2}\left(\frac{\partial u_i}{\partial X_j} + \frac{\partial u_j}{\partial X_i}\right)$ and evaluating the volume average, we obtain

$$\frac{1}{v}\int_v \epsilon_{ij}dv = E_{ij} + \frac{1}{2v}\int_v \left(\frac{\partial w_i}{\partial X_j} + \frac{\partial w_j}{\partial X_i}\right)dv \tag{36}$$

Under the assumption of periodic displacement boundary conditions, the last

term in Eq. (36) vanishes upon application of Gauss' theorem as

$$\frac{1}{2v}\int_v \left(\frac{\partial w_i}{\partial X_j}+\frac{\partial w_j}{\partial X_i}\right) dv = \frac{1}{v}\int_s w_i n_j ds = 0 \tag{37}$$

A sufficient condition for the above equation to hold is

$$w_i^A(\Gamma) n_j^A(\Gamma) + w_i^B(\Gamma) n_j^B(\Gamma) = 0 \tag{38}$$

where Γ is a local coordinate on opposite sides of the unit cell, A and B, for which periodicity is enforced. It is now seen that the periodicity assumption, $w_i^A(\Gamma) = w_i^B(\Gamma)$ and $n_j^A(\Gamma) = -n_j^B(\Gamma)$, fulfills Eq. (38). Hence, the macroscopic strain equals the volume average of microscopic strain as

$$E_{ij} = \frac{1}{v}\int_v \epsilon_{ij} dv \tag{39}$$

The Hill-Mandel energy condition is used to extract the appropriate macroscopic work-conjugate to the macroscopic strain. The microscopic volume average of the variation of the work performed on the unit cell is assumed to be equal to the variation of the internal work per unit of volume at the macro scale as expressed by

$$\frac{1}{v}\int_v [\sigma_{ij}\delta\epsilon_{ij} + (q_{ij} - s_{ij})\delta\epsilon_{ij}^p + m_{ijk}\delta\epsilon_{ij,k}^p] dv = \Sigma_{ij}\delta E_{ij} \tag{40}$$

Using Gauss theorem and the equilibrium equations, Eq. (5), we obtain

$$\frac{1}{v}\int_s [\sigma_{ij} n_j \delta u_i + m_{ijk} n_k \delta\epsilon_{ij}^p] ds = \Sigma_{ij}\delta E_{ij} \tag{41}$$

Taking the variation of Eq. (35), $\delta u_i = (\delta E_{ij} + \delta R_{ij})\, X_j + \delta w_i$, and inserting it in Eq. (41), we get

$$\frac{1}{v}\int_s \sigma_{ij} n_j X_k ds \delta E_{ik} + \frac{1}{v}\int_s \sigma_{ij} n_j X_k ds \delta R_{ik} + \frac{1}{v}\int_s \sigma_{ij} n_j \delta w_i ds + \frac{1}{v}\int_s m_{ijk} n_k \delta\epsilon_{ij}^p ds = \Sigma_{ij}\delta E_{ij} \tag{42}$$

The second term of the above equation vanishes upon application of Gauss' theorem and equilibrium, since R_{ik} is skew-symmetric. Under the assumption

of periodic boundary conditions for the unit cell, the third and fourth term vanish:

$$\frac{1}{v}\int_s \sigma_{ij} n_j \delta w_i ds = \quad \tfrac{1}{v}\textstyle\int_s T_i \delta w_i ds = 0 \tag{43}$$

$$\frac{1}{v}\int_s m_{ijk} n_k \delta \epsilon^p_{ij} ds = \quad \tfrac{1}{v}\textstyle\int_s M_{ij} \delta \epsilon^p_{ij} ds = 0 \tag{44}$$

where $T_i = \sigma_{ij} n_j$ and $M_{ij} = m_{ijk} n_k$ are the traction and higher order traction on the surface of the unit cell. Hence, the macroscopic stress which is work conjugate to E_{ij}, is obtained from

$$\left[\frac{1}{v}\int_s \sigma_{ij} n_j X_k ds\right] \delta E_{ik} = \Sigma_{ik} \delta E_{ik} \tag{45}$$

Using Gauss' theorem and the equilibrium, we can express the macroscopic stress as the volume average of microscopic stress

$$\Sigma_{ij} = \frac{1}{v}\int_v \sigma_{ij} dv \tag{46}$$

Tab. 2 summarizes the connection between the scales.

	Micro scale	Macro scale	Connection
Displacement	u_i	U_i	$u_i = U_i + w_i$
Conventional strain	ϵ_{ij}	E_{ij}	$E_{ij} = \frac{1}{v}\int_v \epsilon_{ij} dv$
Non-conventional strain	$\epsilon^p_{ij,k}$	Not Available	Not Available
Conventional stress	σ_{ij}	Σ_{ij}	$\Sigma_{ij} = \frac{1}{v}\int_v \sigma_{ij} dv$
Non-conventional stress	m_{ijk}	A_{ij}	Not Applicable
Free energy	ψ	Ψ	$\Psi = \frac{1}{v}\int_v \psi dv$
Internal work	w	W	$W = \frac{1}{v}\int_v w dv$
Conventional operator	c_{ijkl}	C_{ijkl}	$\Psi_e = \frac{1}{2} C_{ijkl} E^e_{ij} E^e_{kl}$ $\Psi_e = \frac{1}{v}\int_v \psi_e dv$
Non conventional operator	GL^2_*	P_{ijkl}	$\Psi_T = \frac{1}{2} P_{ijkl} E^p_{ij} E^p_{kl}$ $\Psi_T = \frac{1}{v}\int_v \psi_T dv$

Table 2: Connection between the scales.

4. Unit cell problem formulation

A MMC with parallel circular fibers distributed regularly through the material is considered (see Fig. 2a). Loading paths studied are macroscopic tri-axial normal stress under a generalized plane strain condition and in-plane shear (excluding out-of-plane shear stresses, Σ_{13} and Σ_{23}). A unit cell is extracted as shown in Fig. 2(b), where both macroscopic normal stresses and in-plane shear stress are indicated. At the left-bottom corner of the unit cell, a reference Cartesian coordinate system, x_i, is located and aligned with the sides of the cell. The positive direction of the third axis, x_3, points in the direction of the fibers. Fig. 2(c) shows the displacement boundary conditions and dimensions of the unit cell. The radius of the fibers is denoted by r, the dimensions of the unit cell in the direction of the coordinate axes (perpendicular to the fiber direction) are denoted by a and b, while the thickness of the unit cell is denoted by t.

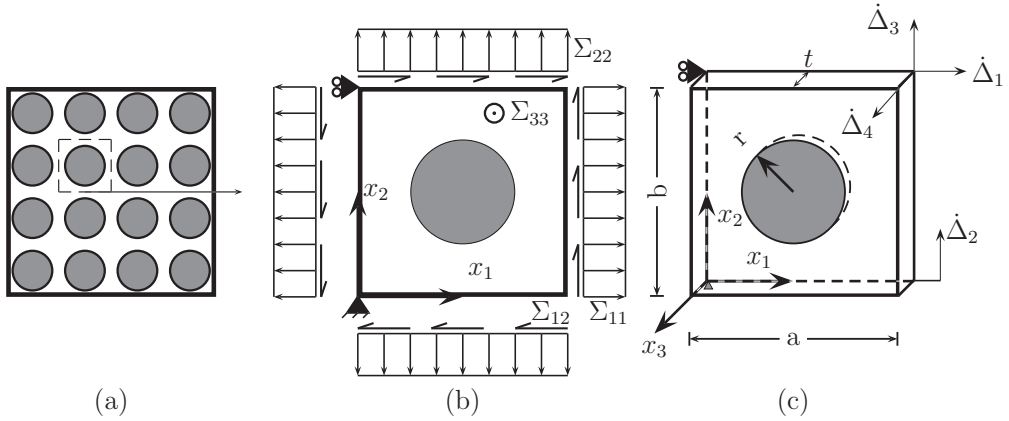

Figure 2: (a) Regular distribution of fibers in the MMC. (b) Unit cell containing one fiber with traction boundary condition. (c) Unit cell containing one fiber with conventional displacement boundary conditions used in numerical simulation representing combined biaxial shear loading as shown in (*b*).

Fibers are considered to be purely elastic, whereas the matrix exhibits an elasto-plastic behavior with gradient effects as described in Section 2. Since plastic strain-gradients are of higher order nature, higher-order boundary conditions must be prescribed in addition to the conventional conditions on

displacements and surface tractions. At the exterior of the cell, periodic boundary conditions are used (see Borg et al., 2008; Hussein et al., 2008; Azizi et al., 2011a),

$$\begin{array}{llll} \dot{u}_1^b = \dot{u}_1^t & \text{and} & \dot{u}_2^b = \dot{u}_2^t - [\dot{\Delta}_3 - \dot{\Delta}_2] \\ \dot{T}_1^b = -\dot{T}_1^t & \text{and} & \dot{T}_2^b = -\dot{T}_2^t \\ \dot{u}_1^l = \dot{u}_1^r - \dot{\Delta}_1 & \text{and} & \dot{u}_2^l = \dot{u}_2^r - \dot{\Delta}_2 \\ \dot{T}_1^l = -\dot{T}_1^r & \text{and} & \dot{T}_2^l = -\dot{T}_2^r \\ \dot{M}_{ij}^b = -\dot{M}_{ij}^t & \text{and} & \dot{M}_{ij}^l = -\dot{M}_{ij}^r \\ [\dot{\epsilon}_{ij}^p]^b = [\dot{\epsilon}_{ij}^p]^t & \text{and} & [\dot{\epsilon}_{ij}^p]^l = [\dot{\epsilon}_{ij}^p]^r \end{array} \tag{47}$$

In the above equations, the super-scripts b, t, l and r refer to bottom, top, left and right of the unit cell, respectively. Note that in the above conditions, displacements and plastic strains are enforced while the tractions and higher order tractions are obtained. In addition to periodic boundary conditions for the displacements and plastic strains, the following conditions are imposed

$$\begin{array}{lll} \dot{u}_1 = \dot{u}_2 = 0, & \text{at} & (x_1, x_2) = (0, 0) \\ \dot{u}_2 = \dot{\Delta}_2, & \text{at} & (x_1, x_2) = (a, 0) \\ \dot{u}_1 = \dot{\Delta}_1,\ \dot{u}_2 = \dot{\Delta}_3, & \text{at} & (x_1, x_2) = (a, b) \\ \dot{u}_3 = 0 & \text{at} & x_3 = 0 \\ \dot{u}_3 = \dot{\Delta}_4 & \text{at} & x_3 = t \\ \dot{\epsilon}_{ij}^p = 0, & \text{at} & (x_1^2 + x_2^2 = r^2) \end{array} \tag{48}$$

where $\dot{\Delta}_1$, $\dot{\Delta}_2$, $\dot{\Delta}_3$ and $\dot{\Delta}_4$ are prescribed displacement rate quantities. The out-of-plane plastic strain, ϵ_{33}^p, depends on the in-plane plastic strain components by plastic incompressibility, $\epsilon_{ii}^p = 0$. Similarly, M_{33} is given in terms of the in-plane components M_{11} and M_{22}, where $M_{ii} = 0$. Finally, out-of-plane deformation is controlled by specifying a constant out-of-plane normal strain increment, $\dot{\epsilon}_{33} = \dot{\Delta}_4/t$, with t denoting the reference thickness of the unit cell. In summary, the problem in its general form has one material length parameter, L_*, and four geometrical length parameters, a, b, r, t, in addition to the conventional material parameters.

A strain based yield criterion at the macro scale is used where an overall effective plastic strain (here calculated as the 2-norm) exceeds some threshold value, ϵ_t, according to

$$\left|E_{ij} - C^{-1}_{ijkl}\Sigma_{kl} - E^{res}_{ij}\right| \geq \epsilon_t \tag{49}$$

Proportionality of the macroscopic stresses is imposed such that

$$\kappa_1 = \frac{\Sigma_{22}}{\Sigma_{11}}, \qquad \kappa_2 = \frac{\Sigma_{33}}{\Sigma_{11}} \qquad \text{and} \qquad \kappa_3 = \frac{\Sigma_{12}}{\Sigma_{11}} \tag{50}$$

are constants within a proportional loading. Details on the numerical implementation can be found in Azizi et al. (2011b).

5. Numerical solution

5.1. Finite element method

Numerical solutions are obtained using the finite element method based on the rate of the principle of virtual work (Gudmundson, 2004)

$$\int_v [\dot{\sigma}_{ij}\delta\dot{\epsilon}_{ij} + (\dot{q}_{ij} - \dot{s}_{ij})\delta\dot{\epsilon}^p_{ij} + \dot{m}_{ijk}\delta\dot{\epsilon}^p_{ij,k}]dv = \int_s [\dot{T}_i\delta\dot{u}_i + \dot{M}_{ij}\delta\dot{\epsilon}^p_{ij}]ds, \tag{51}$$

where $\dot{T}_i$ and $\dot{M}_{ij}$ are traction rate and moment traction rate, respectively. An eight-node quadrilateral element is used for the in-plane displacement interpolation, while a four-node quadrilateral element is used to interpolate the plastic strain components. This choice provides a similar order of interpolation for both plastic strain and the total strain. Additionally, an extra degree of freedom is added for the entire mesh to represent the thickness change of the unit cell (accommodating the generalized plane strain condition). Nodal interpolation is used according to

$$\dot{u}_i = \sum_{n=1}^{2k} N^n_u \dot{d}^n_i, \quad \dot{\epsilon}^p_{ij} = \sum_{m=1}^{3l} O^m_p \dot{e}^m_{ij} \tag{52}$$

where N^n_u and O^m_p are shape functions for the displacement and plastic strain components, respectively and $k = 8$ and $l = 4$ are the number of nodes used for the different interpolation schemes. $\dot{d}^n_i$ and $\dot{e}^m_{ij}$ are nodal values at node n for displacements and at node m for plastic strains, respectively. The appropriate derivatives of the displacement field and the plastic strain field can be expressed as

$$\dot{\epsilon}_{ij} = \sum_{n=1}^{2k} \frac{1}{2}\left(B^n_{uj}\dot{d}^n_i + B^n_{ui}\dot{d}^n_j\right), \quad \dot{\epsilon}^p_{ij,k} = \sum_{m=1}^{3l} Q^m_{pk}\dot{e}^m_{ij} \tag{53}$$

where $B^n_{ij} = (N^n_{i,j} + N^n_{j,i})/2$ and $Q^m_{pk} = O^m_{p,k}$ are appropriate spatial derivatives of the shape functions. The discretized equations obtained from the principle of virtual work can be expressed by

$$\begin{bmatrix} \mathbf{K}_u & -\mathbf{K}_{up} \\ -\mathbf{K}^T_{up} & \mathbf{K}_p \end{bmatrix} \begin{bmatrix} \dot{\mathbf{U}} \\ \dot{\boldsymbol{\epsilon}}^p \end{bmatrix} = \begin{bmatrix} \dot{\mathbf{f}}_u \\ \dot{\mathbf{f}}_p \end{bmatrix} \tag{54}$$

where $\dot{\mathbf{f}}_u = \int_s \mathbf{N}^T \dot{\mathbf{T}} ds$ is the nodal force vector and $\dot{\mathbf{f}}_p = \int_s \mathbf{O}^T \dot{\mathbf{M}} ds$ is the higher order nodal force vector. The system matrices are given by

$$\mathbf{K}_u = \int_v \mathbf{B}^T \mathbf{D}_e \mathbf{B} dv \tag{55}$$

$$\mathbf{K}_p = \int_v [\mathbf{O}^T (\mathbf{D}_e + \mathbf{D}_p)\mathbf{O} + \mathbf{Q}^T \mathbf{D}_h \mathbf{Q}] dv \tag{56}$$

$$\mathbf{K}_{up} = \int_v \mathbf{B}^T \mathbf{D}_e \mathbf{P} dv \tag{57}$$

where $\mathbf{D}_e$ is the isotropic elastic constitutive matrix, $\mathbf{D}_p$ is the matrix of plastic moduli and $\mathbf{D}_h$ is the matrix of higher order moduli. Further details can be found in Fredriksson et al. (2009) and (Azizi et al., 2011b,a).

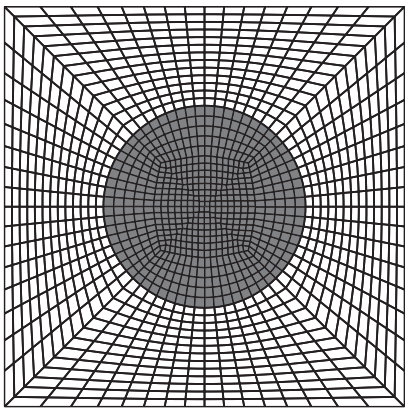

Figure 3: An example of finite element mesh used in the numerical computations.

Fig. 3 shows an example of finite element mesh, with 1408 elements as used in the numerical computations. Numerical integration is performed using the forward Euler method with small load increments. More details on the numerical issues are found in Azizi et al. (2011b).

5.2. Numerical calculation of elastic moduli (C_{ijkl})

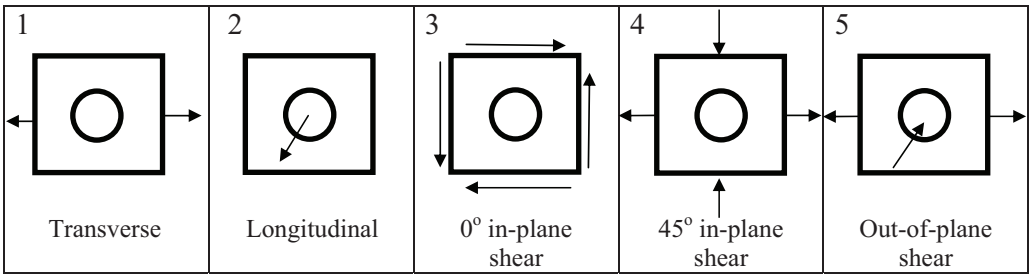

Figure 4: The five loading paths used to obtain both the elastic moduli, C_{ijkl}, and Bauschinger moduli, P_{ijkl}.

It is important to mention that the macroscopic conventional constitutive behavior, $\Sigma_{ij} = C_{ijkl}E^e_{kl}$, has not been identified as a priori during the homogenization. Therefore, the macroscopic elastic operator, C_{ijkl}, can be determined numerically from the relation between variation of the macroscopic free energy and variation of the macroscopic deformation at any point in the elastic regime. For the five loading paths, shown in Fig. 4 (transverse and longitudinal loading, 0^o and 45^o in-plane shear and out-of-plane shear), see Tab. 3 for the κ-values, the microscopic elastic energy is evaluated at pseudo-time τ as

	κ_1	κ_2	κ_3
Transverse	0	0	0
Longitudinal	1	1000	0
0^o-shear	0	0	1000
45^o-shear	-1	0	0
Out-of-plane shear	0	-1	0

Table 3: κ-values for the five different loading paths.

$$\Psi_e^{\tau+\Delta\tau} = \Psi_e^{\tau} + \frac{1}{v}\int_v \sigma_{ij}^{\tau_m}\dot{\epsilon}_{ij}^e dv \cdot \Delta\tau \tag{58}$$

where $\tau_m = \frac{2\tau+\Delta\tau}{2}$ and $\Delta\tau$ is pseudo-time increment. The components of the macroscopic elastic operator, C_{ijkl}, are solved using the relation, $\Psi_e =$

$\frac{1}{2}C_{ijkl}E^e_{ij}E^e_{kl}$. Exploiting the material symmetries for the present problem, all moduli can be solved from the following system of equations:

$$\begin{bmatrix}\Psi^1_e\\ \Psi^2_e\\ \Psi^3_e\\ \Psi^4_e\\ \Psi^5_e\end{bmatrix} = \begin{bmatrix}a^1 & b^1 & c^1 & d^1 & e^1\\ a^2 & b^2 & c^2 & d^2 & e^2\\ a^3 & b^3 & c^3 & d^3 & e^3\\ a^4 & b^4 & c^4 & d^4 & e^4\\ a^5 & b^5 & c^5 & d^5 & e^5\end{bmatrix} \times \begin{bmatrix}C_{1111}\\ C_{1122}\\ C_{1133}\\ C_{3333}\\ C_{1212}\end{bmatrix} \tag{59}$$

where for each of the five loading paths, the constants are defined according to $a = \frac{1}{2}(E^e_{11})^2 + \frac{1}{2}(E^e_{22})^2$, $b = E^e_{11}E^e_{22}$, $c = (E^e_{11} + E^e_{22})E^e_{33}$, $d = \frac{1}{2}(E^e_{33})^2$ and $e = \frac{1}{2}(E^e_{12})^2$. Using a reduced index notation according to $1 \approx 11$, $2 \approx 22$, $3 \approx 33$ and $4 \approx 12$, a matrix of elastic moduli is defined as

$$\boldsymbol{C} = \begin{bmatrix}C_{11} & C_{12} & C_{13} & 0\\ C_{12} & C_{11} & C_{13} & 0\\ C_{13} & C_{13} & C_{33} & 0\\ 0 & 0 & 0 & C_{44}\end{bmatrix} \tag{60}$$

where the decoupling between the shear component and the normal components arises due to the material symmetries. Assuming the transversely isotropic with $a = b$, results in $C_{11} = C_{22}$ and $C_{13} = C_{23}$.

5.3. Numerical calculation of Bauschinger moduli (P_{ijkl})

The main goal is to quantify the composite Bauschinger moduli, P_{ijkl} (Eq. 27), which can be used to represent the trapped energy and the corresponding Bauschinger stress at the macro scale. The details of the computational scheme for evaluating the Bauschinger moduli is described below:

1. For the five loading paths, shown in Fig. 4 (transverse and longitudinal loading, 0^o and 45^o in-plane shear and out-of-plane shear), the microscopic trapped energy is evaluated, see Tab. 3.

The trapped energy at the pseudo-time τ is evaluated as conventionally suggested by Benzerga et al. (2005) according to

$$\Psi_T^{\tau+\Delta\tau} = \Psi_T^{\tau} + \frac{1}{v}\int_v [\sigma_{ij}^{\tau_m}\dot{\epsilon}^e_{ij} + m_{ijk}^{\tau_m}\dot{\epsilon}^p_{ij,k}]dv \cdot \Delta\tau - \frac{1}{2}\Sigma_{ij}^{\tau_m}S_{ijkl}\Sigma_{kl}^{\tau_m} \tag{61}$$

where $S_{ijkl} = C^{-1}_{ijkl}$ is the macroscopic compliance tensor and $\tau_m = \frac{2\tau+\Delta\tau}{2}$.

2. The components of the tensor of Bauschinger moduli, P_{ijkl}, are solved for the maximum load using the relation, $\Psi_T = \frac{1}{2} P_{ijkl} E^p_{ij} E^p_{kl}$. Exploiting the material symmetries for the present problem, all moduli can be solved from the following system of equations:

$$\begin{bmatrix} \Psi_T^1 \\ \Psi_T^2 \\ \Psi_T^3 \\ \Psi_T^4 \\ \Psi_T^5 \end{bmatrix} = \begin{bmatrix} a^1 & b^1 & c^1 & d^1 & e^1 \\ a^2 & b^2 & c^2 & d^2 & e^2 \\ a^3 & b^3 & c^3 & d^3 & e^3 \\ a^4 & b^4 & c^4 & d^4 & e^4 \\ a^5 & b^5 & c^5 & d^5 & e^5 \end{bmatrix} \times \begin{bmatrix} P_{1111} \\ P_{1122} \\ P_{1133} \\ P_{3333} \\ P_{1212} \end{bmatrix} \tag{62}$$

where for each of the five loading paths, the constants are defined according to $a = \frac{1}{2}(E^p_{11})^2 + \frac{1}{2}(E^p_{22})^2$, $b = E^p_{11} E^p_{22}$, $c = (E^p_{11} + E^p_{22}) E^p_{33}$, $d = \frac{1}{2}(E^p_{33})^2$ and $e = \frac{1}{2}(E^p_{12})^2$. Using a reduced index notation according to $1 \approx 11$, $2 \approx 22$, $3 \approx 33$ and $4 \approx 12$, a matrix of Baushinger moduli is defined as, see Eq. (60),

$$\boldsymbol{P} = \begin{bmatrix} P_{11} & P_{12} & P_{13} & 0 \\ P_{12} & P_{11} & P_{13} & 0 \\ P_{13} & P_{13} & P_{33} & 0 \\ 0 & 0 & 0 & P_{44} \end{bmatrix} \tag{63}$$

where the decoupling between the shear component and the normal components arises due to the material symmetries.

3. The four eigenvalues, P_{λ_i} (i=1,...,4), and the corresponding unit eigenvectors, $\boldsymbol{v}^{\lambda_i}$, of $\boldsymbol{P}$ are then found and written as

$$\boldsymbol{P}_\lambda = \begin{bmatrix} P_{\lambda_1} & P_{\lambda_2} & P_{\lambda_3} & P_{\lambda_4} \end{bmatrix} \tag{64}$$

$$\boldsymbol{V} = \begin{bmatrix} v_1^{\lambda_1} & v_1^{\lambda_2} & v_1^{\lambda_3} & v_1^{\lambda_4} \\ v_2^{\lambda_1} & v_2^{\lambda_2} & v_2^{\lambda_3} & v_2^{\lambda_4} \\ v_3^{\lambda_1} & v_3^{\lambda_2} & v_3^{\lambda_3} & v_3^{\lambda_4} \\ v_4^{\lambda_1} & v_4^{\lambda_2} & v_4^{\lambda_3} & v_4^{\lambda_4} \end{bmatrix} \tag{65}$$

where $v_j^{\lambda_i}$ is the j_{th} component of an eigenvector corresponding to the i_{th} eigenvalue.

4. The plastic strain components are then transformed using the transformation matrix of unit eigenvectors according to

$$\begin{bmatrix} E^P_{\lambda_1} \\ E^P_{\lambda_2} \\ E^P_{\lambda_3} \\ E^P_{\lambda_4} \end{bmatrix} = \boldsymbol{V^T} \begin{bmatrix} E^P_{11} \\ E^P_{22} \\ E^P_{33} \\ E^P_{12} \end{bmatrix} \tag{66}$$

where $E^P_{\lambda_i}$ is the transformed plastic strain. Note that this is not a transformation of the plastic strain tensor itself, but rather a tranformation of the vector of plastic strain components.

5. This transformation enables a diagonalized expression for the trapped energy as

$$\Psi_T = \sum_{i=1}^{4} \frac{1}{2} P_{\lambda_i} \left(E^p_{\lambda_i}\right)^2 \tag{67}$$

6. In the transformed plastic strain coordinate system, the Bauschinger stress is calculated according to

$$A_{\lambda_i} = \frac{\partial \Psi_T}{\partial E^p_{\lambda_i}} = P_{\lambda_i} E^p_{\lambda_i} \tag{68}$$

where A_{λ_i} is the transformed Bauschinger stress. To have a consistent analysis, the Cauchy stress, Σ_{ij}, is also transformed according to

$$\begin{bmatrix} \Sigma_{\lambda_1} \\ \Sigma_{\lambda_2} \\ \Sigma_{\lambda_3} \\ \Sigma_{\lambda_4} \end{bmatrix} = \boldsymbol{V^T} \begin{bmatrix} \Sigma_{11} \\ \Sigma_{22} \\ \Sigma_{33} \\ \Sigma_{12} \end{bmatrix} \tag{69}$$

Due to the decoupling of the shear component and the normal components, this is energetically consistent as $\Sigma_{ij} E^p_{ij} = \sum_{i=1}^{3} \Sigma_{\lambda_i} E^p_{\lambda_i} + 2\Sigma_{\lambda_4} E^p_{\lambda_4}$. Without this decoupling, a careful consideration must be taken to transform stresses, while maintaining the work-conjugacy.

It is noted that the above procedure results into the evaluation of the Bauschinger stress, A_{ij}, as the geometrical center of a multi dimensional yield surface. Fig. 5 shows a flowchart, summarizing the described computational procedure.

6. Results

The conventional material parameters used for the matrix are $h/E_m = 0.1$, $\sigma_y/E_m = 0.004$, $\tau_y = \sigma_y/\sqrt{3}$, $\nu_m = 0.3$, and for the fibers, $E_f = 5.7E_m$ and $\nu_f = 0.17$. The dimension of the unit cell is defined by $a = b$, and each numerical computation includes 1408 elements with 500 increments for each sequence of loading, unloading and reloading. For a micron scale length parameter of $L_* = 1\mu m$ in the present model, we analyze cases for $L_*/r = 0$, $L_*/r = 0.2$ and $L_*/r = 0.4$, which corresponds to large fibers, fibers with $r = 5\mu m$ and $r = 2.5\mu m$, respectively.

The eigendirections, $\boldsymbol{v}^{\lambda_i}$, of the $\boldsymbol{P}$-matrix, which are used to transform the Bauschinger stress and plastic strain are plotted in Fig. 6 for a composite with $V_f = 0.2$ and $L_*/r = 0.4$. The initial yield surface of the composite is shown at a number of different hydrostatic stress states, together with the isotropic von Mises yield surface of the matrix material. The yield condition for the composite yield surface is defined as in Azizi et al. (2011a), with some threshold value for the two-norm of the plastic strain according to $|E^p_{ij}| \geq 0.001$. As can be seen, the composite yield surface has an almost elliptical cross section which is expanded compared to the matrix yield surface. It is important to note that the third eigendirection of the $\boldsymbol{P}$-matrix, $\boldsymbol{v}^{\lambda_3}$, is parallel to the cylinder axis of the composite yield surface and it deviates from the cylinder axis (the hydrostatic direction) of the matrix von Mises yield surface. When applying stress along this third eigendirection in the stress space, vanishing plastic strain is expected since the yield surface appears to extend to infinity. The matrix of Bauschinger moduli, $\boldsymbol{P}$, together with the eigenvalues and eigendirections are shown in Tab. 5. The eigendirections corresponding to the two smallest eigenvalues (numbers two and four) define in-plane shear loadings, whereas the eigendirection corresponding to the first eigenvector defines an equi-biaxial loading. These observations can be exploited to rewrite the yield function in a reduced form on what we refer to as the Composite-plane (C-plane), which is the plane perpendicular to the third eigendirection, $\boldsymbol{v}^{\lambda}_3$. This is consistent with the expression for the yield surface proposed in Eq. (32). Note that the material length scale does not seem to affect the orientation of the C-plane.

In Fig. 7, the initial yield surface of the composite is shown on the ($\boldsymbol{v}^{\lambda_1}$,$\boldsymbol{v}^{\lambda_2}$) stress coordinate system for two different material length scales. This means that the yield surfaces are projected on the composite plane (C-plane) passing the origin with the normal vector $\boldsymbol{v}^{\lambda_3} \propto (1, 1, 1.35)$. As can

be seen from Fig. 7, the assumption of expressing the yield surface as an ellipse with the major axis in the Σ_{λ_1} stress-direction and minor axis in the Σ_{λ_2} stress-direction according to Eq.(32) is reasonable. It is observed that the expansion of the initial yield surface for the gradient dependent material compared to the conventional material is considerable as also discussed by (Azizi et al., 2011b,a).

Fig. 8 shows the scaled amount of trapped energy, $2\psi_T/(\sigma_y\epsilon_y)$, and effective plastic strain, ϵ_p^e/ϵ_y, during the loading in longitudinal (a,b), transverse (c,d), 45^o in-plane shear (e,f) and out-of-plane shear (g,h) directions with $V_f = 0.2$ and $L_*/r = 0$. Significant plasticity with a relatively small trapped energy is observed for 45^o in-plane shear, out-of-plane shear and transverse loading, which is opposite to the finding for the longitudinal case. For all the loading paths, an abrupt change in the plastic strain at the fiber matrix interface is seen, where the plastic strain on the matrix side of the interface is non-zero and vanishes on the fiber side of the interface.

Similar contour plots are presented in Fig. 9 for a gradient dependent material with $L_*/r = 0.4$ and $V_f = 0.2$. A relatively limited amount of plasticity together with an enhanced trapped energy are noticed for all the loading paths. An inhomogeneous distribution of the trapped energy for the gradient dependent material is observed, when compared to the conventional material. On the other hand, a smooth transition of the plastic strain from zero level in the elastic fiber to the matrix occurs for the gradient dependent material, which is not the case for the conventional material. This is in accordance to the finding by Shu and Barlow (2000), where they found that while a classical crystal formulation tends to over-predict the spatial gradient of the deformation, the strain gradient formulation is able to predict a more smooth field consistent with the experimental finding.

The trapped energy density is shown in Fig. 10 as a function of (a) $E^p_{\lambda_1}$ and (b) $E^p_{\lambda_2}$, for the gradient dependent material with $L_*/r = 0.4$ and $V_f = 0.2$ under four different loading conditions discussed in relation to Fig. 9. The points represent computational results, and the solid lines represent the macro scale approximation according to Eq. 67, which is observed to give a rather close fit. As very little $E^p_{\lambda_3}$ develops (consistent with the fact that the third eigendirection, $\boldsymbol{v}^{\lambda_3}$, is along the composite cylindrical axis), corresponding plots as a function of $E^p_{\lambda_3}$ are omitted. Eigenvalues as the fitting parameters are $P_{\lambda_1} = 2.02E_m$, $P_{\lambda_2} = 0.37E_m$ and $P_{\lambda_3} = 4901E_m$. Tab. 4 shows further computational data of the loading paths imposed on the unit cell to obtain these results.

The geometric center of the subsequent yield surface is now compared with the Bauschinger stress defined according to Eq. 68. The solid lines in Fig. 11 show the Bauschinger stress on the C-plane for both transverse (x_1 direction) and longitudinal (x_3 direction) loading with $V_f = 0.2$ and $L_*/r = 0.4$. It is seen that transverse loading (Fig. 11a) generates a relatively large Bauschinger stress and small plastic strain in the $\boldsymbol{v}^{\lambda_1}$-direction compared to the $\boldsymbol{v}^{\lambda_2}$-direction. Under longitudinal loading (Fig. 11b), the Bauschinger stress is only significant in the $\boldsymbol{v}^{\lambda_1}$ direction as it vanishes in the other directions ($\boldsymbol{v}^{\lambda_2}$ and $\boldsymbol{v}^{\lambda_3}$). The fact that it vanishes in the $\boldsymbol{v}^{\lambda_2}$-direction is because $\boldsymbol{v}^{\lambda_2}$ represents in-plane shearing and this cannot be activated under longitudinal loading due to the material symmetries. The markers represent the geometric centers of the yield surfaces. A good agreement with the Bauschinger stress using the current approach, Eq. (68), is seen.

Fig. 12 shows the intersection of the C-plane, with $\boldsymbol{v}^{\lambda_3} = (1, 1, 1.35)$ as the normal vector, with the matrix yield surface, initial yield surface and a subsequent yield surface, for $V_f = 0.2$ and $L_*/r = 0.4$. Fig. 12a shows results for loading along the transverse direction until the overall load defined by $\Sigma_{11} = 2\sigma_y$ and Fig. 12b shows results for longitudinal loading until $\Sigma_{33} = 4\sigma_y$. As can be seen, for the longitudinal loading, kinematic hardening dominates over anisotropic hardening (yield surface expansion), while for transverse loading, both kinematic hardening and anisotropic hardening are comparable. Comparing the Bauschinger stress according to Eq. 68 (circle-markers), with the geometric center of the subsequent yield surface (cross-markers), a good agreement is observed.

Fig. 13 shows corresponding results for (a) 45^o in-plane shear direction until the overall load $\Sigma_{11} = -\Sigma_{22} = \sigma_y$ and (b) out-of-plane shear direction until the overall load $\Sigma_{11} = -\Sigma_{33} = 2\sigma_y$. Anisotropic hardening is observed to dominate for the 45^o in-plane shear loading, while kinematic hardening dominates for out-of-plane shear loading. Also here, good agreement is observed between the Bauschinger stress (circle-markers), and the geometric center of the subsequent yield surface (cross-markers).

The effect of the material length scale, L_*/r, on the trapped energy is studied in Fig. 14 for a fiber volume fraction of $V_f = 0.2$ under (a) transverse loading and (b) longitudinal loading. By decreasing the particle size and the distance between the particles for the sake of constant V_f (or conversely increasing the material length scale), the amount of the trapped energy increases significantly under transverse loading and moderately under longitudinal loading. This enhancement of the trapped energy for small fiber sizes is

consistent with findings by Deshpande et al. (2005), where they showed that the stored energy associated with the dislocations is enhanced by decreasing the reinforcement size. The trapped energy for the conventional response by the transverse loading is relatively small and hardly shows a quadratic behavior, while the quadratic function is well suited for the other curves.

In Fig. 15, the Bauschinger stresses corresponding to the results in Fig. 14, A_{λ_i} are plotted. The Figure shows that with higher values of the material length scale, L_*/r, the Bauschinger stresses, A_{λ_i}, increase significantly under transverse loading and moderately under longitudinal loading consistent with the behavior of the trapped energy. The solid lines are the calculated Bauschinger stresses based on the values of P_{λ_i}, shown in Tab. 5 and the points are the geometric centers of the subsequent yield surfaces. The considerable amount of the Bauschinger effect observed in the experiments conducted by Corbin et al. (1996) and Taya et al. (1990) can not be captured by conventional J2 flow theory. However, the gradient dependent analysis here captures the enhanced Bauschinger effect better.

Figs. 16 and 17 show the effect of the material length scale, L_*/r, on the subsequent yield surface for normal and shear loadings, respectively on the C-plane for $V_f = 0.2$. The initial yield surfaces of the composite and the matrix are also shown as references. For the conventional response with $L_*/r = 0$, anisotropic hardening is significant for both transverse (Fig. 16a) and 45^0 in-plane shear loading (Fig. 17a). This is opposite to the finding for longitudinal (Fig. 16b) and out-of-plane shear (Fig. 17b) loadings, where kinematic hardening dominates. For the gradient dependent material, all of the loading paths show a significant amount of the kinematic hardening due to the residual higher order stresses. The geometric center of the subsequent yield surface and the Bauschinger stress using the current energy approach agree adequately.

Fig. 18 shows the trapped energy in the unit cell under 0^o in-plane shear loading with $V_f = 0.2$ for both conventional (a,b) and gradient dependent (c,d) material behavior. The overall loading is $\Sigma_{12} = 1.74\tau_y$. A limited amount of the trapped energy, $2\psi_T/(\sigma_y\epsilon_y)$, is observed for the conventional material (Fig. 18a), even in the presence of a relatively high plastic strain, ϵ_p^e/ϵ_y (Fig. 18b). On the other hand, a considerable amount of energy is trapped for the gradient dependent material (Fig. 18c) even under limited plastic deformations (Fig. 18d). The deformation of the unit cell is here shown with 30 times enlarged, demonstrating that for the gradient dependent material, the unit cells boundaries are less curved due to restricted plasticity.

A quantitative study of the trapped energy is shown in Fig. 19(a) and the corresponding Bauschinger stress in Fig. 19(b), for 0^o in-plane loading. The solid lines are calculated based on the fitted value, $P_{\lambda_4} = 0.12E_m$ as shown in Tab. 5. The amount of trapped energy and the corresponding Bauschinger stress almost vanish for the conventional case, while for the gradient dependent material with $L_*/r = 0.4$ a significant amount of trapped energy is stored leading to a significant Bauschinger stress. Note that due to the material symmetries assumed in the present unit cell model, the 0^o in-plane shear loading trial does not generate plasticity in the $\boldsymbol{v}^{\lambda_1}$, $\boldsymbol{v}^{\lambda_2}$ and $\boldsymbol{v}^{\lambda_3}$ directions. As a result, the Bauschinger stress can be conventionally defined as (see Azizi et al., 2011b,a)

$$A_{\lambda_4} = A_{12} = \frac{(\Sigma_{12}^{f} + \Sigma_{12}^{sy})}{2} \tag{70}$$

where Σ_{12}^{f} is stress at the end of loading and Σ_{12}^{sy} is the stress at the subsequent yield point under reverse loading. In Fig. 19(b), the circles represent the geometric center of the yield surface during loading. The enhanced Bauschinger stress is in accordance with results for pure shear of a slab between rigid plates studied by Niordson and Legarth (2010). It is emphasized that the conventional definition for the Bauschinger stress, Eq. (70), in the composite under multi axial loadings can not represent the geometrical center of the multi dimensional yield surface, while the definition with the current approach, Eq. (68), can.

As it was seen, the material length scale does not affect the orientation of the composite cylinder while it expands. However, the fiber volume fraction, V_f, not only expands the yield surface but also changes the orientation of it. This is shown in Tab. 6, where the expansion is represented by the eigenvalues of $\boldsymbol{P}$-matrix and the orientation is represented by the eigendirections of $\boldsymbol{P}$-matrix. It is seen that for a very small V_f (close to the homogeneous material), the third eigendirection, $\boldsymbol{v}^{\lambda_3}$=(0.57,0.57,0.57), is parallel to the von Mises hydrostatic pressure line as expected.

7. Conclusion

A general modeling approach for the Bauschinger stress in Metal Matrix Composites has been presented, while the intrinsic size-effect due to reinforcement size is modeled using an energetic higher order strain gradient plasticity theory at the micro scale. Homogenization is carried out subject

to the Hill-Mandel energy condition and a conventional plasticity model with kinematic hardening is obtained, where the Bauschinger stress develops due to trapped energy under macroscopic plastic straining. The numerical data is obtained from unit cell studies of a single fiber using five loading paths under generalized plain strain conditions; 1) transverse loading, 2) longitudinal loading, 3) 0^o in-plane shear, 4) 45^o in-plane shear and 5) out-of-plane shear. The thermodynamically consistent models at the micro and macro scales lead to a relationship between the trapped energy (due to residual stresses and residual higher order stresses) and the macroscopic plastic strain state that was approximated by a quadratic relationship. The ensuing linear relationship between the Bauschinger stress and the macroscopic plastic strain was shown to agree well with comparisons of the displaced geometric center of the yield surfaces calculated from unit cell studies.

The eigendirections of the Bauschinger moduli ($\boldsymbol{P}$-matrix) were found to be the cylindrical and planar axes of the composite yield surface. This was exploited to reduce the expression for the yield function whereby the Bauschinger stress was studied on the composite plane (C-plane) perpendicular to the eigendirection corresponding to the largest eigenvalue.

The effect of the reinforcement size on the trapped energy, the Bauschinger stress and the plastic strain level has been investigated. A considerable increase of the trapped energy and the corresponding Bauschinger stress with decreasing fiber size is found, as well as significant suppression of the plastic strain at the fiber-matrix interface. It is concluded that the length scale in the present strain gradient formulation increases the overall hardening of the composite, with decreasing particle size.

It is highlighted that the material length scale does not change the orientation of the composite cylinder, but can expand it. The fiber volume fraction as a conventional parameter can both expand and deviate the orientation of the composite cylinder.

Acknowledgment

This work is supported by the Danish Research Council for Technology and Production Sciences in a project entitled Plasticity Across the Scales. R.A. is grateful for the facilities provided by Eindhoven University of Technology. The computational resources have been provided by a hardware grant from the Danish Center of Scientific Computing (DCSC).

References

Acharya, A., Bassani, J. L., 2000. Lattice incompatibility and a gradient theory of crystal plasticity. Journal of the Mechanics and Physics of Solids 48, 1565–1595.

Azizi, R., Niordson, C., Legarth, B., 2011a. On homogenization of metal matrix composites using strain gradient plasticity. Submitted.

Azizi, R., Niordson, C., Legarth, B., 2011b. Size-effects on yield surfaces for micro reinforced composites. International Journal of Plasticity 27, 1817–1832.

Bassani, J. L., 2001. Incompatibility and a simple gradient theory of plasticity. Journal of the Mechanics and Physics of Solids 49, 1983–1996.

Benzerga, A. A., Brechet, Y., Needleman, A., Van der Giessen, E., 2005. The stored energy of cold work: Predictions from discrete dislocation plasticity. Acta Materialia 53, 4765–4779.

Borg, U., Niordson, C., Kysar, J., 2008. Size effects on void growth in single crystals with distributed voids. International Journal of Plasticity 24, 688–701.

Chaboche, J., 1993a. Cyclic viscoplastic constitutive equations. J. App. Mech. 60, 822–828.

Chaboche, J., 1993b. Cyclic viscoplastic constitutive equations `I`: a thermodynamically consistent formulation. J. Appl. Mech. 60, 813–821.

Coleman, B., Noll, W., 1963. The thermodynamics of elastic materials with heat conduction and viscosity. Arch. Rational Mech. Anal. 13, 176–178.

Corbin, S., Wilkinson, D., Embury, J., 1996. The bauschinger effect in a particulate reinforced al alloy. Materials Science and Engineering A207, 1–11.

Deshpande, V., Needleman, A., Van der Giessen, E., 2005. Size dependence of energy storage and dissipation in a discrete dislocation plasticity analysis of static friction. Materials Science and Engineering A 400-401, 393–396.

Drucker, D., 1951. A more fundamental approach to stress-strain relations. Proc. 1^{st} U.S.Nat. Congr. of Appl. Mech., ASME 487.

Fleck, N. A., Ashby, M., Hutchinson, J. W., 2003. The role of geometrically necessary dislocations in giving material strengthening. Scripta Materialia 48, 179–183.

Fleck, N. A., Hutchinson, J. W., 1997. Strain gradient plasticity. In: Hutchinson, J. W., Wu, T. Y. (Eds.), Advances in Applied Mechanics. Vol. 33. Academic Press, pp. 295–361.

Fleck, N. A., Hutchinson, J. W., 2001. A reformulation of strain gradient plasticity. Journal of the Mechanics and Physics of Solids 49, 2245–2271.

Fleck, N. A., Willis, J. R., 2009a. A mathematical basis for strain-gradient plasticity theory - Part I: Scalar plastic multiplier. Journal of the Mechanics and Physics of Solids 57, 161–177.

Fleck, N. A., Willis, J. R., 2009b. A mathematical basis for strain-gradient plasticity theory - Part II: Tensorial plastic multiplier. Journal of the Mechanics and Physics of Solids, 57, 1045–1057.

Fredriksson, P., Gudmundson, P., L.P., M., 2009. Finite element implementation and numerical issues of strain gradient plasticity with application to metal matrix composites. International Journal of Solids and Structures 46, 3977–3987.

Gao, H., Huang, Y., 2003. Geometrically necessary dislocation and size-dependent plasticity. Scripta Materialia 48, 113–118.

Gao, H., Huang, Y., Nix, W. D., Hutchinson, J. W., 1999. Mechanism-based strain gradient plasticity - I. Theory. Journal of the Mechanics and Physics of Solids 47 (6), 1239–1263.

Gudmundson, P., 2004. A unified treatment of strain gradient plasticity. Journal of the Mechanics and Physics of Solids 52 (6), 1379–1406.

Gurtin, M. E., 2002. A gradient theory of single-crystal viscoplasticity that accounts for geometrically necessary dislocations. Journal of the Mechanics and Physics of Solids 50 (1), 5–32.

Gurtin, M. E., Anand, L., 2005. A theory of strain-gradient plasticity for isotropic, plastically irrotational materials. Part I: Small deformations. Journal of the Mechanics and Physics of Solids 53 (7), 1624–1649.

Hill, R., 1948. A theory of the yielding and plastic flow of anisotropic metals. Proceedings of the Royal Society of London A193, 281–297.

Hill, R., 1963. Elastic properties of reinforced solids: some theoretical principles. Journal of the Mechanics and Physics of Solids 11, 357–372.

Hussein, M., Borg, U., Niordson, C., Deshpande, V., 2008. Plasticity size effects in voided crystals. Journal of the Mechanics and Physics of Solids 56, 114–131.

Hutchinson, J. W., 2000. Plasticity at the micron scale. International Journal of Solids and Structures 37 (1-2), 225–238.

Kapoor, R., Nemat Nasser, S., 1998. Determination of temperature rise during high strain rate deformation. Mech. Mater. 27, 1–12.

Kuhlmann-Wilsdorf, D., 1970. Stored energy and workhardening theories. Scripta Metallurgica 4, 893–898.

Lele, S. P., Anand, L., 2008. A small-deformation strain-gradient theory for isotropic viscoplastic materials. Philosophical Magazine 88 (30), 1478–6435.

Lloyd, D. J., 1994. Particle reinforced aluminium and magnesium matrix composites. International Materials Reviews 39 (1), 1–23.

Lubliner, J., 1972. On the thermodynamic foundations of non-linear solid mechanics. J. Non-Linear Mech. 7, 237.

Lubliner, J., 1990. Plasticity theory. Pearson Education, Inc.

McDanels, D., 1985. Analysis of stress-strain, fracture, and ductility behavior of aluminum matrix composites containing discontinuous silicon carbide reinforcement. Metallurgical Transactions A (Physical Metallurgy and Materials Science) 16A (6), 1105–1115.

Mughrabi, H., 2001. The effect of geometrically necessary dislocations on the flow stress of deformed crystals containing a heterogeneous dislocation distribution. Materials Science and Engineering 319-321, 139–143.

Niordson, C. F., Legarth, B. N., 2010. Strain gradient effecits on cyclic plasticity. Journal of the Mechanics and Physics of Solids 58, 542–557.

Oliferuk, W., Korbel, A., Grabski, M., 1996. Mode of deformation and the rate of energy storage during uniaxial tensile deformation of austenitic steel. Materials Science and Engineering A220, 123–128.

Oliferuk, W., Maj, M., 2009. Stress strain curve and stored energy during uniaxial deformation of polycrystals. European Journal of Mechanics A/Solids 28, 266–272.

Rice, J., 1971. Inelastic constitutive relations for solids: An internal-variable theory and its application to metal plasticity. Journal of the Mechanics and Physics of Solids 19, 433–455.

Rosakis, P., Rosakis, A., Ravichandran, G., Hodowan, J., 2000. A thermodynamic internal variable model for the partition of plastic work into heat and stored energy in metals. Journal of the Mechanics and Physics of Solids 48, 581–607.

Shu, J. Y., Barlow, C. Y., 2000. Strain gradient effects on microscopic strain field in a metal matrix composite. International Journal of Plasticity 16, 563–591.

Suquet, P. M., 1985. Local and global aspects in the mathematical theory of plasticity. Plasticity today: modelling, methods and applications, 279–310.

Taya, M., Lulay, K., Wakashima, K., Lloyd, D., 1990. Bauschinger effect in particulate sic-6061 aluminum composites. Materials Science and Engineering 124, 103–111.

Wolfenden, A., 1970. The ratio of stored to expended energy during the room-temperature deformation of copper single crystals. Scripta Metallurgica 4, 327–332.

Loading direction	L_*/r	Maximum loading	E^p_{11}/ϵ_y	E^p_{22}/ϵ_y	E^p_{33}/ϵ_y	$2\Psi_T/(\sigma_y\epsilon_y)$
Longitudinal	0.4	$\Sigma_{33} = 3\sigma_y$	-0.143	-0.143	0.21	0.284
Longitudinal	0	$\Sigma_{33} = 3\sigma_y$	-0.197	-0.197	0.3	0.329
Transverse	0.4	$\Sigma_{11} = 2\sigma_y$	1.08	-0.854	-0.172	0.812
Transverse	0	$\Sigma_{11} = 1.6\sigma_y$	3.749	-3.291	-0.330	0.399
45^o in-plane shear	0.4	$\Sigma_{11} = -\Sigma_{22} = \sigma_y$	0.929	-0.929	0	0.644
45^o in-plane shear	0	$\Sigma_{11} = -\Sigma_{22} = 0.8\sigma_y$	3.45	-3.45	0	0.048
Out-of-plane shear	0.4	$\Sigma_{11} = -\Sigma_{33} = 2\sigma_y$	1.38	-0.715	-0.497	1.827
Out-of-plane shear	0	$\Sigma_{11} = -\Sigma_{33} = 1.6\sigma_y$	2.339	-1.53	-0.593	1.104

Table 4: Computational results of the imposed loading paths on the unit cell with $V_f = 0.2$.

	$L_*/r = 0$	$L_*/r = 0.2$	$L_*/r = 0.4$
$\frac{1}{E_m}\boldsymbol{P}$	$\begin{bmatrix} 206.9 & 206.9 & 282.9 & 0 \\ 206.9 & 206.9 & 282.9 & 0 \\ 282.9 & 282.9 & 390.1 & 0 \\ 0 & 0 & 0 & 0.004 \end{bmatrix}$	$\begin{bmatrix} 2420.9 & 2420.8 & 3261.7 & 0 \\ 2420.8 & 2420.9 & 3261.7 & 0 \\ 3261.7 & 3261.7 & 4398.3 & 0 \\ 0 & 0 & 0 & 0.031 \end{bmatrix}$	$\begin{bmatrix} 1307.4 & 1307.0 & 1728.3 & 0 \\ 1307.0 & 1307.4 & 1728.3 & 0 \\ 1728.3 & 1728.3 & 2288.9 & 0 \\ 0 & 0 & 0 & 0.123 \end{bmatrix}$
$\frac{1}{E_m}\boldsymbol{P}\lambda_i$	$\begin{bmatrix} 1.59 & 0.002 & 802.2 & 0.004 \end{bmatrix}$	$\begin{bmatrix} 1.966 & 0.126 & 9238 & 0.030 \end{bmatrix}$	$\begin{bmatrix} 2.020 & 0.373 & 4901 & 0.123 \end{bmatrix}$
$\boldsymbol{V}$	$\begin{bmatrix} 0.49 & 0.70 & 0.50 & 0.00 \\ 0.49 & -0.70 & 0.50 & 0.00 \\ -0.71 & 0.00 & 0.69 & 0.00 \\ 0.00 & 0.00 & 0.00 & 1.00 \end{bmatrix}$	$\begin{bmatrix} 0.49 & 0.70 & 0.51 & 0.00 \\ 0.49 & -0.70 & 0.51 & 0.00 \\ -0.72 & 0.00 & 0.69 & 0.00 \\ 0.00 & 0.00 & 0.00 & 1.00 \end{bmatrix}$	$\begin{bmatrix} 0.48 & 0.70 & 0.51 & 0.00 \\ 0.48 & -0.70 & 0.51 & 0.00 \\ -0.73 & 0.00 & 0.68 & 0.00 \\ 0.00 & 0.00 & 0.00 & 1.00 \end{bmatrix}$

Table 5: Effect of the material length scale, L_*/r, on the $\boldsymbol{P}$-matrix, eigenvalues of the $\boldsymbol{P}$-matrix (fitting parameters) and eigendirections of $\boldsymbol{P}$-matrix (composite cylindrical axes) for $V_f = 0.2$.

	$V_f = 0.001$	$V_f = 0.1$	$V_f = 0.3$
$\frac{1}{E_m}\boldsymbol{P}$	$\begin{bmatrix} 27.97 & 27.97 & 27.99 & 0 \\ 27.97 & 27.97 & 27.99 & 0 \\ 27.99 & 27.99 & 28.03 & 0 \\ 0 & 0 & 0 & 0.0001 \end{bmatrix}$	$\begin{bmatrix} 1075.1 & 1074.9 & 1260.9 & 0 \\ 1074.9 & 1075.1 & 1260.9 & 0 \\ 1260.9 & 1260.9 & 1480.0 & 0 \\ 0 & 0 & 0 & 0.032 \end{bmatrix}$	$\begin{bmatrix} 1143.8 & 1142.3 & 1749.0 & 0 \\ 1142.3 & 1143.8 & 1749.0 & 0 \\ 1749.0 & 1749.0 & 2685.1 & 0 \\ 0 & 0 & 0 & 0.40 \end{bmatrix}$
$\frac{1}{E_m}\boldsymbol{P}_{\lambda_i}$	$\begin{bmatrix} 0.004 & 0.0002 & 83.96 & 0.0001 \end{bmatrix}$	$\begin{bmatrix} 0.585 & 0.147 & 3629 & 0.032 \end{bmatrix}$	$\begin{bmatrix} 4.19 & 1.51 & 4967 & 0.40 \end{bmatrix}$
$\boldsymbol{V}$	$\begin{bmatrix} 0.41 & 0.70 & 0.57 & 0.00 \\ 0.41 & -0.70 & 0.57 & 0.00 \\ -0.81 & 0.00 & 0.57 & 0.00 \\ 0.00 & 0.00 & 0.00 & 1.00 \end{bmatrix}$	$\begin{bmatrix} 0.45 & 0.70 & 0.54 & 0.00 \\ 0.45 & -0.70 & 0.54 & 0.00 \\ -0.77 & 0.00 & 0.64 & 0.00 \\ 0.00 & 0.00 & 0.00 & 1.00 \end{bmatrix}$	$\begin{bmatrix} 0.52 & 0.70 & 0.48 & 0.00 \\ 0.52 & -0.70 & 0.48 & 0.00 \\ -0.68 & 0.00 & 0.73 & 0.00 \\ 0.00 & 0.00 & 0.00 & 1.00 \end{bmatrix}$

Table 6: Effect of the fiber volume fraction, V_f, on the $\boldsymbol{P}$-matrix, eigenvalues of the $\boldsymbol{P}$-matrix (fitting parameters) and eigendirections of $\boldsymbol{P}$-matrix (composite cylindrical axes) for $L_*/r = 0.4$.

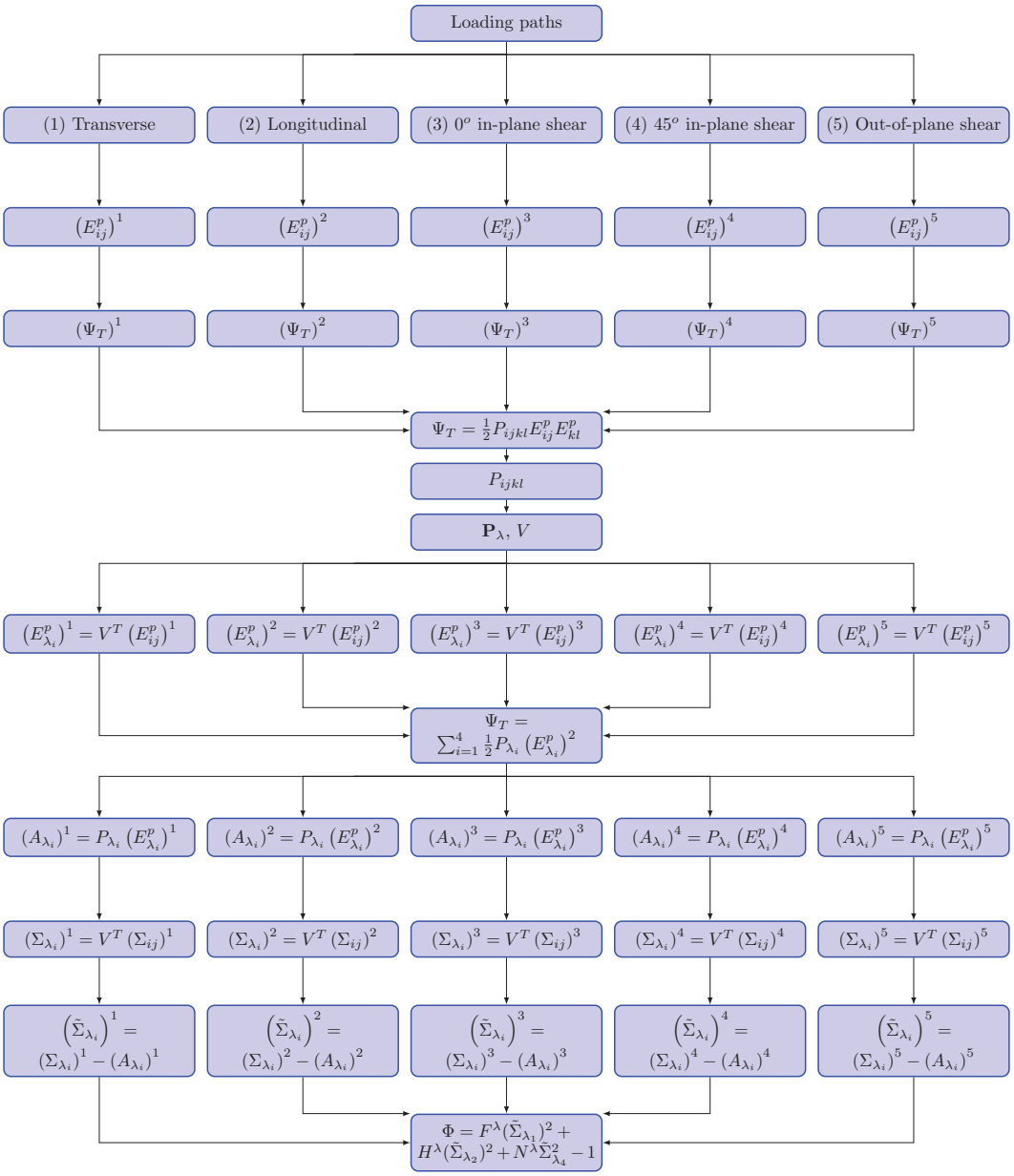

Figure 5: The computational procedure for identifying the material model's parameters at the macro scale.

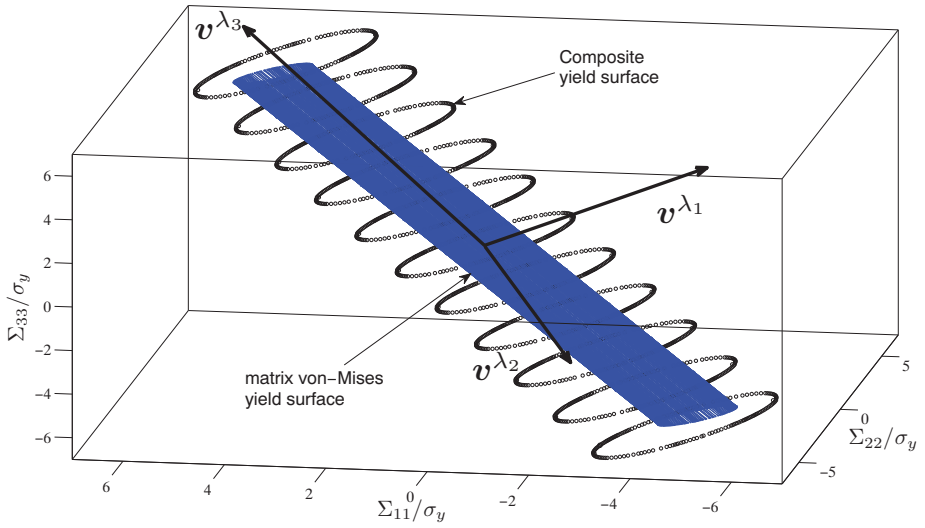

Figure 6: Initial yield surface of the composite for $V_f = 0.2$ and $L_*/r = 0.4$ and the eigendirections, $\boldsymbol{v}^{\lambda_i}$, of the $\boldsymbol{P}$-matrix.

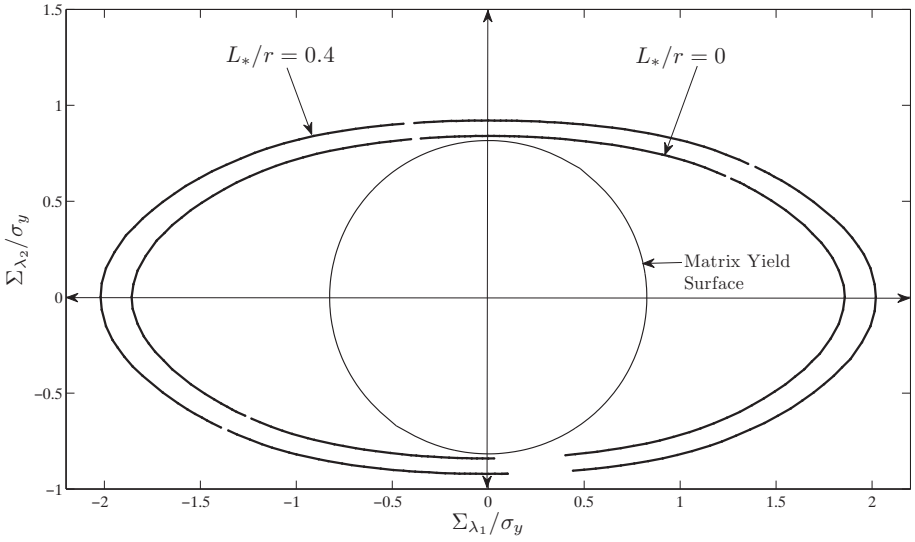

Figure 7: Effect of the material length scale, L_*/r, on the initial yield surface of the composite for $V_f = 0.2$ projected on the Composite plane (C-plane) with normal vector as $\boldsymbol{v}^{\lambda_3} = (1, 1, 1.35)$.

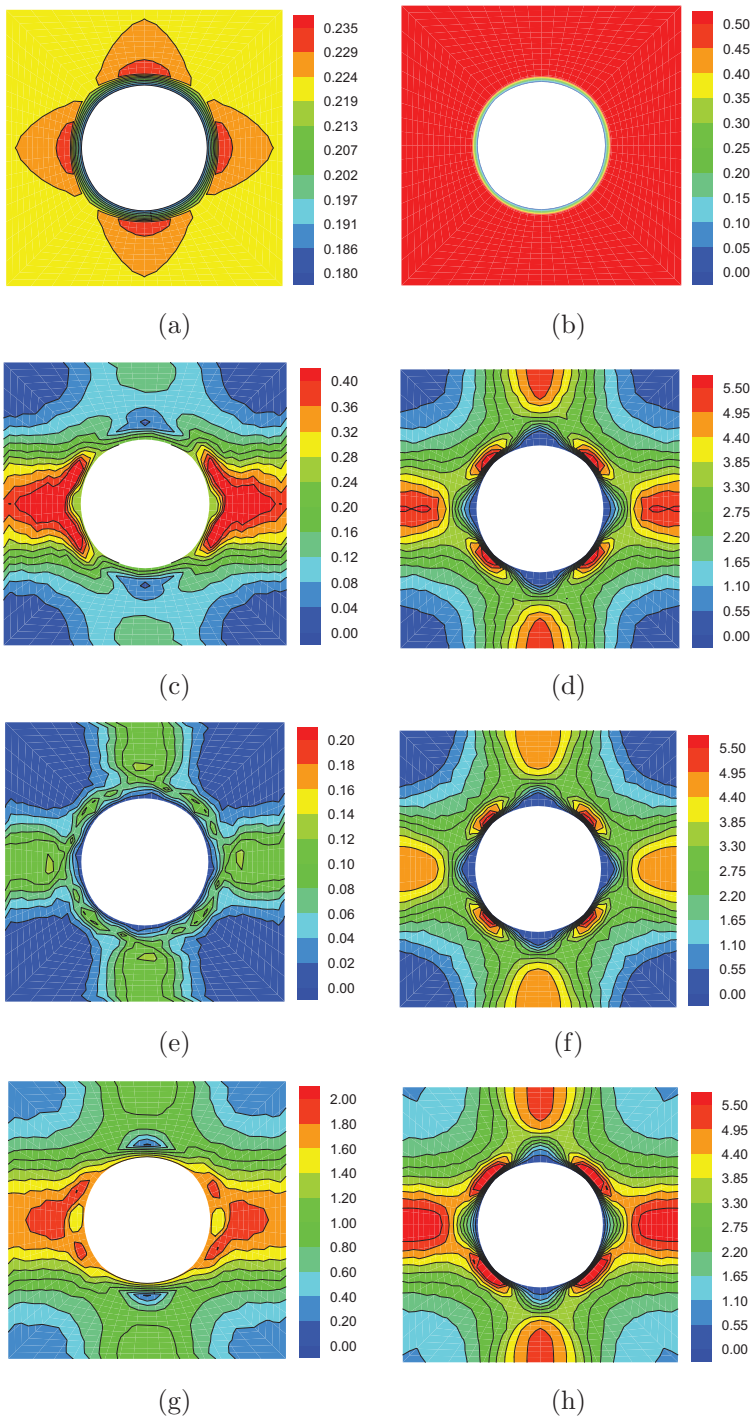

Figure 8: Contours of microscopic trapped energy, $2\psi_T/(\sigma_y\epsilon_y)$, (a,c,e,g) and the corresponding effective plastic strain, ϵ_p^e/ϵ_y, (b,d,f,h) with $V_f = 0.2$ and $L_*/r = 0$ in (a,b) longitudinal, (c,d) transverse, (e,f) 45^o in-plane shear, and (g,h) out-of-plane shear.

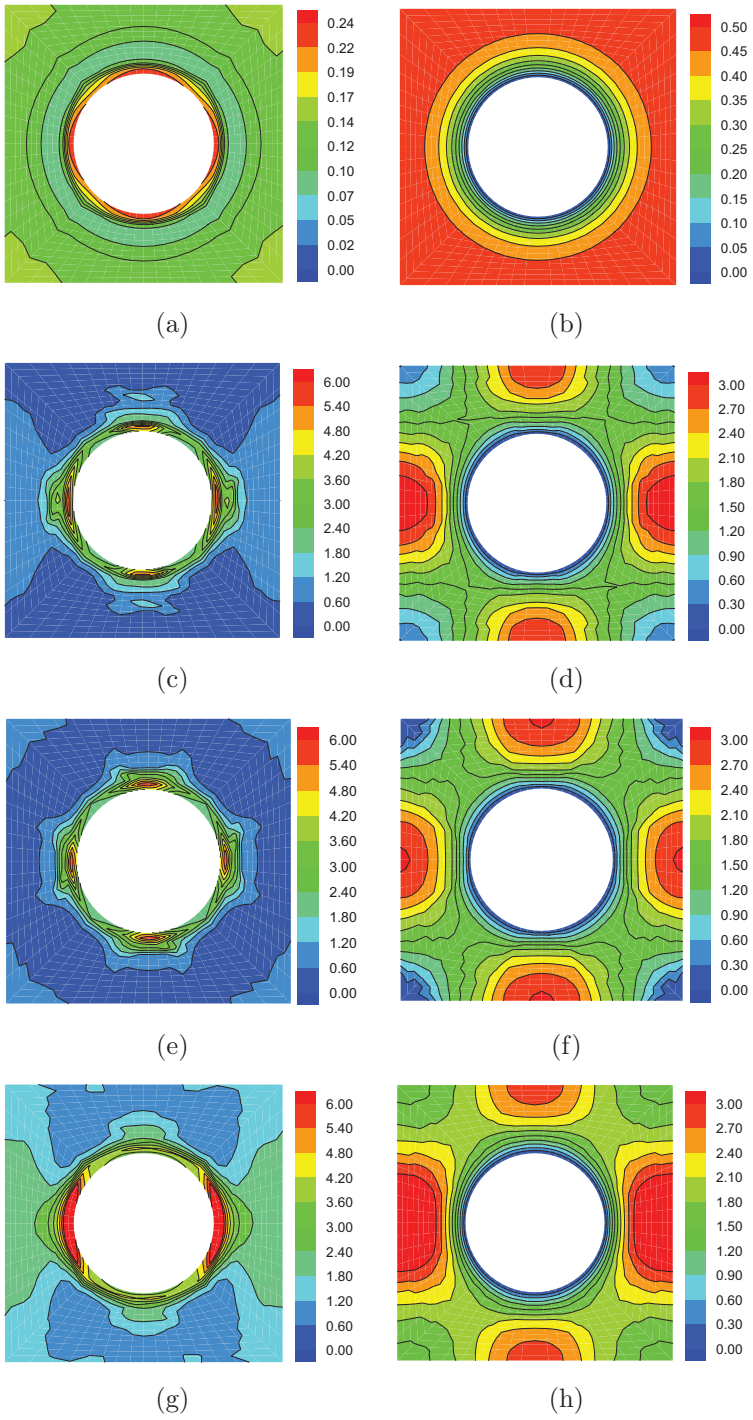

Figure 9: Trapped energy, $2\psi_T/(\sigma_y\epsilon_y)$, (a,c,e,g) and the corresponding effective plastic strain, ϵ_p^e/ϵ_y, (b,d,f,h) with $V_f = 0.2$ and $L_*/r = 0.4$ in (a,b) longitudinal, (c,d) transverse, (e,f) 45^o in-plane shear, and (g,h) out-of-plane shear.

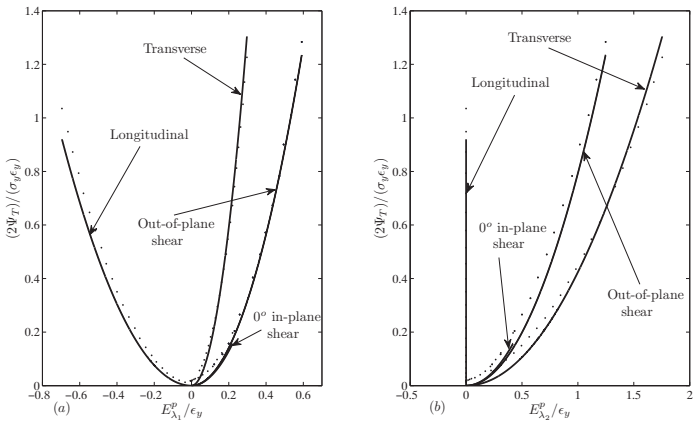

Figure 10: Trapped energy, $2\psi_T/(\sigma_y\epsilon_y)$, versus (a) $E^p_{\lambda_1}/\epsilon_y$. (b) $E^p_{\lambda_2}/\epsilon_y$. with $V_f = 0.2$ and $L_*/r = 0.4$. The solid lines are the numerical fits with $P_{\lambda_1} = 2.02E_m$, $P_{\lambda_2} = 0.37E_m$ and $P_{\lambda_3} = 4901E_m$.

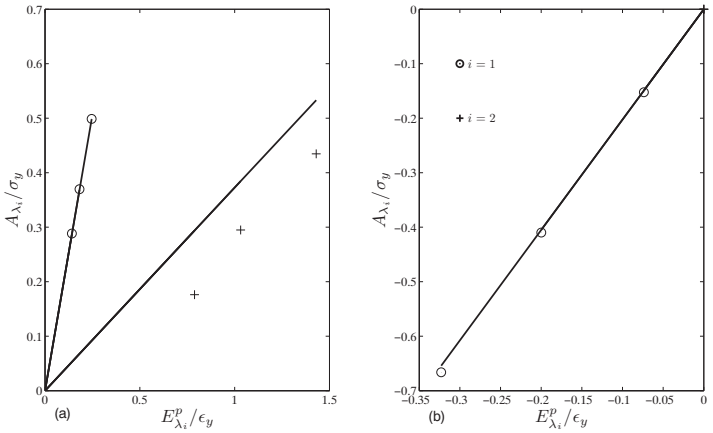

Figure 11: Geometric center of the subsequent yield surface in the transformed coordinate system with $V_f = 0.2$ and $L_*/r = 0.4$ for (a) transverse loading. (b) longitudinal loading. The solid lines are the numerical fits with $P_{\lambda_1} = 2.02E_m$, $P_{\lambda_2} = 0.37E_m$ and $P_{\lambda_3} = 4901E_m$.

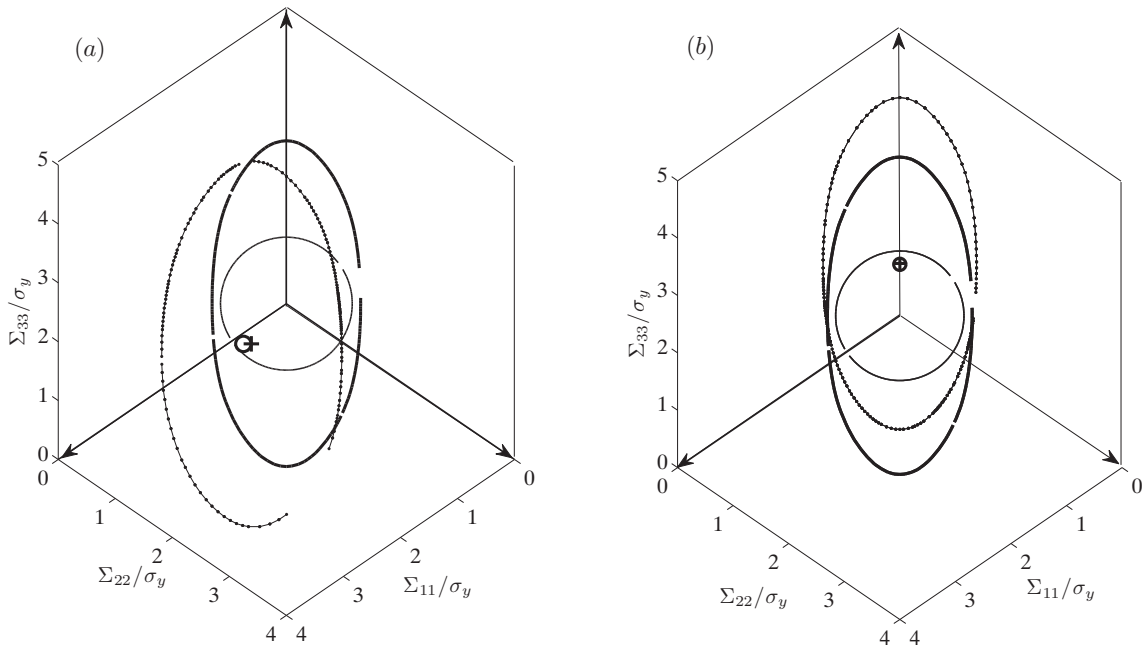

Figure 12: Matrix yield surface (thin solid line), initial yield surface (thick solid line) and subsequent yield surface (dot-line) on the C-plane with $\boldsymbol{v}^{\lambda_3} = \vec{e}_n = (1, 1, 1.35)$ as normal vector and with $V_f = 0.2$ and $L_*/r = 0.4$ for loading in (a) transverse direction until $\Sigma_{11} = 2\sigma_y$. (b) longitudinal direction until $\Sigma_{33} = 4\sigma_y$. Cross point is the geometric center of the SYS and circle point is the computed Bauschinger stress, given by Eq. 68.

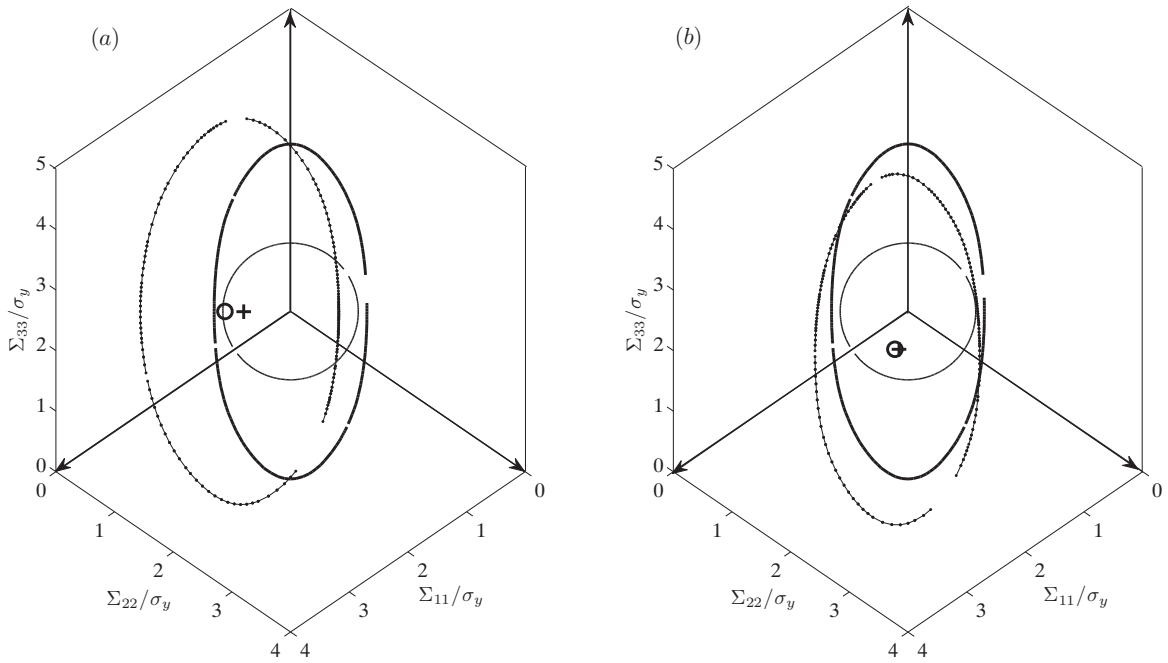

Figure 13: Matrix yield surface (thin solid line), initial yield surface (thick solid line) and subsequent yield surface (dot-line) on the C-plane with $\boldsymbol{v}^{\lambda_3} = \vec{e}_n = (1, 1, 1.35)$ as normal vector and with $V_f = 0.2$ and $L_*/r = 0.4$ for loading in (a) 45^o in-plane shear direction till $\Sigma_{11} = \sigma_y$. (b) out-of-plane shear direction till $\Sigma_{11} = 2\sigma_y$. Cross point is the geometric center of the SYS and circle point is the computed Bauschinger stress, Eq. 68.

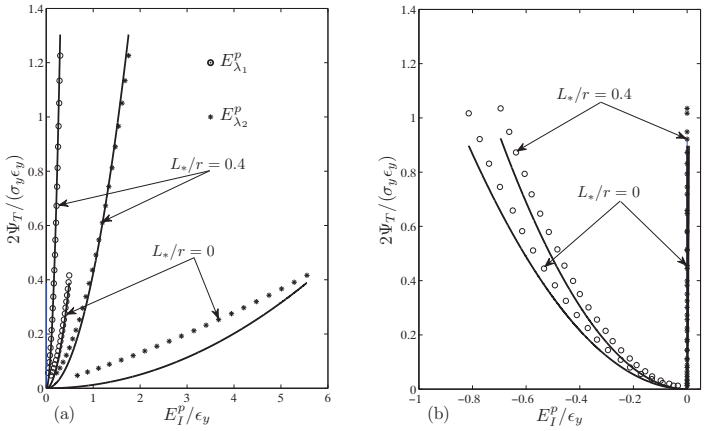

Figure 14: Effect of the material length scale, L_*/r, on the trapped energy, $2\Psi_T/(\sigma_y\epsilon_y)$, with $V_f = 0.2$ for (a) transverse loading (x_1). (b) longitudinal loading (x_3). Solid line is the macroscopic approximation with the parameters shown in Tab. 5.

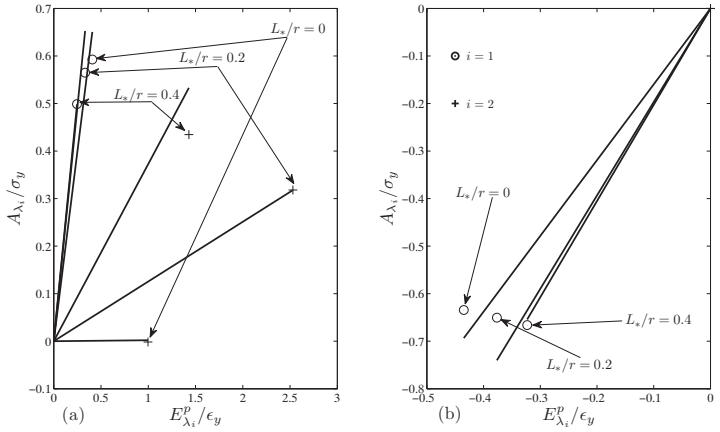

Figure 15: Effect of the material length scale, L_*/r, on the geometric center of the subsequent yield surface in the transformed coordinate system with $V_f = 0.2$ for (a) transverse loading (x_1). (b) longitudinal loading (x_3). Solid line is the macroscopic approximation with the parameters shown in Tab. 5 and the points are the geometric center of the SYS.

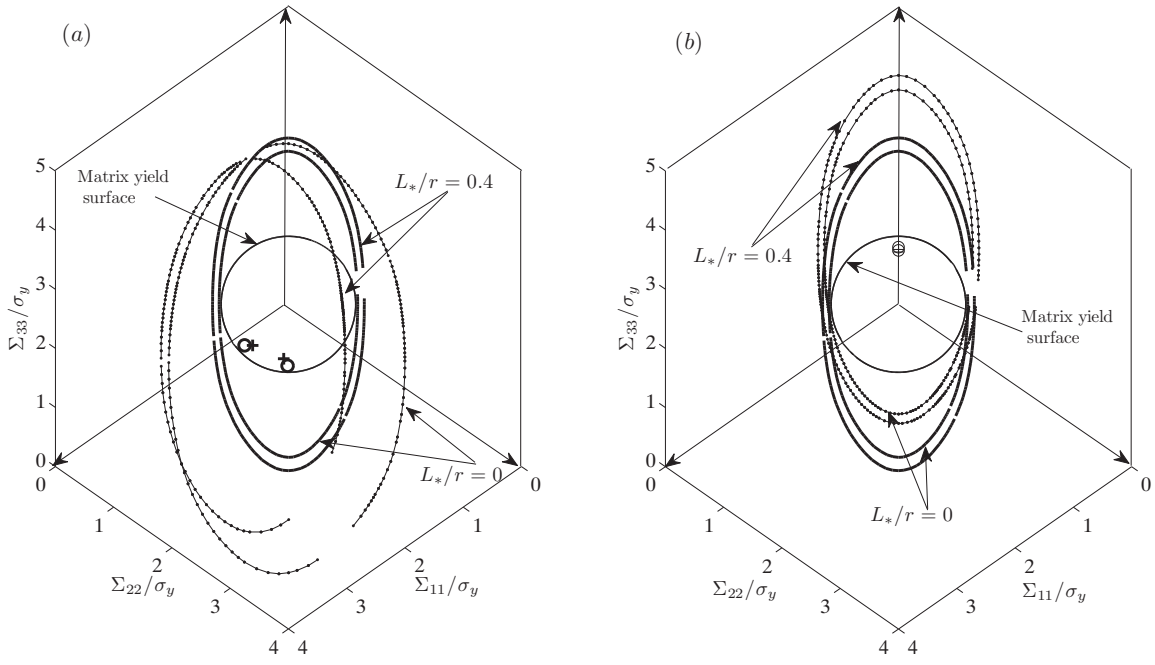

Figure 16: Effect of the material length scale, L_*/r, on the matrix yield surface (thin solid line), initial yield surface (thick solid line) and subsequent yield surface (dot-line) on a plane with $\boldsymbol{v}^{\lambda_3} = (1, 1, 1.35)$ as the normal vector and with $V_f = 0.2$ for (a) transverse loading. (b) longitudinal loading. Cross point is the geometric center of the SYS and circle point is the computed center of the SYS using Eq. 68.

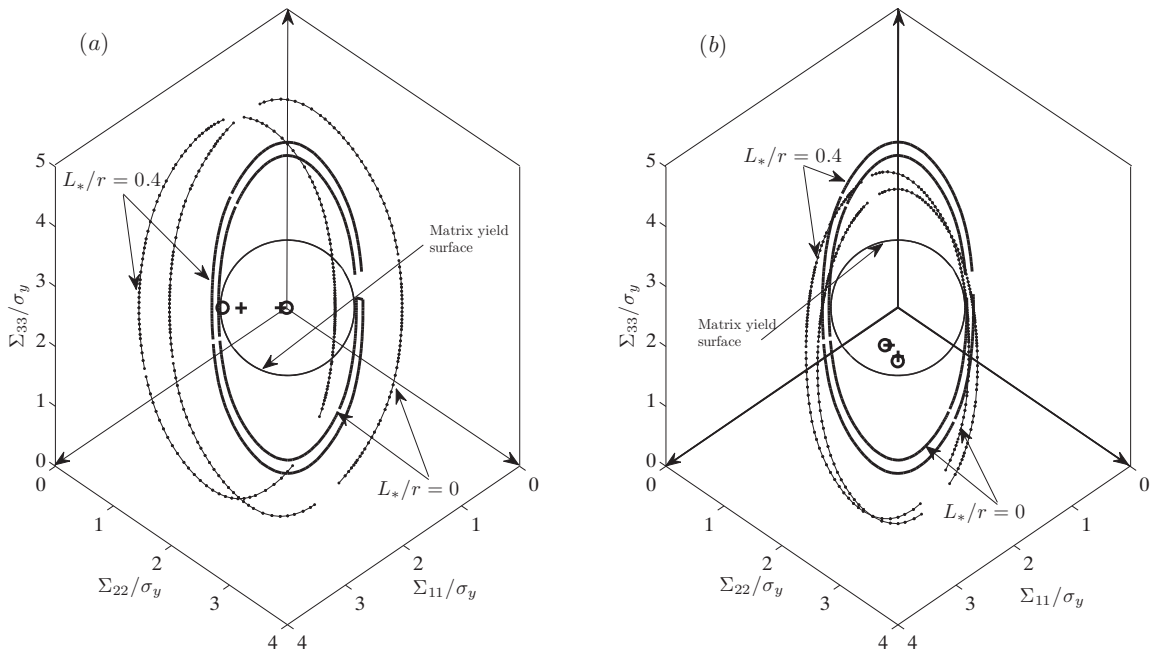

Figure 17: Effect of the material length scale, L_*/r, on the matrix yield surface (thin solid line), initial yield surface (thick solid line) and subsequent yield surface (dot-line) on a plane with $\boldsymbol{v}^{\lambda_3} = (1, 1, 1.35)$ as the normal vector and with $V_f = 0.2$ and $L_*/r = 0.4$ for (a) 45^o in-plane shear loading. (b) out-of-plane shear loading. Cross point is the geometric center of the SYS and circle point is the computed center of the SYS using Eq. 68.

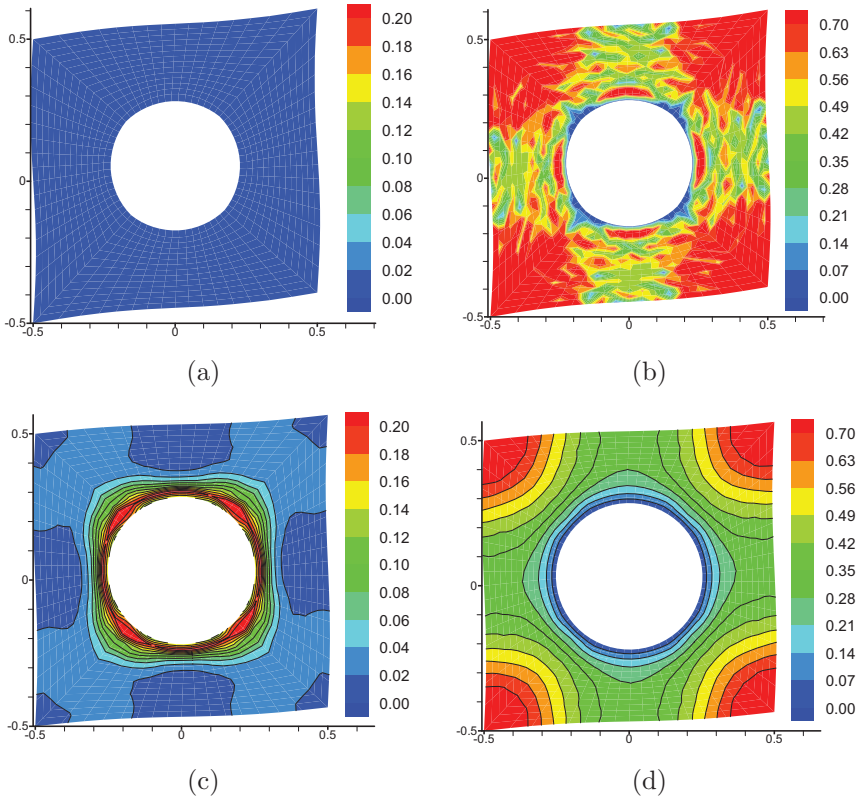

Figure 18: Trapped energy, $2\psi^T/(\sigma_y\epsilon_y)$, (a,c) and corresponding effective plastic strain, ϵ_p^e/ϵ_y, (b,d) in 0^o in-plane shear with $V_f = 0.2$. (a) and (b) $L_*/r = 0$. (c) and (d) $L_*/r = 0.4$. (Deformation is 30 times scaled)

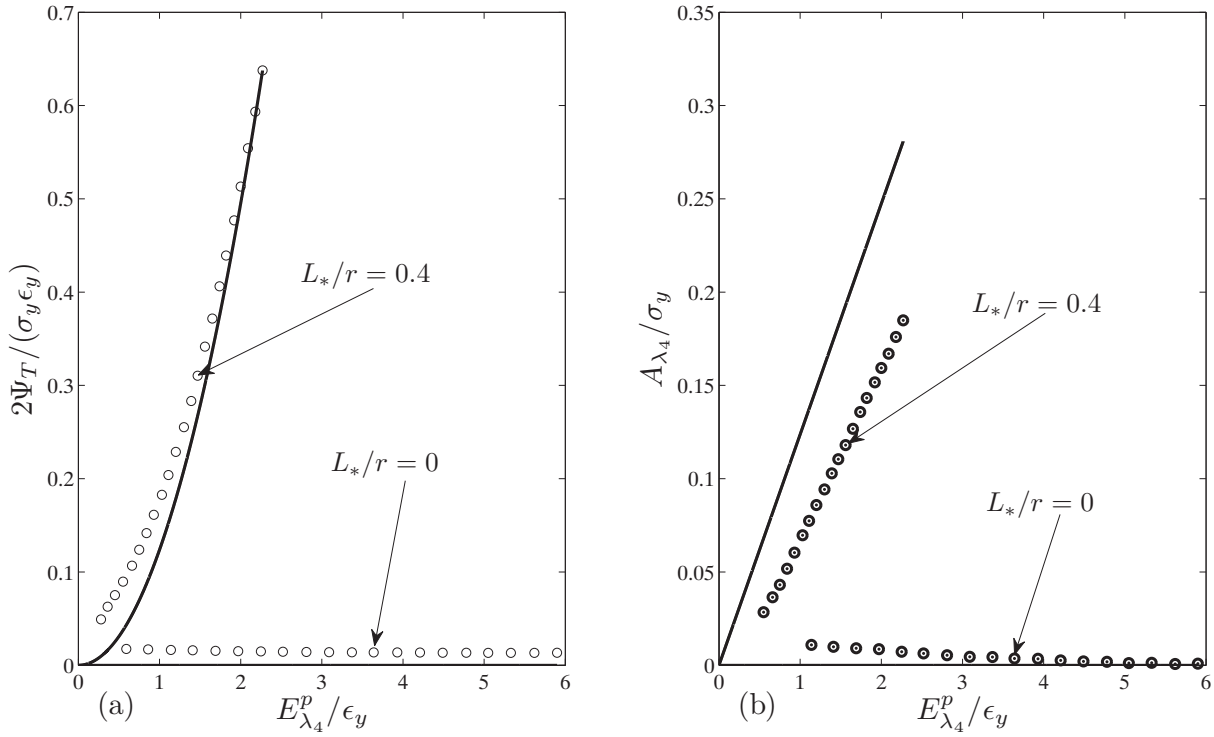

Figure 19: 0^o in-plane shear with $V_f = 0.2$ and the effect of the material length scale, L_*/r, on (a) trapped energy, $2\psi^T/(\sigma_y\epsilon_y)$. (b) Bauschinger stress, A_{λ_4}/σ_y. Solid line is the macroscopic approximation with the parameters shown in Tab. 5.

Publication [P6]

A new anisotropic pressure dependent yield function for metal matrix composite using strain gradient theory

A new anisotropic pressure dependent yield function for metal matrix composite using strain gradient theory

Reza Azizi*, Brian Nyvang Legarth, Christian F. Niordson

Department of Mechanical Engineering, Solid Mechanics, Technical University of Denmark, DK-2800 Kgs. Lyngby, Denmark

Abstract

Metal Matrix Composites with long aligned elastic fibers are studied using a conventional plasticity theory with an anisotropic pressure dependent yield function at the macro scale and the energetic rate independent strain gradient plasticity theory with an isotropic pressure independent yield function at the micro scale. Free energy includes both elastic strains and plastic strain gradients at the micro scale, whereas it depends on the elastic strains and plastic strains at the macro scale. The nature of the theory demands higher order boundary conditions. Considering both conventional and higher order periodic boundary conditions, a unit cell containing one fiber is extracted and studied with a finite element cell model under generalized plane strain condition. Hill's anisotropic yield criterion is extended such that hydrostatic pressure dependency, Bauschinger stress and size-effects are considered. It is found that depending on the fiber volume fraction, the anisotropic yield surface of composite is inclined compared to the standard isotropic Mises yield surface. The evolution of the macroscopic yield surface is investigated by tracking both anisotropic hardening (expansion) and kinematic hardening (translation), where the corresponding coefficients of anisotropy and the Bauschinger stress are extracted.

Keywords: Metal matrix composite, initial and subsequent yield surfaces, anisotropic yield function, strain gradient plasticity

*Corresponding Author

Email addresses: reaz@mek.dtu.dk (Reza Azizi*), bnl@mek.dtu.dk (Brian Nyvang Legarth), cn@mek.dtu.dk (Christian F. Niordson)

1. Introduction

Metal Matrix Composites (MMCs) are widely used due to their improved properties, e.g. high stiffness, low density, good damping capabilities, high wear and corrosion resistance. However, disadvantages like poor ductility and fracture properties also occur (see McDanels, 1985).

Even though both the pure matrix material and the reinforcing fiber material are isotropic at the micro scale, MMC at the macro scale behaves as a heterogeneous media. Thus, the heterogeneity changes the phenomenological behavior at the macroscopic scale in terms of the yield surface, the flow rule and the hardening. Experimental results show a distinctive change of the shape of yield surfaces depending on loading conditions and load paths, (see Phillips and Juh-Ling, 1972; Gupta and H.A., 1983; Kowalsky et al., 1999).

To capture such experimental observations different hardening rules were proposed in the past to specify the evolution of the yield surface during plastic deformation, see Jansson (1992, 1995); Iyer et al. (2000); Lee et al. (2004); Suprun (2006); Chung and Ryou (2009); Lissenden (2010). The models try to capture both anisotropic hardening (expansion) and kinematic hardening (translation). Even for pure homogeneous materials subjected to a large deformation, anisotropic hardening may occur due to the rotation and elongation of the grains. Such phenomena have been investigated by specifying an evolution law for the coefficients of anisotropy in the anisotropic yield function by Hill (1948), see for instance Kuroda (1997). For an anisotropic non-local material model, anisotropic hardening has also been considered when analyzing necking (Legarth, 2008).

An interesting result obtained by micromechanical finite element analyses is that the overall response of a MMC is not necessarily pressure independent even if the response for the elastic fibers and the inelastic metal matrix are pressure independent, see Dvorak et al. (1973). This is associated with the constraint provided by the fibers and the large difference between the local stress field compared to the overall stress. Aboudi (1990) derived a somewhat general micromechanical theory for predicting the overall behavior of MMCs. Both initial and subsequent yield surfaces under a variety of mechanical loadings and anisothermal conditions were found. Drucker and Prager (1952), Liu et al. (1997), Deshpande et al. (2001) improved previous proposed yield criteria of Hill (1948) and Barlat et al. (1991) to consider the hydrostatic pressure dependency. Voyiadjis and Thiagarajan (1995) developed a pressure dependent yield function which can be reduced to an existing

conventional anisotropic yield function.

Hutchinson (2000) have shown that for problems with lengths falling in the range from roughly a fraction of a micron to tens of microns a size-effect exists which conventional plasticity cannot capture. Keeping the fiber volume fraction of SiC reinforcement constant, Lloyd (1994) showed that the response of the composite, depends on whether the reinforcement size was 16 μm or only 7.5 μm. Thus, composite materials exhibit a size-effect. The macroscopic yield function of MMCs should also include such intrinsic size-effect of the fibers. Furthermore, Mughrabi (2001), Fleck et al. (2003) and Gao and Huang (2003) showed that for composite materials, dislocations cannot pass from matrix into the fiber and consequently pile up at the fiber/matrix interface. This behavior cannot be modeled by conventional plasticity since no size effects exist in the model. Theories of strain gradient plasticity have such capabilities to consider constraints on the plastic flow, (e.g. Aifantis, 1984; Fleck and Hutchinson, 1997; Bassani, 2001; Gurtin, 2004; Gudmundson, 2004; Lele and Anand, 2008; Fleck and Willis, 2009a,b), and this has been investigated by several authors, see Borg et al. (2006); Legarth and Niordson (2010). The anisotropic property of MMCs incorporating the gradient theories have also been investigated. Legarth (2007) generalized the isotropic single-parameter strain-gradient plasticity model of Fleck and Hutchinson (2001) in order to account for plastic anisotropy in a finite strain elastic viscoplastic formulation. Feng et al. (2010) investigated the pressure sensitivity of the yield surface using strain gradient plasticity theory and Drucker Prager yield function.

In this paper, MMC consisting of regular distributed elastic fibers embedded in an elasto-plastic material is analyzed by a finite element unit cell model under generalized plane strain conditions. At the micro scale, the matrix is governed by the strain gradient plasticity theory proposed by Gudmundson (2004), while a conventional plasticity theory is desirable at the macro scale. The relationship between local flow in the matrix and overall flow of the composite is explored. The classical anisotropic Hill yield function, Hill (1948), is extended such that the pressure dependency, the Bauschinger stress and the size effects are considered. It will be shown, that depending on the fiber volume fraction, the anisotropic yield surface of the MMC is inclined compared to the standard isotropic Mises yield surface. Both initial and subsequent yield surfaces are studied and the corresponding coefficients of anisotropy and the Bauschinger stresses are extracted.

2. Material Model

2.1. Material model at the micro scale

The material model inside the micro structure is the rate independent energetic strain-gradient plasticity theory proposed by Gudmundson (2004), which accounts for the gradients of the full plastic strain tensor. The first and second law of thermodynamics in the incremental form are written as, Chaboche (1993)

$$\begin{aligned} \dot{w} &= \dot{d} + \dot{\psi} \\ \dot{d} &= \dot{w} - \dot{\psi} \geq 0 \end{aligned} \tag{1}$$

where $\dot{w}$ is the rate of total work, $\dot{d}$ is the dissipation rate and $\dot{\psi}$ is the rate of the free energy. In a more general thermodynamic framework Eq. (1) would contain additional heat flux and entropy production terms but the purely mechanical calculations here provide no basis for including these contributions. The variation of the internal virtual work, δw_I, is considered as

$$\delta w_I = \int_v [\sigma_{ij}\delta\epsilon_{ij} + (q_{ij} - s_{ij})\delta\epsilon^p_{ij} + m_{ijk}\delta\epsilon^p_{ij,k}]dv \tag{2}$$

where v is the micro volume and ϵ_{ij} is the total strain given as the summation of elastic strain, ϵ^e_{ij}, and plastic strain, ϵ^p_{ij}, i.e. $\epsilon_{ij} = \epsilon^e_{ij} + \epsilon^p_{ij}$. The Cauchy stress, the deviatoric part of the Cauchy stress, the micro stress (work conjugate to the plastic strain) and the higher order stress (work conjugate to the plastic strain gradients) are denoted by σ_{ij}, s_{ij}, q_{ij} and m_{ijk}, respectively. By application of the Gauss theorem on Eq. (2), one finds

$$\begin{aligned} \delta w_I = &\int_s [\sigma_{ij} n_j \delta u_i + m_{ijk} n_k \delta\epsilon^p_{ij}]ds \\ &- \int_v [\sigma_{ij,j}\delta u_i + (m_{ijk,k} + s_{ij} - q_{ij})\delta\epsilon^p_{ij}]dv \end{aligned} \tag{3}$$

where n_i is the outward unit normal vector to the surface of the micro volume, s, and u_i is the displacement vector. For arbitrary variations of displacements and plastic strains, the last term has to vanish and two sets of equilibrium equations are obtained as

$$\begin{aligned} \sigma_{ij,j} = 0 \quad &\text{in} \quad v \\ m_{ijk,k} + s_{ij} - q_{ij} = 0 \quad &\text{in} \quad v \end{aligned} \tag{4}$$

Eq. (3) may then be rewritten as

$$\int_s [\sigma_{ij} n_j \delta u_i + m_{ijk} n_k \delta \epsilon^p_{ij}] ds = \int_s [T_i \delta u_i + M_{ij} \delta \epsilon^p_{ij}] ds \tag{5}$$

where $T_i = \sigma_{ij} n_j$ and $M_{ij} = m_{ijk} n_k$ are traction and moment traction, respectively. This surface integral may be identified as the external work, δw_E, done on the volume, v. The principle of virtual work can then be written as $\delta w_I = \delta w_E$, or

$$\int_v [\sigma_{ij} \delta \epsilon_{ij} + (q_{ij} - s_{ij}) \delta \epsilon^p_{ij} + m_{ijk} \delta \epsilon^p_{ij,k}] dv = \int_s [T_i \delta u_i + M_{ij} \delta \epsilon^p_{ij}] ds \tag{6}$$

or in the incremental form

$$\int_v [\dot{\sigma}_{ij} \delta \dot{\epsilon}_{ij} + (\dot{q}_{ij} - \dot{s}_{ij}) \delta \dot{\epsilon}^p_{ij} + \dot{m}_{ijk} \delta \dot{\epsilon}^p_{ij,k}] dv = \int_s [\dot{T}_i \delta \dot{u}_i + \dot{M}_{ij} \delta \dot{\epsilon}^p_{ij}] ds \tag{7}$$

which will be used for the finite element formulation.

By imposing the incremental version of the work, $\dot{w} = \dot{w}_I = \dot{w}_E$, from Eq. (2), on the second law of the thermodynamics, Eq. (1)b, and using $\sigma_{ij} \dot{\epsilon}^p_{ij} = s_{ij} \dot{\epsilon}^p_{ij}$, one can have

$$\left(\sigma_{ij} - \frac{\partial \psi}{\partial \epsilon^e_{ij}} \right) \dot{\epsilon}^e_{ij} + \left(q_{ij} - \frac{\partial \psi}{\partial \epsilon^p_{ij}} \right) \dot{\epsilon}^p_{ij} + \left(m_{ijk} - \frac{\partial \psi}{\partial \epsilon^p_{ij,k}} \right) \dot{\epsilon}^p_{ij,k} \geq 0 \tag{8}$$

where the free energy, ψ, may in general depend on the elastic strain as well as the plastic strain and its gradients. However, here the free energy is assumed to depend only on the elastic strains and plastic strain gradients, see Fredriksson et al. (2009), as

$$\psi \left(\epsilon^e_{ij}, \epsilon^p_{ij,k} \right) = \frac{1}{2} c_{ijkl} \epsilon^e_{ij} \epsilon^e_{kl} + \frac{1}{2} G L_*^2 \epsilon^p_{ij,k} \epsilon^p_{ij,k} \tag{9}$$

Here, c_{ijkl} is the isotropic tensor of the elastic moduli, defined in terms of Young's modulus, E, and Poisson's ratio, ν, L_* is a material length scale parameter and G is the elastic shear modulus. Assuming that both the Cauchy stress and the higher order stress are purely energetic, two constitutive equations are extracted as

$$\sigma_{ij} = \frac{\partial \psi}{\partial \epsilon^e_{ij}} = c_{ijkl} \epsilon^e_{kl}, \quad m_{ijk} = \frac{\partial \psi}{\partial \epsilon^p_{ij,k}} = G L_*^2 \epsilon^p_{ij,k} \tag{10}$$

The second law of thermodynamics, Eq. (8), then reads

$$q_{ij}\dot{\epsilon}^p_{ij} \geq 0 \tag{11}$$

as $\frac{\partial \psi}{\partial \epsilon^p_{ij}} = 0$. In order to fulfill this inequality, and thereby ensure non-negative dissipation, a dissipation potential function, $f^* = f^*(q_{ij})$, is defined as

$$\dot{\epsilon}^p_{ij} = \dot{\lambda}\frac{\partial f^*}{\partial q_{ij}} \tag{12}$$

where $\dot{\lambda}$ is a microscopic scalar plastic multiplier and f^* is a convex function. Moreover, Eq. (12) implies that the plastic strain increment is normal to the dissipation potential function. Associative plastic flow is assumed, such that plastic potential function can be substituted by the yield surface, f, see Lubliner (1990)

$$f^*(q_{ij}) = f(q_{ij}) \tag{13}$$

The microscopic yield surface, f, is then defined as

$$f = \sqrt{\frac{3}{2}q_{ij}q_{ij}} - \sigma_f = 0 \tag{14}$$

where the instantaneous flow stress is given by $\sigma_f = \sigma_y + h\epsilon^p_e$, with σ_y denoting the initial yield stress, h denoting the linear hardening modulus and ϵ^p_e denoting the accumulated effective plastic strain, i.e. $\epsilon^p_e = \int \dot{\epsilon}^p_e d\tau$ in which τ is "pseudo-time" and $\dot{\epsilon}^p_e = \sqrt{\frac{2}{3}\dot{\epsilon}^p_{ij}\dot{\epsilon}^p_{ij}}$. Then the flow rule which ensures the normality of the plastic strain increment to the yield surface is obtained by

$$\dot{\epsilon}^p_{ij} = \dot{\lambda}\frac{\partial f}{\partial q_{ij}} = \frac{3}{2}\frac{q_{ij}}{q_e}\dot{\epsilon}^p_e = r_{ij}\dot{\epsilon}^p_e \tag{15}$$

where $q_e = \sqrt{\frac{3}{2}q_{ij}q_{ij}}$ is the effective micro stress and $r_{ij} = \frac{3}{2}\frac{q_{ij}}{q_e}$ is the direction of the plastic strain increment.

For the numerical implementation, the evolution law of the micro stress, $\dot{q}_{ij}$, needs to be extracted. By considering $r_{ij} = \frac{3}{2}\frac{q_{ij}}{q_e}$, or equivalently $q_{ij} = \frac{2}{3}q_e r_{ij}$, one finds

$$\dot{q}_{ij} = \dot{\overline{\frac{2}{3}q_e r_{ij}}} = \frac{2}{3}\left(\dot{q}_e r_{ij} + q_e \dot{r}_{ij}\right) \tag{16}$$

More discussion on the computational implementation of the above material model can be found in Fredriksson et al. (2009) and Azizi et al. (2011c).

2.2. Material model at the macro scale

At the macroscopic scale, a conventional plasticity is considered where the first and second law of thermodynamics are satisfied, see also Lubliner (1972) and Chaboche (1993). Capital symbols are used to represent macroscopic quantities. Thus

$$\begin{aligned} \dot{W} &= \dot{D} + \dot{\Psi} \\ \dot{D} &= \dot{W} - \dot{\Psi} \geq 0 \end{aligned} \tag{17}$$

where $\dot{W}$ is the rate of total energy, $\dot{D}$ is the dissipation rate, and $\dot{\Psi}$ is the rate of the free energy. Again, heat flux and entropy production terms are ignored. The rate of the total energy is considered as

$$\dot{W} = \Sigma_{ij}\dot{E}_{ij} \tag{18}$$

where $\dot{E}_{ij} = \dot{E}^e_{ij} + \dot{E}^p_{ij}$ is the rate of total strain given as the sum of the elastic and plastic parts. An engineering definition for the macroscopic plastic strain, E^p_{ij}, is considered as

$$E^p_{ij} = E_{ij} - C^{-1}_{ijkl}\Sigma_{kl} \tag{19}$$

where Σ_{ij} is the Cauchy stress and C_{ijkl} is the tensor of the elastic moduli for the composite defined according to the numerical differentiation of the macroscopic quantities in the elastic regime as $C_{ijkl} = \frac{\partial \Sigma_{ij}}{\partial E_{kl}} = \frac{\Sigma^{\tau+\Delta\tau}_{ij} - \Sigma^{\tau}_{ij}}{E^{\tau+\Delta\tau}_{kl} - E^{\tau}_{kl}}$ where $\Delta\tau$ is the "pseudo-time" increment, see also Miehe (1996).
Due to the assumption that no plastic strain gradient effects occur at the macroscale, the macroscopic free energy is taken to depend on the macroscopic elastic and plastic strains, $\Psi = \Psi(E^e_{ij}, E^p_{ij})$, and not on the gradients of the macroscopic plastic strains. Thus, the specific form adopted here is, see also Rice (1971) and Rosakis et al. (2000)

$$\Psi(E^e_{ij}, E^p_{ij}) = \frac{1}{2}C_{ijkl}E^e_{ij}E^e_{kl} + \frac{1}{2}P_{ijkl}E^p_{ij}E^p_{kl} \tag{20}$$

with

$$\dot{\Psi}(E^e_{ij}, E^p_{ij}) = \frac{\partial \Psi}{\partial E^e_{ij}}\dot{E}^e_{ij} + \frac{\partial \Psi}{\partial E^p_{ij}}\dot{E}^p_{ij} \tag{21}$$

where P_{ijkl} are the moduli providing the plastic strain contribution to the free energy. Upon using $\dot{E}_{ij} = \dot{E}^e_{ij} + \dot{E}^p_{ij}$ and imposing Eqs. (18) and (21)

on the macroscopic second law of thermodynamics, Eq. (17)b, the inequality reads

$$\left(\Sigma_{ij} - \frac{\partial \Psi}{\partial E^e_{ij}}\right) \dot{E}_{ij} + \left(\frac{\partial \Psi}{\partial E^e_{ij}} - \frac{\partial \Psi}{\partial E^p_{ij}}\right) \dot{E}^p_{ij} \geq 0 \tag{22}$$

Since $\dot{E}_{ij}$ can be chosen arbitrarily, one way to ensure that the first term of Eq. (22) is always non-negative, is to enforce that

$$\Sigma_{ij} = \frac{\partial \Psi}{\partial E^e_{ij}} = C_{ijkl} E^e_{kl} \tag{23}$$

It is seen that the Cauchy stress, Σ_{ij}, is work conjugate to the elastic strains, E^e_{ij}.

The second term of Eq. (22) depends on the internal variable $\dot{E}^p_{ij}$, which cannot be chosen arbitrarily. Hence, to fulfill the inequality of Eq. (22) the Bauschinger stress, A_{ij}, is defined as, see also Rice (1971), Chaboche (1993) and Rosakis et al. (2000)

$$A_{ij} = \frac{\partial \Psi}{\partial E^p_{ij}} = P_{ijkl} E^p_{kl} \tag{24}$$

Then the dissipation rate, Eq. (22), is rewritten as

$$(\Sigma_{ij} - A_{ij}) \dot{E}^p_{ij} \geq 0 \tag{25}$$

also known as Drucker's postulate, Drucker (1951). For the above equation to be always non-negative, a dissipation potential function, $\Phi^* = \Phi^*(\Sigma_{ij} - A_{ij})$, is defined as

$$\dot{E}^p_{ij} = \dot{\Lambda} \frac{\partial \Phi^*(\Sigma_{ij} - A_{ij})}{\partial (\Sigma_{ij} - A_{ij})} = \dot{\Lambda} \frac{\partial \Phi^*(\Sigma_{ij} - A_{ij})}{\partial \Sigma_{ij}} \tag{26}$$

where $\dot{\Lambda}$ is a macroscopic scalar plastic multiplier and the last equality are justified due to the fact that the Bauschinger stress, A_{ij}, is constant within each increment. In view of the principle of maximum plastic resistance, Lubliner (1990), this approach is a mathematical statement of two ideas: (I) The dissipation potential function is convex, and (II) the plastic strain is normal to the dissipation potential function. Incorporating the Drucker's postulate, Drucker (1951), as a non-thermodynamical approach for the plastic work definition, it is obtained that the yield surface is itself a plastic

potential. Hence, normality is associated with the yield criterion or in other words an associative flow rule is considered as

$$\Phi^*(\Sigma_{ij} - A_{ij}) = \Phi(\Sigma_{ij} - A_{ij}) \tag{27}$$

where $\Phi(\Sigma_{ij} - A_{ij})$ is the macroscopic yield function and A_{ij} is the center of the yield surface.

The macroscopic yield function, $\Phi(\Sigma_{ij} - A_{ij})$, for a composite material is generally anisotropic and pressure dependent. Therefore, we here choose to extend the classical anisotropic pressure independent yield function by Hill, Hill (1948), to have pressure dependency and to account for the Bauschinger stress, A_{ij}, as the center of the yield surface, see also Kuroda (1999). The two out-of-plane shear components, Σ_{13} and Σ_{23}, are ignored, such that only four stress components enter, namely $\Sigma_{11}, \Sigma_{22}, \Sigma_{33}$ and Σ_{12}. Following the ideas of Azizi et al. (2011a) for the pressure dependency, the four eigenvalues, P_{λ_i}, and the corresponding eigenvectors, $\vec{v}^{(P_{\lambda_i})}, i = 1 \dots 4$, of the $\boldsymbol{P}$-modulus, P_{ijkl}, are calculated and written as

$$P_\lambda = \begin{bmatrix} P_{\lambda_1} & P_{\lambda_2} & P_{\lambda_3} & P_{\lambda_4} \end{bmatrix} \tag{28}$$

$$\mathbf{V} = \begin{bmatrix} v_1^{(P_{\lambda_1})} & v_1^{(P_{\lambda_2})} & v_1^{(P_{\lambda_3})} & v_1^{(P_{\lambda_4})} \\ v_2^{(P_{\lambda_1})} & v_2^{(P_{\lambda_2})} & v_2^{(P_{\lambda_3})} & v_2^{(P_{\lambda_4})} \\ v_3^{(P_{\lambda_1})} & v_3^{(P_{\lambda_2})} & v_3^{(P_{\lambda_3})} & v_3^{(P_{\lambda_4})} \\ v_4^{(P_{\lambda_1})} & v_4^{(P_{\lambda_2})} & v_4^{(P_{\lambda_3})} & v_4^{(P_{\lambda_4})} \end{bmatrix} \tag{29}$$

where $v_j^{(P_{\lambda_i})}$ is the $j-$th component of an eigenvector corresponding to the $i-$th eigenvalue. The Cauchy stress, Σ_{ij}, and the Bauschinger stress, A_{ij}, are then transformed as

$$\begin{bmatrix} \Sigma_{\lambda_1} \\ \Sigma_{\lambda_2} \\ \Sigma_{\lambda_3} \\ \Sigma_{\lambda_4} \end{bmatrix} = \mathbf{V}^T \begin{bmatrix} \Sigma_{11} \\ \Sigma_{22} \\ \Sigma_{33} \\ \Sigma_{12} \end{bmatrix} \tag{30}$$

$$\begin{bmatrix} A_{\lambda_1} \\ A_{\lambda_2} \\ A_{\lambda_3} \\ A_{\lambda_4} \end{bmatrix} = \mathbf{V}^T \begin{bmatrix} A_{11} \\ A_{22} \\ A_{33} \\ A_{12} \end{bmatrix} \tag{31}$$

where Σ_{λ_i} and A_{λ_i} are the transformed Cauchy stress and Bauschinger stress, respectively, see also Karafillis and Boyce (1993). It is emphasized that the transformation in Eqs. (30) and (31) is a change of basis in which the same four stress components exist, but labelled with the subscript λ_i. Fig. 1 shows the new components of the Cauchy stresses as compared to the normal stresses in the Cartesian coordinate system.

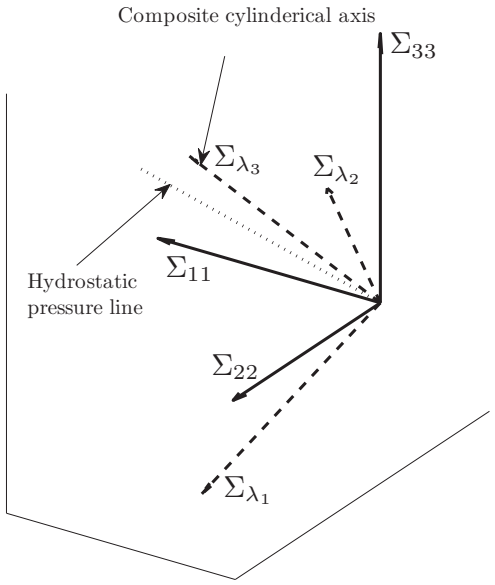

Figure 1: Stress, Σ_{ij}, and transformed stress, Σ_{λ_i}, used to define the pressure dependent composite yield surface.

The stress component Σ_{λ_3} is parallel to the composite yield surface axis. This implies that infinite large loading by Σ_{λ_3} alone yields zero plastic deformations. Or in other words, an infinite large Σ_{λ_3}-loading of the composite is similar to infinite large loading along the hydrostatic pressure line, $(\Sigma_{11}, \Sigma_{22}, \Sigma_{33}) = (1, 1, 1)$, on an isotropic material. Hence, Σ_{λ_3} may be excluded from the formulation of anisotropic yield function here. Thus, three stress components remain, namely Σ_{λ_1}, Σ_{λ_2} and Σ_{λ_4}. Furthermore, Σ_{λ_1} and Σ_{λ_2} are the major and minor axes of the elliptic cross section of the composite yield surface cylinder, yielding a reduced expression of the composite yield function as

$$\Phi = F^{\lambda}\tilde{\Sigma}^2_{\lambda_1} + H^{\lambda}\tilde{\Sigma}^2_{\lambda_2} + N^{\lambda}\tilde{\Sigma}^2_{\lambda_4} - 1 \tag{32}$$

where $\tilde{\Sigma}_{\lambda_i} = \Sigma_{\lambda_i} - A_{\lambda_i}$ and F^λ, H^λ and N^λ are the coefficients of anisotropy having units of [MPa^{-2}]. For plastic deformations to happen, the stress state must not leave the flow surface, and a consistency relation has to be fulfilled as

$$\begin{aligned}\dot{\Phi} = \frac{\partial \Phi}{\partial \tilde{\Sigma}_{\lambda_1}} \dot{\tilde{\Sigma}}_{\lambda_1} + \frac{\partial \Phi}{\partial \tilde{\Sigma}_{\lambda_2}} \dot{\tilde{\Sigma}}_{\lambda_2} + \frac{\partial \Phi}{\partial \tilde{\Sigma}_{\lambda_4}} \dot{\tilde{\Sigma}}_{\lambda_4} + \\ \frac{\partial \Phi}{\partial F^\lambda} \dot{F}^\lambda + \frac{\partial \Phi}{\partial H^\lambda} \dot{H}^\lambda + \frac{\partial \Phi}{\partial N^\lambda} \dot{N}^\lambda = 0\end{aligned} \tag{33}$$

Kinematic hardening is considered by the evolution of A_{λ_i} and anisotropic hardening is accounted for through the evolution of F^λ, H^λ and N^λ.
The anisotropic parameters are assumed to be defined as a linear function of the transformed plastic strains, $E^P_{\lambda_i}$, as

$$\begin{aligned}F^\lambda &= F^\lambda_0 (1 + f_1 E^P_{\lambda_1} + f_2 E^P_{\lambda_2} + f_4 E^P_{\lambda_4}) \\ H^\lambda &= H^\lambda_0 (1 + h_1 E^P_{\lambda_1} + h_2 E^P_{\lambda_2} + h_4 E^P_{\lambda_4}) \\ N^\lambda &= N^\lambda_0 (1 + n_1 E^P_{\lambda_1} + n_2 E^P_{\lambda_2} + n_4 E^P_{\lambda_4})\end{aligned} \tag{34}$$

where F^λ_0, H^λ_0 and N^λ_0 are parameters of the initial anisotropic yield surface and f_i, h_i and n_i are anisotropic hardening coefficients. The transformed plastic strain, $E^P_{\lambda_3}$, does not enter Eq. (34) due to the same argument excluding Σ_{λ_3} from the yield function, Eq. (32). The initial anisotropic parameters, F^λ_0, H^λ_0 and N^λ_0, are determined by three numerically calculated stress points at the initial composite yield surface, $\left(\Sigma^2_{\lambda_1}\right)_i$, $\left(\Sigma^2_{\lambda_2}\right)_i$ and $\left(\Sigma^2_{\lambda_4}\right)_i$ for $i = 1, 2, 3$ (that is nine data values). Imposing the initial conditions, $E^P_{\lambda_i} = A_{\lambda_i} = 0$, on Eq. (32) results into the following linear system of equation to be solved

$$\begin{bmatrix} a_1 & b_1 & c_1 \\ a_2 & b_2 & c_2 \\ a_3 & b_3 & c_3 \end{bmatrix} \begin{bmatrix} F^\lambda_0 \\ H^\lambda_0 \\ N^\lambda_0 \end{bmatrix} = \begin{bmatrix} 1 \\ 1 \\ 1 \end{bmatrix} \tag{35}$$

where $a_i = \left(\Sigma^2_{\lambda_1}\right)_i$, $b_i = \left(\Sigma^2_{\lambda_2}\right)_i$, $c_i = \left(\Sigma^2_{\lambda_4}\right)_i$ and $i = 1, 3$ are the three chosen stress points on the initial composite yield surfaces.

During subsequent loading expansion of the composite yield surface has to be considered. Having nine unknowns, h_i, f_i and n_i where $i = 1, 2$, and 4, see Eq. (34), sufficient numerical data have to be generated. Therefore,

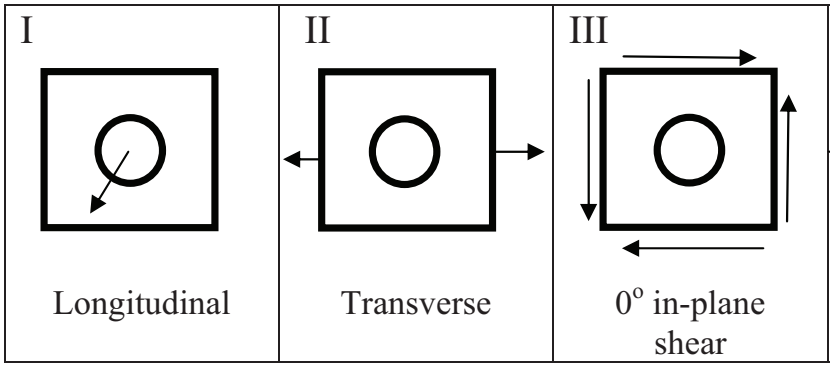

Figure 2: Three loading trials for computation of the anisotropic hardening coefficients, h_i, f_i and n_i, see Eq. (34).

three different loading trials including longitudinal, transverse and 0^o in-plane shear are considered as shown in Fig. 2.
The subsequent anisotropic coefficients are then calculated similar to the initial coefficients, Eq. (35), as

$$\begin{bmatrix} a_1 & b_1 & c_1 \\ a_2 & b_2 & c_2 \\ a_3 & b_3 & c_3 \end{bmatrix}^i \begin{bmatrix} F^\lambda \\ H^\lambda \\ N^\lambda \end{bmatrix}^i = \begin{bmatrix} 1 \\ 1 \\ 1 \end{bmatrix} \tag{36}$$

where $a_j = (\tilde{\Sigma}^2_{\lambda_1})_j$, $b_j = (\tilde{\Sigma}^2_{\lambda_2})_j$, $c_j = (\tilde{\Sigma}^2_{\lambda_4})_j$, $j = 1, 2, 3$ are three chosen points on each subsequent yield surface and $i = I, II, III$ are the three imposed loading trials shown in Fig. 2.
Knowing the parameters of anisotropy, F^λ,H^λ and N^λ, Eq. (34) is rewritten as

$$\begin{aligned} \frac{F^\lambda}{F_0^\lambda} - 1 &= \dot{F}^\lambda / F_0^\lambda = f_1 E^P_{\lambda_1} + f_2 E^P_{\lambda_2} + f_4 E^P_{\lambda_4} \\ \frac{H^\lambda}{H_0^\lambda} - 1 &= \dot{H}^\lambda / H_0^\lambda = h_1 E^P_{\lambda_1} + h_2 E^P_{\lambda_2} + h_4 E^P_{\lambda_4} \\ \frac{N^\lambda}{N_0^\lambda} - 1 &= \dot{N}^\lambda / N_0^\lambda = n_1 E^P_{\lambda_1} + n_2 E^P_{\lambda_2} + n_4 E^P_{\lambda_4} \end{aligned} \tag{37}$$

Incorporating the plastic strains, $E^P_{\lambda_i}$, computed by the three loading trials, one has to solve the following linear system of equations to find the

anisotropic hardening coefficients

$$\begin{bmatrix} \dot{F}_I^\lambda/F_0^\lambda \\ \dot{F}_{II}^\lambda/F_0^\lambda \\ \dot{F}_{III}^\lambda/F_0^\lambda \end{bmatrix} = \begin{bmatrix} a_I & b_I & c_I \\ a_{II} & b_{II} & c_{II} \\ a_{III} & b_{III} & c_{III} \end{bmatrix} \begin{bmatrix} f_1 \\ f_2 \\ f_4 \end{bmatrix} \tag{38}$$

$$\begin{bmatrix} \dot{H}_I^\lambda/H_0^\lambda \\ \dot{H}_{II}^\lambda/H_0^\lambda \\ \dot{H}_{III}^\lambda/H_0^\lambda \end{bmatrix} = \begin{bmatrix} a_I & b_I & c_I \\ a_{II} & b_{II} & c_{II} \\ a_{III} & b_{III} & c_{III} \end{bmatrix} \begin{bmatrix} h_1 \\ h_2 \\ h_4 \end{bmatrix}$$

$$\begin{bmatrix} \dot{N}_I^\lambda/N_0^\lambda \\ \dot{N}_{II}^\lambda/N_0^\lambda \\ \dot{N}_{III}^\lambda/N_0^\lambda \end{bmatrix} = \begin{bmatrix} a_I & b_I & c_I \\ a_{II} & b_{II} & c_{II} \\ a_{III} & b_{III} & c_{III} \end{bmatrix} \begin{bmatrix} n_1 \\ n_2 \\ n_4 \end{bmatrix}$$

where $a_i = (E^P_{\lambda_1})_i$, $b_i = (E^P_{\lambda_2})_i$ and $c_i = (E^P_{\lambda_4})_i$ where $i = I, II, III$ are three imposed loading trials shown in Fig. 2.

Finally, Tab. 1 comparatively summarizes the defined material models at both micro and macro scale. Furthermore, Fig. 3 shows, in a flowchart, the computational procedure for calculating the necessary coefficients of anisotropy.

3. Problem Formulation

A metal matrix composite (MMC) with long, regularly distributed, parallel fibers of circular cross-sections is considered, see Fig. 4a. Uniaxial loading in transverse (Σ_{11} or Σ_{22}) and longitudinal (Σ_{33}) direction, 0^o in-plane shear (Σ_{12}) and hydrostatic pressure loading are considered ($\Sigma_{11} = \Sigma_{22} = \Sigma_{33}$). A unit cell is extracted as shown in Fig. 4b, where the macroscopic normal stresses and shear stress are indicated. Fig. 4c shows the displacement boundary conditions and dimensions. At the lower left corner of the unit cell, a reference Cartesian coordinate system, x_i, is located and aligned with the sides of the cell. The positive direction of the third axis, x_3, points out of the (x_1, x_2)-plane.
Fibers are considered to be purely elastic, whereas the matrix exhibits an elasto-plastic behavior with gradient effects as described in section, 2.1. Since plastic strain gradients are of higher order nature, higher-order boundary conditions must be prescribed in addition to the conventional boundary conditions in displacements and surface tractions. At the exterior of the cell

Micro scale	Macro scale
$\dot{w} = \dot{d} + \dot{\psi}$	$\dot{W} = \dot{D} + \dot{\Psi}$
$\dot{d} = \dot{w} - \dot{\psi} \geq 0$	$\dot{D} = \dot{W} - \dot{\Psi} \geq 0$
$\dot{w} = \sigma_{ij}\dot{\epsilon}^e_{ij} + q_{ij}\dot{\epsilon}^p_{ij} + m_{ijk}\dot{\epsilon}^p_{ij,k}$	$\dot{W} = \Sigma_{ij}\dot{E}_{ij}$
$\psi = \frac{1}{2}c_{ijkl}\epsilon^e_{ij}\epsilon^e_{kl} + \frac{1}{2}GL^2_*\epsilon^p_{ij,k}\epsilon^p_{ij,k}$	$\Psi = \frac{1}{2}C_{ijkl}E^e_{ij}E^e_{kl} + \frac{1}{2}P_{ijkl}E^p_{ij}E^p_{kl}$
$\left(\sigma_{ij} - \frac{\partial\psi}{\partial\epsilon^e_{ij}}\right)\dot{\epsilon}^e_{ij} + \left(q_{ij} - \frac{\partial\psi}{\partial\epsilon^p_{ij}}\right)\dot{\epsilon}^p_{ij} + \left(m_{ijk} - \frac{\partial\psi}{\partial\epsilon^p_{ij,k}}\right)\dot{\epsilon}^p_{ij,k} \geq 0$	$(\Sigma_{ij} - \frac{\partial\Psi}{\partial E^e_{ij}})\dot{E}_{ij} + (\frac{\partial\Psi}{\partial E^e_{ij}} - \frac{\partial\Psi}{\partial E^p_{ij}})\dot{E}^p_{ij} \geq 0$
$\sigma_{ij} = \frac{\partial\psi}{\partial\epsilon^e_{ij}} = c_{ijkl}\epsilon^e_{kl}$	$\Sigma_{ij} = \frac{\partial\Psi}{\partial E^e_{ij}} = C_{ijkl}E^e_{kl}$
$m_{ijk} = \frac{\partial\psi}{\partial\epsilon^p_{ij,k}} = GL^2_*\epsilon^p_{ij,k}$	$A_{ij} = \frac{\partial\Psi}{\partial E^p_{ij}} = P_{ijkl}E^p_{kl}$
$q_{ij}\dot{\epsilon}^p_{ij} \geq 0$	$(\Sigma_{ij} - A_{ij})\,\dot{E}^p_{ij} \geq 0$
$\dot{\epsilon}^p_{ij} = \dot{\lambda}\frac{\partial f^*(q_{ij})}{\partial q_{ij}}$	$\dot{E}^p_{ij} = \dot{\Lambda}\frac{\partial\Phi^*(\Sigma_{ij}-A_{ij})}{\partial\Sigma_{ij}}$
$f^*(q_{ij}) = f(q_{ij})$	$\Phi^*\left(\Sigma_{ij} - A_{ij}\right) = \Phi\left(\Sigma_{ij} - A_{ij}\right)$
$f = \sqrt{\frac{3}{2}q_{ij}q_{ij}} - \sigma_f$	$\Phi = F^\lambda(\tilde{\Sigma}_{\lambda_1})^2 + H^\lambda(\tilde{\Sigma}_{\lambda_2})^2 + N^\lambda\tilde{\Sigma}^2_{\lambda_4} - 1$
$\sigma_f = \sigma_y + h\epsilon^p_e$	$F^\lambda = F^\lambda_0(1 + f_1E^P_{\lambda_1} + f_2E^P_{\lambda_2} + f_4E^P_{\lambda_4})$ $H^\lambda = H^\lambda_0(1 + h_1E^P_{\lambda_1} + h_2E^P_{\lambda_2} + h_4E^P_{\lambda_4})$ $N^\lambda = N^\lambda_0(1 + n_1E^P_{\lambda_1} + n_2E^P_{\lambda_2} + n_4E^P_{\lambda_4})$
$\dot{f} = \frac{3}{2}\frac{q_{ij}}{q_e}\dot{q}_{ij} - \dot{\sigma}_f = 0$	$\dot{\Phi} = \frac{\partial\Phi}{\partial\tilde{\Sigma}_{\lambda_1}}\dot{\tilde{\Sigma}}_{\lambda_1} + \frac{\partial\Phi}{\partial\tilde{\Sigma}_{\lambda_2}}\dot{\tilde{\Sigma}}_{\lambda_2} + \frac{\partial\Phi}{\partial\tilde{\Sigma}_{\lambda_4}}\dot{\tilde{\Sigma}}_{\lambda_4} + \frac{\partial\Phi}{\partial F^\lambda}\dot{F}^\lambda + \frac{\partial\Phi}{\partial H^\lambda}\dot{H}^\lambda + \frac{\partial\Phi}{\partial N^\lambda}\dot{N}^\lambda = 0$
$\dot{\sigma}_f = h\dot{\epsilon}^p_e$	$\dot{F}^\lambda/F^\lambda_0 = f_1\dot{E}^P_{\lambda_1} + f_2\dot{E}^P_{\lambda_2} + f_4\dot{E}^P_{\lambda_4}$ $\dot{H}^\lambda/H^\lambda_0 = h_1\dot{E}^P_{\lambda_1} + h_2\dot{E}^P_{\lambda_2} + h_4\dot{E}^P_{\lambda_4}$ $\dot{N}^\lambda/N^\lambda_0 = n_1\dot{E}^P_{\lambda_1} + n_2\dot{E}^P_{\lambda_2} + n_4\dot{E}^P_{\lambda_4}$

Table 1: Material model at both micro and macro scale.

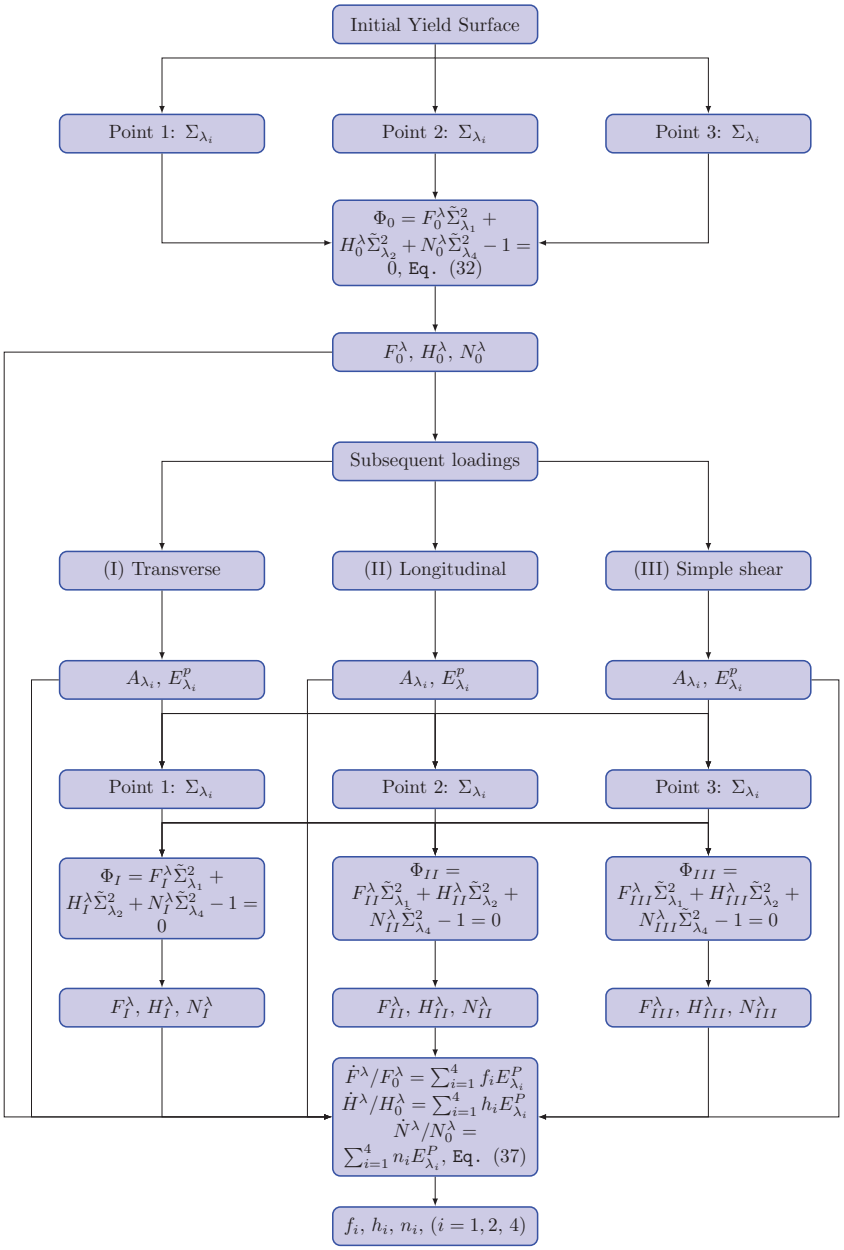

Figure 3: The computational procedure for calculation of the anisotropic coefficients.

the periodic boundary conditions are considered as (see Borg et al., 2008; Hussein et al., 2008; Azizi et al., 2011b)

$$\begin{array}{llll} \dot{u}_1^b = \dot{u}_1^t & \text{and} & \dot{u}_2^b = \dot{u}_2^t - [\dot{\Delta}_3 - \dot{\Delta}_2] \\ \dot{T}_1^b = -\dot{T}_1^t & \text{and} & \dot{T}_2^b = -\dot{T}_2^t \\ \dot{u}_1^l = \dot{u}_1^r - \dot{\Delta}_1 & \text{and} & \dot{u}_2^l = \dot{u}_2^r - \dot{\Delta}_2 \\ \dot{T}_1^l = -\dot{T}_1^r & \text{and} & \dot{T}_2^l = -\dot{T}_2^r \\ \dot{M}_{ij}^b = -\dot{M}_{ij}^t & \text{and} & \dot{M}_{ij}^l = -\dot{M}_{ij}^r \\ [\dot{\epsilon}_{ij}^p]^b = [\dot{\epsilon}_{ij}^p]^t & \text{and} & [\dot{\epsilon}_{ij}^p]^l = [\dot{\epsilon}_{ij}^p]^r \end{array} \tag{39}$$

where l, r, b and t are left, right, bottom and top of the unit cell borders, respectively. In addition to standard periodic boundary conditions for the displacements, tractions, plastic strains and higher order tractions the following conditions are imposed

$$\begin{array}{ll} \dot{u}_1 = \dot{u}_2 = 0, & (x_1, x_2) = (0, 0) \\ \dot{u}_2 = \dot{\Delta}_2, & (x_1, x_2) = (L, 0) \\ \dot{u}_1 = \dot{\Delta}_1,\ \dot{u}_2 = \dot{\Delta}_3, & (x_1, x_2) = (L, h) \\ \dot{u}_3 = \dot{\Delta}_4 & x_3 = t \\ \dot{\epsilon}_{ij}^p = 0, & (x_1^2 + x_2^2 = R^2) \end{array} \tag{40}$$

The out-of-plane plastic strain, ϵ_{33}^p, is given in terms of in-plane plastic strain components by plastic incompressibility, $\epsilon_{ii}^p = 0$. Similarly, M_{33} is given in terms of the in-plane components M_{11} and M_{22}, where $M_{ii} = 0$. The out-of-plane deformation is controlled by specifying a constant out-of-plane normal strain increment, $\dot{\epsilon}_{33} = \dot{\Delta}_4/t$, with t denoting the reference thickness of the unit cell. The prescribed displacement incremental quantities are denoted $\dot{\Delta}_1$, $\dot{\Delta}_2$, $\dot{\Delta}_3$, and $\dot{\Delta}_4$. They are calculated such that the ratio of macroscopic stress rates ($\dot{\Sigma}_{11}$, $\dot{\Sigma}_{22}$, $\dot{\Sigma}_{33}$ and $\dot{\Sigma}_{12}$) remain fixed, see Azizi et al. (2011c), as

$$\frac{\dot{\Sigma}_{22}}{\dot{\Sigma}_{11}} = K_1, \qquad \frac{\dot{\Sigma}_{33}}{\dot{\Sigma}_{11}} = K_2, \qquad \frac{\dot{\Sigma}_{12}}{\dot{\Sigma}_{11}} = K_3 \tag{41}$$

These stresses are calculated as

$$\begin{array}{rcll} \dot{\Sigma}_{11} & = & \dfrac{1}{b}\displaystyle\int_0^b [\dot{T}_1] dx_2; & \text{at} \quad x_1 = a \\ \dot{\Sigma}_{22} & = & \dfrac{1}{a}\displaystyle\int_0^a [\dot{T}_2] dx_1; & \text{at} \quad x_2 = b \\ \dot{\Sigma}_{12} & = & \dfrac{1}{b}\displaystyle\int_0^b [\dot{T}_2] dx_2; & \text{at} \quad x_1 = a \end{array} \tag{42}$$

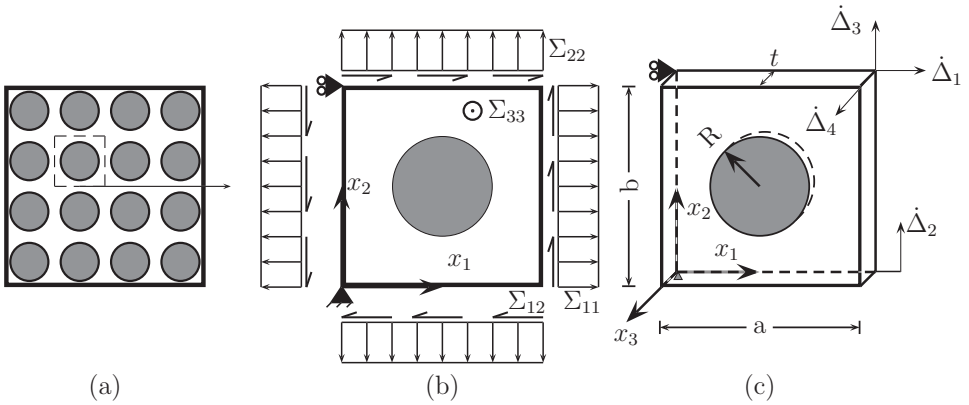

Figure 4: (a) Regular distribution of fibers in the composite. (b) A unit cell containing one fiber with traction boundary condition. (c) A unit cell containing one fiber with conventional displacement boundary conditions used in numerical simulation representing combined normal and shear loading as shown in (*b*).

and the strains are considered as

$$\begin{aligned} \dot{E}_{11} &= \frac{\dot{\Delta}_1}{a} \\ \dot{E}_{22} &= \frac{\dot{\Delta}_3 - \dot{\Delta}_2}{b} \\ \dot{E}_{12} &= \frac{\dot{\Delta}_2}{a} \end{aligned} \tag{43}$$

After calculating these stresses and strains, the composite yield surface is found by the strain based condition

$$\left\| E_{ij} - C^{-1}_{ijkl}\Sigma_{kl} - E^{res}_{ij} \right\| \geq \epsilon_t \tag{44}$$

where ϵ_t is the threshold value and E^{res}_{ij} is the macroscopic residual strains defined as the components of the plastic strain after unloading. Note that the residual strain is zero for initial yielding.

The K-values for all load cases are summarized in Tab. 2.

	K_1	K_2	K_3
Transverse loading ($\Sigma_{11} \neq 0$)	0	0	0
Longitudinal loading ($\Sigma_{33} \neq 0$)	1	1000	0
Simple shear ($\Sigma_{12} \neq 0$)	0	0	1000
Hydrostatic pressure ($\Sigma_{11} = \Sigma_{22} = \Sigma_{33} \neq 0$)	1	1	0

Table 2: K-values ensuring the stress proportionality.

4. Computational method

Eight-node quadrilateral elements are considered for the in-plane displacement interpolation, while four-node quadrilateral elements are considered to interpolate the plastic strain components. Additionally, an extra degree of freedom is added to represent the unique change of unit cell thickness. Nodal interpolation is performed according to

$$\dot{u}_i = \sum_{n=1}^{2k} N_i^n \dot{U}_n, \quad \dot{\epsilon}_{ij}^p = \sum_{m=1}^{3l} P_{ij}^m \dot{\epsilon}_m^p \tag{45}$$

where N_i^n and P_{ij}^m are shape functions for the displacement and plastic strain components, respectively, and k and l are the number of nodes used for different interpolation schemes. Hence, $k = 8$ and $l = 4$. The appropriate derivatives of the displacement field and the plastic strain field can be expressed as

$$\dot{\epsilon}_{ij} = \sum_{n=1}^{2k} B_{ij}^n \dot{U}_n, \quad \dot{\epsilon}_{ij,k}^p = \sum_{m=1}^{3l} Q_{ijk}^m \dot{\epsilon}_m^p \tag{46}$$

where, $B_{ij}^n = (N_{i,j}^n + N_{j,i}^n)/2$ and $Q_{ijk}^m = P_{ij,k}^m$ are spatial derivatives of both interpolation functions. Inserting into the incremental form of the principle of virtual work, Eq. (7), the following matrix form arises

$$\begin{bmatrix} \mathbf{K}_u & -\mathbf{K}_{up} \\ -\mathbf{K}_{up}^T & \mathbf{K}_p \end{bmatrix} \begin{bmatrix} \dot{\mathbf{U}} \\ \dot{\boldsymbol{\epsilon}}^p \end{bmatrix} = \begin{bmatrix} \dot{\mathbf{f}}_u \\ \dot{\mathbf{f}}_p \end{bmatrix} \tag{47}$$

where $\dot{\mathbf{f}}_u = \int_s \mathbf{N}^T \dot{\mathbf{T}} ds$ is nodal force and $\dot{\mathbf{f}}_p = \int_s \mathbf{P}^T \dot{\mathbf{M}} ds$ is nodal higher order force. Stiffness matrices are given by

$$\mathbf{K}_u = \int_v \mathbf{B}^T \mathbf{D}_e \mathbf{B} dv \tag{48}$$

$$\mathbf{K}_p = \int_v [\mathbf{P}^T(\mathbf{D}_e + \mathbf{D}_p)\mathbf{P} + \mathbf{Q}^T\mathbf{D}_h\mathbf{Q}]dv \tag{49}$$

$$\mathbf{K}_{up} = \int_v \mathbf{B}^T\mathbf{D}_e\mathbf{P}dv \tag{50}$$

where $\mathbf{D}_e$ is the microscopic isotropic constitutive matrix, $\mathbf{D}_p$ is the microscopic plastic moduli and $\mathbf{D}_h$ is microscopic higher order moduli. Further details can be found in Fredriksson et al. (2009) and Azizi et al. (2011c).

Finally, Fig. 5 shows the mesh used for the computations presented in the paper. The elastic fiber consists of 576 elements, whereas the elastic-plastic matrix is modeled using 832 element.

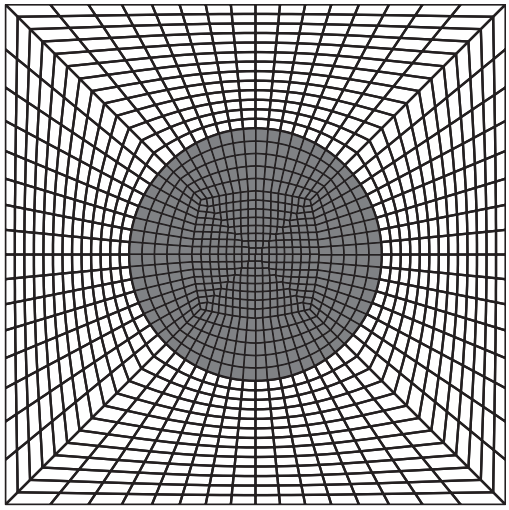

Figure 5: Mesh used for the finite element discretization.

5. Results

The conventional material parameters used for the matrix are $h/E_m = 0.1$, $\sigma_y/E_m = 0.004$, $\tau_y = \sigma_y/\sqrt{3}$, $\upsilon_m = 0.3$, and for the fibers, $E_f = 5.7E_m$ and $\upsilon_f = 0.17$. The dimension of the unit cell is defined by $a/b = 1$. The fiber volume fraction, V_f, is given by $V_f = (\pi R^2)/(ab)$. Each numerical computation includes 1408 elements with 1000 increments at each step of loading, unloading and reloading. For a micron scale length parameter of

$L_* = 1\mu m$ in the present model, we analyze cases for $L_*/R = 0$, $L_*/R = 0.2$ and 0.4 which corresponds to large fibers, fibers with $R = 5\mu m$ and $R = 2.5\mu m$, respectively. The threshold value defining the initial yield surface, ϵ_t in Eq. (44), is taken to be $\epsilon_t = 0.001$.

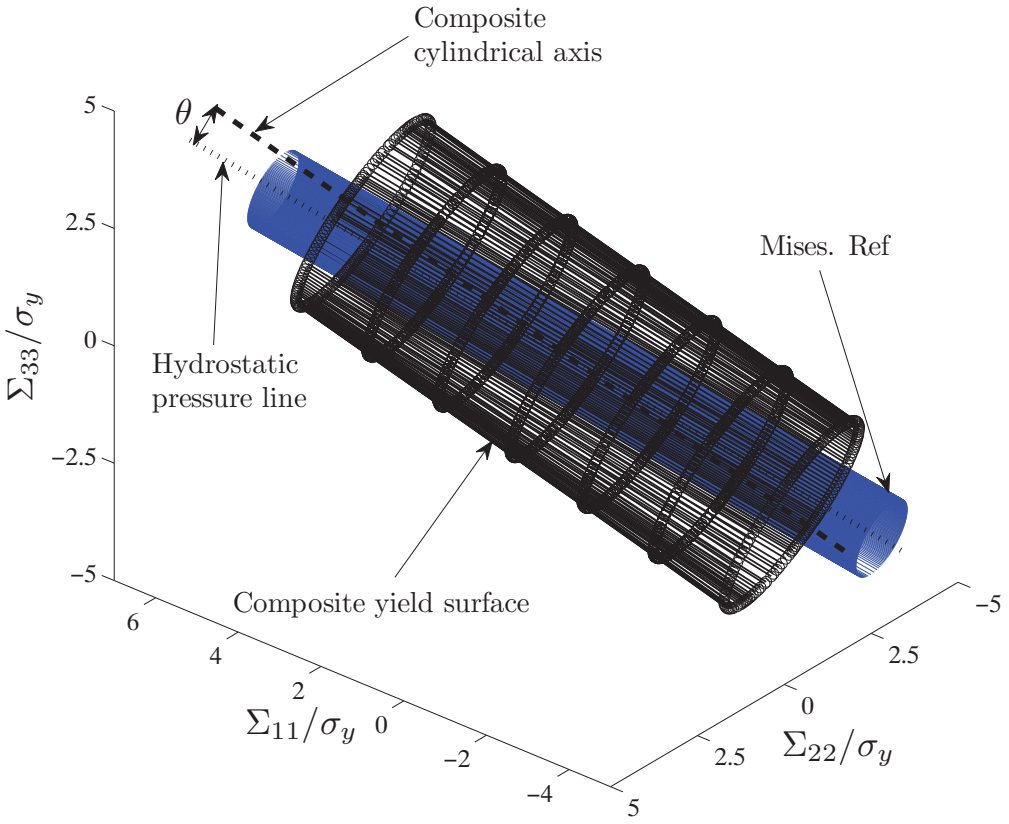

Figure 6: Plot of the initial yield surface of the composite with $V_f = 0.2$ and $L_*/R = 0.4$ using seven different planes each consisting of 80 points. The Mises yield surface for the pure matrix material is also shown.

For $V_f = 0.2$ and $L_*/R = 0.4$, the initial yield surface of composite in the conventional 3D stress coordinate system, $(\Sigma_{11}, \Sigma_{22}, \Sigma_{33})$, is shown in Fig. 6. Seven different planes, on which Σ_{λ_3} is constant, are plotted where each plane consists of 80 points. The Mises yield surface for the pure matrix

material is also shown. Compared to the Mises yield surface, the composite yield surface is expanded and has a non-circular cross section unlike the Mises yield surface. The cross section of the composite yield surface is almost elliptic. In addition, the axis of the composite yield surface, is given by $(\Sigma_{11}, \Sigma_{22}, \Sigma_{33}) = (1, 1, 1.35)$, and it deviates from the axis of the Mises yield surface, $(\Sigma_{11}, \Sigma_{22}, \Sigma_{33}) = (1, 1, 1)$. Depending on the fiber volume fraction, the angle, θ, between the two axes of the yield surfaces changes. Tab. 3 shows the angle for different fiber volume fractions. It is seen that with higher fiber volume fraction, V_f, the angle increases. This implies that for a composite material, hydrostatic loading along the Mises axis, $\Sigma_{11} = \Sigma_{22} = \Sigma_{33}$, eventually cause macroscopic plastic flow. On the other hand, zero plastic straining is expected when purely Σ_{λ_3} loading is applied. In conclusion, the pressure *independency* of fiber and matrix at the micro scale, does in fact result into a pressure *dependency* at the macroscopic scale. This is now further investigated in details for different material length scales, L_*/R, and fiber volume fractions, V_f.

	$V_f = 0.0$	$V_f = 0.1$	$V_f = 0.2$	$V_f = 0.3$
θ [degrees]	0.00^0	2.79^0	9.15^0	12.65^0

Table 3: Effect of the fiber volume fraction, V_f, on the angle between the axes of the composite yield surface and the Mises yield surface, see Fig 6, when $L_*/R = 0.4$.

Mughrabi (2001), Fleck et al. (2003) and Gao and Huang (2003) showed that for composite materials, dislocations cannot pass from matrix into the fiber and consequently pile up at the fiber/matrix interface. This leads to the plastic strain suppression at the interfaces as stated in Eq. (40). Defining the uniaxial yield strain, $\epsilon_y = \sigma_y/E_m$, Fig. 7 shows the normalized effective plastic strain distribution, ϵ_e^p/ϵ_y, when the unit cell is loaded through the hydrostatic pressure line until $\Sigma_{11} = \Sigma_{22} = \Sigma_{33} = 3\sigma_y$ and $\Sigma_{12} = 0$. It is seen that plastic flow has occurred for all cases. The maximum value of the effective plastic strain is higher in the conventional analysis, Fig. 7a, compared to the corresponding gradient dependent analysis, Fig. 7b. With the conventional material model, the plastic strain is not suppressed at the fiber/matrix interface, whereas the constraint on the plastic flow considered

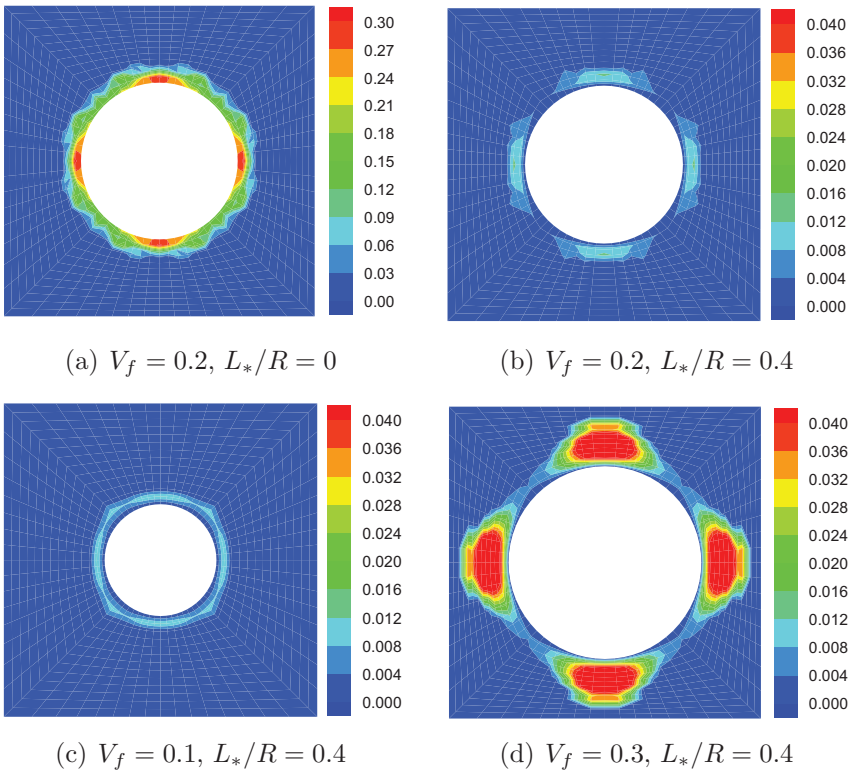

(a) $V_f = 0.2$, $L_*/R = 0$ (b) $V_f = 0.2$, $L_*/R = 0.4$

(c) $V_f = 0.1$, $L_*/R = 0.4$ (d) $V_f = 0.3$, $L_*/R = 0.4$

Figure 7: The effective plastic strain distribution, ϵ_e^p/ϵ_y, with hydrostatic pressure loading until $\Sigma_{11} = \Sigma_{22} = \Sigma_{33} = 3\sigma_y$

in the gradient dependent material is observed to suppress plasticity close to the elastic fiber, Fig. 7b, consistent with the findings by Mughrabi (2001), Fleck et al. (2003) and Gao and Huang (2003). Effect of the fiber volume fraction with a constant material length scale, $L_*/R = 0.4$, is also studied through Figs. 7b, c and d. By increasing the fiber volume fraction, the plasticity starts to grow close to the interface from a thin line distribution in Fig. 7c for $V_f = 0.1$ to a more clustered distribution in Fig. 7b for $V_f = 0.2$ and more severe clustered distribution in Fig. 7d for $V_f = 0.3$. This behavior reveals as the rotation of composite yield surface shown in Fig. 6 and Tab. 3.

The corresponding normalized effective Mises stress, $\sqrt{\frac{3}{2}s_{ij}s_{ij}}/\sigma_y$, under same hydrostatic pressure loading is shown in Fig. 8. A marginal increase

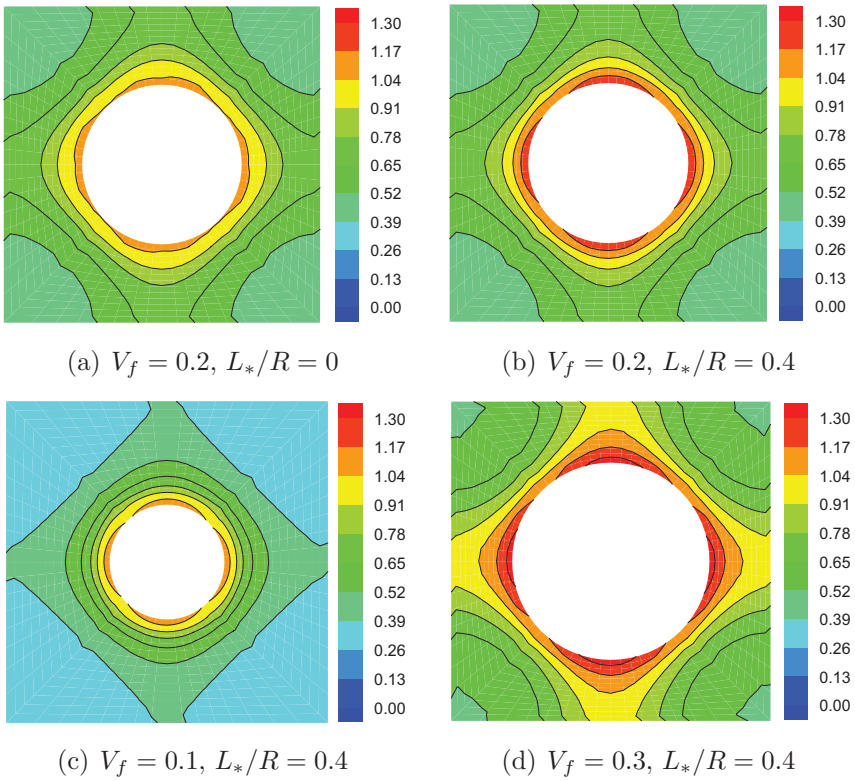

(a) $V_f = 0.2$, $L_*/R = 0$ (b) $V_f = 0.2$, $L_*/R = 0.4$

(c) $V_f = 0.1$, $L_*/R = 0.4$ (d) $V_f = 0.3$, $L_*/R = 0.4$

Figure 8: The effective stress distribution, $\sqrt{\frac{3}{2}s_{ij}s_{ij}}/\sigma_y$, under hydrostatic pressure loading until $\Sigma_{11} = \Sigma_{22} = \Sigma_{33} = 3\sigma_y$

of the Mises stress occurs in the gradient dependent material, Fig. 8b, compared to the conventional material, Fig. 8a. Higher fiber volume fraction results in a larger Mises stress as observed from Fig. 8d and lower fiber volume fraction suppresses the Mises stress as observed from Fig. 8c. Generally, it is concluded that higher fiber volume fractions of composites give rise to earlier onset of plasticity when loaded by a hydrostatic pressure.

For $L_*/R = 0.4$ and $V_f = 0.2$, a two-dimensional projection of the yield surfaces, Fig. 6, on the $(\Sigma_{\lambda_1}, \Sigma_{\lambda_2})$-plane for $\Sigma_{\lambda_3} = 0$ is depicted in Fig. 9. It is seen that the assumption of having an elliptic shape with major axis in Σ_{λ_1} direction and minor axis in Σ_{λ_2} direction is reasonable, see Eq. (32). Note

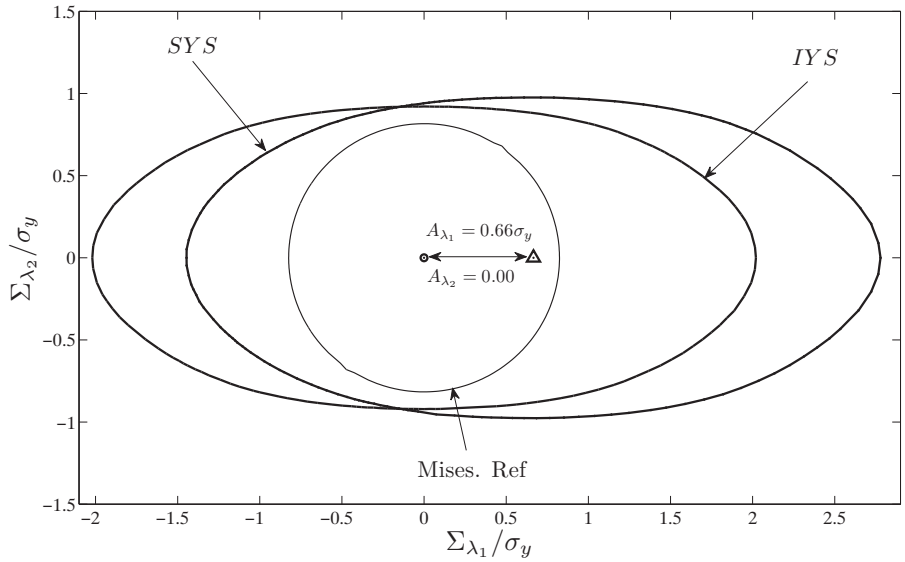

Figure 9: Initial (IYS) and subsequent (SYS) yield surface of composite with longitudinal loading until $\Sigma_{33} = 3\sigma_y$ when $L_*/R = 0.4$ and $V_f = 0.2$.

	$L_*/R = 0$	$L_*/R = 0.2$	$L_*/R = 0.4$
$F_0^\lambda \sigma_y^2$	0.29	0.27	0.25
$H_0^\lambda \sigma_y^2$	1.41	1.29	1.18
$N_0^\lambda \sigma_y^2$	2.53	2.33	2.15

Table 4: Effect of the material length scale, L_*/R, on the initial parameters of anisotropy for $V_f = 0.2$.

that using this projection, the matrix Mises yield surface is not completely circular. A subsequent yield surface (SYS) is also shown under longitudinal loading until $\Sigma_{33} = 3\sigma_y$, where a considerable amount of kinematic hardening as well as a slight expansion is noticeable. Still, the assumption of having an elliptic shape of the SYS with major axis in Σ_{λ_1} direction and minor axis in Σ_{λ_2} direction is acceptable. The geometric center of the SYS is extracted as the Bauschinger stress, A_{λ_i}, used to calculate the anisotropic parameters in Eq. (36).

Fig. 10 shows the SYS of composite with transverse loading until $\Sigma_{11} =$

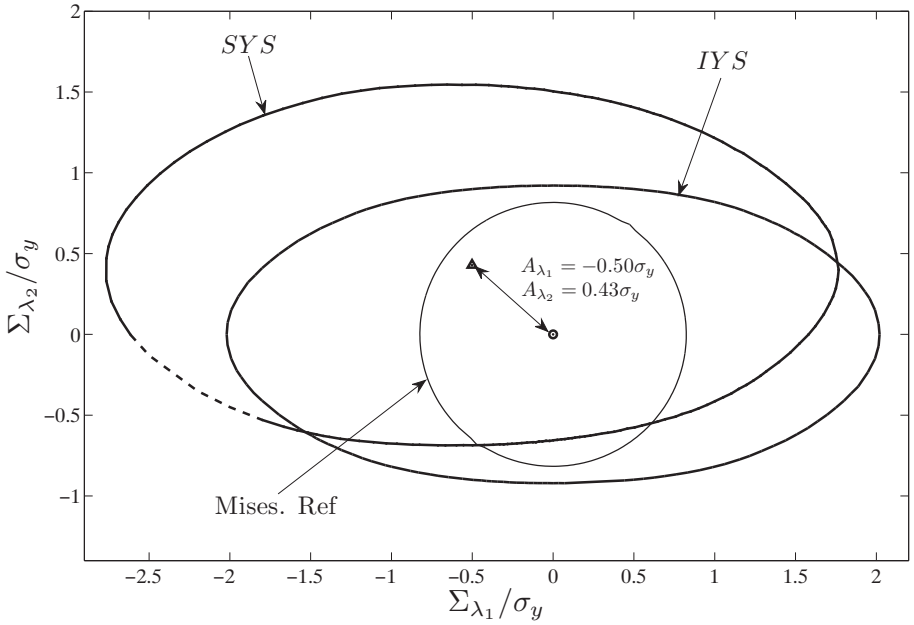

Figure 10: Initial (IYS) and subsequent (SYS) yield surface of composite with transverse loading until $\Sigma_{11} = 2\sigma_y$ while $L_*/R = 0.4$ and $V_f = 0.2$ (the dashed line related to SYS is the extrapolated part of the surface).

$2\sigma_y$ while $L_*/R = 0.4$ and $V_f = 0.2$. As in Fig. 9, the Mises yield surface and the initial yield surface are also shown. The SYS shows a considerable amount of both kinematic hardening (translation) and anisotropic hardening (expansion), see also Azizi et al. (2011c). Again, the assumed elliptic shape with the major axis in Σ_{λ_1} direction and the minor axis in Σ_{λ_2} direction seems fulfilled.

Choosing three points of the initial yield surface shown in Figs. 9 and using Eq. (35), one can compute the initial anisotropic parameters, F_0^λ, H_0^λ and N_0^λ, see also section 2.2 and Fig. 3. For various material length scale parameters, L_*/R, Tab. 4 summarizes the estimated coefficients of anisotropy. Increasing the material length scale, the initial coefficients decrease corresponding to an expansion of the initial yield surface. This is explained by the suppression of the plastic deformation close to the fiber/matrix interface, Fig. 7, which tends to postpone the overall plasticity of the unit cell at the

macroscopic scale. This is consistent with the experimental investigation by Yan et al. (2007) where the enhancement of the composite yield stress is observable with smaller particle size (here equivalent to higher material length scale parameters).

Evolution of the anisotropic parameters in Eq. (36) which tracks the expansion of the composite yield surface under three loading trials shown in Fig. 2 is now studied. The anisotropic hardening coefficients, Eq. (38), are computed using three loading trials in Fig. 2. Tab. 5 shows the effect of L_*/R on the hardening coefficients, f_i, h_i and n_i, $i = 1, 2, 4$.

	$L_*/R = 0$	$L_*/R = 0.2$	$L_*/R = 0.4$
$\begin{bmatrix} f_1 & h_1 & n_1 \\ f_2 & h_2 & n_2 \\ f_4 & h_4 & n_4 \end{bmatrix}$	$\begin{bmatrix} 30 & 76 & 158 \\ -28 & -39 & -30 \\ -30 & -37 & -29 \end{bmatrix}$	$\begin{bmatrix} 5 & 85 & 173 \\ -37 & -54 & -59 \\ -49 & -75 & -45 \end{bmatrix}$	$\begin{bmatrix} 66 & 85 & 156 \\ -47 & -69 & -100 \\ -74 & -132 & -42 \end{bmatrix}$

Table 5: Effect of the material length scale, L_*/R, on the anisotropic hardening coefficients when $V_f = 0.2$.

Defining the macroscopic plastic strain as $E_e^p = \sqrt{E_{\lambda_i}^p E_{\lambda_i}^p}$, Figs. 11, 12 and 13 show the effect of the material length scale, L_*/R, on F^λ, H^λ and N^λ, respectively. As can be seen, for increasing material length scale, all the initial and subsequent anisotropic coefficients decrease, which indicates that both initial and subsequent yield surface undergo expansion. However, the reduction rate of the anisotropic coefficients (the slope) is different depending on the loading condition and the material length scale. Hence, for longitudinal loading the variation in F^λ, H^λ and N^λ is rather small, whereas the other loadings result in a quite strong dependency upon the plastic strain. The small variation of anisotropic parameters for longitudinal loading justifies the limited amount of expansion observed in Fig. 9.

For the normal loadings, the elongation of both minor and major axes of the yield surfaces shown in Figs. 9 and 10 can be defined as

$$R^s = \sqrt{H_0^\lambda / H^\lambda} R_0^s, \quad R^l = \sqrt{F_0^\lambda / F^\lambda} R_0^l \tag{51}$$

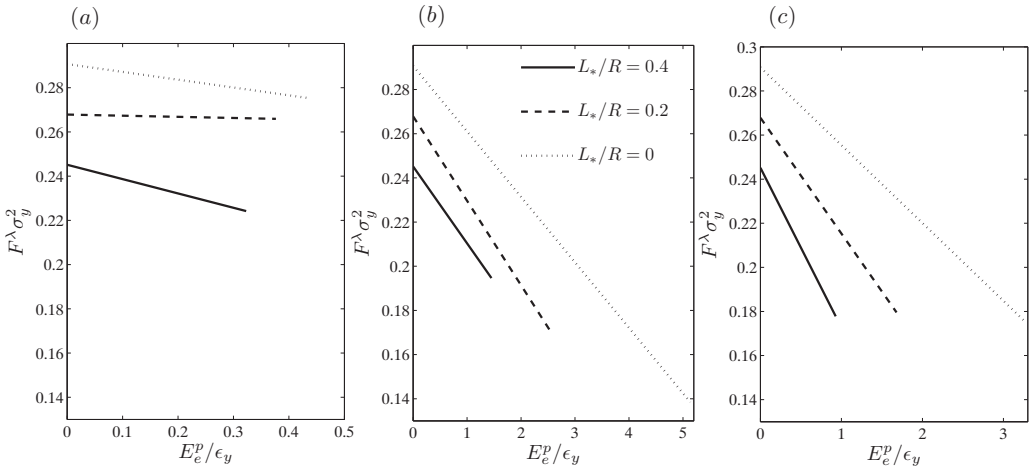

Figure 11: Effect of the material length scale on F^λ when $V_f = 0.2$ for (a) Longitudinal loading until $\Sigma_{33} = 3\sigma_y$. (b) Transverse loading until $\Sigma_{11} = 2\sigma_y$. (c) 0^0 in-plane shear loading until $\Sigma_{12} = 0.8\sigma_y$.

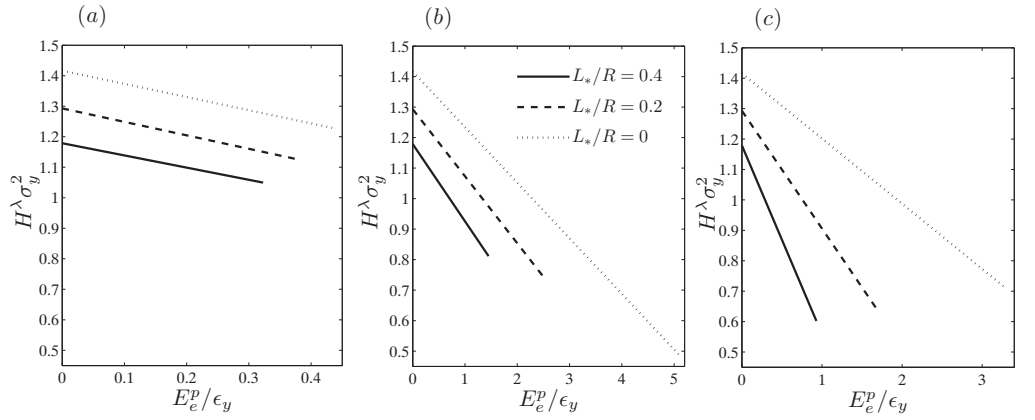

Figure 12: Effect of the material length scale on H^λ when $V_f = 0.2$ for (a) Longitudinal loading until $\Sigma_{33} = 3\sigma_y$. (b) Transverse loading until $\Sigma_{11} = 2\sigma_y$. (c) 0^0 in-plane shear loading until $\Sigma_{12} = 0.8\sigma_y$.

where R_0^s and R_0^l are the initial length of the minor and major axes, respectively and R^s and R^l are the subsequent length of the minor and major axes, respectively. Note that due to the transformation of the stresses, see Fig. 1, these lengths are not directly interpretable as uniaxial yield stresses. In Figs.

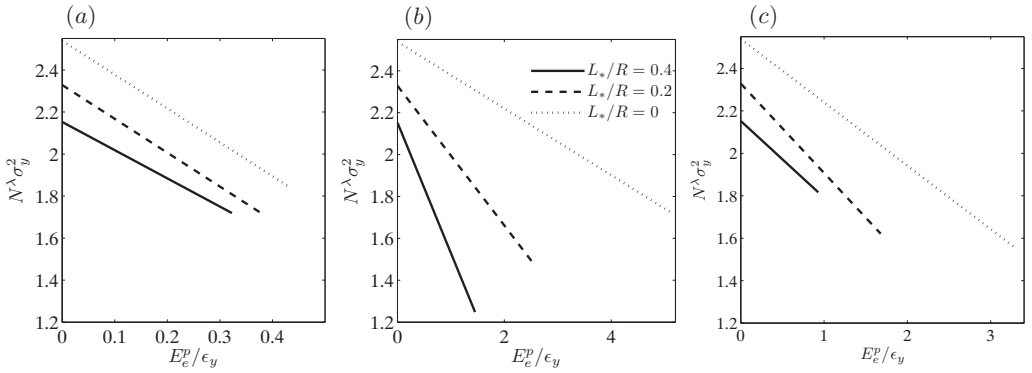

Figure 13: Effect of the material length scale on N^λ when $V_f = 0.2$ for (a) Longitudinal loading until $\Sigma_{33} = 3\sigma_y$. (b) Transverse loading until $\Sigma_{11} = 2\sigma_y$. (c) 0^0 in-plane shear loading until $\Sigma_{12} = 0.8\sigma_y$.

9 (longitudinal) and 10 (transverse), the minor axes are $R^s = 1.06R_0^s$ and $R^s = 1.20R_0^s$ while the major axes are $R^l = 1.05R_0^l$ and $R^l = 1.13R_0^l$ corresponding to longitudinal and transverse loading, respectively. It is concluded that the expansion of yield surface is higher along the minor axis compared to the major axis for both normal loadings. This is most clearly seen in Fig. 10. For $L_*/R = 0.4$ and $V_f = 0.2$, Tab. 6 shows both geometric center (kinematic hardening, A_{λ_i}/σ_y) and anisotropic hardening (expansion) of the subsequent yield surfaces under normal loadings.

Loading direction	Maximum loading	A_{λ_1}/σ_y	A_{λ_2}/σ_y	R^s/R_0^s	R^l/R_0^l
Longitudinal	$\Sigma_{33} = 3\sigma_y$	0.67	0	1.06	1.05
Transverse	$\Sigma_{11} = 2\sigma_y$	-0.50	0.43	1.2	1.13

Table 6: Hardening results including both geometric center (kinematic hardening) and expansion (anisotropic hardening) of the subsequent yield surfaces under normal loadings with $L_*/R = 0.4$ and $V_f = 0.2$.

Tab. 7 shows in more details the results for the 0^o in-plane shear loading until maximum loading of $\Sigma_{12} = 1.4\tau_y$. With larger material length scale parameter, $L_*/R = 0.2$, the initial yield stress, Σ_{12}^{IY}, enhances, the kinematic hardening, A_{12}, increases and the plasticity is suppressed. This has also been

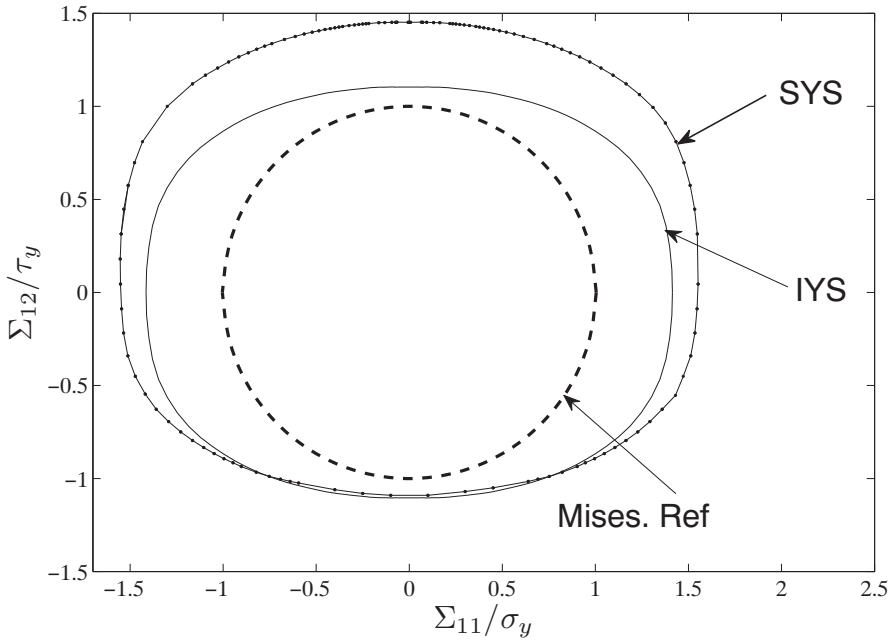

Figure 14: Initial and subsequent yield surface in transverse-shear, $(\Sigma_{11}, \Sigma_{12})$, stress coordinate system with $V_f = 0.2$, $L_*/R = 0.4$.

observed in pure shear for homogeneous materials (Anand et al., 2005; Niordson and Legarth, 2010).

Fig. 14 shows both initial and subsequent yield surfaces at $\Sigma_{12} = 1.4\tau_y$ in transverse-shear stress coordinate system, $(\Sigma_{11}, \Sigma_{12})$, with $V_f = 0.2$ and $L_*/R = 0.4$. For the pure matrix material, the Mises yield surface is circular whereas the composite yield surface tends to be an elliptic-like shaped surface with the major axis in transverse direction, Σ_{11}/σ_y, and minor axis in-plane direction, Σ_{12}/τ_y. Finally, both kinematic and anisotropic hardening are observable during the subsequent loading in 0^o in-plane shear, see also (Sung et al., 2011; Voyiadjis and Thiagarajan, 1995). A precise track of the yield surface expansion due to the 0^o in-plane shear is seen in Figs. 11c, 12c and 13c.

L_*/R	0.0	0.2	0.4
Σ_{12}^{IY}/τ_y	1.09	1.14	1.18
A_{12}/τ_y	0.0	0.028	0.18
E_{12}^{p}/γ_y	2.13	1.09	0.6

Table 7: Numerical results of the 0^0 in-plane shear loading until $\Sigma_{\lambda_4} = 1.4\tau_y$ with $V_f = 0.2$.

6. Conclusion

The aim of this work is to define a conventional anisotropic plasticity model in which the yield function depends on the hydrostatic pressure. The application of the model is illustrated through a study of the deformations of a metal matrix composite (MMC) with long isotropic elastic aligned fibers. It is assumed the matrix of the composite obeys an isotropic strain gradient enhanced plasticity model. It has been shown that such materials exhibit plastic deformations when subjected to hydrostatic loading. In addition, three loading trials including longitudinal, transverse and 0^o in-plane shear are imposed on the unit cell under the generalized plane strain condition.

Upon calculating and drawing the 3D yield surface $(\Sigma_{11}, \Sigma_{22}, \Sigma_{33})$ of the composite, a cylindrical yield surface of elliptical cross section is seen, Fig. 6. It was found that the yield surface axis was inclined relatively to the hydrostatic pressure line and that the inclination increases for increasing fiber volume fractions. The yield surface axes are identified as the eigendirections of the introduced $\boldsymbol{P}$-modulus in the expression for the macroscopic free energy. A procedure for numerical investigation of both initial and subsequent yield surfaces are described. Then, by exploiting the minor and major axes of the elliptical cross section together with the axis of the yield surface, all of the macroscopic quantities including the Cauchy stress, Σ_{ij}, Bauschinger stress, A_{ij}, and plastic strain, E_{ij}^{p} are transformed to the new directions. Expressed in the new quantities, the yield surface properties like pressure dependency, anisotropic hardening (expansion), kinematic hardening (translation) and size-effects are considered by extending the classical anisotropic Hill yield functions, see Hill (1948). The geometric center of the subsequent yield surface is extracted as the Bauschinger stress, A_{λ_i}, and used as the kinematic hardening in Eq. (32). The results show that with higher material length scale parameter, both initial and subsequent anisotropic parameters,

F^λ, H^λ and N^λ, decrease which indicates an expansion of the yield surface. Finally, the macroscopic hardening coefficients, f_i,h_i and n_i, affected by the L_*/R are introduced.

In conclusion, by knowing the anisotropic hardening coefficients and the Bauschinger stress, one can use the newly defined anisotropic pressure dependent yield function, Eq. (32), to solve a rather general problem involving aligned fiber composites using conventional plasticity.

Acknowledgment

This work is supported by the Danish Research Council for Technology and Production Sciences in a project entitled Plasticity Across the Scales. Fruitful discussions with M.G.D. Geers and R.H.J. Peerlings in Eindhoven University of Technology is appreciated. The computational resources have been provided by a hardware grant from the Danish Center of Scientific Computing (DCSC).

References

Aboudi, J., 1990. Micromechanical prediction of initial and subsequent yield surfaces of metal matrix composites. International Journal of Plasticity 6, 471–484.

Aifantis, E. C., 1984. On the microstructural origin of certain inelastic models. Transactions of the ASME. Journal of Engineering Materials and Technology 106 (4), 326–330.

Anand, L., Gurtin, M., Lele, S., Gething, C., 2005. A one-dimensional theory of strain-gradient plasticity: Formulation, analysis, numerical results. Journal of the Mechanics and Physics of Solids 53, 1789–1826.

Azizi, R., Niordson, C. F., Geers, R. G. D., Peerlings, R. H. J., Legarth, B. N., 2011a. On the bauschinger effect and kinematic hardening in metal matrix composites modeled by strain gradient plasticity. Technical report, Technical University of Denmark.

Azizi, R., Niordson, C. F., Legarth, B. N., 2011b. On homogenization of metal matrix composites using strain gradient theory. Submitted.

Azizi, R., Niordson, C. F., Legarth, B. N., 2011c. Size-effects on yield surfaces for micro reinforced composites. International Journal of Plasticity 27, 1817–1832.

Barlat, F., Lege, D., Brem, J., 1991. A six-component yield function for anisotropic materials. Int. J. Plast 7, 693–712.

Bassani, J. L., 2001. Incompatibility and a simple gradient theory of plasticity. Journal of the Mechanics and Physics of Solids 49, 1983–1996.

Borg, U., Niordson, C., Kysar, J., 2008. Size effects on void growth in single crystals with distributed voids. International Journal of Plasticity 24, 688–701.

Borg, U., Niordson, C. F., Fleck, N. A., Tvergaard, V., 2006. A viscoplastic strain gradient analysis of materials with voids or inclusions. International Journal of Solids and Structures 43 (16), 4906–4916.

Chaboche, J., 1993. Cyclic viscoplastic constitutive equations- i: a thermodynamically consistent formulation. J. Appl. Mech. 60, 813–821.

Chung, K., Ryou, H., 2009. Development of viscoelastic/rate-sensitive-plastic constitutive law for fiber-reinforced composites and its applications. part i: Theory and material characterization. Composites Science and Technology 69, 284–291.

Deshpande, V. S., Fleck, N. A., Ashby, M. F., 2001. Effective properties of the octet-truss lattice material. Journal of the Mechanics and Physics of Solids 49 (8), 1747–1769.

Drucker, D., 1951. A more fundamental approach to stress-strain relations. Proc. 1^st U.S.Nat. Congr. of Appl. Mech., ASME 487.

Drucker, D. C., Prager, W., 1952. Soil mechanics and plastic analysis for limit design. Quarterly of Applied Mathematics 10 (2), 157–165.

Dvorak, G., Rao, M., Tarn, J., 1973. Yielding in unidirectional composites under external loads and temperature changes. J Compos Mater 7, 194–216.

Feng, L., Kang, Y., Zhang, G., Wanga, S., 2010. Mechanism-based strain gradient drucker-prager elastoplasticity for pressure-sensitive materials. International Journal of Solids and Structures 47, 2693–2705.

Fleck, N. A., Ashby, M., Hutchinson, J. W., 2003. The role of geometrically necessary dislocations in giving material strengthening. Scripta Materialia 48, 179–183.

Fleck, N. A., Hutchinson, J. W., 1997. Strain gradient plasticity. In: Hutchinson, J. W., Wu, T. Y. (Eds.), Advances in Applied Mechanics. Vol. 33. Academic Press, pp. 295–361.

Fleck, N. A., Hutchinson, J. W., 2001. A reformulation of strain gradient plasticity. Journal of the Mechanics and Physics of Solids 49, 2245–2271.

Fleck, N. A., Willis, J. R., 2009a. A mathematical basis for strain-gradient plasticity theory - Part I: Scalar plastic multiplier. Journal of the Mechanics and Physics of Solids 57, 161–177.

Fleck, N. A., Willis, J. R., 2009b. A mathematical basis for strain-gradient plasticity theory - Part II: Tensorial plastic multiplier. Journal of the Mechanics and Physics of Solids, 57, 1045–1057.

Fredriksson, P., Gudmundson, P., L.P., M., 2009. Finite element implementation and numerical issues of strain gradient plasticity with application to metal matrix composites. International Journal of Solids and Structures 46, 3977–3987.

Gao, H., Huang, Y., 2003. Geometrically necessary dislocation and size-dependent plasticity. Scripta Materialia 48, 113–118.

Gudmundson, P., 2004. A unified treatment of strain gradient plasticity. Journal of the Mechanics and Physics of Solids 52 (6), 1379–1406.

Gupta, N., H.A., L., 1983. A study of yield surface upon reversal of loading under biaxial stress. ZAMM 63, 497–504.

Gurtin, M. E., 2004. A gradient theory of small-deformation isotropic plasticity that accounts for the Burgers vector and for dissipation due to plastic spin. Journal of the Mechanics and Physics of Solids 52 (11), 2545–2568.

Hill, R., 1948. A theory of the yielding and plastic flow of anisotropic metals. Proceedings of the Royal Society of London A193, 281–297.

Hussein, M., Borg, U., Niordson, C., Deshpande, V., 2008. Plasticity size effects in voided crystals. Journal of the Mechanics and Physics of Solids 56, 114–131.

Hutchinson, J. W., 2000. Plasticity at the micron scale. International Journal of Solids and Structures 37 (1-2), 225–238.

Iyer, S., Lissenden, C., Arnold, S., 2000. Local and overall flow in composites predicted by micromechanics. Composites Part B Engineering 31, 327–343.

Jansson, S., 1992. Homogenized nonlinear constitutive properties and local stress concentrations for composites with periodic internal structure. Int. J. Solids Sturctures 29, 2181–2200.

Jansson, S., 1995. Non-linear constitutive equations for strongly bonded fibre-reinforced metal matrix composites. Composites 26, 415–124.

Karafillis, A. P., Boyce, M. C., 1993. A general anisotropic yield criterion using bounds and a transformation weighting tensor. Journal of the Mechanics and Physics of Solids 41 (12), 1859–1886.

Kowalsky, U., Ahrens, H., Dinkler, D., 1999. Distorted yield surfaces - modelling by higher order anisotropic hardening tensors. Computational Materials Science 16, 81–88.

Kuroda, M., 1997. Interpretation of the behavior of metals under large plastic shear deformation: A macroscopic approach. International Journal of Plasticity 13 (4), 359–383.

Kuroda, M., 1999. Interpretation of the behavior of metals under large plastic shear deformations: comparison of macroscopic predictions to physically based predictions. International Journal of Plasticity, 1217–1236.

Lee, M., Kim, D., Chung, K., Youn, J., Kang, T., 2004. Combined isotropic-kinematic hardening laws with anisotropic back-stress evolution for orthotropic fiber-reinforced composites. POLYMERS and POLYMER COMPOSITES 12, 225–233.

Legarth, B. N., 2007. Strain-gradient effects in anisotropic materials. Modeling and Simulation in Materials Science and Engineering 15, S71–S81.

Legarth, B. N., 2008. Necking of anisotropic micro-films with strain-gradient effects. Acta Mechanica Sinica 24, 557–567.

Legarth, B. N., Niordson, C. F., 2010. Debonding failure and size effects in micro-reinforced composites. International journal of plasticity 26 (1), 149–165.

Lele, S. P., Anand, L., 2008. A small-deformation strain-gradient theory for isotropic viscoplastic materials. Philosophical Magazine 88 (30), 1478–6435.

Lissenden, 2010. Experimental investigation of initial and subsequent yield surfaces for laminated metal matrix composites. International Journal of Plasticity 26, 1606–1628.

Liu, C., Huang, Y., Stout, M. G., 1997. On the asymmetric yield surface of plastically orthotropic materials: A phenomenological study. Acta Materialia 45 (6), 2397–2406.

Lloyd, D. J., 1994. Particle reinforced aluminium and magnesium matrix composites. International Materials Reviews 39 (1), 1–23.

Lubliner, J., 1972. On the thermodynamic foundations of non-linear solid mechanics. J. Non-Linear Mech. 7, 237.

Lubliner, J., 1990. Plasticity theory. Pearson Education, Inc.

McDanels, D., 1985. Analysis of stress-strain, fracture, and ductility behavior of aluminum matrix composites containing discontinuous silicon carbide reinforcement. Metallurgical Transactions A (Physical Metallurgy and Materials Science) 16A (6), 1105–1115.

Miehe, C., 1996. Numerical computation of algorithmic (consistent) tangent moduli in large-strain computational inelasticity. Comput. Methods Appl. Mech. Engrg. 134, 223–240.

Mughrabi, H., 2001. The effect of geometrically necessary dislocations on the flow stress of deformed crystals containing a heterogeneous dislocation distribution. Materials Science and Engineering, 139–143.

Niordson, C. F., Legarth, B. N., 2010. Strain gradient effecits on cyclic plasticity. Journal of the Mechanics and Physics of Solids 58, 542–557.

Phillips, A., Juh-Ling, T., 1972. The effect of loading path on the yield surface at elevated temperatures. Internat. J. Solids Struct. 8, 463–474.

Rice, J., 1971. Inelastic constitutive relations for solids: An internal-variable theory and its application to metal plasticity. J. Mech. Phys. Solids 19, 433–455.

Rosakis, P., Rosakis, A., Ravichandran, G., Hodowan, J., 2000. A thermodynamic internal variable model for the partition of plastic work into heat and stored energy in metals. Journal of the Mechanics and Physics of Solids 48, 581–607.

Sung, S., Liu, L., Hong, H., Wua, H., 2011. Evolution of yield surface in the 2d and 3d stress spaces. International Journal of Solids and Structures 48, 1054–1069.

Suprun, A., 2006. A constitutive model with three plastic constants: the description of anisotropic work hardening. Int. J. Plasticity 7, 1217–1233.

Voyiadjis, G., Thiagarajan, G., 1995. An anisotropic yield surface model for directionally reinforced metal-matrix composites. International Journal of Plasticity 11, 867–894.

Yan, Y., Geng, L., Li, A., 2007. Experimental and numerical studies of the effect of particle size on the deformation behavior of the metal matrix composites. Materials Science and Engineering 448, 315–325.

Publication [P7]

Micromechanical modeling of damage in periodic composites using strain gradient plasticity

Micromechanical modeling of damage in periodic composites using strain gradient plasticity

Reza Azizi*

Department of Mechanical Engineering, Solid Mechanics, Technical University of Denmark, DK-2800 Kgs. Lyngby, Denmark

Abstract

Damage evolution at the fiber matrix interface in Metal Matrix Composites (MMCs) is studied using strain gradient theory of plasticity. The study includes the rate independent formulation of energetic strain gradient plasticity for the matrix, purely elastic model for the fiber and cohesive zone model for the fiber-matrix interface. Inside the micro structure, free energy holds both elastic strains and plastic strain gradients which demands to consider the higher order boundary conditions. A unit cell with a circular elastic fiber is studied by the numerical finite element cell model under simple shear and transverse uniaxial tension using plane strain and periodic boundary conditions. The result of the overall response curve, effective plastic strain, effective stress and higher order stress distributions are shown. The effect of the material length scale, maximum stress carried by the interface, the work of separation per unit interface area and the fiber volume fraction on the composites overall behavior are investigated. The results are compared with strong interface.

Keywords: Damage, cohesive zone model, metal matrix composite, strain gradient plasticity

1. Introduction

The increasing application of reinforced metal matrix composites (MMCs) is due to the improved properties like high stiffness, high tensile strength,

*Corresponding Author
Email address: reaz@mek.dtu.dk (Reza Azizi*)

creep resistance, wear resistance, low density and damping capabilities. These useful properties are accessible with the cost of poor ductility and fracture properties. Therefore, a comprehensive knowledge of all types of the properties is necessary, which requires an understanding of both constitutive and failure behaviors. Several works have studied the perfectly bonded reinforced metal matrix composites, (e.g. Teply and Dvorak, 1988; Brockenbroughi et al., 1991; Niordson and Tvergaard, 2001; Niordson, 2003; Azizi et al., 2011b,a). However, experimental evidences show the availability of damage upon deformation in composites by debonding at the fiber-matrix interface, particle fracture and void growth in the matrix, (e.g. Cornwell and Schapery, 1975; Christman et al., 1989; Vratsanos and Farris, 1993; Park and Schapery, 1997). Interfacial debonding can be a major failure in composites with certain constituent as shown by Perng et al. (1993). One of the widely used method in the literature for simulation of the interfacial debonding in composites is the cohesive zone model. The idea for the cohesive model is based on the consideration that the damage analysis knows the existence of the crack in advance. In MMCs, fiber-matrix interface appears to be a critical region for the damage and a reasonable presuppose for the cohesive elements as was shown by Niordson and Tvergaard (2002) and Legarth and Niordson (2010). Several cohesive zone models have been developed to face different type of crack propagation, (e.g. Dugdale, 1960; Tvergaard, 1990; Tvergaard and Hutchinson, 1992; Xu and Needleman, 1994; Geubelle and Baylor, 1998). Xu and Needleman (1994) used polynomial and exponential types of traction separation equations to study the void nucleation at the interface of particle and matrix metal. Tvergaard (1990) extended the Needleman (1987) model of pure normal separation to both normal and tangential separation. Tvergaard and Hutchinson (1992) used a trapezoidal shape of the traction separation model to calculate the crack growth resistance in elasto-plastic materials.

Recent experiments have shown that the macroscopic behavior of MMCs depends on not only the volume fraction but also the size of reinforcing particles or fibers. Lloyd (1994) showed that the response of composites with the same volume fraction of SiC particles depends on the size of the particles. Further investigations by Hutchinson (2000), Mughrabi (2001), Fleck et al. (2003) and Gao and Huang (2003) showed that dislocations can not pass from matrix into the fiber (plastic strain suppression at the fiber-matrix interface) and consequently pile up at the interface. Strain gradient plasticity has capability to consider this fact since they can capture observed size-effects

and non-conventional boundary conditions. Several non local plasticity theories have been developed to face these issues. While some of these are of lower-order nature (see Acharya and Bassani, 2000; Bassani, 2001), most of the proposed theories are of higher order nature, employing higher order stress-measures as work-conjugates to strain gradients, thus demanding non-conventional higher order boundary conditions (e.g. Fleck and Hutchinson, 1997, 2001; Gao et al., 1999; Gurtin, 2002; Gudmundson, 2004; Gurtin and Anand, 2005; Lele and Anand, 2008; Fleck and Willis, 2009a,b).

Two competing mechanisms in MMCs affect the overall behavior, where the interfacial debonding reduces the strength and smaller particle size enhances the strength. Several works have been done to model the damage like Carrere et al. (2004), Moraleda et al. (2009) and Totry et al. (2010), while others considered the stiffening and damage, (e.g. Niordson and Tvergaard, 2002; Huang and Li, 2005; Borg et al., 2006). Zhang et al. (2005) studied the effect of interface damage on the rate-dependent constitutive behavior of MMCs. Legarth and Niordson (2010) studied the interfacial damage using a visco-plastic version of strain gradient plasticity. Recently, Yao and Huang (2011) considered a new analytical method to determine the cohesive law in the framework of nonlocal continuum mechanics.

In the present study, our previous works, Azizi et al. (2011b) and Azizi et al. (2011a), are extended such that the mentioned competing mechanisms in the strength of the MMCs can be investigated using the thermodynamically consistent model of the energetic higher order strain gradient plasticity proposed by Gudmundson (2004) and later elaborated by Fredriksson et al. (2009). The cohesive zone model developed by Needleman (1987) and improved by Tvergaard (1990) is considered for the damage failure. The macroscopic simple shear in addition to the transverse tension are imposed on a unit cell with full circular fiber considering plane strain and periodic boundary conditions. The result of the overall response curve, plastic strain, stress and higher order stress distributions are shown. The effect of the material length scale, maximum stress carried by the interface, the work of separation per unit interface area and the fiber volume fraction on the composites behavior are investigated and compared with the strong interface bonding.

2. Material model

2.1. Rate independent strain gradient model

The matrix is considered to be a gradient enhanced isotropic elasto-plastic material governed by the rate independent energetic strain-gradient plasticity theory proposed by Gudmundson (2004), while the fibers are purely elastic and never yield. The material model accounts for gradients of the full plastic strain tensor. The internal virtual work for the volume of the unit cell containing fiber-matrix interfaces is written as

$$\delta w_i = \int_v [\sigma_{ij}\delta\epsilon_{ij} + (q_{ij} - s_{ij})\delta\epsilon^p_{ij} + m_{ijk}\delta\epsilon^p_{ij,k}]dv + \int_{s^I} \left(T^I_n \delta u^I_n + T^I_t \delta u^I_t + M^I_{ij}\delta\epsilon^{pI}_{ij}\right) ds^I \tag{1}$$

where v is the volume of the unit cell, s^I is the surface of the fiber-matrix interfaces, u^I_n and u^I_t are the normal and tangential displacements of the interface, respectively and σ_{ij} is the Cauchy stress tensor with $s_{ij} = \sigma_{ij} - \frac{1}{3}\delta_{ij}\sigma_{kk}$ denoting the stress deviator. The total strain, ϵ_{ij}, is the summation of the plastic strain, ϵ^p_{ij}, and the elastic strain, ϵ^e_{ij} and $\epsilon^p_{ij,k}$ and ϵ^{pI}_{ij} are the gradient of plastic strain and plastic strain at the fiber-matrix interface, respectively. The micro stress, q_{ij}, and the higher order stress, m_{ijk}, are work conjugate to the plastic strain and the gradient of plastic strain, respectively. The interface normal and tangential tractions, T^I_n and T^I_t and the higher order traction, M^I_{ij}, are surface quantities work-conjugate to the displacements, u^I_n and u^I_t, and the plastic strain tensor, ϵ^{pI}_{ij}, respectively.

The free energy in the present formulation, $\psi = \psi(\epsilon^e_{ij}, \epsilon^p_{ij,k})$, is assumed to depend on the elastic strains and plastic strain gradients which is taken according to Fredriksson et al. (2009) as

$$\psi\left(\epsilon^e_{ij}, \epsilon^p_{ij}\right) = \frac{1}{2}D_{ijkl}\epsilon^e_{ij}\epsilon^e_{kl} + \frac{1}{2}GL^2_*\epsilon^p_{ij,k}\epsilon^p_{ij,k} \tag{2}$$

where L_* is a material length scale parameter, G is the elastic shear modulus and D_{ijkl} is the isotropic tensor of elastic moduli, defined in terms of Young's modulus, E_m, and Poisson's ratio, ν_m, of the matrix. The Cauchy and moment stresses can be derived as

$$\sigma_{ij} = \frac{\partial\psi}{\partial\epsilon^e_{ij}} = D_{ijkl}\epsilon^e_{kl}, \quad m_{ijk} = \frac{\partial\psi}{\partial\epsilon^p_{ij,k}} = GL^2_*\epsilon^p_{ij,k} \tag{3}$$

The yield surface, f, depends on the micro stress, q_{ij}, through

$$f\left(q_{ij},\sigma_f\right)=\sqrt{\frac{3}{2}q_{ij}q_{ij}}-\sigma_f=0 \tag{4}$$

where the flow stress is given by $\sigma_f=\sigma_y+H\epsilon_e^p$, with σ_y denoting the initial yield stress, H denoting the hardening modulus and ϵ_e^p denoting the accumulated effective plastic strain as $\epsilon_e^p=\int\dot{\epsilon}_e^p d\tau$ in which τ is a "pseudo-time" and $\dot{\epsilon}_e^p=\sqrt{\frac{2}{3}\dot{\epsilon}_{ij}^p\dot{\epsilon}_{ij}^p}$.
The flow rule which ensures normality of the plastic strain increment to the flow surface is given by

$$\dot{\epsilon}_{ij}^p=\dot{\gamma}\frac{\partial f}{\partial q_{ij}}=\frac{3}{2}\frac{q_{ij}}{q_e}\dot{\epsilon}_e^p=r_{ij}\dot{\epsilon}_e^p \tag{5}$$

where $\dot{\gamma}$ is the plastic multiplier, $q_e=\sqrt{\frac{3}{2}q_{ij}q_{ij}}$ is the effective micro stress and $r_{ij}=\frac{3}{2}\frac{q_{ij}}{q_e}$ is the direction of the plastic strain increment. More details on the incremental implementation of the above formulations can be found in Fredriksson et al. (2009) and Azizi et al. (2011b).

2.2. Cohesive zone model

The cohesive zone model proposed by Tvergaard (1990) accounting on both normal and tangential separation at the interface is considered. This model uses a polynomial relation between the traction and the separation. A non-dimensional parameter, λ, describing the separation of matrix material from the fiber is defined as

$$\lambda=\sqrt{\left(u_n/\delta_n\right)^2+\left(u_t/\delta_t\right)^2} \tag{6}$$

where u_n and u_t are normal and tangential separation, respectively. δ_n and δ_t are the corresponding maximum separations at which the total decohesion occurs. A function $F(\lambda)$ is considered as

$$F(\lambda)=\frac{27}{4}\sigma_{max}(\lambda^2-2\lambda+1),\qquad 0\leq\lambda\leq 1 \tag{7}$$

from which the normal traction, T_n, and the tangential traction, T_t, are calculated according to

$$\begin{aligned}T_n&=\frac{u_n}{\delta_n}F(\lambda)\\ T_t&=\alpha\frac{u_t}{\delta_t}F(\lambda)\end{aligned} \tag{8}$$

In pure normal separation, $u_t = 0$, the maximum stress is σ_{max} at $\lambda = \frac{u_n}{\delta_n} = \frac{1}{3}$. Similarly, in pure tangential separation, $u_n = 0$, the maximum stress is $\alpha\sigma_{max}$ at $\lambda = \frac{u_t}{\delta_t} = \frac{1}{3}$. Generally, total debonding occurs when $\lambda = 1$. The model requires four damage parameters including δ_n, δ_t, σ_{max} and α. More details on the rate form of the above equations is found in Tvergaard (1990).

3. Problem Formulation

Metal Matrix Composite with parallel circular fibers distributed through the entire structure is considered, see Fig. 1a. A unit cell is extracted, Fig. 1b, where both uniaxial normal stress under plane strain condition and simple shear are imposed. Fig. 1c. shows the displacement boundary conditions, coordinate system and dimensions. At the left-bottom corner of the unit cell, a reference right-hand Cartesian coordinate system, x_i, is located and aligned with the sides of the cell. Fibers are considered to be purely elastic whereas the matrix exhibits an elasto-plastic behavior with gradients effects. Throughout the deformation of the cell, two constant stress ratios, $K_1 = \dot{\Sigma}_{22}/\dot{\Sigma}_{11}$ and $K_2 = \dot{\Sigma}_{12}/\dot{\Sigma}_{11}$, are prescribed such that the stress proportionality is ensured, see Azizi et al. (2011b). The stresses are computed as

$$\begin{aligned}
\dot{\Sigma}_{11} &= \frac{1}{h}\int_0^h [\dot{T}_1]dx_2; \qquad \texttt{at} \qquad x_1 = L \\
\dot{\Sigma}_{22} &= \frac{1}{L}\int_0^L [\dot{T}_2]dx_1; \qquad \texttt{at} \qquad x_2 = h \\
\dot{\Sigma}_{12} &= \frac{1}{h}\int_0^h [\dot{T}_2]dx_2; \qquad \texttt{at} \qquad x_1 = L
\end{aligned} \tag{9}$$

and the strains are considered as

$$\begin{aligned}
\dot{E}_{11} &= \frac{\dot{\Delta}_1}{L} \\
\dot{E}_{22} &= \frac{\dot{\Delta}_3 - \dot{\Delta}_2}{h} \\
\dot{E}_{12} &= \frac{\dot{\Delta}_2}{L}
\end{aligned} \tag{10}$$

and $\dot{E}_{33} = 0$ due to the plane strain assumption.
Since plastic strain-gradient is of higher order nature, higher-order boundary

conditions must be prescribed in addition to the conventional BCs. At the exterior of the cell the periodic boundary conditions are (see Borg et al., 2008; Hussein et al., 2008),

$$\begin{array}{llll} \dot{u}_1^{\mathbf{b}} = \dot{u}_1^{\mathbf{t}} & \text{and} & \dot{u}_2^{\mathbf{b}} = \dot{u}_2^{\mathbf{t}} - [\dot{\Delta}_3 - \dot{\Delta}_2] \\ \dot{T}_1^{\mathbf{b}} = -\dot{T}_1^{\mathbf{t}} & \text{and} & \dot{T}_2^{\mathbf{b}} = -\dot{T}_2^{\mathbf{t}} \\ \dot{u}_1^{\mathbf{l}} = \dot{u}_1^{\mathbf{r}} - \dot{\Delta}_1 & \text{and} & \dot{u}_2^{\mathbf{l}} = \dot{u}_2^{\mathbf{r}} - \dot{\Delta}_2 \\ \dot{T}_1^{\mathbf{l}} = -\dot{T}_1^{\mathbf{r}} & \text{and} & \dot{T}_2^{\mathbf{l}} = -\dot{T}_2^{\mathbf{r}} \\ \dot{M}_{ij}^{\mathbf{b}} = -\dot{M}_{ij}^{\mathbf{t}} & \text{and} & \dot{M}_{ij}^{\mathbf{l}} = -\dot{M}_{ij}^{\mathbf{r}} \\ [\dot{\epsilon}_{ij}^p]^{\mathbf{b}} = [\dot{\epsilon}_{ij}^p]^{\mathbf{t}} & \text{and} & [\dot{\epsilon}_{ij}^p]^{\mathbf{l}} = [\dot{\epsilon}_{ij}^p]^{\mathbf{r}} \end{array} \tag{11}$$

where $\mathbf{l}, \mathbf{r}, \mathbf{b}$ and $\mathbf{t}$ stand for left, right, bottom and top of the unit cell borders, respectively. In addition to the standard periodic boundary conditions, displacement BC and two different sets of the higher order BCs at the fiber-matrix interface are considered as

$$\begin{array}{lll} \dot{u}_1 = \dot{u}_2 = 0, & (x_1, x_2) = (0, 0) \\ \dot{u}_2 = \dot{\Delta}_2, & (x_1, x_2) = (L, 0) \\ \dot{u}_1 = \dot{\Delta}_1,\ \dot{u}_2 = \dot{\Delta}_3, & (x_1, x_2) = (L, h) \end{array}$$

$$\begin{array}{llll} \text{set I:} & \dot{\epsilon}_{ij}^p = 0, & \text{on} & s^I(\texttt{bonded}) \\ & \dot{M}_{ij} = 0, & \text{on} & s^I(\texttt{debonded}) \end{array}$$

$$\text{set II:} \quad \dot{\epsilon}_{ij}^p = 0, \quad \text{on} \quad s^I \tag{12}$$

where $\dot{\Delta}_1$, $\dot{\Delta}_2$ and $\dot{\Delta}_3$ are prescribed displacement increment quantities, $s^I(\texttt{bonded})$ is the surface of interface without decohesion and $s^I(\texttt{debonded})$ is the surface of interface with total decohesion. The out-of-plane plastic strain, $\dot{\epsilon}_{33}^p$, is given in terms of in-plane plastic strain components by plastic incompressibility, $\dot{\epsilon}_{ii}^p = 0$. Similarly, $\dot{M}_{33}$ is given in terms of the in-plane components $\dot{M}_{11}$ and $\dot{M}_{22}$, where $\dot{M}_{ii} = 0$. In summary, the problem in its general form has one material length parameter, L_*, and three geometrical length parameters, h, R, L in addition to both conventional and damage parameters.

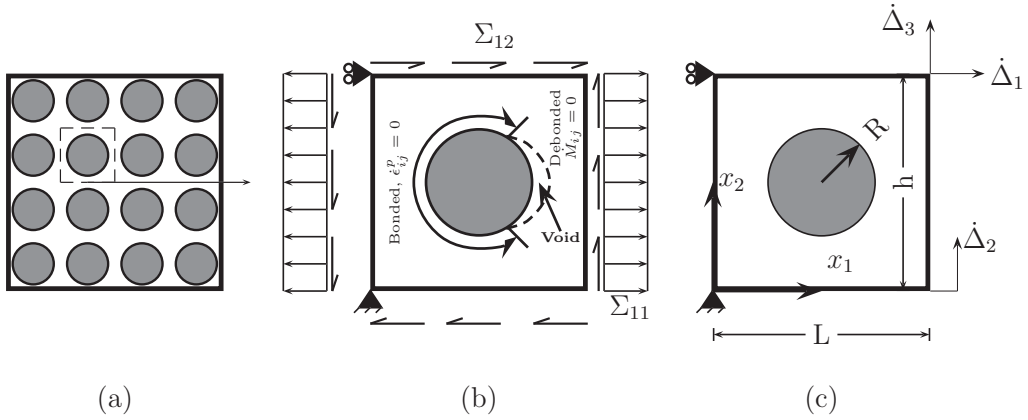

Figure 1: (a) Regular distribution of fibers in the composite. (b) A unit cell containing one fiber with traction boundary condition. (c) A unit cell containing one fiber with conventional displacement boundary conditions used in numerical simulation.

4. Numerical method

For the purpose of numerical implementation, the incremental version of the principle of virtual work is written as

$$\int_v [\dot{\sigma}_{ij}\delta\dot{\epsilon}_{ij} + (\dot{q}_{ij} - \dot{s}_{ij})\delta\dot{\epsilon}^p_{ij} + \dot{m}_{ijk}\delta\dot{\epsilon}^p_{ij,k}]dv + \int_{s^I} \left(\dot{T}^I_n\delta\dot{u}^I_n + \dot{T}^I_t\delta\dot{u}^I_t + \dot{M}^I_{ij}\delta\dot{\epsilon}^{pI}_{ij}\right) ds^I = \int_s [\dot{T}_i\delta\dot{u}_i + \dot{M}_{ij}\delta\dot{\epsilon}^p_{ij}]ds, \quad (13)$$

where s is the surface of the unit cell and $\dot{T}_i$ and $\dot{M}_{ij}$ are traction increments and moment traction increments, respectively. Quadrilateral elements with eight nodes are used for in-plane displacement interpolation, while bilinear four node elements are used to interpolate the plastic strain components. Considering both elements at the same time, each corner node has five degrees of freedom (two for displacements and three for plastic strains) and each middle node has two degrees of freedom for displacement. Nodal interpolation is used according to

$$\dot{u}_i = \sum_{N=1}^{2k} N_i^N \dot{U}_N, \quad \dot{\epsilon}_{ij}^p = \sum_{M=1}^{3l} P_{ij}^M \dot{\epsilon}_M^p \tag{14}$$

$$\dot{u}_n = \sum_{N=1}^{2k} \left[N_i^N p_i^n\right] \dot{U}_N, \quad \dot{u}_t = \sum_{N=1}^{2k} \left[N_i^N p_i^t\right] \dot{U}_N \tag{15}$$

where p^n and p^t are the normal and tangential unit vectors at the fiber-matrix interface, N_i^N and P_{ij}^M are shape functions for the displacement and plastic strain components, respectively, and k and l are the number of nodes used for the different interpolation schemes. The derivatives of both displacement and plastic strain fields are expressed as

$$\dot{\epsilon}_{ij} = \sum_{N=1}^{2k} B_{ij}^N \dot{U}_N, \quad \dot{\epsilon}_{ij,k}^p = \sum_{M=1}^{3l} Q_{ijk}^M \dot{\epsilon}_M^p \tag{16}$$

where, $B_{ij}^N = (N_{i,j}^N + N_{j,1}^N)/2$ and $Q_{ijk}^M = P_{ij,k}^M$ are spatial derivatives of both interpolation functions. The discretized equation obtained from the incremental version of the principle of virtual work, Eq. (14), is written as

$$\begin{bmatrix} \mathbf{K}_u & -\mathbf{K}_{up} \\ -\mathbf{K}_{up}^T & \mathbf{K}_p \end{bmatrix} \begin{bmatrix} \dot{\mathbf{D}} \\ \dot{\boldsymbol{\epsilon}}^p \end{bmatrix} = \begin{bmatrix} \dot{\mathbf{f}}_u \\ \dot{\mathbf{f}}_p \end{bmatrix} \tag{17}$$

where $\dot{\mathbf{f}}_u = \int_s \mathbf{N}^T \dot{\mathbf{T}} ds$ is nodal force and $\dot{\mathbf{f}}_p = \int_s \mathbf{P}^T \dot{\mathbf{M}} ds$ is the nodal higher order force. Stiffness matrices are given by

$$\mathbf{K}_u = \int_v \mathbf{B}^T \mathbf{D}_e \mathbf{B} dv + \int_{s^I} \mathbf{N^T R^T a R N} ds^I \tag{18}$$

$$\mathbf{K}_p = \int_v [\mathbf{P}^T (\mathbf{D}_e + \mathbf{D}_p) \mathbf{P} + \mathbf{Q}^T \mathbf{D}_h \mathbf{Q}] dv \tag{19}$$

$$\mathbf{K}_{up} = \int_v \mathbf{B}^T \mathbf{D}_e \mathbf{P} dv \tag{20}$$

where $\mathbf{R}$ is the rotation matrix, $\mathbf{D}_e$ is the isotropic elastic moduli, $\mathbf{D}_p$ is the plastic moduli and $\mathbf{D}_h$ is higher order moduli as

$$\mathbf{D}_e = \frac{E}{(1+\upsilon)(1-2\upsilon)} \begin{bmatrix} 1-\upsilon & \upsilon & \upsilon & 0 \\ \upsilon & 1-\upsilon & \upsilon & 0 \\ \upsilon & \upsilon & 1-\upsilon & 0 \\ 0 & 0 & 0 & \frac{1-2\upsilon}{2} \end{bmatrix} \tag{21}$$

$$\mathbf{D}_p = \frac{2}{3}\left(\frac{2}{3}(H - E_0)\mathbf{r}\mathbf{r}^T + E_0\boldsymbol{I}_p\right) \tag{22}$$

$$\mathbf{D}_h = GL_*^2\boldsymbol{I} \tag{23}$$

$$\mathbf{R} = \begin{bmatrix} p_1^n & p_2^n \\ p_1^t & p_2^t \end{bmatrix} \tag{24}$$

where E and ν are taken as the fiber or matrix moduli in the corresponding elements, p_1^n, p_2^n, p_1^t and p_2^t are the components of the normal and tangential vector at the interface, E_0 is the penalty factor, G is the shear modulus, $\boldsymbol{I}_{(8\times 8)}$ is the identity matrix, $\boldsymbol{I}_p$=diag$(1 \quad 1 \quad 1 \quad 1/2)$ and $\mathbf{r} = (r_{11}, r_{22}, r_{33}, r_{12})^T$. The cohesive modulus, $\mathbf{a} = \begin{bmatrix} a_{11} & a_{12} \\ a_{21} & a_{22} \end{bmatrix}$, relates the traction to the separation in the cohesive elements as

$$\begin{bmatrix} \dot{T}_n \\ \dot{T}_t \end{bmatrix} = \begin{bmatrix} a_{11} & a_{12} \\ a_{21} & a_{22} \end{bmatrix} \times \begin{bmatrix} \dot{u}_n \\ \dot{u}_t \end{bmatrix} \tag{25}$$

where a_{11}, a_{12}, a_{21} and a_{22} are determined from cohesive zone model.
Fig. 2 shows an example of the finite element mesh with 1408 elements used in numerical computations. Numerical integration is performed using forward Euler method with small load increments. To avoid plastic flow in the elastic regime, the plastic stiffness is chosen to be large as suggested by Fredriksson et al. (2009). However, in the limit of conventional plasticity this would lead to an artificial boundary layer effect with a width scaling with the element size. Hence, when using the computational method in the conventional limit, the plastic stiffness matrix has instead been defined by $\mathbf{K}_p = 10^{-8}E\boldsymbol{I}_{(12\times 12)}$ (with E being either E_m or E_f) and the coupling matrix $\mathbf{K}_{up} = \mathbf{0}$ for elastic integration points, while plastic strain quantities are only updated in integration points that are in the plastic regime.

5. Results

The conventional material parameters used for the matrix are $H/E_m = 0.1$, $\epsilon_y = \sigma_y/E_m = 0.004$, $\upsilon_m = 0.3$, and for the fibers, $E_f = 5.7E_m$ and $\upsilon_f = 0.17$. The penalty factor is taken to be $E_0 = 1000H$ for the case of simple shear and $E_0 = 100H$ for the case of uniaxial transverse tension due to the numerical stability. The dimension of the unit cell is defined by $L = h = 1$.

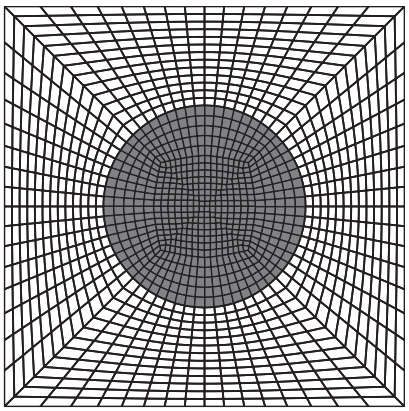

Figure 2: An example of finite element mesh used in the numerical computation.

A reinforcement volume fraction of $V_f = 0.2$, $\alpha = 1$ and the first set of the higher order BC are assumed unless else is stated. Each numerical computation includes 1408 elements with 300 increments. Primary attention will be given to the overall average stress strain response, (Σ_{11}, E_{11}) for uniaxial tension and (Σ_{12}, E_{12}) for simple shear, of the micro-reinforced composite. Investigations by a number of authors, e.g. Hutchinson (2000) have shown that for problems with lengths falling in the range from roughly a fraction of a micron to ten microns a size-effect exists that conventional plasticity cannot capture. Furthermore, it was argued that the material length scale for metals is in the range of $0.25\mu m$ to $1\mu m$ for a slightly different but related model. For a micron scale length parameter of $L_* = 1\mu m$ in the present model, we analyze cases for $L_*/R = 0$, $L_*/R = 0.2$ and 0.4 which corresponds to large fibers, fibers with $R = 5\mu m$ and $R = 2.5\mu m$, respectively.

5.1. Simple shear

Simple shear is imposed on the unit cell, where $K_1 = 1$ and $K_2 = 1000$. These values ensure that the macro shear stress, Σ_{12}, is sufficiently large compared to Σ_{11} and Σ_{22}. The unit cell is loaded until the macroscopic shear strain of $E_{12} = 2\gamma_y$ is achieved.

Fig. 3 shows the effect of the material length scale, L_*/R, on the stress strain curve with $\sigma_{max} = 0.52\tau_y$ and $\delta_n = \delta_t = \delta = 0.012R$. The load carrying capacity enhances with higher material length scale corresponding

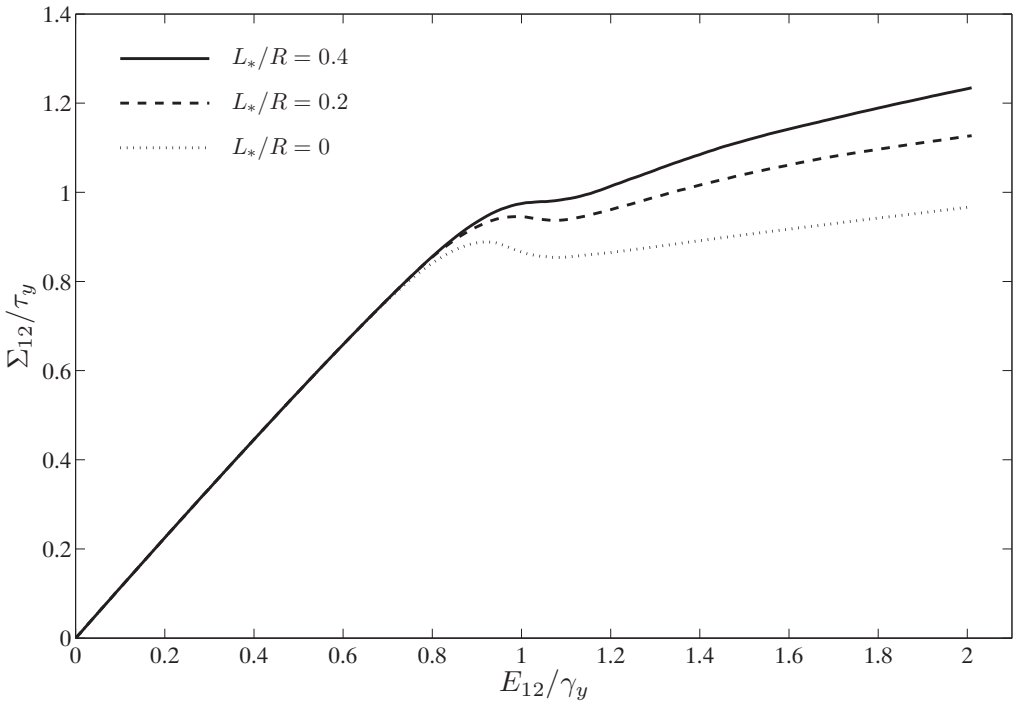

Figure 3: Effect of the material length scale, L_*/R, on the stress strain curve of simple shear with $\sigma_{max} = 0.52\tau_y$ and $\delta_n = \delta_t = \delta = 0.012R$.

to the smaller fiber size. For the conventional material, the stress drops at $\Sigma_{12} = 0.88\tau_y$ where debonding initiates. The corresponding point for the gradient dependent material ($L_*/R = 0.2$) is $\Sigma_{12} = 0.95\tau_y$. The stress for the case of $L_*/R = 0.4$ never drops although the debonding initiates at $\Sigma_{12} = 0.98\tau_y$ and continues with an almost constant load carrying capacity until the end of total possible decohesion at the interface. For all the cases, a gradual enhancement of the hardening is observable after the interface decohesion.

Fig. 4 shows the effect of the critical separation distances (work of separation per unit interface area), $\delta_n = \delta_t = \delta$, on the stress strain curve with $\sigma_{max} = 0.52\tau_y$ and $L_*/R = 0.2$. The result for the strong interface bonding is also plotted. As can be seen, the material with weak interface bonding has smaller shear modulus compared to the strong interface bonding. This is explained by the cohesive zone model, where a limited amount of fiber-matrix

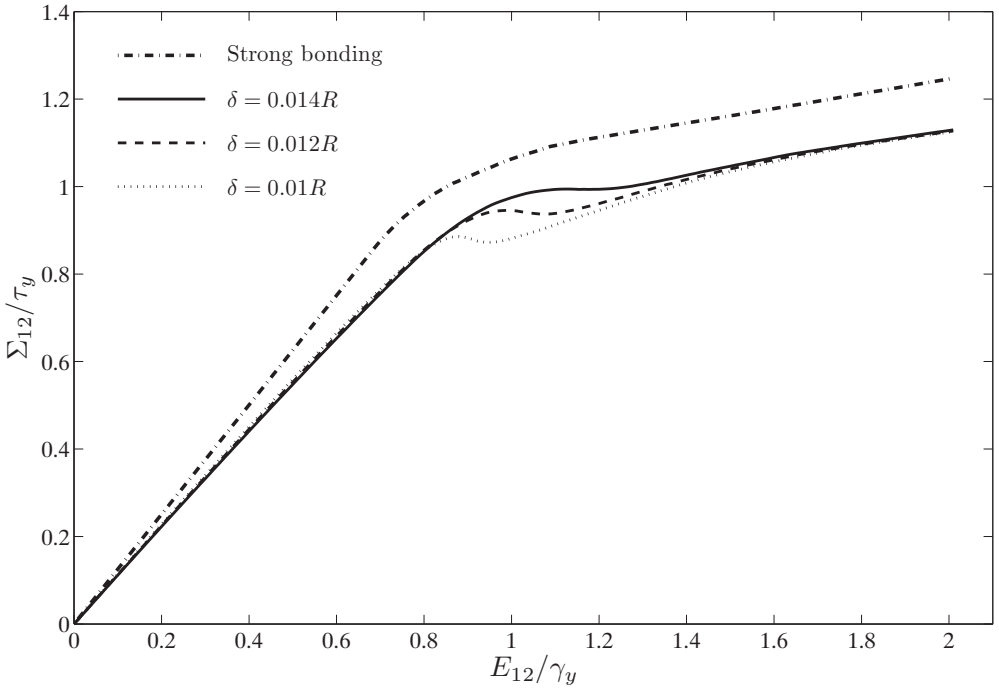

Figure 4: Effect of the critical separation distances, $\delta_n = \delta_t = \delta$, on the stress strain curve of simple shear with $\sigma_{max} = 0.52\tau_y$ and $L_*/R = 0.2$.

separation initiates before the stress reaches the maximum stress carried by the interface, σ_{max}. By increasing the critical separation distances, δ, the debonding is postponed from $\Sigma_{12} = 0.88\tau_y$ corresponding to $\delta = 0.01R$ towards $\Sigma_{12} = 0.99\tau_y$ corresponding to $\delta = 0.014R$. For all the values of the δ, the hardening enhances after the total possible debonding of the interface and the enhancement rate is higher for the lower δ. For all cases, the load carrying capacities seem to converge with subsequent loading after the total decohesion.

Fig. 5 shows the effect of the maximum stress carried by the interface, σ_{max}, on the stress strain curve with $\delta = 0.012R$ and $L_*/R = 0.2$. As can be seen, the stress-drop is significantly postponed from $\Sigma_{12} = 0.95\tau_y$ corresponding to $\sigma_{max} = 0.52\tau_y$ towards $\Sigma_{12} = 1.14\tau_y$ corresponding to $\sigma_{max} = 0.87\tau_y$. It is also seen that with higher σ_{max}, the overall elastic shear modulus gets

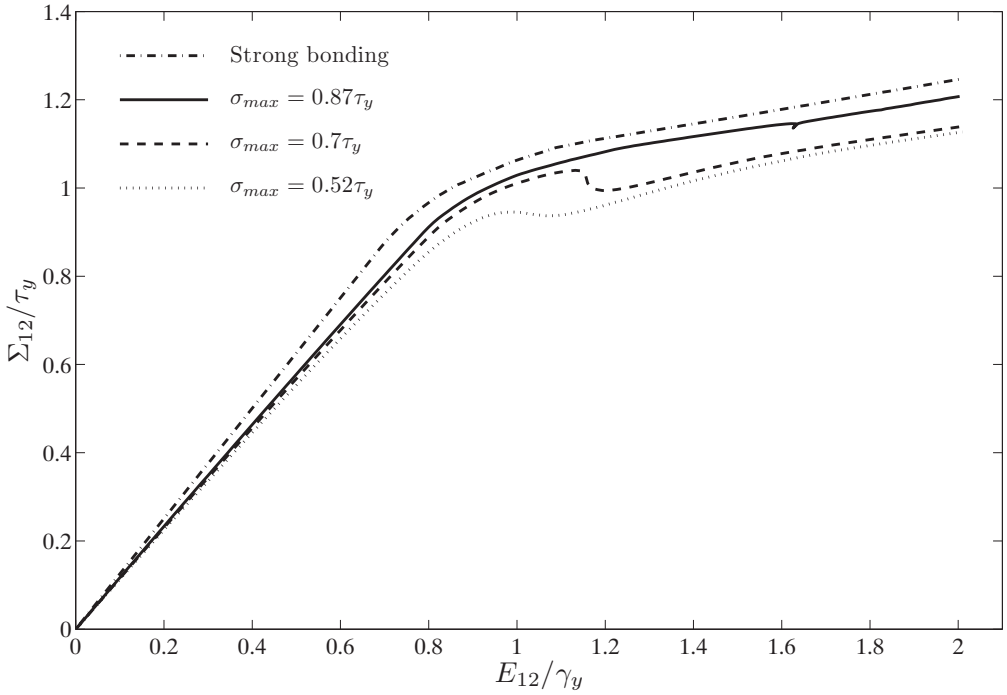

Figure 5: Effect of the maximum stress carried by the interface, σ_{max}, on the stress strain curve of simple shear with $\delta = 0.012R$ and $L_*/R = 0.2$.

closer to the shear modulus of the strong interface. It is concluded that debonding behavior is more sensitive to the maximum stress carried by the interface compared to the work of separation per unit interface area. Similar behavior has been shown by Totry et al. (2010).

The contour plots of the accumulative plastic strain, ϵ_e^p/ϵ_y, at the end of loading where $E_{12} = 2\gamma_y$ with $\delta = 0.012R$ and $\sigma_{max} = 0.52\tau_y$ is shown in Fig. 6 with 5 times scaling of the deformation field. As can be seen, for the conventional material, a large amount of the plastic strain is concentrated at the tip of the crack. The amount of the plastic strain decreases significantly at the crack tip of the conventional material (Fig. 6a) to somewhere inside the matrix of the gradient dependent material (Fig. 6b). The conventional result is in agreement to the finding by Hinz et al. (2007) using Ansys. The size of the void is seen to be smaller in the gradient dependent material

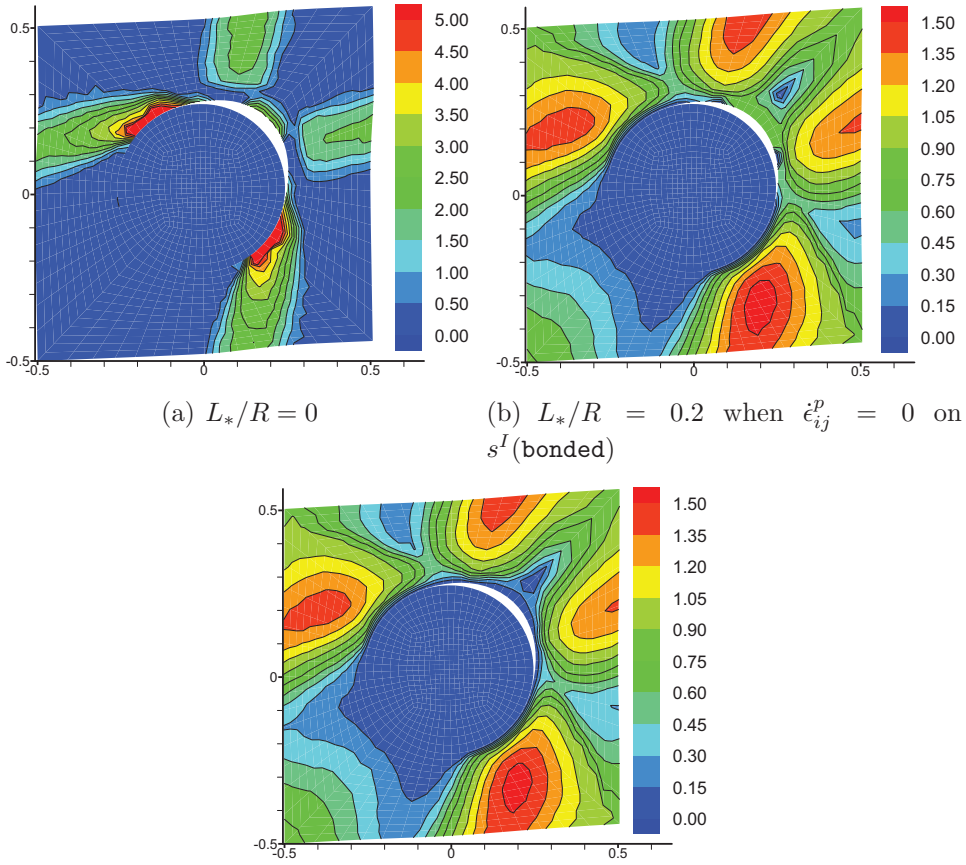

(a) $L_*/R = 0$

(b) $L_*/R = 0.2$ when $\dot{\epsilon}^p_{ij} = 0$ on s^I(bonded)

(c) $L_*/R = 0.2$ when $\dot{\epsilon}^p_{ij} = 0$ on s^I

Figure 6: Effective plastic strain, ϵ^p_e/ϵ_y, for simple shear with $\delta = 0.012R$ and $\sigma_{max} = 0.52\tau_y$ at the end of loading where $E_{12} = 2\gamma_y$ with 5 times scaling of the deformation field.

compared to the conventional material. The effect of two sets of the higher order BC on the ϵ^e_p is also shown. Fig. 6c shows the result for the second set of the higher order BC, Eq. (12), where the plastic strain is entirely suppressed at both bonded and debonded part of the interface. This does not occur for the first set of the higher order BC (Fig. 6b).

Fig. 7 shows the corresponding effective stress, $\sigma_e/\sigma_y = \sqrt{\frac{3}{2}s_{ij}s_{ij}}/\sigma_y$, at the end of loading where $E_{12} = 2\gamma_y$ with $\delta = 0.012R$ and $\sigma_{max} = 0.52\tau_y$.

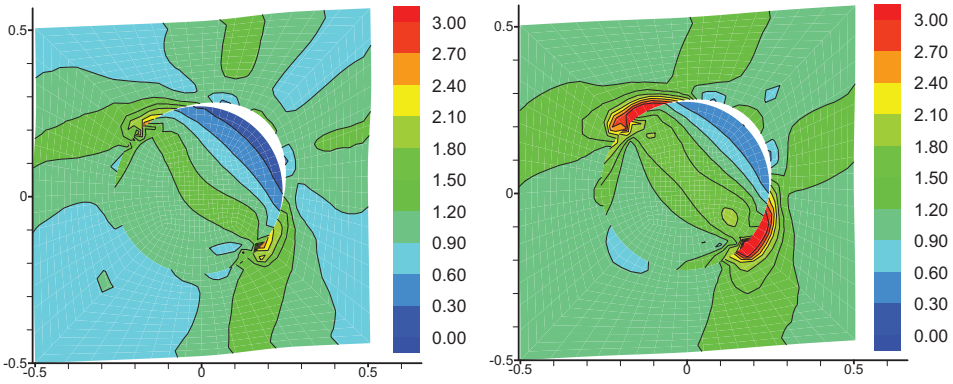

(a) $L_*/R = 0$ (b) $L_*/R = 0.2$

Figure 7: Effective stress, σ_e/σ_y, for simple shear with $\delta = 0.012R$ and $\sigma_{max} = 0.52\tau_y$ at the end of loading where $E_{12} = 2\gamma_y$ with 5 times scaling of the deformation field.

For both cases, the stress concentration is seen to be close to the crack tip, where it is higher for the gradient dependent material, Fig. 7b, compared to the conventional material, Fig. 7a. This is due to the suppression of the plasticity at the crack tip for the gradient dependent material.

The corresponding higher order stresses are plotted in Fig. 8 where Fig. 8a shows $m_{121}/(L_*\sigma_y)$ and Fig. 8b shows $m_{122}/(L_*\sigma_y)$. The higher order stress is mainly observable at the interface, where the plastic strain gradients are significant. Using the first set of the higher order BC, an almost zero higher order stress is seen close to the point, where complete separation is noticed.

As it was shown in the boundary condition, two different sets of higher order BCs are considered, Eq. (12). Fig. 9 shows the effect of the material length scale, L_*/R, on the relative load carrying capacity, $\Sigma_{12}^{(\dot{\epsilon}^p_{ij}=0 \text{on} s^I)}/\Sigma_{12}^{(\dot{\epsilon}^p_{ij}=0 \text{on} s^I(bonded))}$. For the conventional material, the higher order BC does not play any role while for the gradient dependent material the load carrying capacity enhances slightly from 0.58% corresponding to $L_*/R = 0.2$ towards 0.97% corresponding to $L_*/R = 0.4$ at the end of loading where $E_{12} = 2\gamma_y$. However, in the beginning of the plastic deformation, the lower material length scale has higher load carrying capacity. This agrees with the fact that a large value of L_* suppresses plastic deformations such that higher-order boundary con-

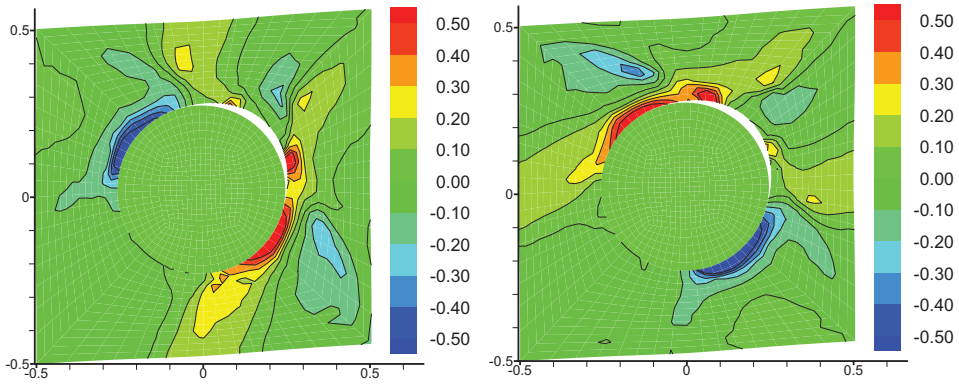

(a) $m_{121}/(L_*\sigma_y)$ (b) $m_{122}/(L_*\sigma_y)$

Figure 8: Higher order stress for simple shear with $L_*/R = 0.2$, $\delta = 0.012R$ and $\sigma_{max} = 0.52\tau_y$ at the end of loading where $E_{12} = 2\gamma_y$ with 5 times scaling of the deformation field.

ditions prescribing zero plastic strain becomes less important.

The effect of fiber volume fraction, V_f, on the response of the unit cell under simple shear loading is also studied. Fig. 10 shows the effect of V_f on the stress strain curve with $L_*/R = 0.2$, $\delta = 0.012R$ and $\sigma_{max} = 0.52\tau_y$. As can be seen, the higher V_f has a small effect on the elastic shear modulus and the yield stress of the weak interface compared to the ones by strong interface. The stress-drop is postponed slightly and the hardening shows a small enhancement. Generally, it is concluded that the fiber volume fraction of the unit cell, V_f, does not play an important role on the strength of the material under simple shear loading.

Fig. 11 shows the effect of the fiber volume fraction, V_f, on the effective plastic strain, ϵ_e^p/ϵ_y, with $L_*/R = 0.2$, $\delta = 0.012R$ and $\sigma_{max} = 0.52\tau_y$. It is seen that the void nucleation increases with the higher fiber volume fraction proportional to the length of the fiber-matrix interface. The maximum amount of the plastic strain is almost unaffected with the higher fiber volume fraction, while it dominates the matrix for the higher V_f.

5.2. Uniaxial tension

Uniaxial loading in transverse direction is analysed by using $K_1 = K_2 = 0$. These K-values ensure a non-zero macroscopic transverse stress, Σ_{11}, while

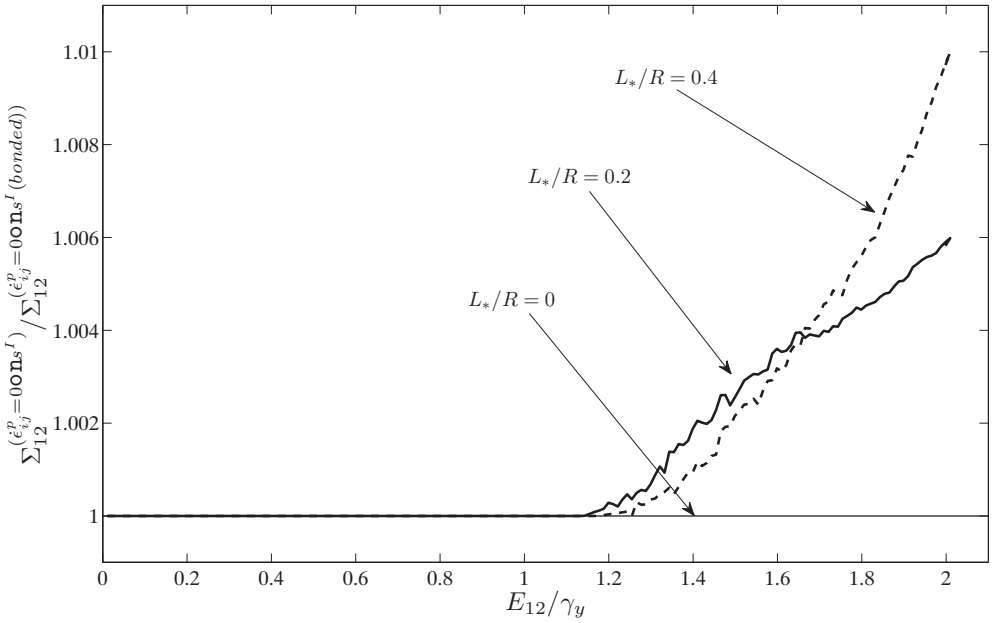

Figure 9: Effect of the material length scale, L_*/R, on the relative load carrying capacity, $\Sigma_{12}^{(\dot{\epsilon}_{ij}^p=0 \mathtt{ons}^I)}/\Sigma_{12}^{(\dot{\epsilon}_{ij}^p=0 \mathtt{ons}^I(bonded))}$, with two sets of higher order boundary condition as shown in Eq. (12).

suppressing other stress components as $\Sigma_{22} = \Sigma_{12} = 0$. The unit cell is loaded until the maximum deformation of $E_{11} = 5\epsilon_y$ is achieved.

Fig. 12 shows the effect of the material length scale, L_*/R, on the stress strain curve with $\sigma_{max} = \sigma_y$ and $\delta_n = \delta_t = \delta = 0.03R$. It is seen that the material length scale does not affect the elastic modulus but it slightly increases the yield point and hardening as it was investigated experimentally by Nan and Clarke (1996). The stress-drops, due to the interface debonding, are $\Sigma_{11} = 1.27\sigma_y$ corresponding to $L_*/R = 0$, $\Sigma_{11} = 1.39\sigma_y$ corresponding to $L_*/R = 0.2$ and $\Sigma_{11} = 1.46\sigma_y$ corresponding to $L_*/R = 0.4$. A similar behavior is reported by Legarth and Niordson (2010). After failure by debonding, the load carrying capacity is almost constant for the conventional material, where an enhancement is seen for the gradient dependent material.

Fig. 13 shows the effect of the critical separation distances (work of separation per unit interface area), $\delta_n = \delta_t = \delta$, on the stress strain curve

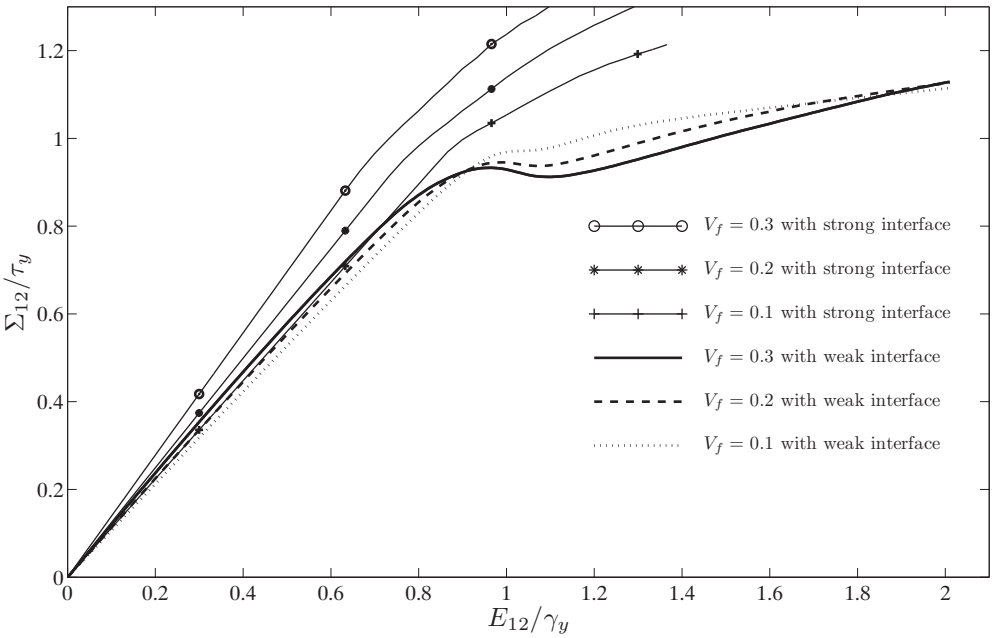

Figure 10: Effect of the fiber volume fraction, V_f, on the stress strain curve of simple shear with $L_*/R = 0.2$, $\delta = 0.012R$ and $\sigma_{max} = 0.52\tau_y$.

of the uniaxial tension with $\sigma_{max} = \sigma_y$ and $L_*/R = 0.4$. It is seen that a little more elastic modulus is obtainable with lower δ. However, the elastic modulus of the strong interface is still higher compared to the weak interfaces. This is due to the cohesive zone model, where the traction-displacement curve before the onset of debonding, $\lambda = 1/3$, is loosening the strength of material, see also Arnold et al. (1996), Zhang et al. (2005) and Segurado and LLorca (2005). A considerable delay in debonding is observable with the higher value of δ from $\Sigma_{11} = 1.32\sigma_y$ corresponding to $\delta = 0.02R$ until $\Sigma_{11} = 1.63\sigma_y$ corresponding to $\delta = 0.04R$, see also Tvergaard (1990). The hardening after total decohesion is as same as the one before it.

Fig. 14 shows the effect of the maximum stress carried by the interface, σ_{max}, on the stress strain curve with $\delta = 0.03R$ and $L_*/R = 0.4$. Both elastic modulus and yield stress increase slightly. The onset of debonding is significantly postponed from $\Sigma_{11} = 1.46\sigma_y$ corresponding to $\sigma_{max} = \sigma_y$ towards $\Sigma_{11} = 2.08\sigma_y$ corresponding to $\sigma_{max} = 2\sigma_y$. The stress-drop occurs

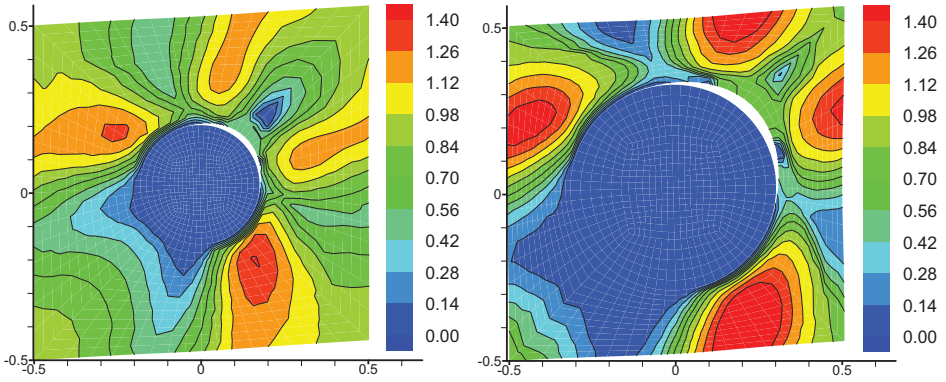

(a) $V_f = 0.1$ (b) $V_f = 0.3$

Figure 11: Effect of the fiber volume fraction, V_f, on the effective plastic strain, ϵ^p_e/ϵ_y, for simple shear with $L_*/R = 0.2$, $\delta = 0.012R$ and $\sigma_{max} = 0.52\tau_y$ at the end of loading where $E_{12} = 2\gamma_y$ with 5 times scaling of the deformation field.

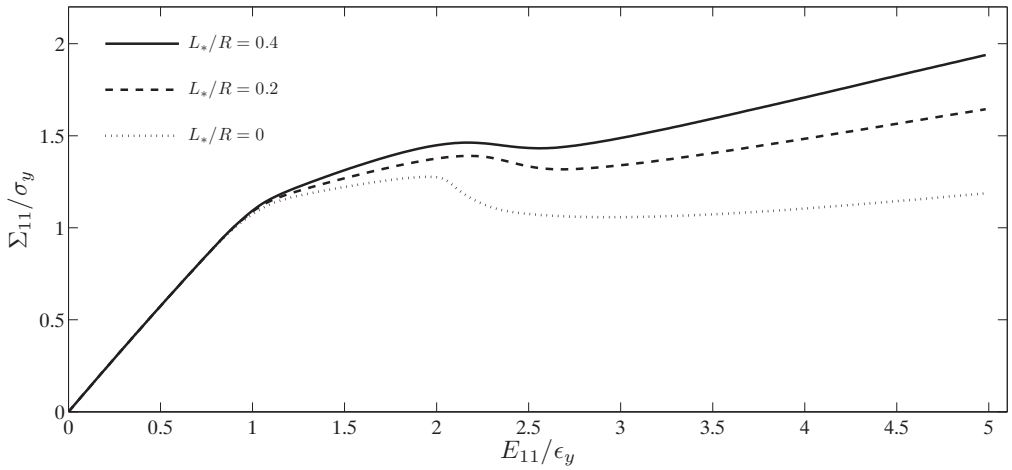

Figure 12: Effect of the material length scale, L_*/R, on the stress strain curve of uniaxial tension with $\sigma_{max} = \sigma_y$ and $\delta_n = \delta_t = \delta = 0.03R$.

more suddenly for the higher value of σ_{max}. Thereafter, the hardening is seen

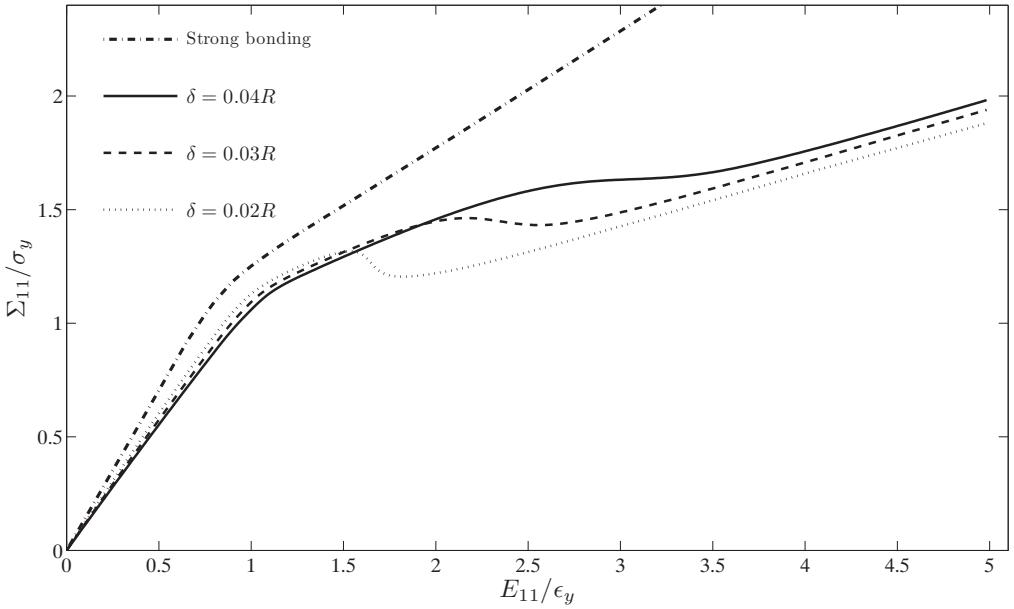

Figure 13: Effect of the critical separation distances, $\delta_n = \delta_t = \delta$, on the stress strain curve of the uniaxial tension with $\sigma_{max} = \sigma_y$ and $L_*/R = 0.4$.

to be the same for all the cases. A similar behavior is reported by Xu and Needleman (1993), Needleman et al. (2010) and Zhang et al. (2005).

Fig. 15 shows the effect of the length scale, L_*/R, on the effective plastic strain, ϵ_e^p/ϵ_y, with $\delta = 0.03R$ and $\sigma_{max} = \sigma_y$. For the case of conventional material (Fig. 15a), a significant amount of plasticity is observable at the crack tip, see also Ghassemieh (2002) and Zhang et al. (2005), where the suppression of the plastic strain at the crack tip is noticeable for the gradient dependent material (Fig. 15b). A smooth transition of the plastic strain from fiber towards the matrix is highlighted for the gradient dependent material as it was shown by Legarth and Niordson (2010). This smooth transition pushes the maximum plastic strain towards the borders. For the second set of the higher order boundary conditions, Eq. (12), Fig. 15c is plotted. Suppression of the plastic strain close to the debonded void is seen, which is not the case for the first set, Fig. 15b. Due to the debonding failure, straight deformation of the unit cell borders is not guaranteed as also shown by Legarth (2004).

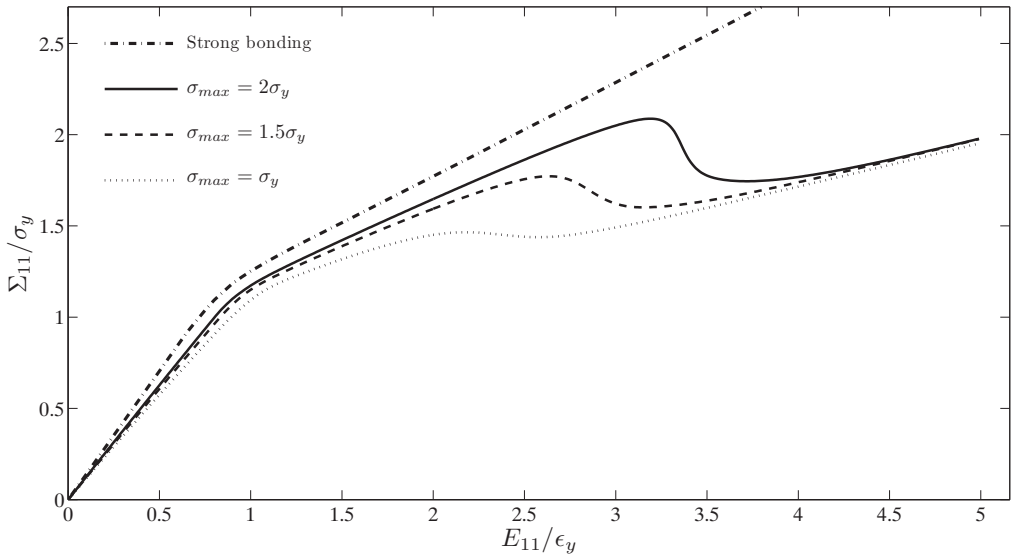

Figure 14: Effect of the maximum stress carried by the interface, σ_{max}, on the stress strain curve of the uniaxial tension with $\delta = 0.03R$ and $L_*/R = 0.4$.

Fig. 16 shows the corresponding effective stress, σ_e/σ_y, for both conventional, Fig. 16a, and gradient dependent material, Fig. 16b. Stress concentration close to the crack tip is seen for both cases, where it is much more higher for the gradient dependent material compared to the conventional one. Comparing with the effective plastic strain in Fig. 15, higher stress with lower plastic strain is seen for the gradient dependent material which is opposite to the finding for the conventional material. For both cases, the load carrying capacity is significantly lower close to the totally debonded point compared to the other points inside the matrix. The corresponding higher order stresses are also plotted in Fig. 17a, $m_{111}/(L_*\sigma_y)$, and 17b, $m_{112}/(L_*\sigma_y)$, for $L_*/R = 0.4$. As can be seen, the higher order stresses are concentrated close to the interface, where a considerable amount of plastic strain gradients is available. However, vanishing higher order stress at the totally debonded point is observable due to the first set of the imposed higher order BC, Eq. (12).

Regarding the implementation of the two sets of higher order BC, Fig. 18 is plotted to highlight the effect of the material length scale, L_*/R, on

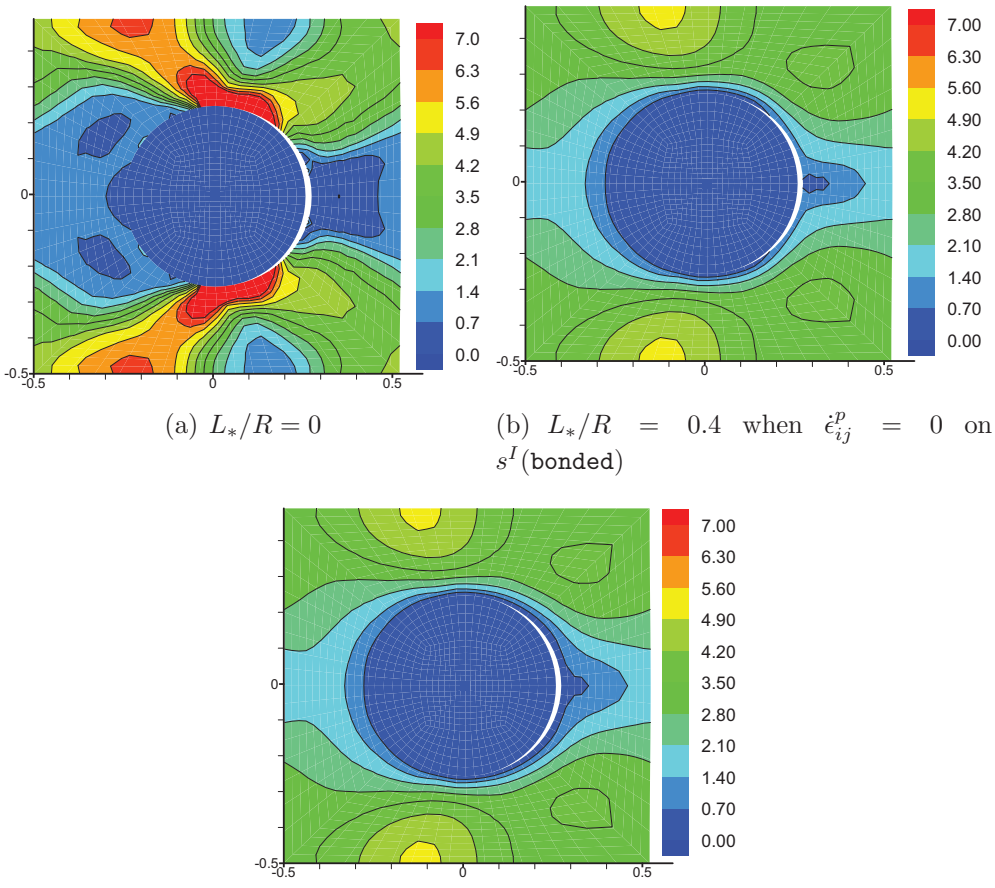

(a) $L_*/R = 0$

(b) $L_*/R = 0.4$ when $\dot{\epsilon}^p_{ij} = 0$ on $s^I(\texttt{bonded})$

(c) $L_*/R = 0.4$ when $\dot{\epsilon}^p_{ij} = 0$ on s^I

Figure 15: Effective plastic strain, ϵ^p_e/ϵ_y, for uniaxial tension with $\delta = 0.03R$ and $\sigma_{max} = \sigma_y$ at the end of loading where $E_{11} = 5\epsilon_y$ with real deformation field.

the relative load carrying capacity, $\Sigma_{11}^{(\dot{\epsilon}^p_{ij}=0 \text{on} s^I)}/\Sigma_{11}^{(\dot{\epsilon}^p_{ij}=0 \text{on} s^I(bonded))}$. As can be seen, with higher value of the material length scale, L_*/R, the load carrying capacity increases from 1.07% to 1.014% corresponding to $L_*/R = 0.2$ and $L_*/R = 0.4$, respectively.

Fig. 19 shows the effect of the fiber volume fraction, V_f, on the stress strain curve with $L_*/R = 0.4$, $\delta = 0.03R$ and $\sigma_{max} = \sigma_y$. Both elastic modulus and hardening enhance with higher fiber volume fraction, which is

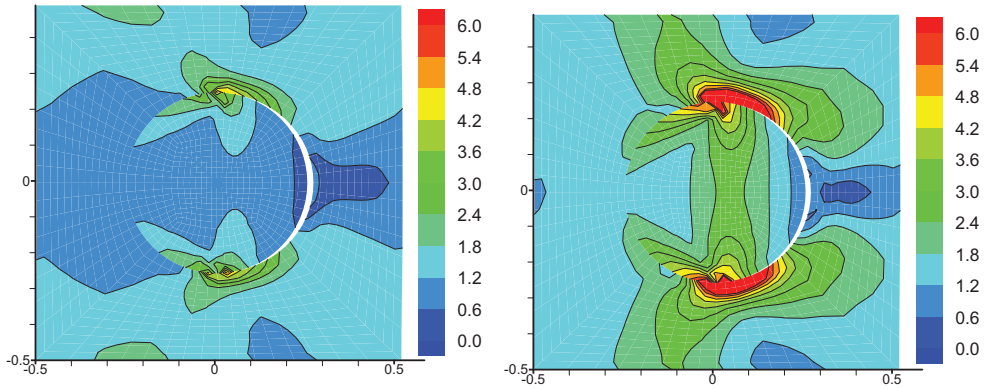

(a) $L_*/R = 0$ (b) $L_*/R = 0.4$ when $\dot{\epsilon}^p_{ij} = 0$ on $s^I(\texttt{bonded})$

Figure 16: Effective stress, σ_e/σ_y, for the uniaxial tension with $\delta = 0.03R$ and $\sigma_{max} = \sigma_y$ at the end of loading where $E_{11} = 5\epsilon_y$ with real deformation field.

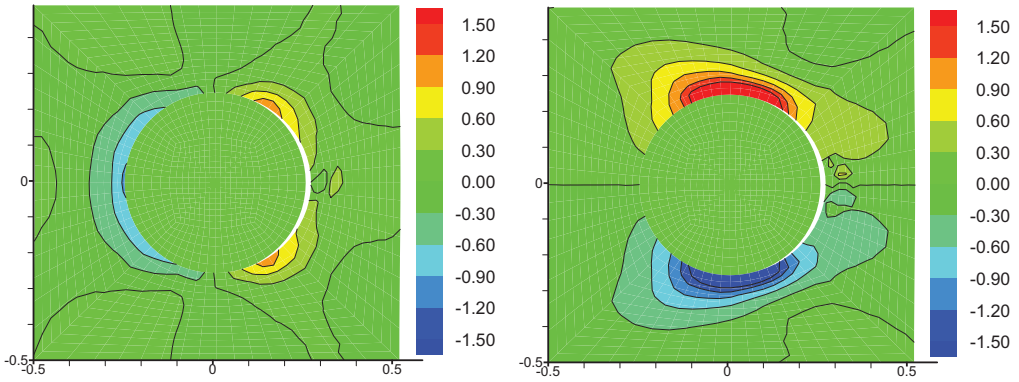

(a) $m_{111}/(L_*\sigma_y)$ (b) $m_{112}/(L_*\sigma_y)$

Figure 17: Higher order stress for uniaxial tension with $L_*/R = 0.4$, $\delta = 0.03R$ and $\sigma_{max} = \sigma_y$ at the end of loading where $E_{11} = 5\epsilon_y$ with real deformation field.

much more intense for the strong interface compared to the weak interface, see also Suh et al. (2009). For the weak interface, the stress-drop occurs at

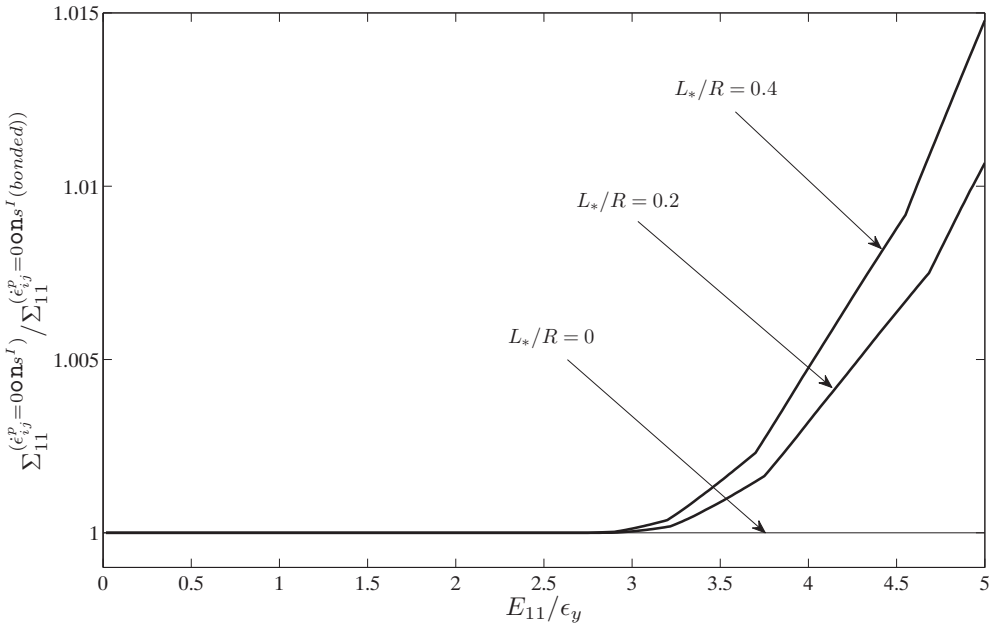

Figure 18: Effect of the material length scale, L_*/R, on the relative load carrying capacity, $\Sigma_{11}^{(\dot{\epsilon}_{ij}^p=0 \mathrm{on} s^I)} / \Sigma_{11}^{(\dot{\epsilon}_{ij}^p=0 \mathrm{on} s^I (bonded))}$, for two sets of the higher order boundary condition, Eq. (12).

$\Sigma_{11} = 1.32\sigma_y$, $1.46\sigma_y$ and $1.49\sigma_y$ corresponding to $V_f = 0.1$, $V_f = 0.2$ and $V_f = 0.3$, respectively. After the total decohesion, the hardening is mainly equal to the one before the onset of decohesion.

The corresponding effective plastic strain is shown in Fig. 20 with $L_*/R = 0.4$, $\delta = 0.03R$ and $\sigma_{max} = \sigma_y$. To precisely observe the deformation, the Fig is plotted with 5 times scaling of the displacement field. As can be seen, having higher fiber volume fraction, the plastic strain decreases moderately while the void evolves significantly. Wavy deformation of the unit cell borders is larger for the higher V_f.

6. Conclusion

The elastic plastic response of metal matrix composites considering the failure has been studied. The study includes the rate independent formulation of energetic strain gradient plasticity for the matrix, purely elastic model

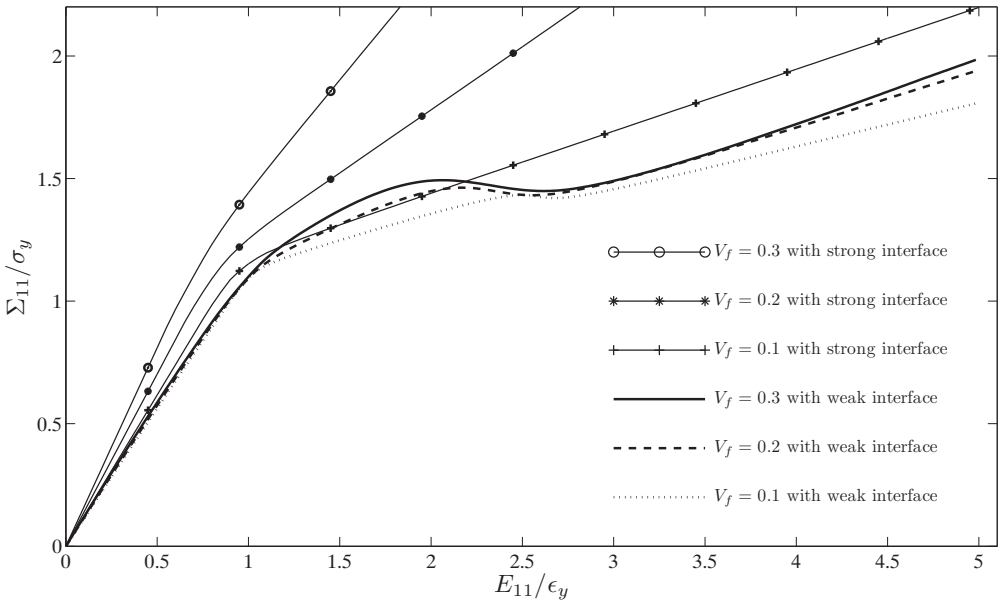

Figure 19: Effect of the fiber volume fraction, V_f, on the stress strain curve of uniaxial tension with $L_*/R = 0.4$, $\delta = 0.03R$ and $\sigma_{max} = \sigma_y$.

for the fiber and cohesive zone model for the fiber-matrix interface. A unit cell, containing a circular fiber is analyzed under both simple shear and uniaxial transverse tension using plane strain and periodic boundary conditions.

It is shown that the material length scale, L_*/R, does not affect the elastic modulus but it enhances the hardening. Mainly, hardening enhancement occurs due to the fact that gradient dependent material has a smooth transition of plasticity from zero plastic strain at the interface towards the matrix compared to the conventional material which has an abrupt change. As a result, the yield stress is enhanced. Regarding the damage, with the higher L_*/R, the plastic strain is significantly suppressed at the crack tip results into a later decohesion of the fiber-matrix interface. Thereafter, the void evolves slowly for the gradient dependent material compared to the conventional one.
The effect of both critical separation distances (work of separation per unit interface area), $\delta_n = \delta_t = \delta$, and maximum stress carried by the interface,

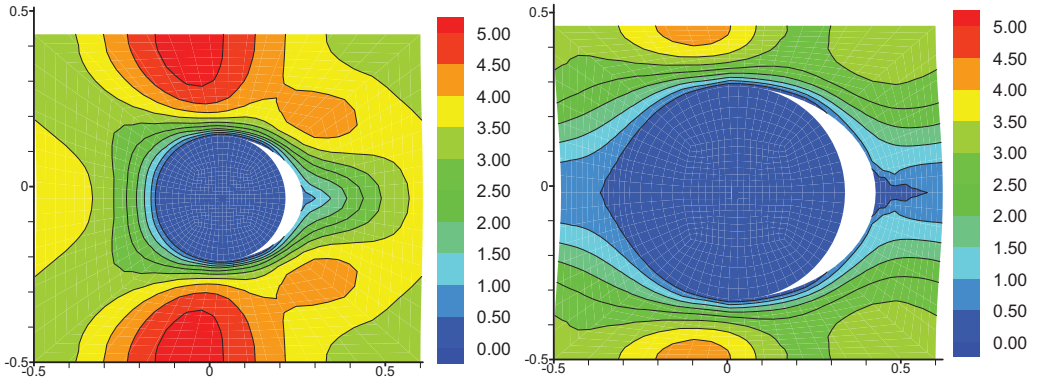

(a) $V_f = 0.1$ (b) $V_f = 0.3$

Figure 20: Effect of the fiber volume fraction, V_f, on the effective plastc strain, ϵ_e^p/ϵ_y, for uniaxial tension with $L_*/R = 0.4$, $\delta = 0.03R$ and $\sigma_{max} = \sigma_y$ at the end of loading where $E_{11} = 5\epsilon_y$ with 5 times scaling of the displacement field.

σ_{max}, on the stress strain curve has been investigated. It was shown that by increasing of both of those parameters, the stress-drop corresponding to the onset of debonding is postponed. However, the effect of σ_{max} is stronger on the strength of the interface compared to the effect of δ. Comparing the weak and strong interfaces, it was observed that the elastic modulus for the material with weak interface is lower compared to the one with strong interface. This is due to the cohesive zone model, where the traction-displacement curve is loosening the material strength before the onset of debonding at $\lambda = 1/3$. The results of two different sets of higher order boundary condition have been compared. It was shown that zero higher order stress after debonding (first set of the higher order BC) has lower load carrying capacity compared to the second set of higher order BC. This is expected since for the second set, plastic suppression at the interface even after total debonding enhances the load carrying capacity.

A significant concentration of the higher order stress at the interface was seen, where the plastic strain gradient is significant. Studying the effect of fiber volume fraction, V_f, on the material response with weak fiber-matrix interface, a small effect on the onset of debonding was seen while the void grows faster with higher V_f. With higher fiber volume fraction, an enhancement of

the hardening was seen for both loading trials.

Acknowledgment

The author would like to thank Associate Prof. Brian N. Legarth, Associate Prof. Christian F. Niordson and Prof. Viggo Tvergaard, Technical University of Denmark for ideas, discussions and comments. This work is supported by the Danish Research Council for Technology and Production Sciences in a project entitled Plasticity Across the Scales. The computational resources have been provided by a hardware grant from the Danish Center of Scientific Computing (DCSC).

References

Acharya, A., Bassani, J. L., 2000. Lattice incompatibility and a gradient theory of crystal plasticity. Journal of the Mechanics and Physics of Solids 48, 1565–1595.

Arnold, S., Pindera, M., Wilt, T., 1996. Influence of fiber architecture on the inelastic response of metal matrix composites. International Journal of Plasticity 12, 507–545.

Azizi, R., Niordson, C., Legarth, B., 2011a. On homogenization of metal matrix composites using strain gradient plasticity. Submitted.

Azizi, R., Niordson, C., Legarth, B., 2011b. Size-effects on yield surfaces for micro reinforced composites. International Journal of Plasticity 27, 1817–1832.

Bassani, J. L., 2001. Incompatibility and a simple gradient theory of plasticity. Journal of the Mechanics and Physics of Solids 49, 1983–1996.

Borg, U., Niordson, C., Kysar, J., 2008. Size effects on void growth in single crystals with distributed voids. International Journal of Plasticity 24, 688–701.

Borg, U., Niordson, C. F., Fleck, N. A., Tvergaard, V., 2006. A viscoplastic strain gradient analysis of materials with voids or inclusions. International Journal of Solids and Structures 43 (16), 4906–4916.

Brockenbroughi, J., Suresh, S., Wienecke, H., 1991. Deformation of metal-matrix composites with continuous fibers: geometrical effects of fiber distribution and shape. Acta metall, mater 39, 735–752.

Carrere, N., Valle, R., Bretheau, T., Chaboche, J., 2004. Multiscale analysis of the transverse properties of ti-based matrix composites reinforced by sic fibres: from the grain scale to the macroscopic scale. International Journal of Plasticity 20, 783–810.

Christman, T., Needleman, A., Nutt, S., Suresh, S., 1989. On microstructural evolution and micromechanical modelling of deformation of a whisker-reinforced metal-matrix composite. Materials Science & Engineering A107 (1), 49–61.

Cornwell, L., Schapery, R., 1975. Sem study of microcracking in strained solid propellant. Metallography 8, 445–452.

Dugdale, D., 1960. Yielding of steel sheets containing slits. J. Mech. Phys. Solids 8, 100–104.

Fleck, N. A., Ashby, M., Hutchinson, J. W., 2003. The role of geometrically necessary dislocations in giving material strengthening. Scripta Materialia 48, 179–183.

Fleck, N. A., Hutchinson, J. W., 1997. Strain gradient plasticity. In: Hutchinson, J. W., Wu, T. Y. (Eds.), Advances in Applied Mechanics. Vol. 33. Academic Press, pp. 295–361.

Fleck, N. A., Hutchinson, J. W., 2001. A reformulation of strain gradient plasticity. Journal of the Mechanics and Physics of Solids 49, 2245–2271.

Fleck, N. A., Willis, J. R., 2009a. A mathematical basis for strain-gradient plasticity theory - Part I: Scalar plastic multiplier. Journal of the Mechanics and Physics of Solids 57, 161–177.

Fleck, N. A., Willis, J. R., 2009b. A mathematical basis for strain-gradient plasticity theory - Part II: Tensorial plastic multiplier. Journal of the Mechanics and Physics of Solids, doi:10.1016/j.jmps.2009.03.007.

Fredriksson, P., Gudmundson, P., L.P., M., 2009. Finite element implementation and numerical issues of strain gradient plasticity with application

to metal matrix composites. International Journal of Solids and Structures 46, 3977–3987.

Gao, H., Huang, Y., 2003. Geometrically necessary dislocation and size-dependent plasticity. Scripta Materialia 48, 113–118.

Gao, H., Huang, Y., Nix, W. D., Hutchinson, J. W., 1999. Mechanism-based strain gradient plasticity - I. Theory. Journal of the Mechanics and Physics of Solids 47 (6), 1239–1263.

Geubelle, P., Baylor, J., 1998. The impact-induced delamination of laminated composites: a 2d simulation. Composites Part B 29, 589–602.

Ghassemieh, E., 2002. Micro-mechanical analysis of bonding failure in a particle-filled composite. Composites Science and Technology 62, 67–82.

Gudmundson, P., 2004. A unified treatment of strain gradient plasticity. Journal of the Mechanics and Physics of Solids 52 (6), 1379–1406.

Gurtin, M. E., 2002. A gradient theory of single-crystal viscoplasticity that accounts for geometrically necessary dislocations. Journal of the Mechanics and Physics of Solids 50 (1), 5–32.

Gurtin, M. E., Anand, L., 2005. A theory of strain-gradient plasticity for isotropic, plastically irrotational materials. Part I: Small deformations. Journal of the Mechanics and Physics of Solids 53 (7), 1624–1649.

Hinz, S., Jones, F., Schulte, K., 2007. Micromechanical modelling of shear deformation of a 90-ply in glare at elevated temperatures. Computational Materials Science 39, 142–148.

Huang, M., Li, Z., 2005. Size effects on stress concentration induced by a prolate ellipsoidal particle and void nucleation mechanism. International Journal of Plasticity 21 (8), 1568 – 1590.

Hussein, M., Borg, U., Niordson, C., Deshpande, V., 2008. Plasticity size effects in voided crystals. Journal of the Mechanics and Physics of Solids 56, 114–131.

Hutchinson, J. W., 2000. Plasticity at the micron scale. International Journal of Solids and Structures 37 (1-2), 225–238.

Legarth, B. N., 2004. Unit cell debonding analyses for arbitrary orientations of plastic anisotropy. International Journal of Solids and Structures 41 (26), 7267–7285.

Legarth, B. N., Niordson, C. F., 2010. Debonding failure and size effects in micro-reinforced composites. International journal of plasticity 26 (1), 149–165.

Lele, S. P., Anand, L., 2008. A small-deformation strain-gradient theory for isotropic viscoplastic materials. Philosophical Magazine 88 (30), 1478–6435.

Lloyd, D. J., 1994. Particle reinforced aluminium and magnesium matrix composites. International Materials Reviews 39 (1), 1–23.

Moraleda, J., Segurado, J., Llorca, J., 2009. Effect of interface fracture on the tensile deformation of fiber-reinforced elastomers. International Journal of Solids and Structures 46, 4287–4297.

Mughrabi, H., 2001. The effect of geometrically necessary dislocations on the flow stress of deformed crystals containing a heterogeneous dislocation distribution. Materials Science and Engineering, 139–143.

Nan, C., Clarke, D., 1996. The influence of particle size and particle fracture on the elastic/plastic deformation of metal matrix composites. Acta mater 44, 3801–3811.

Needleman, A., 1987. A continuum model for void nucleation by inclusion debonding. Transactions of the ASME. Journal of Applied Mechanics 54 (3), 525–531.

Needleman, A., Borders, T., Brinson, L., Flores, V., Schadler, L., 2010. Effect of an interphase region on debonding of a cnt reinforced polymer composite. Composites Science and Technology 70, 2207–2215.

Niordson, C. F., 2003. Strain gradient plasticity effects in whisker-reinforced metals. Journal of the Mechanics and Physics of Solids 51 (10), 1863 – 1883.

Niordson, C. F., Tvergaard, V., 2001. Nonlocal plasticity effects on the tensile properties of a metal matrix composite. European Journal of Mechanics - A/Solids 20 (4), 601–613.

Niordson, C. F., Tvergaard, V., 2002. Nonlocal plasticity effects on fibre debonding in a whisker-reinforced metal. European Journal of Mechanics - A/Solids 21 (2), 239–248.

Park, S., Schapery, R., 1997. A viscoelastic constitutive model for particulate composites with growing damage. International Journal of Solids and Structures 34, 931–947.

Perng, C., Hwang, J., Doong, J., 1993. High strain rate tensile properties of an (a1203 particles)-(al alloy 606l-t6) metal matrix composite. Materials Science and Engineering A171, 213–221.

Segurado, J., LLorca, J., 2005. A computational micromechanics study of the effect of interface decohesion on the mechanical behavior of composites. Acta Materialia 53, 4931–4942.

Suh, Y., Joshi, S., Ramesh, K., 2009. An enhanced continuum model for size-dependent strengthening and failure of particle-reinforced composites. Acta Materialia 57, 5848–5861.

Teply, J., Dvorak, G., 1988. Bounds on overall instantaneous properties of elastic-plastic composites. J. Mech.Phys. Solids 36, 29–58.

Totry, E., Molina, A., Gonzalez, C., LLorca, J., 2010. Effect of fiber, matrix and interface properties on the in plane shear deformation of carbon-fiber reinforced composites. Composites Science and Technology 70, 970–980.

Tvergaard, V., 1990. Effect of fibre debonding in a whisker-reinforced metal. Materials Science and Engineering A125, 203–213.

Tvergaard, V., Hutchinson, J. W., 1992. The relation between crack growth resistance and fracture process parameters in elastic-plastic solids. Journal of the Mechanics and Physics of Solids 40 (6), 1377–1397.

Vratsanos, L., Farris, R., 1993. A predictive model for the mechanical behavior of particulate composites. part i: model derivation. Polymer Engineering and Science 33, 1458–1464.

Xu, X., Needleman, A., 1994. Numerical simulation of fast crack growth in brittle solids. J. Mech. Phys. Solids 42, 1397–1434.

Xu, X.-P., Needleman, A., 1993. Void nucleation by inclusion debonding in a crystal matrix. Modelling and Simulation in Materials Science and Engineering 1, 111–132.

Yao, Y., Huang, Z., 2011. A new nonlocal cohesive stress law and its applicable range. Engineering Fracture Mechanics 78, 1101–1113.

Zhang, H., Ramesh, K., Chin, E., 2005. Effects of interfacial debonding on the rate-dependent response of metal matrix composites. Acta Materialia 53, 4687–4700.

DTU Mechanical Engineering
Section of Solid Mechanics
Technical University of Denmark

Nils Koppels Allé, Bld. 404
DK- 2800 Kgs. Lyngby
Denmark
Phone (+45) 45 25 42 50
Fax (+45) 45 93 14 75
www.mek.dtu.dk
ISBN: 978-87-90416-63-8

DCAMM
Danish Center for Applied Mathematics and Mechanics

Nils Koppels Allé, Bld. 404
DK-2800 Kgs. Lyngby
Denmark
Phone (+45) 4525 4250
Fax (+45) 4593 1475
www.dcamm.dk
ISSN: 0903-1685